University of Rochester
Laboratory for Laser Energetics

DOE/SF/19460-52
January 1995

LLE 1994 Annual Report

October 1993 – September 1994

Inertial Fusion Program and National Laser Users Facility Program

MASTER

DISCLAIMER

Contents

Executive Summary

The fiscal year ending September 1994 (FY94) concluded the second year of the cooperative agreement (DE-FC03-92SF19460) with the U. S. Department of Energy. This report summarizes research at the Laboratory for Laser Energetics (LLE) and progress on the OMEGA Upgrade construction project for FY94.

OMEGA Upgrade Program

Much progress has been made since the beginning of the system-integration phase of the OMEGA Upgrade project. In November 1993 all of the main target bay structures were installed, and all of the structures for the laser system were installed in the laser bay. Progress has been significant on the power conditioning system, the control system, the opto-mechanical system, and the targeting system for OMEGA. A summary of the OMEGA Upgrade system status at the beginning of the fiscal year is described beginning on p. 32. During much of FY94, the OMEGA Upgrade project focused on the fabrication, assembly, and testing of all components installed in the system, followed by system integration activities. We completed a facility operations readiness review, designed all laser drivers, and activated the pulse-generation room. We began assembly of the laser amplifiers and took delivery of a number of the major subsystems for the upgrade. A summary of these activities begins on p. 157.

We have tested a large-aperture (37-mm) ring amplifier (LARA)—the main component of the OMEGA Upgrade driver line—that delivers output energies in excess of 15 J in a 1-ns pulse at a wavelength of 1.053 μm (p. 90).

The LARA delivers a beam at full aperture with approximately 1-wave (peak-to-valley) distortion on the wavefront quality with a prepulse contrast ratio greater than 10,000.

The environmental stability of thin-film coatings is essential for successful operation of the OMEGA system. We report (p. 97) on the effect on water-induced surface damage using an atomic force microscope.

It is important that a high-power laser beam maintain a high degree of wavefront quality after propagating a long distance through air. Laser drivers for inertial fusion use intense laser beams that propagate tens of meters through air. We report (p. 109) on the effect of stimulated rotational Raman scattering and propagation though a spatial filter at various vacuum pressures on the spatial uniformity of a high-power laser beam in support of the OMEGA Upgrade project.

In FY95, we will complete the construction and system activation for the OMEGA Upgrade. The project schedule calls for submission and acceptance of both an Operational Readiness Review Plan and an Acceptance Test Plan. After approval of these two plans, the project will move from a period of transition to operations to Key Decision IV "Project Complete/Start Operations" (KD IV) during FY95.

Diagnostics Development

Diagnostics development has been an important focus of the experimental and engineering divisions this year. Much of the effort is directed at the development, engineering, and testing of advanced diagnostic packages to be used on the OMEGA Upgrade after KD IV is achieved.

Grid image refractometry is a new technique for determining the two-dimensional density profiles of long-scale-length, laser-produced plasmas. This technique (p. 10) includes some unique features that make it applicable to laser-produced plasmas with millimeter scale lengths.

We have devoted considerable attention to target imaging and backlighting diagnostics for the OMEGA Upgrade. The expected backlighting and self-emission images of a particular CH target to be imploded on the OMEGA Upgrade have been calculated (p. 57). To overcome the problem of target self-emission, the image is monochromatized with a diffracting crystal. A computer study delineates the interesting images that may be expected.

Beginning on p. 114, we discuss the use of x-ray backlighting to diagnose an imploding target subject to mixing. The expected images from targets exhibiting mixing at the fuel-pusher interface that are either doped with a high-Z element or undoped CH shells show the utility of using a monochromatic backlighter to study this interface. The simulations indicate that data from this diagnostic technique will be used to deduce both the low-order nonuniformity and compression of the final core.

A large scintillator array (*m*ulti-*e*lement *d*etector *u*sing a *s*cintillator *a*rray—*MEDUSA*) has been built to measure the secondary neutron emission from ICF targets (p. 121). The MEDUSA diagnostic will be used to study the details of the neutron energy spectrum about the 14-MeV neutron emitted from the $d(t,He^4)n$ secondary reaction for targets filled with D_2. The ability to monitor the individual channels (960) of this diagnostic is important to the interpretation of the data. A technique that uses cosmic rays to determine the status of each scintillator-photomultiplier detector is shown to provide the necessary information to evaluate the performance of the MEDUSA diagnostic.

Progress in Laser Fusion

Analysis of observed emission of radiation near the 3/2 harmonic of the irradiating laser frequency conducted previously on OMEGA (p. 27) shows that any interpretation in terms of self-interaction of the laser beam with primary plasmons it created via the two-plasmon instability (TPI) is not credible. Rather it seems necessary to invoke a secondary electron-plasma-wave decay (EPD) of the "blue" plasmon from the two-plasmon instability. The EPD has its own threshold, exceeded only when the TPI is well above its threshold. Hence, onset of the 3/2 signal is not a good measure of the onset of the TPI. The k-dependence of the EPD explains also why only spectral splitting corresponding to the Landau cutoff is observed.

Experiments have been conducted to observe the acceleration of electrons from an underdense gas in the focal volume of a high-intensity laser (p. 103). First-order relativistic effects are expected to occur for laser intensities of $\geq 10^{18}$ W/cm^2. The longitudinal acceleration of electrons from the magnetic-field term in the Lorentz force has been observed for the first time.

Since future OMEGA targets will have much thicker cryogenic fuel layers than those dealt with previously, improved interferometric methods are necessary for accurate characterization. In response, a convergent beam interferometer has been developed (p. 83) and its properties described.

In a recent collaboration with the University of Michigan, an extensive set of experiments demonstrated the second-harmonic conversion at efficiencies of ~80% using 500-fs, 1053-nm laser pulses. The experimental data are in agreement with simulations that indicate that self-phase modulation and cross-phase modulation are important in experiments to extend ultra-intense laser-matter experiments to shorter wavelengths.

Theoretical efforts this year have investigated a number of important aspects of laser-matter interaction. The collisional damping of ion-acoustic waves was calculated for a mixture of light and heavy ions (p. 22). The results are strikingly different from those using a single-species average-ion model. The improved result includes a new joule term as well as thermal diffusion and viscous damping contributions. The overall damping rate can be increased as much as 58-fold, when evaluated properly.

In related work, a Fokker-Planck code (p. 76) has allowed us to include electron-electron collisions as well as ion-electron collisions in calculations of the damping rate of ion-acoustic waves. We note significant corrections can occur for low-Z plasmas in the moderate collisional range. We have also determined the effect on the thermal conductivity.

The threshold of the absolute stimulated Brillouin scattering (SBS) instability and its steady-state spatial growth rate are independent of the scattering angle for homogeneous plasmas of relevance to inertial confinement fusion. The saturation time of the convective instability does exhibit, however, a strong inverse dependence on the scattering angle (p. 142). Although this analysis was directed at SBS, certain results apply to other parametric instabilities, such as stimulated Raman scattering.

In support of short-pulse, high-intensity experiments, we have conducted particle-in-cell simulations of the interaction of a laser with a plasma. A very-short-scale-length regime, with vacuum heating, and long-scale-length regime, with classic resonance absorption, have been identified (p. 76). Between these limits, there is an interesting and complex transition regime.

Theoretical hydrodynamic analysis of unsteady ablation fronts has been carried out for a semi-infinite uniform medium.

For a laser-accelerated target, it is shown that a properly selected modulation of the laser intensity can lead to the dynamic stabilization or growth-rate reduction of a large portion of the unstable spectrum. The theory (p. 1) is in qualitative agreement with the numerical results obtained by using the two-dimensional hydrodynamic code *ORCHID*. The cutoff wave number of the incompressible ablative Rayleigh-Taylor instability (p. 131) is calculated using the physical optics approximation of the WKB (Wentzel, Kramers, and Brillouin) theory. A single value for the cutoff wave number can correspond to multiple modes with different eigenfunctions and growth rates.

Advanced Technology

We have investigated the carrier-refraction effect to modulate the refractive index of silicon (p. 138). This modulation will allow one to construct an all-silicon, light-intensity modulator for use as a transmitter of integrated-circuit optical communication. The bandwidth of the proposed modulator will be limited only by the RC time constant and is calculated to be about 40 GHz.

In other advanced optical material applications, we have investigated femtosecond excited-state dynamics of a conjugated ladder polymer. Among the known classes of nonlinear optical materials, π-conjugated polymers are attractive because of the large third-order susceptibilities and ultrafast response times. Transient photoinduced bleaching of the π–π^* transition accompanied with photoinduced absorption in the optical gap was observed for a thin-film, conjugated-ladder polymer. Femtosecond, time-resolved measurements of both a 2-eV (620-nm) optical pump and a white-light-continuum probe show an absorption decay with a fast subpicosecond component and a slow (~20-ps) component.

National Laser Users Facility

The National Laser Users Facility (NLUF) continues to be active during the construction of the OMEGA Upgrade. Six NLUF proposals for FY94 were selected for funding by DOE. These proposals continue support for the principal investigators and their students, with most of the work devoted to the development of advanced diagnostics that will be tested on the OMEGA Upgrade. The NLUF news and individual summaries of the approved proposals are discussed beginning on p. 159. Table I summarizes the approved users' proposals.

Education at LLE

Education continues to be a central activity and one of the most important missions of the Laboratory for Laser Energetics. Our students include graduate students performing Masters and Ph.D. research, undergraduate students working part-time during the school year and in cooperative education programs, and high school students participating in the summer research program. The educational program is supported by the strong

Table I: NLUF proposals approved by the Department of Energy for FY94.

Investigator	Institution	Proposal Title
J. Reader	National Institute of Standards and Technology	Measurements of Quantum Electrodynamic Sensitive Transitions in Na-like and Cu-like Ions
J. F. Seely	Naval Research Laboratory	Normal-Incidence Multilayer Mirror X-Ray Microscope
A. Honig	Syracuse University	Temperature-Dependent Tensile Strength, Surface Roughness Diagnostics, and Magnetic Support and Positioning of Polymer ICF Shells at Temperatures Between 4K and 300K
K. Mizuno	Plasma Physics Research Institute University of California, Davis	The Ion Acoustic Decay Instability in a Large-Scale, Hot Plasma Relevant to Direct-Drive Laser Fusion—Applications to a Critical Surface Diagnostic and Thermal Smoothing
C. F. Hooper, Jr.	University of Florida	Plasma Spectroscopy: Theoretical and Experimental Diagnostic Development/Tests
H. R. Griem	University of Maryland	Development of Density and Temperature Profile Diagnostics for ICF Targets

participation of University faculty. Seventeen faculty members at the University of Rochester collaborate with the scientists or engineers at LLE. The faculty and students come from many departments and schools within the University, including Mechanical Engineering, Chemical Engineering, Electrical Engineering, Optics, and Physics and Astronomy.

The graduate program provides education and training in inertial-confinement fusion and related areas, notably plasma physics, ultrafast technology, laser development, and materials sciences. There are approximately 50 students pursuing all or part of their graduate research at LLE. Twenty of these students receive Frank J. Horton Fellowships.

During the past year, seven students received their Ph.D. degrees at the May 1994 commencement. Table II lists those students and their dissertation titles.

LLE employs approximately 50 undergraduate students, including cooperative education program students. Most of the students provide technical support for the scientific and engineering projects at LLE. During the past year, many students were actively involved in the installation of the OMEGA Upgrade laser system. Most of the students are employed in areas related to their undergraduate major to afford them the opportunity to apply classroom concepts in a professional laboratory environment.

Eight students who completed their junior year in high school participated in the 1994 Summer Research Program at LLE. This is the sixth year that the Laboratory has conducted such a program. The program is eight weeks in duration and receives partial support from the National Science Foundation. The program exposes students to state-of-the-art research in science and technology, and many of the students have been motivated to pursue technical careers.

Robert L. McCrory
Director

Table II: Ph.D.'s awarded and thesis titles for May 1994.

Student Name	Thesis Title
Elizabeth Murphy	Experimental Studies of Surface Melting and Time-Resolved Superheating of Metal Surfaces
Justin Peatross	The Far-Field Angular Distribution of High-Order Harmonics Produced in Light Scattering from a Thin, Low-Density Gas Target
Sotiris Alexandrou	The Bent Coplanar Waveguide at Sub-Terahertz Frequencies
Paul Ballentine	High-Temperature Superconducting Thin Films: Sputter Deposition and Fast Optical Switching
John Herman	Time-Resolved Structural Studies of the Low-Index Faces of Lead
Conor Twomey	Poly [(Methylene Oxide) Oligo (Ethylene Oxide)] and Poly (Ethylene Oxide) Doped with Rare Earth Metal Compounds: Solubility, Complex Formation, Morphology, and Applications
Bradford Tousley	Ultrafast Carrier Dynamics of Bulk InGaAs, Low-Temperature-Grown InGaAs, and MQW InGaAs

Stability Analysis of Unsteady Ablation Fronts

The classical Rayleigh-Taylor instability[1] occurs when a heavy fluid is accelerated by a lighter fluid. In inertial-confinement fusion (ICF) the heavy fluid is the compressed ablated target material that is accelerated by the low-density ablated plasma. The classical treatment of the incompressible Rayleigh-Taylor instability leads to a linear growth rate given by $\gamma = \sqrt{|kg|A}$, where k is the instability wave number, g is the acceleration, and A is the Atwood number $A = (\rho_h - \rho_l)/(\rho_h + \rho_l)$. ($\rho_l$ and ρ_h represent the light- and heavy-fluid densities, respectively.) For typical (ICF) parameters, a classical Rayleigh-Taylor instability would produce an unacceptably large amount of distortion in the unablated target, resulting in a degraded capsule performance with respect to the final core conditions. Thus, it is important to study the possible means for suppression of the ablation surface instability in ICF. It has been recently shown that the ablation process leads to convection of the perturbation away from the interface between the two fluids.[2–5] Since the instability is localized at the interface, the ablative convection stabilizes short-wavelength modes. The typical growth rate of the ablative Rayleigh-Taylor instability can be written in the following approximate form:[3]

$$\gamma = \sqrt{|kg|A} - \beta|kV_a| \,, \tag{1}$$

where V_a is the ablation velocity and β is a numerical factor ($\beta \simeq 3-4$).

In this article we show that a properly selected modulation of the laser intensity can significantly reduce the unstable spectrum and the maximum growth rate. To treat the analytic linear stability of unsteady ablation fronts, we consider a simplified sharp boundary model consisting of a heavy fluid, with density ρ_h, adjacent to a lighter fluid (ρ_l), in the force field $\mathbf{g}(t) = g(t)\mathbf{e}_y$ in a direction opposite to the density gradient [$g(t) < 0$ and $\mathbf{e}_y$ is the unit vector in the direction of the density gradient] and with an arbitrary time dependence. The heavy fluid is moving downward with velocity $\mathbf{U}_h = -V_a\mathbf{e}_y$, and the lighter fluid is ejected with velocity U_l. The equilibrium velocities $U_l(t)$ and $U_h(t)$ are both dependent on the ablation ratio per unit surface $\dot{m}(t)$ that is treated as an arbitrary function of time. The equilibrium can be readily derived from conservation of mass and momentum. We consider a class of equilibria with nonuniformities localized at the interface between the two fluids. Continuity of the mass flow and the pressure balance across the interface lead to the following conditions:

$$\rho_l U_l(t) = \rho_h U_h(t) \tag{2}$$

$$P_h - P_l = \rho_l U_l^2(t) - \rho_h U_h^2(t) \,, \tag{3}$$

where P_h and P_l represent the pressure of the heavy and light fluid, respectively, at the interface. Notice that U_l and U_h are negative in the chosen frame of reference. We assume that the discontinuities in the equilibrium quantities can be removed by including the physics of the ablation process.

The linear stability problem can be greatly simplified by an appropriate choice of the linearized equation of state. It is widely known that the most Rayleigh-Taylor unstable perturbations are incompressible. Furthermore, ablative stabilization is a convective process and is, therefore, independent of the equation of state. It follows that the essential physics of the instability can be captured by a simple incompressible flow model. The stability analysis proceeds in a standard manner. All perturbed quantities are written as $Q_1 = \tilde{Q}(y,t)\exp(ikx)$, and the system of equations describing the linear evolution of the perturbation assumes the following form:

$$\begin{aligned}
&(\partial_t + U_j\partial_y)\tilde{\rho}_j = 0, \\
&\rho_j(\partial_t + U_j\partial_y)\tilde{v}_{jx} = -ik\tilde{p}_j \\
&\rho_j(\partial_t + U_j\partial_y)\tilde{v}_{jy} + \tilde{\rho}_j\partial_t U_j = -\partial_y\tilde{p}_j + \tilde{\rho}_j g \\
&ik\tilde{v}_{jx} + \partial_y\tilde{v}_{jy} = 0,
\end{aligned} \tag{4}$$

where the subscript j denotes the heavy fluid region ($j = h$) and the light fluid region ($j = l$) and $\partial_y = \partial/\partial y$, $\partial_t = \partial/\partial t$. The two regions are separated by an interface (the ablation front) that moves with the heavy fluid. In order to match the solutions in the two regions, an equation describing the evolution of the interface is needed. Such an equation can be easily derived by a comparison with a nonablative equilibrium ($U_h = 0$). In that case the interface $\left[y = \tilde{\eta}(t)\exp(ikx)\right]$ moves with the heavy fluid, and the rate of distortion $\left(\partial_t\tilde{\eta}\right)$ is equal to the normal component of the velocity, $\partial_t\tilde{\eta} = \tilde{v}_{hy}(y = 0, t)$. In the ablative case, the heavy fluid is moving toward the ablation front with velocity $U_h = -V_a$. A Lagrangian surface, coming from $y = +\infty$, would become distorted as it approaches the interface where the instability is localized (Fig. 57.1). As for static equilibria, the rate of distortion $\left(\tilde{\xi}\right)$ of that surface is still equal to the normal component of the velocity:

$$\frac{d\tilde{\xi}}{dt} = \tilde{v}_{hy}. \tag{5a}$$

However, since the surface is moving, the time derivative has to be convective $\left(d_t = \partial_t + U_h\partial_y\right)$. From Eq. (5a) the distortion of a Lagrangian surface can be written in the following integral form:

$$\tilde{\xi}(t) = \int_{-\infty}^{t} \tilde{v}_{hy}\left[y_0(t'), t'\right]dt', \tag{5b}$$

where

$$y_0(t') = \int^{t'} U_h(t'')dt'' + constant$$

is the unperturbed trajectory of a Lagrangian surface. In the absence of smoothing effects, the ablation front coincides with that Lagrangian surface whose equilibrium orbit overlaps the ablation front ($y = 0$) at time $t' = t$. The unperturbed trajectory of such a surface is given by

$$y_0(t') = \int_{t}^{t'} U_h(t'')dt'',$$

and the equation for the evolution of the ablation front $\left(\tilde{\eta}\right)$ can be written in the following differential form:

$$\partial_t\tilde{\eta} = \tilde{v}_{hy}[0,t] - U_h(t)\int_{-\infty}^{t}\frac{\partial\tilde{v}_{hy}}{\partial y}\left[y_0(t'), t'\right]dt'. \tag{5c}$$

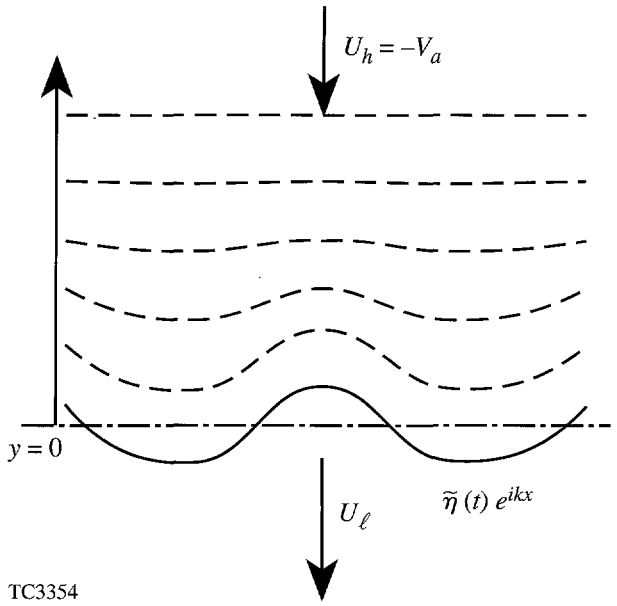

Figure 57.1
Deformation of a Lagrangian surface approaching the ablation front.

Once $\tilde{\eta}$ is known, a set of jump conditions relating the values of the physical quantities in the two regions can be derived by writing the time derivative of any perturbed quantity at the ablation front as $\partial_t\tilde{Q} = -\left(Q_h - Q_l\right)\partial_t\tilde{\eta}\,\delta(y)$ and integrating the incompressibility and conservation equations across the thin ablative layer. A short calculation yields

$$\begin{aligned}
&\tilde{v}_{hy} = \tilde{v}_{ly}\\
&\left(\rho_h - \rho_l\right)\left(\partial_t\tilde{\eta} - \tilde{v}_{hy}\right) - U_h\tilde{\rho}_h + U_l\tilde{\rho}_l = 0\\
&\tilde{v}_{hx} - \tilde{v}_{lx} + ik\tilde{\eta}\left(U_h - U_l\right) = 0\\
&\tilde{p}_h - \tilde{p}_l + \tilde{\rho}_h U_h^2 - \tilde{\rho}_l U_l^2 + g\left(\rho_h - \rho_l\right)\tilde{\eta} = 0.
\end{aligned} \tag{6}$$

The first of Eqs. (6) follows directly from the incompressibility condition $\nabla\cdot\tilde{\mathbf{v}} = 0$. A better representation of the perturbation at the interface can be obtained by using an equation of state and calculating the jump in the energy.[2] This approach would greatly complicate the calculation. However, as shown in Appendix A, when the flow is subsonic

$$\left[U_h^2, U_l^2 << p_h/\rho_h, p_l/\rho_l\right],$$

the flow of internal energy across the interface has to be conserved and the incompressible result is recovered.

The next step is to solve Eqs. (4) in the two regions and then apply the jump conditions and the boundary conditions at $y = \pm\infty$. Since the heavy and light fluids extend to infinity and the instability is localized at the interface, the perturbation must vanish at $y = \pm\infty$.

The solution of the linearized equation in the heavy-fluid region (h) is greatly simplified by the following transformation: $y_h = y - \int_0^t U_h(t')dt'$. A straightforward calculation leads to the following form of the perturbed variables in region h:

$$\begin{aligned}
\tilde{v}_{hy} &= \tilde{u}_h(t)\exp(-ky_h) + \tilde{a}(y_h) \\
\tilde{v}_{hx} &= \frac{i}{k}\frac{\partial\,\tilde{v}_{hy}}{\partial y_h} \\
\tilde{\rho}_h &= \tilde{\rho}_h(y_h) \\
\tilde{p}_h &= -\frac{\rho_h}{k^2}\frac{\partial^2\tilde{v}_{hy}}{\partial t\partial y_h},
\end{aligned} \tag{7}$$

where $\tilde{u}_h(t)$, $\tilde{\rho}_h(y_h)$, and $\tilde{a}(y_h)$ are arbitrary functions of t and y_h, and k is chosen to be positive $(k > 0)$. In order to satisfy the boundary conditions, $\tilde{a}$ and $\tilde{\rho}_h$ must vanish at $y_h \to \infty$. Since $\lim_{t\to\infty} y_h = \infty$, it follows that $\tilde{a}$ and $\tilde{\rho}_h$ asymptotically vanish in time. In our asymptotic stability analysis, we neglect all the quantities that do not grow in time. Thus, we set $\tilde{a} = 0$ and $\tilde{\rho}_h = 0$. Furthermore, because of the incompressibility condition and negative flow velocity, $\tilde{\rho}_h = 0$ at all times.

We apply the same procedure to the light-fluid region (l) and define the new coordinates $y_l = y - \int_0^t U_l(t')dt'$. The solution of the linearized equations in region l can be written in the following form:

$$\begin{aligned}
\tilde{v}_{ly} &= \tilde{u}_l(t)\exp(ky_l) + \tilde{b}(y_l) + \tilde{c}(y_l)f(t) \\
\tilde{v}_{lx} &= \frac{i}{k}\frac{\partial\,\tilde{v}_{ly}}{\partial y_l} \\
\tilde{\rho}_l &= \tilde{\rho}_l(y_l) \\
\tilde{p}_l &= -\frac{\rho_l}{k^2}\frac{\partial^2\tilde{v}_{ly}}{\partial t\partial y_l},
\end{aligned} \tag{8}$$

where $\tilde{b}(y_l)$ and $\tilde{\rho}_l(y_l)$ are free functions of y_l that vanish at $y_l \to -\infty$, and $\tilde{u}_l(t)$ is an arbitrary function of t. The functions $\tilde{c}(y_l)$ and $f(t)$ satisfy the following differential equations:

$$\begin{aligned}
&\left[\frac{d^2}{dy_l^2} - k^2\right]\tilde{c} + k^2\frac{\tilde{\rho}_l}{\rho_l} = 0 \\
&\frac{df}{dt} = G(t),
\end{aligned} \tag{9}$$

where

$$G(t) \equiv g(t) - \frac{\partial U_l}{\partial t}. \tag{10}$$

The next step is to recognize that, using Eqs. (7) in Eq. (5c), the interface equation can be rewritten in the following form: $(\partial_t - kU_h)\tilde{\eta} = \tilde{v}_{hy}(y = 0, t)$.

After substituting Eqs. (7) and (8) into the jump conditions [Eqs. (6)] and using the differential form of the interface equation, the following ordinary differential equation for $\tilde{\eta}(t)$ is derived:

$$\begin{aligned}
&(\partial_t - kU_l)G^{-1}\{(\partial_t - kU_l)(\partial_t - kU_h)\tilde{\eta} \\
&+ A[kU_l(\partial_t - kU_h) + kg]\tilde{\eta}\} \\
&- Ak^2U_h\tilde{\eta} = 0,
\end{aligned} \tag{11}$$

where

$$A \equiv (\rho_h - \rho_l)/(\rho_h + \rho_l)$$

is the Atwood number. For ICF applications, the appropriate ordering

$$U_h/U_l = \rho_l/\rho_h \sim (1 - A) << 1 \text{ and } g > \partial U_l/\partial t.$$

To lowest order in 1-A, the last term in Eq. (11) can be neglected, yielding

$$\{(\partial_t - kU_l)(\partial_t - kU_h) + A[kU_l(\partial_t - kU_h) + kg]\}\tilde{\eta} = 0. \tag{12}$$

Equation (12) can be further simplified by using the Ansatz

$$\tilde{\eta}(t) = \xi(t)\exp\left[\frac{3}{2}k\int_0^t U_h(t')dt'\right] \qquad (13)$$

and by neglecting other terms of order $(1-A) << 1$. After some straightforward manipulations, we obtain

$$\frac{d^2\xi}{dt^2} + k\left[Ag - \frac{1}{2}\frac{dV_a}{dt} - \frac{1}{4}kV_a^2\right]\xi = 0\ , \qquad (14)$$

where g and V_a are functions of time with V_a the ablation velocity. Observe that, for steady equilibrium configurations, Eqs. (13) and (14) yield the normal mode solution for $\tilde{\eta} \sim \exp(\gamma t)$, with γ satisfying the dispersion relation

$$\gamma = \sqrt{\left(|kg|A\right) + \frac{1}{4}k^2V_a^2} - \frac{3}{2}|kV_a|\ . \qquad (15)$$

It is easy to recognize that the contribution of the second term under the square root is relevant only at very small wavelengths, where the mode is already strongly stabilized by convection [the last term in Eq. (15)]. Neglecting such a term in Eqs. (14) and (15) would cause only a small shift of the cutoff wave number $\left[\Delta k_c/k_c = 1/9\right]$, which is consistent with the order of magnitude of the previous approximations. After neglecting such a term, Eq. (15) reproduces the numerically derived growth rate of Ref. 3 with β = 1.5. Equations (13) and (14), which are valid for arbitrary unsteady configurations, can now be applied to the particular equilibrium obtained by temporally modulating the laser intensity. Consider a planar target of thickness d and density ρ_0 irradiated by a uniform laser beam. The periodically modulated laser intensity $\left[I(t) = I_0\left(1+\Delta\sin\omega_0 t\right), \Delta \le 1\right]$ induces an oscillating ablation pressure $P_a(t) = P_0\left(1+\Delta_p\sin\omega_0 t\right)$ and ablation velocity $V_a(t) = V_{a0}\left(1+\Delta_a\sin\omega_0 t\right)$ with $\Delta_p \lesssim \Delta$ and $\Delta_a \lesssim \Delta$. For simplicity, we assume that the ablation pressure and the ablation velocity are directly proportional to the laser intensity, and the ablation process develops on a very slow time scale compared to an oscillation period and the sound transit time through the target [$V_a << c_s$, c_s is the sound speed]. Although the scaling $V_a \sim \sqrt{I} \sim \left[1+\Delta\sin(\omega_0 t)\right]^{1/2}$ is more appropriate than a simple linear dependence, the numerical simulations show that the ablation velocity is almost insensitive to the oscillations in the laser intensity $\left(\Delta_a << 1\right)$ and $V_a \simeq V_{a0}$. I_0 and P_0 are two slowly varying functions of time

$$\left[V_a/d < (1/I_0)(dI_0/dt) = (1/P_0)(dP_0/dt) << \omega_0 \sim c_s/d\right].$$

A simple estimate of the acceleration of the ablation front can be derived by solving the one-dimensional compressible fluid equations of Ref. 6 for a target accelerated by the ablation pressure. As shown in Appendix B, the time-dependent acceleration can be written in the following form:

$$g(t) = -\frac{dV_a}{dt} - L^{-1}\left\{\coth\left[\frac{s}{c_s}\left(d-\bar{y}_a\right)\right]\frac{s\hat{p}_a(s)}{\rho_0 c_s}\right\}, \qquad (16)$$

where L^{-1} denotes the inverse Laplace transform, s is the Laplace variable, and $\hat{p}_a(s)$ is the Laplace transform of the ablation pressure. The quantity $\bar{y}_a = \int_0^t V_a(t')dt'$ is the position of the ablation front in the Lagrangian frame of the moving target. In deriving Eq. (16), the slow ablation time scale $\left(\sim d/V_a\right)$ has been treated as an independent variable. A simple expression for $g(t)$ can be derived in the asymptotic limit $\left(d/V_a\right) > t >> \left(d/c_s\right)$, yielding

$$g(t) = -g_0\left[1+\alpha\sin\omega_0 t + \epsilon\cos\omega_0 t\right]\ , \qquad (17)$$

where $g_0 \equiv P_0/\rho_0 d_a$, $\alpha \equiv \Delta_p\left(\omega_0 d_a/c_s\right)\cot\left(\omega_0 d_a/c_s\right)$, and $\epsilon = V_{a0}\,\Delta_a\omega_0/g_0$, $d_a = d - \bar{y}_a$. A more accurate estimate of $g(t)$ (and of the parameters g_0, α, and ϵ) can be obtained by using a one-dimensional code. Later in this article we will use the one-dimensional hydrodynamic code *LILAC*[7] to derive g_0, α, and ϵ. However, Eq. (17) gives some physical insight into the relevant quantities that affect the oscillation amplitude in the target acceleration. In particular, large oscillations can be achieved for values of the modulation period shorter than the sound transit time through the target $\left[T_0 \equiv 2\pi/\omega_0 < d/c_s\right]$. Before proceeding further, it is important to define the range of validity of the stability model for the prescribed equilibrium. The oscillations in the ablation pressure propagate inside the target at the sound speed. Thus, the equilibrium parameters can be considered as uniform over a distance $\Delta y < c_s T_0$. The stability analysis, carried out for a uniform semi-infinite medium, can be applied to perturbations with sufficiently short wavelength $k\Delta y > 1$. It follows that a necessary condition for the validity of the stability model is $kc_s T_0 >> 1$. For such wavelengths, Eq. (17) can be used in

Eq. (14) to derive the function $\xi(t)$. Thus, Eq. (14) can be written in the following form:

$$\frac{d^2\xi}{dt^2} - \gamma_c^2\left[1 + q\sin(\omega_0 t + \phi)\right]\xi = 0 \ , \qquad (18)$$

where $\gamma_c = \sqrt{A|kg_0|}$ is the classical growth rate,

$$q = \sqrt{\alpha^2 + 9\epsilon^2/4} \ ,$$

and

$$\phi = \tan^{-1}(3\epsilon/2\alpha) \ .$$

Notice that Eq. (18) is a Mathieu equation, whose solution has the form $\xi(t) = \sigma(t)\exp(\mu t)$, with $\sigma(t)$ being periodic with period ω_0. Using Eq. (13), the growth rate of the instability can be easily derived:

$$\gamma = -k\beta\frac{1}{T_0}\int_0^{T_0} V_a(t')dt' + \mu \ , \qquad (19)$$

where $\beta = 1.5$ for the simplified stability model. However, when Eq. (19) is compared to the Takabe formula, we let $\beta = \beta^T = 3-4$. In order to find μ, one needs to numerically solve Eq. (18) for one period of oscillation. Figure 57.2 shows the parameter μ, plotted versus the wave number k, for the following equilibrium parameters: $d = 20\ \mu$m, $g_0 = 5 \times 10^{15}$ cm/s^2, $A = 1$, $\langle V_a \rangle = 7 \times 10^4$ cm/s, $c_s = 10^6$ cm/s, $T_0 = 0.3 \times 10^{-9}$ s, $\phi = 0$, and $q = 0$, 2.5, and 3.5. The validity of the stability model requires $\lambda = 2\pi/k << 20\,\mu$m. For any value of q and ω_0, it is possible to identify intervals of the k axis, where $Re[\mu] = 0$. We denote such intervals as dynamically stabilized (DS) regions, and we emphasize the importance of ablative convection [see Eq. (19)] at shorter wavelengths. According to Eqs. (1) and (19), the short-wavelength modes are stabilized by convection, and the cutoff wave number is $k_c = gA/\beta^2 V_A^2$. It follows that an efficient dynamic stabilization can be achieved by choosing values of q and ω_0 that cause the first DS region to be located inside the interval $0 < k < k_c$. In Fig. 57.3, the growth rates derived from Eq. (19) for q = 0, 2.5, and 3.5 and β = 3.5 (as given by Takabe *et al.*[3]) are shown. Observe that as q increases, a better stabilization is induced at longer wavelengths, but shorter wavelengths can be destabilized (q = 3.5). This short-wavelength instability is driven by the oscillations in the acceleration, with the perturbation having the characteristic structure of an oscillatory mode with an exponentially increasing amplitude. For convenience, we denote these short-wavelength modes as "parametric instabilities."

Furthermore, when the mode wavelength is smaller than the density gradient scale length

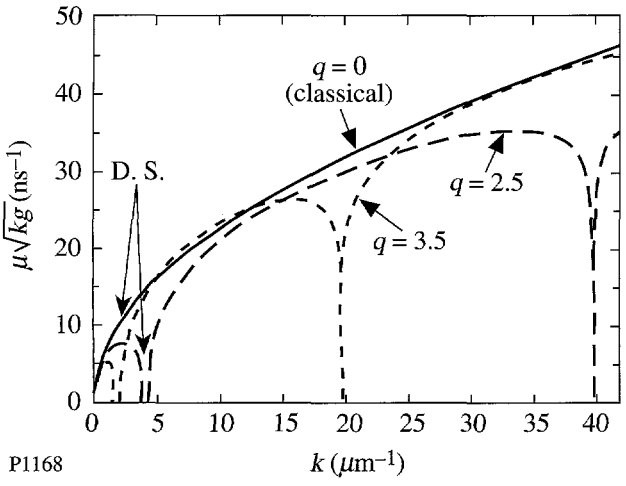

Figure 57.2
Plot of the instability drive term μ versus the mode wave number k for modulated ($q \neq 0$) and unmodulated ($q = 0$) laser intensity, assuming $d = 20\ \mu$m, $g_0 = 5 \times 10^{15}$ cm/s^2, the Atwood number $A = 1$, $\langle V_a \rangle = 7 \times 10^4$ cm/s, $T_0 = 0.3$ ns, and $\phi = 0$.

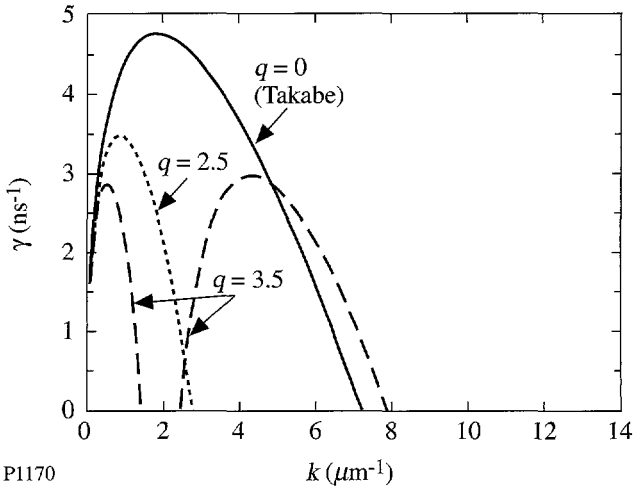

Figure 57.3
Plot of the instability growth rate versus the mode wave number k for modulated ($q \neq 0$) and unmodulated ($q = 0$) laser intensity, assuming the same equilibrium parameters as in Fig. 57.1.

$$\left[\delta = \left|(1/\rho)\, d\rho/dy\right|^{-1}\right],$$

the sharp boundary model is not valid and Eq. (19) cannot be used.

The results of the analytic theory have been compared with two-dimensional simulations obtained using the code *ORCHID*.[8] We have considered an 18-μm CH planar target irradiated by a uniform laser beam of wavelength 1.06 μm. The laser intensity is modulated in time with a period of 0.3 ns. The modulation amplitude is 100%, and the flat-top average intensity is 50 TW/cm^2. For an accurate comparison with the analytic stability theory, we derive the equilibrium parameters g, $\langle V_a \rangle$, and q from the one-dimensional code *LILAC*.[7] The result is $g = 4.5 \cdot 10^{15}\,\mathrm{cm/s^2}$, $\langle V_a \rangle = 7 \cdot 10^4\,\mathrm{cm/s}$, $\delta \simeq 1.5$ to 2 μm, $\phi = 0$, and $q = 3.5$ to 5.5. In the two-dimensional simulation, an initial single-wavelength perturbation evolves for 3 ns. Because of the short modulation period, the simulation shows no significant change in the foil isentrope with respect to the unmodulated case. Figure 57.4 shows a comparison between the linear growth rate derived from the simulation with the one given by Eq. (19). Three regions of the k-axis can be identified: (1) The long-wavelength region with $k < 0.2\ \mu\mathrm{m}^{-1}$, where the growth rate is virtually insensitive to the modulation of the laser intensity and very close to the classical value. (2) The intermediate wavelength region with $0.2 < k < 1$. For these values of the wave number, the dynamic stabilization is particularly effective. Observe that for $\lambda = 2\pi/k \approx 7\,\mu\mathrm{m}$ the mode is completely stabilized. (3) The short-wavelength region is defined as having a wave number $k > 1$. In this region $k\delta > 1$ and the effect of finite density-gradient scale length cannot be neglected. Notice that the simulation shows the presence of an unstable mode with wavelength $\lambda \approx 5$ μm. Using Eq. (19) beyond its limit of validity ($k\delta < 1$) and dividing γ_c^2 by $(1 + \theta k\delta)$ with $\theta < 1$, we would predict the existence of parametric instabilities at shorter wavelengths (Fig. 57.4). However, the structure of the perturbation observed in the numerical simulation does not clearly show the characteristics of a parametric instability. Furthermore, the cutoff wave number observed in the numerical simulation (with or without laser-intensity modulation) is much shorter than the one predicted by Eqs. (1) and (19). The stability of very-short-wavelength perturbations needs further investigation to determine an accurate value of the cutoff wave number.

The dynamic stabilization of the Rayleigh-Taylor instability in ICF targets was first observed in numerical simulations by J. Boris.[9] In this article we have shown the derivation of the linear stability theory for unsteady ablation fronts and the conditions for the dynamic stabilization of the ablative Rayleigh-Taylor instability. The growth rate of the instability has been calculated for a sinusoidal modulation of the laser intensity. It is shown that an appropriate modulation frequency and amplitude can stabilize a large portion of the unstable spectrum and significantly reduce the maximum growth rate.

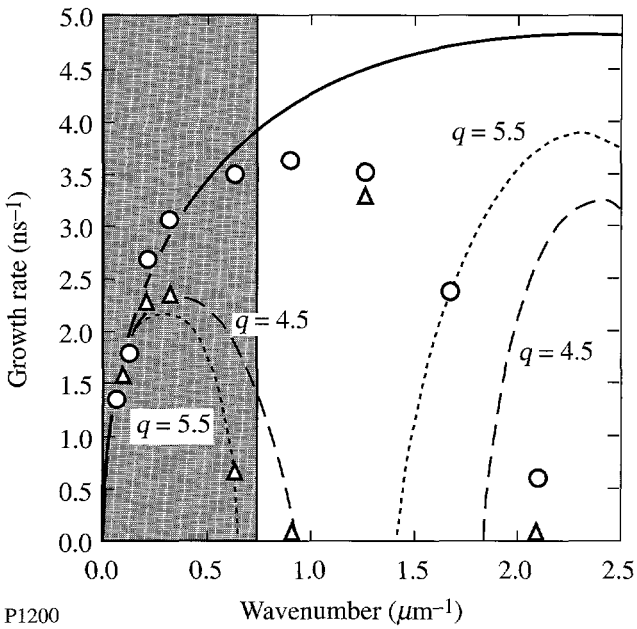

Figure 57.4
Comparison of the growth rate obtained from numerical simulations (with modulation Δ and without modulation O) and the modified Eq. (19). Here, $d = 18$ μm, $g_0 = 4.5 \times 10^{15}$ cm/s^2, $\langle V_a \rangle = 7 \times 10^4$ cm/s, $T_0 = 0.3$ ns, $\phi = 0$, $A = 1$, $\beta = 3$, $\theta\delta = 1.5 \times 10^{-5}$ cm, $q = 5.5$ (dotted), $\beta = 4$, $\theta\delta = 0.3 \times 10^{-5}$ cm, $q = 4.5$ (dashed). The solid line represents the Takabe formula, and the shaded area represents the region with $\kappa\delta \leq 1$.

ACKNOWLEDGMENT

This work was supported by the U.S. Department of Energy Office of Inertial Confinement Fusion under Cooperative Agreement No. DE-FC03-92SF19460, the University of Rochester, and the New York State Energy Research and Development Authority. The support of DOE does not constitute an endorsement by DOE of the views expressed in this article.

APPENDIX A: CONDITIONS FOR INCOMPRESSIBLE FLOW

A better model for the Rayleigh-Taylor instability can be obtained by replacing the incompressibility condition with an adiabatic equation of state. In the heavy- and light-fluid regions, where the velocity and density equilibrium profiles are uniform, the linearized adiabatic equation of state can be written as

$$\left(\partial_t + U_j\partial_y\right)\tilde{p}_j + \tilde{v}_{jy}\frac{dP_J}{dy} + \frac{5}{3}P_j\nabla\cdot\tilde{v}_j = 0, \quad \text{(A.1)}$$

where P_j represents the equilibrium pressure in the region j. Ordering $\partial_t \sim \sqrt{kg} \sim kU_h$ and using the momentum conservation equation, one finds that $\tilde{p}_j \sim \rho_j U_j \tilde{v}_j$, $\partial_y \tilde{p}_j \sim k\tilde{p}_j$, and $\left(dP_J/dy\right) \sim \rho g$. A simple comparison between the two terms in Eq. (A.1) yields

$$\frac{P_j\nabla\cdot\tilde{v}_j}{\left(\partial_t + U_j\partial_y\right)\tilde{p}_j + v_{jy}\left(dP_J/dy\right)} \sim \frac{1}{M_j^2}, \quad \text{(A.2)}$$

where $M_j^2 = 3\rho_j U_j^2/5P_j$ is the Mach number in region j. For subsonic flows ($M_j << 1$), Eq. (A.1) leads to the incompressibility condition $\nabla\cdot\tilde{v}_j \simeq 0$. Although the flow in the two regions is clearly incompressible, at the interface between the fluids, where the equilibrium velocity and density have very sharp gradients, the conclusions derived above do not immediately apply.

A jump condition relating the energies in the two regions can be derived by integrating the adiabatic equation of state across the ablative layer. Following the work of Ref. 2, the calculation can be greatly simplified by using the conservative form of the equation of state:

$$\partial_t\left(\frac{1}{2}\rho v^2 + \frac{3}{2}p\right) + \nabla\cdot\left[\left(\frac{1}{2}\rho v^2 + \frac{5}{2}p\right)\mathbf{v}\right]$$

$$= \rho\mathbf{g}\cdot\mathbf{v} + I\delta\left(y-\tilde{\eta}\right), \quad \text{(A.3)}$$

where I is the power deposited at the ablation front. Integrating Eq. (A.3) and linearizing the variables yields the following jump condition for the fluid energy:

$$\partial_t\tilde{\eta}\left(\rho_h U_h^2 - \rho_l U_l^2\right) + \left(\frac{3}{2}\rho_h U_h^2 + \frac{5}{2}P_h\right)\tilde{v}_{hy}$$

$$-\left(\frac{3}{2}\rho_l U_l^2 + \frac{5}{2}P_l\right)\tilde{v}_{ly} + \frac{5}{2}\tilde{p}_h U_h$$

$$-\frac{5}{2}\tilde{p}_l U_l - \frac{1}{2}\tilde{\rho}_l U_l^3 = 0, \quad \text{(A.4)}$$

where all the quantities are calculated at the unperturbed ablation front ($y = 0$). In the derivation of Eq. (A.4), the incompressible results in the two regions have been used. The ordering for the perturbed quantities can be derived from the conservation equations

$$\partial_t\tilde{\eta} \sim \tilde{v}_{hy}/kU_h \qquad \tilde{p}_j \sim \rho_j U_j \tilde{v}_j \qquad \tilde{\rho}_l \sim \rho_h\tilde{v}_{hy}/U_l \quad \text{(A.5)}$$

Substituting the relations in Eq. (A.5) into Eq. (A.4) yields the following equation for the perturbed normal velocities at the ablation front:

$$\left[1 + O\left(M_h^2\right)\right]\tilde{v}_{hy} = \left[1 + O\left(M_l^2\right)\right]\tilde{v}_{ly} \quad \text{(A.6)}$$

For $M_j^2 \to 0$, Eq. (A.6) reduces to

$$\tilde{v}_{hy} = \tilde{v}_{ly}. \quad \text{(A.7)}$$

Observe that the latter can also be derived from the incompressibility condition $(\nabla\cdot\mathbf{v} = 0)$ integrated across the ablative layer. Thus, the assumption of incompressible flow holds at the ablation front as well as at the two uniform regions on both sides of the interface when the Mach number is much less than unity, i.e., the flow is subsonic.

APPENDIX B: UNSTEADY EQUILIBRIUM OF AN ACCELERATED TARGET

The time evolution of the equilibrium of a planar target accelerated by an externally applied pressure $P_a(t)$ can be obtained by solving the one-dimensional fluid equations of Ref. 6. In ICF the accelerating pressure is induced by the laser irradiation. In order to simplify the calculation, we rewrite the fluid equations in a Lagrangian frame, and we neglect the reduction of the target thickness due to ablation. Let $y_T(\bar{y},t)$ be the trajectories of the fluid elements and $\bar{y}$ the Lagrangian coordinate: i.e., the position of the fluid elements at time $t = 0$. As shown in Ref. 6, a linear wave equation describing the evolution of the fluid trajectories can be derived from the nonlinear set of equations

$$\frac{\partial^2 y_T}{\partial t^2} = c_s^2 \frac{\partial^2 y_T}{\partial \bar{y}^2}, \tag{B.1}$$

where c_s is the sound speed of the target at rest. We consider a planar target of thickness $d\left(0 \le \bar{y} \le d\right)$ with the irradiated side at $\bar{y} = 0$ $\left[p(0,t) = P_a(t)\right]$. On the surface opposite to the laser $\left(\bar{y} = d\right)$, the external pressure is negligible $\left[p(d,t) = 0\right]$. These boundary conditions lead to the following equations for the trajectories at $\bar{y} = 0$ and $\bar{y} = d$:

$$\frac{\partial y_T}{\partial \bar{y}}(0,t) = 1 - \frac{P_a(t)}{\rho c_s^2} \qquad \frac{\partial y_T}{\partial \bar{y}}(d,t) = 1\,. \tag{B.2}$$

We let the laser irradiation start at time $t = 0$ (target at rest). Thus, the velocity at $t = 0$ is zero through the target:

$$\frac{\partial y_T}{\partial t}(\bar{y},0) = 0 \qquad y_T(\bar{y},0) = \bar{y}. \tag{B.3}$$

Equation (B.1), together with the boundary and initial conditions [Eqs. (B.2) and (B.3)], can be solved in the Laplace transform domain. A short calculation yields the following form of the Laplace transform (L) of the acceleration:

$$\hat{g}(s,\bar{y}) = \frac{\hat{P}(s)}{\rho c_s}\, s\, \frac{\cosh\left[\dfrac{s}{c_s}(d-\bar{y})\right]}{\sinh\left(\dfrac{sd}{c_s}\right)}, \tag{B.4}$$

where

$$g(\bar{y},t) = \frac{\partial^2 y_T}{\partial t^2} \qquad \hat{g}(\bar{y},s) = L\left[g(\bar{y},t)\right]$$
$$\hat{P}_a(s) = L\left[P_a(t)\right] \tag{B.5}$$

and s is the Laplace variable. Using the identity

$$\frac{1}{\sinh z} \equiv 2\sum_{n=0}^{\infty} e^{-(2n+1)z}$$

and taking the inverse transform of Eq. (B.4), we obtain the acceleration of the ablation front

$$g(0,t) = \frac{1}{\rho c_s}\left\{\frac{dP_a}{dt}\left[t - \frac{\bar{y}}{c_s}\right] + 2\sum_{n=1}^{\infty}\frac{dP_a}{dt}\left[t - \frac{2nd}{c_s}\right]\Theta\left[t - \frac{2nd}{c_s}\right]\right\}, \tag{B.6}$$

where $\Theta(t)$ is the Heaviside step function. Focusing on an oscillating applied pressure induced by an oscillating laser intensity

$$\left[P_a(t) = P_0\left(1 + \Delta_p \sin\omega_0 t\right)\right],$$

we determine the asymptotic value of the acceleration after many periods of the oscillation $\left(t\omega_0 >> 1\right)$. A short calculation yields

$$g(0,t) = \frac{P_0}{\rho d}\left(1 + \alpha \sin\omega_0 t\right), \tag{B.7}$$

where $\alpha = \Delta_p\left(\omega_0 d/c_s\right)\cot\left(\omega_0 d/c_s\right)$. The first term on the RHS represents the incompressible component of the acceleration. The other terms are induced by the oscillation in the applied pressure and vanish for $c_s \to \infty$, i.e., incompressible fluid. Observe that Eq. (B.7) yields the resonant condition for the oscillations, $\omega_0 d/\pi c_s = n$, where $n = 1,2,\ldots$.

A more accurate expression of the acceleration can be obtained by retaining the effect of finite ablation velocity (V_a). For a subsonic ablation flow ($V_a << c_s$) and times shorter than the ablation time $\left(2\pi/\omega_0 << t << d/V_a\right)$, the ablative flow can be treated as a perturbation of the equilibrium. Thus, the acceleration becomes

$$g(0,t) = g_0\left(1+\alpha\sin\omega_0 t + \in \cos\omega_0 t\right), \qquad \text{(B.8)}$$

where $g_0 = P_0/\rho d_a$, $d_a = d - \int_0^t V_a dt'$ is the target thickness at time t, and the ablation velocity has been taken proportional to the laser intensity $\left[V_a = V_{a0}\left(1+\Delta_a \sin\omega_o t\right) \propto I(t)\right]$. For typical ICF parameters and oscillation periods of the order of hundreds of picoseconds, the term $\in = \Delta_a V_{a0}\omega_0/g_0$ is much less than unity and can be neglected.

REFERENCES

1. Lord Rayleigh, *Scientific Papers* (Cambridge University Press, Cambridge, England, 1900), Vol. II, p. 200.
2. S. E. Bodner, Phys. Rev. Lett. **33**, 761 (1974).
3. H. Takabe, K. Mima, L. Montierth, and R. L. Morse, Phys. Fluids **28**, 3676 (1985).
4. H. J. Kull and S. I. Anisimov, Phys. Fluids **29**, 2067 (1986).
5. A. B. Bud'ko and M. A. Liberman, Phys. Rev. Lett. **68**, 178 (1992).
6. N. Rostoker and H. Tahsiri, Comments Plasma Phys. Cont. Fusion **3**, 39 (1977).
7. E. B. Goldman, Laboratory for Laser Energetics Report No. 16, 1973 (unpublished); J. Delettrez and E. B. Goldman, Laboratory for Laser Energetics Report No. 36, 1976 (unpublished).
8. R. L. McCrory and C. P. Verdon, *Computer Applications in Plasma Science and Engineering*, edited by Adam T. Drobot (Springer-Verlag, NY, 1991), pp. 291–325.
9. J. P. Boris, Comments Plasma Phys. Cont. Fusion **3**, 1 (1977).

Characterization of Laser-Produced Plasma Density Profiles Using Grid Image Refractometry

Grid image refractometry (GIR)[1] is proposed as a new technique for determining the two-dimensional density profiles of long-scale-length laser-produced plasmas such as will be generated on the OMEGA Upgrade. Interferometry, which has been successfully used to diagnose smaller plasmas, is unsuited to these plasmas because of problems associated with high fringe counts and fringe blurring.

The distinctive feature of GIR is that an optical probe beam is broken up into "rays" by being passed through a grid before traversing the plasma. The refraction angles of these rays are measured by imaging the plasma at two or more object planes and are integrated to yield the phase front. For cylindrically symmetric plasmas the density profile is then determined using Abel inversion. The feasibility of GIR is illustrated here by an analysis of an experiment carried out at KMS Fusion. The inferred density profile is substantially larger than any previously reported using interferometry and compares quite closely with *SAGE* hydrodynamic simulations.

Introduction

A fundamental concern in the study of laser-plasma interactions is the characterization of the plasma density profile that results when one or more laser beams irradiate a solid target. Knowledge of quantities including the plasma density, scale length, and temperature is especially important for the understanding of stimulated plasma physics processes, which can lead to a reduction in the overall laser-target coupling efficiency and/or the production of energetic electrons that potentially preheat the fusion fuel. In addition, it is desirable to compare experimental density profiles with predictions of hydrodynamic simulations in order to check the accuracy of computer modeling, especially in two dimensions where there is a sparsity of experimentally determined density profiles. Such comparisons might also provide insight into different models of thermal transport in the underdense corona.

The primary diagnostic of plasma density profiles has for many years been interferometry. Typically a short, 0.26-μm optical probe beam, derived from frequency quadrupling a Nd:glass laser, has been used to diagnose electron densities (n_e) up to ~1×10^{21} cm^{-3}. Generally the plasma is cylindrically symmetric, and Abel inversion (see, for example, Refs. 2–4) has been used to obtain the two-dimensional density profile. (Regrettably, very few such two-dimensional profiles have ever been published.) Notable results from interferometry have included the observation of profile steepening for 1-μm laser wavelengths,[5,6] where the high spatial resolution of interferometry has allowed scale lengths of ~1 μm to be measured. However, plasmas of current interest are less amenable to interferometric characterization for a number of reasons—the primary reason being their size. Exploding-foil plasmas with density scale length L_n ~0.5–1 mm have been produced on lasers such as NOVA[7] at the Lawrence Livermore National Laboratory and OMEGA[8] at the University of Rochester, and plasmas with true reactor scale lengths ($L_n \gtrsim 1$ mm) have recently been produced on NOVA using foams and high-density gas targets.[9] Interferograms of these plasmas would contain hundreds of fringes with spacing d_F (in the plane of the plasma) ranging from a few microns to around a millimeter. (The minimum spacing $d_{\min}$ is approximately equal to $2F\lambda_p$, where F is the f number of the collection optics and λ_p is the probe wavelength, and the maximum spacing is comparable to the plasma scale length at the density corresponding to the outer fringe.) A large field of view would thus be required. Moreover, the fringe pattern can change very rapidly in time and be smeared out unless a sufficiently short probe beam is used.

To illustrate the limitations of plasma interferometry it is worth noting that, to the best of our knowledge, there are no reports in the literature of laser-produced plasma density profiles that have been determined from interferograms with over 20 fringes. (One fringe corresponds to a path length of 8 μm for a 0.25-μm probe and a plasma density of 10^{21} cm^{-3}.) In experiments in which small microballoon targets[5,6,10,11] or fiber tips[12,13] were irradiated with short laser pulses of 1-μm wavelength, ~5 fringes were typically observed. For 10-μm laser irradiation of somewhat bigger microballoons,[14] ~10 fringes were observed (after the subtraction of back-

ground fringes). In later experiments on the CHROMA laser, in which targets were irradiated at 0.5 μm and diagnosed with a four-frame holographic system,[15] 10–20 fringes were observed both for exploding-foil targets[16,17] and cryogenic microballoon targets.[18] Large fringe counts (up to ~75) were seen in other (unpublished) experiments on CHROMA and were often limited by blurring due to plasma motion and inhomogeneities. Of all the experiments cited here, only in the 10-μm case[14] were the two-dimensional density contours reported.

A further problem, not unique to interferometry but shared by all optical probing techniques, is that it is unrealistic to probe to (electron) densities higher than 1 (or possibly 2) $\times$ 10^{21} cm^{-3}. This density is independent of the plasma size but does depend (usually weakly) on the plasma shape. (Simple estimates of this density are given in Ref. 1.) While this allows probing to the critical density (n_c) for 1-μm radiation, information can generally be obtained only up to ~0.1–0.2 n_c for the short laser wavelengths ($\lambda \lesssim 0.35$ μm) of current interest. This is not a substantial concern since stimulated Raman scattering, one parametric process of great interest, occurs strongly at densities $n_e \sim 0.1\ n_c$, and sometimes parametric processes at lower densities are also of interest.[19] Moreover, in the exploding-foil geometries that are often used for plasma physics experiments (see Ref. 8 and references therein), the density gradients tend to zero in the center of the plasma, the refractive limitation does not apply there, and higher densities can be diagnosed.

The long-scale-length plasmas generated on OMEGA[8] were diagnosed using a simple Schlieren technique in which the inner portion of the collection optic was blocked by a disk of f number F_s. Images of the plasma thus provided two contours of deflection angle, $\theta_{\min} = \tan^{-1}\ (2F_s)^{-1}$ and $\theta_{\max} = \tan^{-1}\ (2F)^{-1}$, where F is the f number of the collection optic. Comparison of these images with two-dimensional hydrodynamic/ray-tracing simulations using the code *SAGE*[20] showed good agreement, increasing confidence in the predicted density profiles. However, insufficient information was obtained to enable the density profile to be arrived at independent of simulations.

Grid image refractometry (GIR), as described in this article, is a more general Schlieren technique that can permit the independent experimental determination of density profiles. It permits, in principle, every contour of deflection angle (up to $\theta_{\max}$) to be obtained, thus providing sufficient information for the density profile to be inferred for plasmas with cylindrical symmetry. The term "refractometry" is used to describe the well-established technique whereby the refractive index $\mu(\mathbf{r})$ of an optical medium is inferred from the refraction angles $\Delta\theta(p)$ of a one- or two-dimensional set of probe rays parametrized by an impact parameter p. For the common case of cylindrical symmetry, Abel inversion of $\Delta\theta(p)$ to give $\mu(\mathbf{r})$ is straightforward.[3]

With GIR, the refraction angles are measured by passing an optical probe beam through a grid before it propagates through the plasma. An image of the grid is formed within the plasma with a relatively long depth of focus. The probe beam is effectively broken up into a two-dimensional set of "rays," one ray corresponding to each point on the grid. The collection optics are then used to form two or more images of the grid corresponding to different object planes within the plasma. The refraction angles of each ray (in the two orthogonal directions) may be determined simply from the difference between the apparent positions of the associated grid element in two object planes divided by the distance between those planes.

A wide variety of alternative methods for measuring the refraction angles have been reported. The technique closest to GIR is known as the "point-grid method" and is described by Vasil'ev.[21] Here a two-dimensional square grid is placed at an appropriate point in the path of the probe beam (after the medium being probed and near a focal plane of the imaging optics). Again, each grid point may be thought of as corresponding to a ray. By comparing the grid-point positions in the images taken with and without the optical medium present (the working and reference images, respectively), the ray deflection angles in each direction can be obtained from a knowledge of the parameters of the optical system. This was illustrated in Ref. 21 with a cylindrical medium (air flowing around a heated pipe) probed parallel to its axis. Essentially the same method was used by Gurfein *et al.* to measure the density profile of a very compressible fluid (near-critical CO_2) in the Earth's gravitational field,[22] and by Miyanaga *et al.*[23] and Benattar[24] to determine the density profile in the overdense region of a laser-produced plasma using x rays as the probing radiation. In Ref. 23, kilo-electron-volt x rays from a point source passed through a laser-irradiated spherical target, through a zone plate (used as a grid), and onto film; from the observed distortion of the image of the zone plate the ray refraction angles (up to 8 mrad) and hence the electron-density profile (10^{23}–10^{24} cm^{-3} with a scale length ~20 μm) were determined. A closely related technique, moiré deflectometry,[25] has also been demonstrated for x-ray

wavelengths.[26] Moiré deflectometry provides the ray refraction angles in one direction. A similar principle is embodied in Hartmann sensors used for the testing of optical surfaces.[27] Here the phase front is broken up into rays by being passed through a screen perforated with an array of holes; the ray deflection angles are then calculated from the ray locations in a far-field recording plane. Photothermal deflection provides yet another form of refractometry and has been used, for example, to diagnose the laser ablation of materials.[28] Here the whole-beam deflection is measured of a probe beam whose diameter is small in comparison with the scale length of the medium being probed. A separate shot is needed for each impact parameter, although a single shot suffices if the shape of the refractive index profile in the medium is known independently.

Interferometry may be considered to be a form of refractometry in which wave rather than geometrical optics are used to measure the refraction angle. The fringe spacing d_F determines the angle $\Delta\theta$ between the actual and reference wavefronts: for small angles, $d_F \approx \lambda_p/\Delta\theta$. In the approximation of weak refraction, integration of the refraction angle (or equivalently fringe counting) yields the phase front, although the case of strong refraction, where fringe distortion and ray crossing can occur, is more complicated.

One advantage of GIR is that the impact parameters of all probe rays are known. The point-grid and other methods described above are all diagnostics of the emerging wavefront, requiring the impact parameter of each ray to be inferred. Distortion of the fringe count and the apparent fringe positions due to small focusing errors (between the object plane of the probe beam and the symmetry axis of the irradiating laser) has been a major problem in plasma interferometry. GIR, however, is not sensitive to this error; indeed, in the data reduction reported here, no knowledge of the absolute location of any of the object planes was needed. For the diagnosis of long-scale-length plasmas, GIR can provide essentially the same density information as interferometry, but it does not suffer from the major drawbacks of interferometry. The micron spatial resolution of interferometry is lost, but this is not usually an important consideration for millimeter scale lengths.

In this article the GIR technique is illustrated by an experiment carried out at KMS Fusion on the CHROMA laser. Useful data were obtained from just one shot. From this data, it has been possible to extract very plausible density profiles that compare quite closely with two-dimensional hydrodynamic simulations using the code *SAGE*.

Experiment

The layout of the KMS experiment is shown schematically in Fig. 57.5(a). An incident laser of wavelength $\lambda_L = 527$ nm irradiated a 50-μm-thick solid CH disk target. The plasma was diagnosed using a short (~30-ps), 263-nm probe beam (of energy ~10 μJ) that was passed in the z direction through a copper-mesh grid, of spatial periodicity 50 μm × 50 μm, before passing through the plasma. The optical system relayed an image of the grid into the plasma, with unit magnification, onto the plane $z = z_0$ containing the incident laser axis, using a fairly slow, $f/10$, source lens. The refracted probe light was collected by an $f/2$ catadioptric reflector system[15] and relayed to a plane where it interfered with a reference beam and was recorded on holographic film. On reconstruction, an image of the grid was formed on the film plane with a magnification of ~10. The advantage of the holographic recording used was that by varying the position of the film plane, images were obtained corresponding to various different object planes (14 in total) within the plasma.

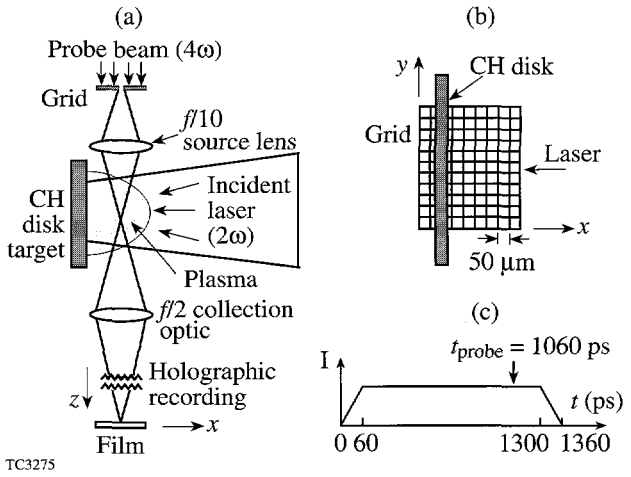

Figure 57.5
Schematic of GIR experiment carried out on the CHROMA laser at KMS Fusion. (a) Solid CH disk target, irradiated by a 527-nm laser. The plasma was diagnosed with a 263-nm probe beam with optics that relayed an image of a 50-μm grid into the plasma and then (holographically) onto film. (b) Grid as viewed by the probe beam. (c) Laser time history.

The grid location with respect to the disk target is shown in Fig. 57.5(b). [Unfortunately, due to a lack of comparison images from a plasma-free reference shot, the absolute location of the disk in the (x,y) plane and the y coordinate of the laser axis were not known.] The (x,y,z) coordinate system shown in Figs. 57.5(a) and 57.5(b) is used consistently throughout this article; thus the cylindrically symmetric *SAGE*

simulations are carried out with x the symmetry axis and y the radial direction.

The temporal history of the laser pulse, as modeled by *SAGE*, is shown in Fig. 57.5(c). It is essentially a flat pulse of 1.3-ns duration with the probe beam timed at 1.06 ns. The beam energy was 107 J and the beam diameter on target was d_0 ~ 400 μm. Since the exact on-target spatial profile was not known, simulations were carried out for two spatial shapes that should bracket the actual profile: (a) a flat profile truncated to zero at radius $d_0/2$, giving a laser intensity of 6.5×10^{13} W/cm^2 for $d_0 = 400$ μm, and (b) a Gaussian profile whose intensity falls to 10% of the peak at a radius $d_{90}/2$, truncated to zero at this radius, giving an on-axis intensity of 1.1×10^{14} W/cm^2 for $d_{90} = 400$ μm. (Simulations were also carried out with different spot diameters.)

Three representative images, resulting from holographic reconstruction and corresponding to different object planes, are shown in Fig. 57.6. The first image corresponds to an object plane closer to the grid ($z < z_0$) and the third to a plane closer to the collection optic ($z > z_0$). The left portion of the dark band is due to obscuration by the unirradiated target, which could present a width of >50 μm if not perfectly aligned. The right portion results from probe rays that are incident close to the target surface and are refracted through angles outside the *f*/2 cone of the catadioptric optic. The images have slightly different magnifications due to their different object planes.

A number of features may be seen in Fig. 57.6. The positions of the grid points behind the target appear to be unchanged from image to image. This is not surprising since simulations show that no significant plasma is expected to form behind the target. On the other hand, the grid points to the right of the target, especially those close to the target, shift to the right with increasing z. This shift is greater for grid points near the laser axis, resulting in a change of curvature between images that can be best perceived in the vertical line just to the right of the dark band. Image quality degrades toward the edge of the image, some (ideally square) grid images degrade into double images, and interference effects between neighboring grid elements are apparent. In image (c) there appears to be a caustic on the right edge of the dark band, pointing to an overlap of grid-point images resulting from strong refraction. In all the images there appears to be an up-down skew to the vertical lines: i.e., those on the right do not appear to be quite parallel to those behind the target. This is unlikely to result from an up-down asymmetry in the expanding plasma since the distortion persists (and may even be greatest) on the far right where the plasma density is the lowest. Rather, the distortion is presumed to be due to a nonuniformity in the grid or an aberration in the optical system. Qualitatively, then, most features of the images may be understood; however, digitization of the images is essential to enable GIR to provide quantitative information.

The principle of GIR is illustrated schematically in Fig. 57.7(a). Here, a set of parallel probe rays is shown incident on the plasma, one per grid element. A typical ray, which would appear to come from point P if the plasma were absent, is refracted through an angle θ_x in the (x,z) plane [and a corresponding angle θ_y in the (y,z) plane]. Depending on the

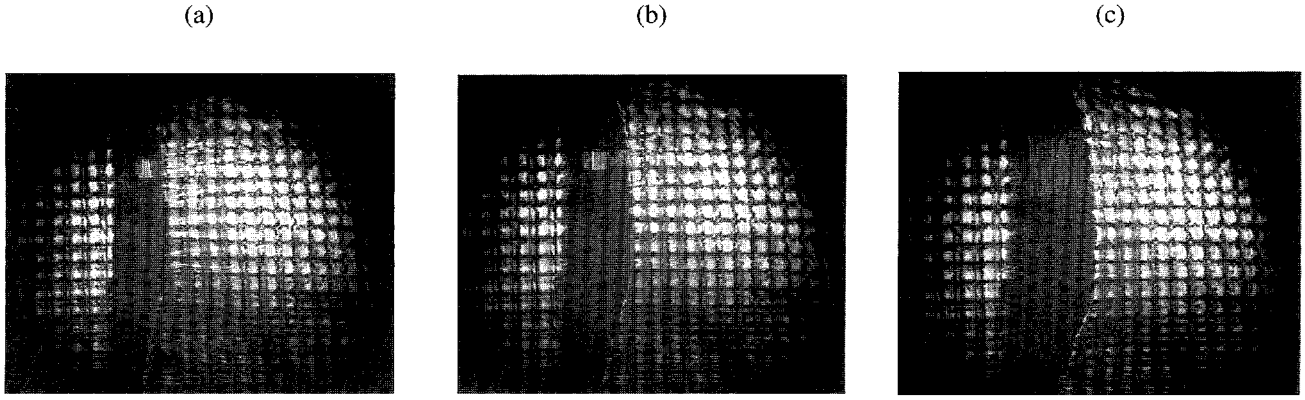

TC3089

Figure 57.6
Images after holographic reconstruction at object planes (a) $z = 200$ μm, (b) $z = 600$ μm, and (c) $z = 800$ μm, in the same orientation as Fig. 57.5(b). Image (b) corresponds approximately to the center of the plasma. The dark band is due partially to obscuration by the CH target and partially to refraction of probe rays close to the target surface through angles outside the *f*/2 cone of the collection optics.

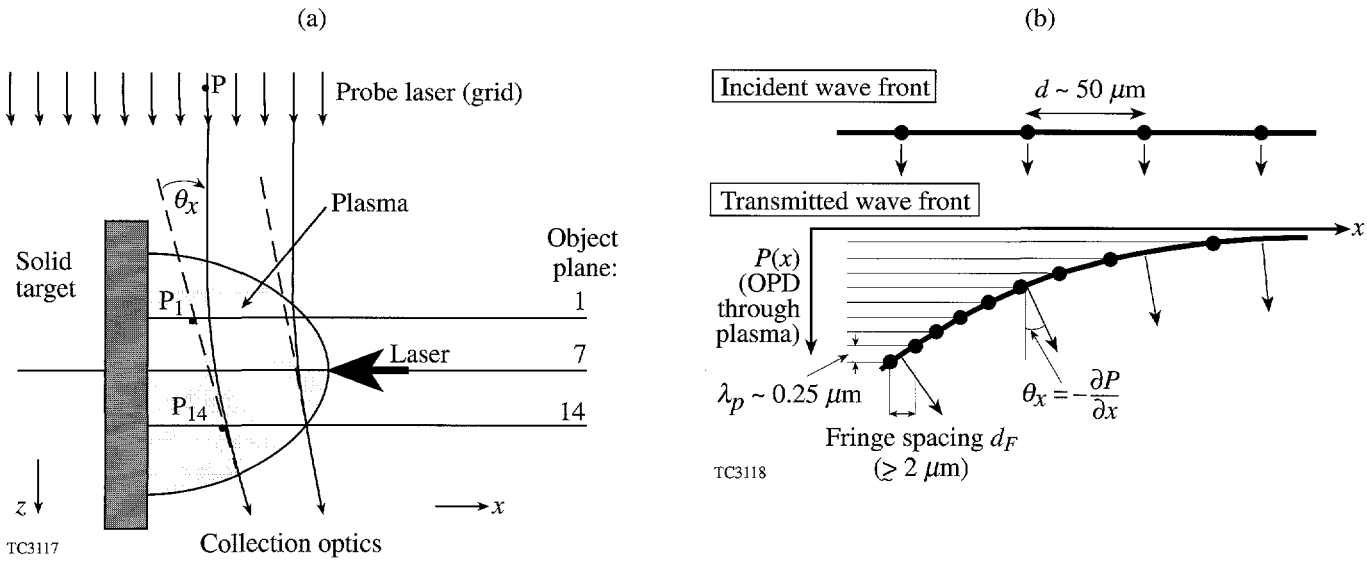

Figure 57.7
(a) Principle of GIR. The apparent position of each probe ray P must be measured for at least two object planes, thereby enabling its deflection angles (θ_x in the x, z plane and θ_y in the y, z plane) to be obtained. (b) Relationship between GIR and interferometry (simplified to omit effects due to strong refraction). In GIR the wavefront $P(x)$ transmitted through the plasma is sampled at uniform intervals (the grid spacing d) in x while, with interferometry, data are obtained each time $P(x)$ changes by the probe wavelength λ_p.

object plane being imaged, the ray will appear to come from points such as P_1 or P_{14}. Provided that images are obtained in a minimum of two such object planes, the angles θ_x and θ_y are calculated very simply by dividing the measured differences of x and y coordinates in the images by the (known) distance between the object planes.

In the present experiment, in which the use of holographic recording provided images for multiple object planes, a more accurate determination of θ_x and θ_y was possible using a least-squares fit to the positions P_i. However, holography shares many of the problems of interferometry, in particular the need for short exposure times to avoid blurring the interference pattern, so that for applications to plasmas with longer scale lengths, such as plasmas anticipated for the OMEGA Upgrade, holography is best avoided. A preferable system would include, instead, a means for directly recording two (or more) images on each shot corresponding to different object planes. This could be accomplished by the insertion of a beam splitter near the film plane of Fig. 57.5(a) and the use of two cameras focused to different object planes. It should be noted that the ability of the holographic system to handle multiple, time-staggered probe pulses[15] would be lost with the GIR system proposed here, which would accommodate a single probe pulse.

The close relationship between GIR and interferometry is illustrated in Fig. 57.7(b) for the case where curvature of the ray path through the plasma can be neglected. (This approximation will be discussed in the following two paragraphs.) Here, the plasma converts a plane incident wave front into a curved transmitted wave front $P(x)$, where $P(x) = \int (1-\mu) ds$ is the optical path difference through the plasma of a ray entering the plasma with impact parameter x. [The refractive index μ in the plasma is equal to $\left(1 - n_e/n_{cp}\right)^{1/2}$, where n_{cp} is the critical electron density corresponding to the probe wavelength, and s measures distance along the ray path.] The difference between the two techniques lies in the way this wave front is sampled. With GIR, sampling occurs every grid spacing d in x; with interferometry, data are obtained every time $P(x)$ changes by λ_p. (It is assumed that, with interferometry, it is feasible to extract only the fringe locations and not information based on intensity variations between fringes.) With GIR the phase-front normal, $\left(\theta_x, \theta_y\right) = \left(-\partial P/\partial x, -\partial P/\partial y\right)$, is measured directly; with interferometry, θ_x is given from the local fringe spacing d_F by $\theta_x = \tan^{-1}\left(\lambda/d_F\right)$. With GIR the phase P is obtained by integrating θ_x along x from vacuum, or by integrating θ_y along y; with interferometry, this integration is performed simply by counting fringes from the outermost fringe. The maximum plasma density that is in principle accessible is

the same in both cases, and a function solely of the f number of the collection optic. In both cases the field of view should be sufficient, to allow a clear zero for the integration of (θ_x, θ_y) in GIR and to allow for the identification of the first fringe in interferometry.

The picture shown in Fig. 57.7(b) is slightly simplified since it is really the emerging phase front as projected back to the appropriate object plane that is imaged onto the plane in which the interferogram is formed. As with grid images such as those of Fig. 57.6, interferograms are dependent on the object plane. This problem has been known for a long time[3,12] and has led to considerable difficulties in the interpretation of experimental interferograms, especially those showing profile steepening and other features around the critical density for 1-μm laser irradiation.[13,29] The problem is minimized by focusing on the plane containing the plasma axis,[3] and it is notable that the difficulties associated with focusing conventional interferometers to the necessary accuracy led to the introduction of holographic interferometry for laser-produced plasmas[30] because then, as with the GIR experiment described in this article, the object plane can be varied during reconstruction.

Even correct focusing is not a complete solution to the problem of reconstructing the density profile. Regardless of whether GIR or interferometry is being used, further errors are introduced by the Abel inversion procedure. This is always carried out in a two-dimensional plane, usually perpendicular to the irradiating laser axis (assumed to be an axis of symmetry). Usually it is assumed, with some justification,[3] that $P(x)$ corresponds to an integral of $(1\text{-}\mu)$ along a straight-line path in this plane. Refraction in this plane could be included exactly if the experimental measurement were the refraction angle as a function of impact parameter,[31] but this is not usually the case. However, significant error can arise due to refraction out of the plane of Abel inversion, the dominant refractive effect for steep density profiles, and it may then be preferable to simulate the interferogram directly.[17] Fortunately, Abel inversion is applicable to a good approximation to the experiment reported in this article and to long-scale-length plasmas in general since the lateral displacement of the ray is smaller than the plasma-density scale length (see Ref. 1, Appendix B).

Data Reduction

The data reduction proceeded in two stages: first, the refraction angles (θ_x, θ_y) were extracted; then the plasma density was obtained under the assumption of cylindrical symmetry.

The first stage is illustrated in Fig. 57.8; a typical hand-digitized grid image [corresponding to Fig. 57.6(b)] is shown in Fig. 57.8(a). (The grid-point centers were located by eye on the original photographs and entered into a computer using a digitizer pad.) After the photographs were digitized, it was discovered that two were identical. Their digitizations are superposed in Fig. 57.8(a). The close correspondence indicates that the photographs could be repeatably digitized, even though the image quality and contrast degraded around the periphery. Even though diffractive effects were evident in the images, the locations of the cell centers could be accurately found. In order to register all images on a common coordinate system (x',y'), it was assumed that three grid points, labeled A–C and easily identified in each image, were invariant—points A and B because they were behind the target and point C because it was sufficiently far to the right of the plasma. In this way the varying orientations and translations of the images as placed on the digitizer pad and the varying magnifications of the images could be accounted for. At a later stage it became apparent that the experimental field of view was too small and the ray through point C must have had a non-zero deflection angle. A value of $\theta_x = 0.75°$ was adopted as a plausible deflection for this point (see later). A more accurate registration of the images would obviously have been possible had comparison images been obtained from a reference, plasma-free shot.

Each point in each image was assigned unique (i,j) coordinates. For each (i,j) point it was then possible to plot the apparent (x',y') position in the image as a function of object plane position z and extract the slopes (θ_x, θ_y) using a least-squares fit [see Fig. 57.8(b)]. These angles were obtained without knowing which value of z corresponded to the center of the plasma; it was sufficient to know the spacing between images (100 μm). With the exception of a few points around the periphery of the image where the probe-beam intensity was weak, good straight-line fits were obtained for all (i,j) points. Results with nearly the same accuracy could evidently have been obtained from just two images separated by ~1 mm.

The (x',y') coordinates of Fig. 57.8(a) are arbitrary, and for comparison to be made with *SAGE* simulations a translated coordinate system (x,y) was defined. The choice $x = x' - 100$ μm enabled the closest comparison to be made with the simulations below, and the choice $y = y' - 850$ μm was made so that $y = 0$ corresponded to the axis of symmetry as could best be determined experimentally. The uncertainty in the horizontal shift would of course have been removed if

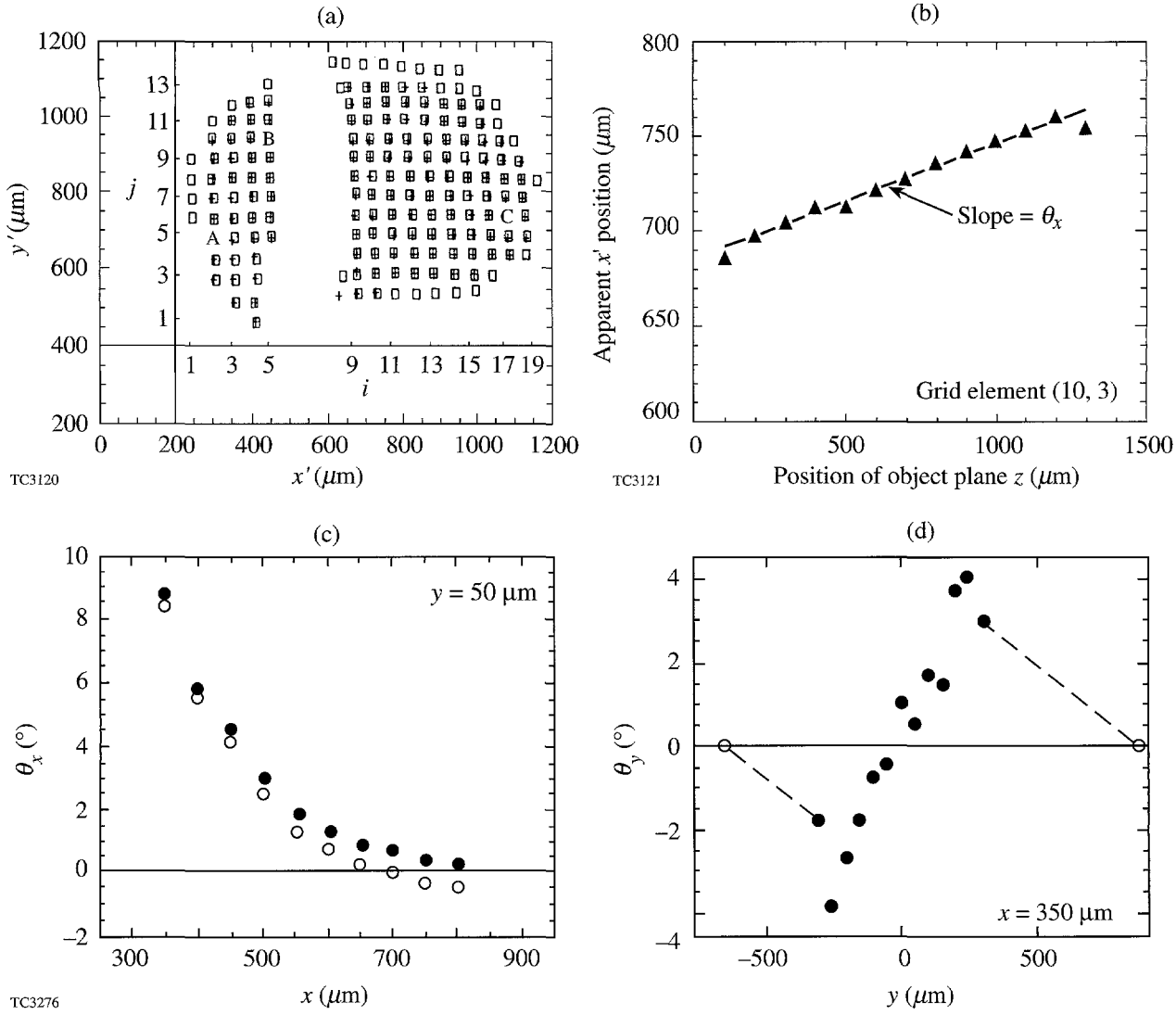

Figure 57.8
Extraction of deflection angles from the grid images. (a) Typical digitized image, with two identical images superposed to illustrate the repeatability of the digitization. All 13 images were then scaled to a common coordinate system (x', y') using reference points A, B, and C. (b) Apparent x' position as a function of object plane position z for a typical grid element. A least-squares fit to the 13 points yields the slope of the ray, θ_x. (c) Lineout of θ_x as a function of x for $y = 50$ μm. Solid (open) points were obtained assuming $\theta_x = 0.75°$ (0°) at reference point C. (d) Lineout of θ_y as a function of y for $x = 350$ μm. Dashed lines indicate extrapolations used outside the experimental field of view.

reference images (of the target and grid in the absence of a plasma) had been available.

Typical lineouts of $\theta_x(x)$ and $\theta_y(y)$ are shown in Figs. 57.8(c) and 57.8(d), respectively. The θ_x lineout, taken approximately along the laser axis, shows why it was necessary to assign a finite deflection angle to point C: the resulting curve (solid circles) asymptotes to zero. If point C were assumed to have no deflection angle (open circles), unphysical negative values of θ_x would be found at large x. The largest standard deviation obtained from least-squares straight-line fits is ±0.25° in θ_x for the point with $\theta_x \approx 9°$, and ≤ ±0.5° for the leftmost and rightmost solid θ_y points. The standard deviation for all other points is less than the symbol size used in the plots. The θ_y lineout, taken at the smallest x (350 μm) at which data existed, reveals an inadequate experimental field of view in the y direction: while θ_y should tend to zero at large |y|, the maximum θ_y is observed near the edge of the image. (Further discussion of this problem follows.)

Contour plots of θ_x and θ_y are shown in Fig. 57.9, where experimental and simulated contours are compared. All con-

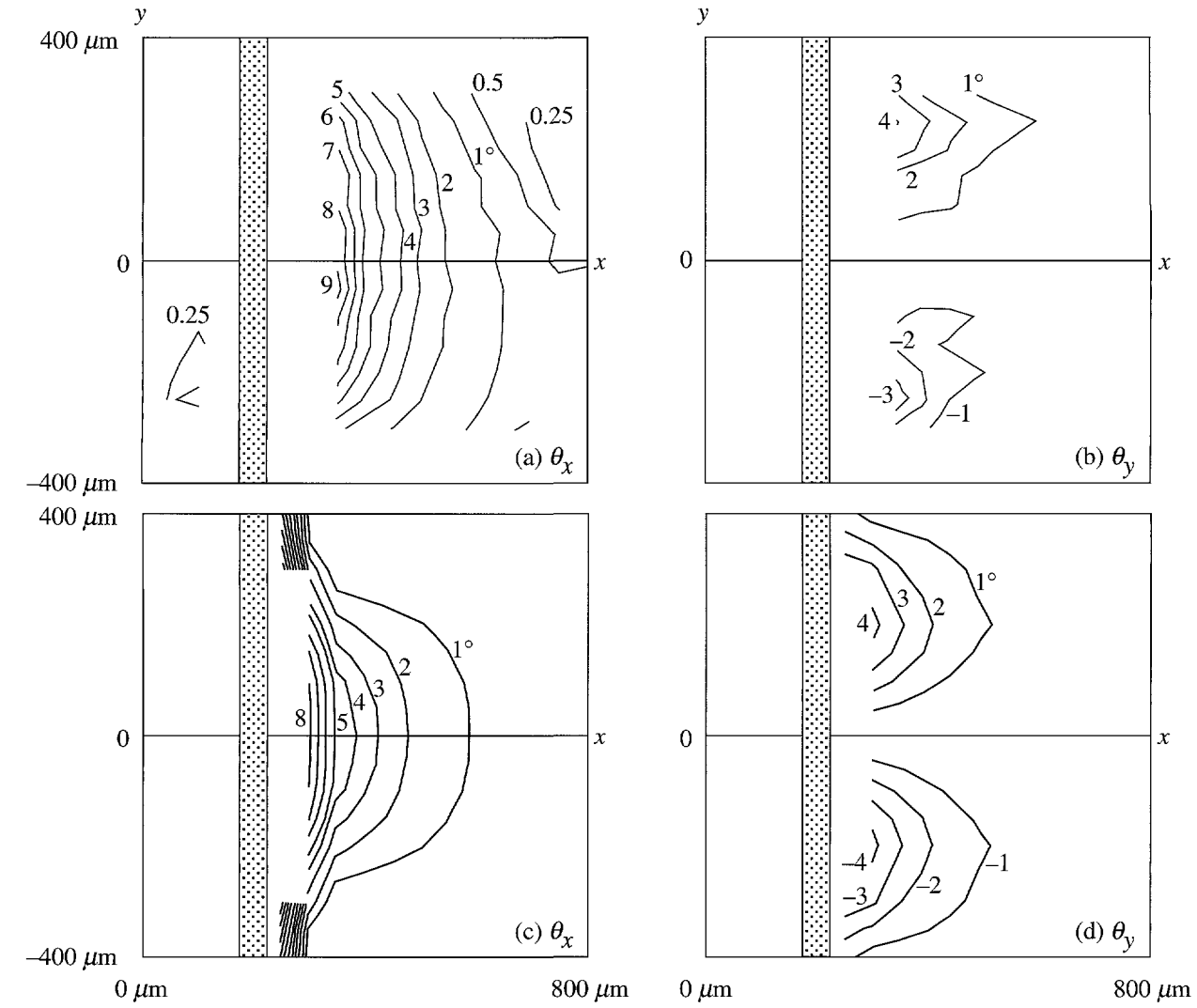

Figure 57.9
Comparison of measured and calculated refraction angles: (a) θ_x and (b) θ_y from GIR; (c) θ_x and (d) θ_y from *SAGE*. The actual positioning of the experimental data relative to the initial solid target (shaded area) and the x axis is unknown. The simulations were performed in cylindrical geometry with x and y the axial and radial coordinates, respectively.

tours are in 1° intervals, except for two additional experimental contours at 0.5° and 0.25°. Reasonable agreement is found for many features of the contours. The main difference appears to be that the experimental contours extend further in the radial (y) direction. The experimental asymmetry seen especially in the 0.5° and 0.25° contours is probably not due to a plasma asymmetry, as discussed above. The least-squares fitting procedure was also applied to the undistorted grid points behind the target, and the 0.25° contour behind the target thus indicates the error associated with the digitization process as applied to the current experimental data.

The second stage of data reduction is illustrated in Fig. 57.10. The phase P was calculated in two ways: integrating θ_x along x to yield P_x, and integrating θ_y along y to yield P_y. Ideally, both P_x and P_y should be equal. However, as observed above, values of θ_y were not available at sufficiently large y, and integration of θ_y from the largest y for which data existed ($y = y_{\text{edge}}$, say) yielded values of P_y that in some cases were as low as $0.5\,P_x$. To resolve this problem, a constant was added to each such integral to represent the integral from y_{edge} to ∞, such that P_y matched P_x at $y = 0$.

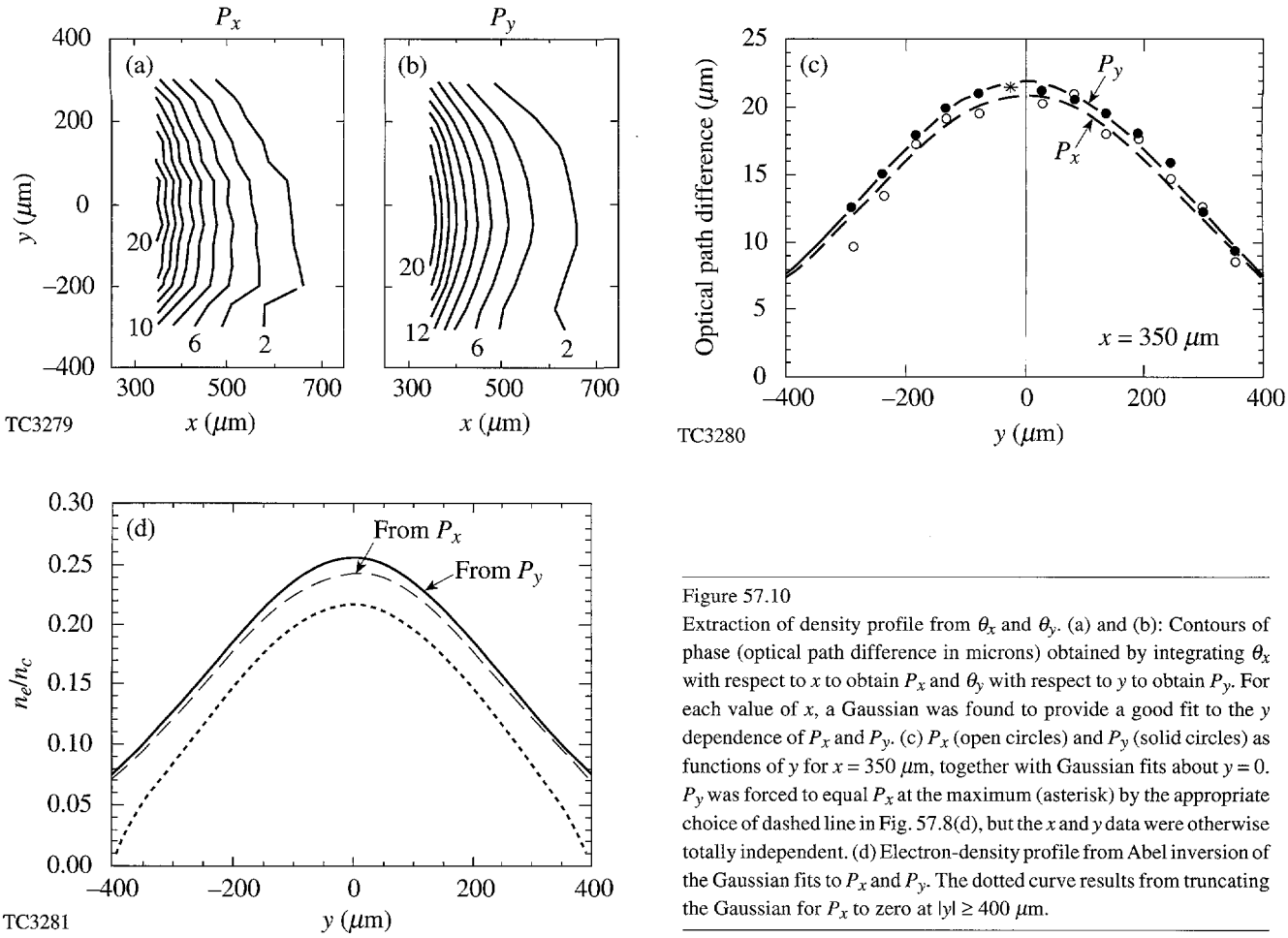

Figure 57.10
Extraction of density profile from θ_x and θ_y. (a) and (b): Contours of phase (optical path difference in microns) obtained by integrating θ_x with respect to x to obtain P_x and θ_y with respect to y to obtain P_y. For each value of x, a Gaussian was found to provide a good fit to the y dependence of P_x and P_y. (c) P_x (open circles) and P_y (solid circles) as functions of y for $x = 350$ μm, together with Gaussian fits about $y = 0$. P_y was forced to equal P_x at the maximum (asterisk) by the appropriate choice of dashed line in Fig. 57.8(d), but the x and y data were otherwise totally independent. (d) Electron-density profile from Abel inversion of the Gaussian fits to P_x and P_y. The dotted curve results from truncating the Gaussian for P_x to zero at $|y| \geq 400$ μm.

Contours of P_x, for which the field of view was (just) adequate, and P_y, adjusted as described, are shown in Figs. 57.10(a) and 57.10(b). The contours have been forced to agree at $y = 0$, but otherwise their shapes correspond very closely. This is notable since, aside from the adjustment, P_x and P_y have been obtained independently from the x and y coordinates of the digitization. This correspondence confirms the self-consistency that the digitized data should possess. It is also worth noting that an interferogram could be simulated simply by plotting contours every 0.26 μm (the probe wavelength) in P rather than every 2 μm. The fringe count at the center would be 80, substantially more than has previously been reported for the interferometric determination of a laser-produced plasma-density profile.

The correspondence between P_x and P_y is shown in Fig. 57.10(c) for the line $x = 350$ μm (the line corresponding to the highest densities that could be probed). Solid circles correspond to P_y and open circles to P_x. The asterisk indicates the point at which P_y was forced to equal P_x. The solid and dashed lines indicate least-squares Gaussian fits to P_y and P_x, respectively. These fits were obtained for each line on the grid, and good symmetry was found with respect to $y = 0$. These curves were then Abel-inverted to yield the density profiles shown in Fig. 57.10(d). By fitting the phase data to smooth curves (Gaussian and truncated Gaussian), problems associated with the differentiation of experimental data were avoided.[4] It is questionable whether the Gaussian fits of Fig. 57.10(c) should be extrapolated to ∞ [leading to the upper curves of Fig. 57.10(d)] or truncated to zero at $|y| = 400$ μm (giving the dotted curve) since $|y| = 400$ μm was in any case outside the field of view. It is likely that the actual density profile lies somewhere in between. This uncertainty was the greatest for the value of x shown here, but even so it did not make a large difference in the density of ~ 0.25 n_c obtained for $y = 0$. The Abel inversions were carried out numerically in all cases, although the Gaussian inverse is known analytically to be a Gaussian.

One interesting difference between the contours of P_x and P_y shown in Fig. 57.10 may be noted: the P_x contours include some fine structure, correlated along horizontal lines, similar to the fine structure in the contour plot of θ_x [Fig. 57.9(a)]. Integration of θ_x along horizontal lines preserves this structure, whereas integration of θ_y perpendicular to these lines evidently does not. It is probable that this structure is physical and results from hot spots in the laser, as similar structures can be seen in interferograms obtained on the CHROMA laser reported in Ref. 32 (and reproduced in Ref. 17). Also, the experimental determination of θ_x is carried out independently for each grid point, so that it would be hard to explain the θ_x correlations seen in Fig. 57.9(a) as noise resulting from the data-reduction process.

Comparison with Simulations

Contours of electron density resulting from the Abel inversion are compared with the predictions of five *SAGE* simulations in Fig. 57.11. The simulations included the *SESAME* equation of state,[33] a multigroup diffusion model for radiation transport (which led to some minor heating of the target surface as seen near $y = 400$ μm),[34] and ray tracing for the incident laser.[20] The experimental contours, shown as heavy lines, are the same in each case: the dashed lines corresponding to extrapolation of the Gaussian fit for $P(y)$ to infinity and the solid lines to truncation at $|y| = 400$ μm. As discussed above, the difference between these lines should be indicative of the experimental uncertainty associated with the restricted field of view in the y direction. In each figure it is the contours

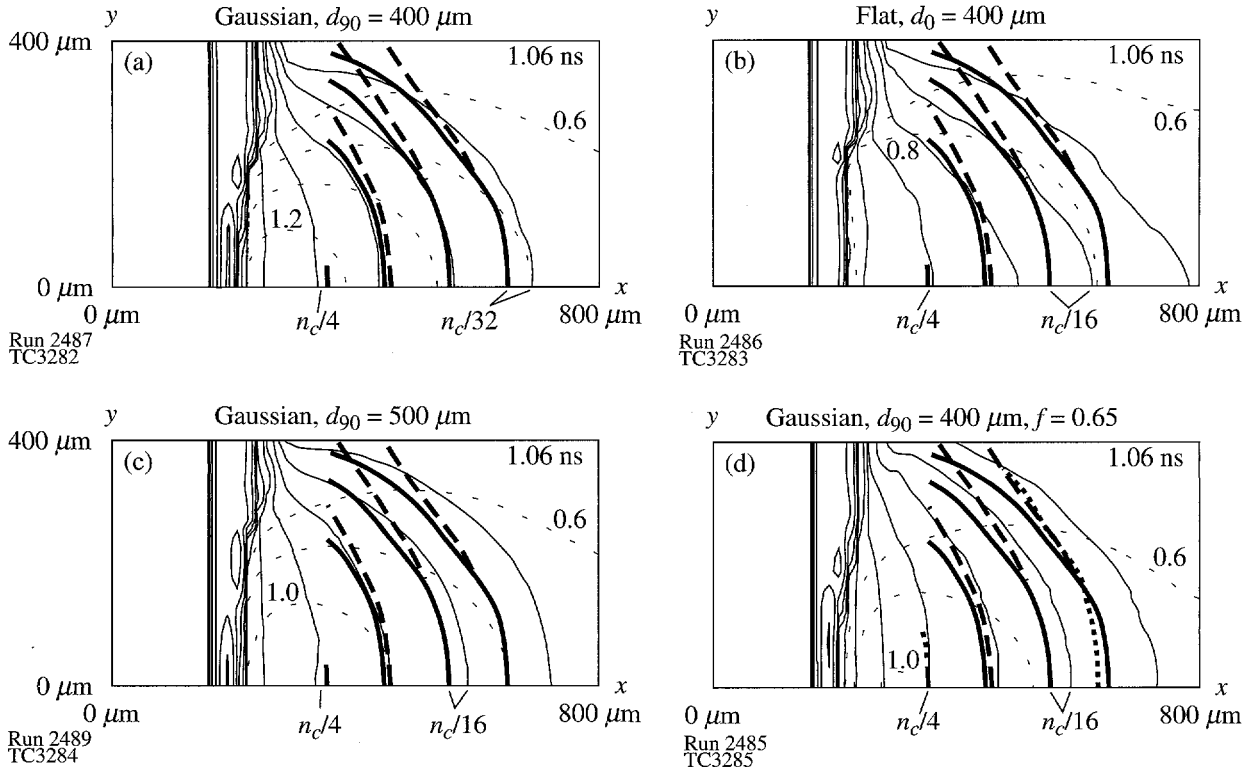

Figure 57.11
Comparison of measured density contours with *SAGE* simulations under various assumptions: (a) Gaussian spot of diameter $d_{90} = 400$ μm (standard case); (b) flat spot of diameter 400 μm; (c) Gaussian spot of diameter $d_{90} = 500$ μm; (d) standard case but with flux limiter $f = 0.65$; (e) standard case 0.2 ns after nominal probe time. Contours are plotted in intervals of a factor of 2 and referenced to $n_c = 4 \times 10^{21}$ cm^{-3}. The experimental contours (heavy lines, the same in each figure) correspond to extrapolation of the Gaussian fit to the phase P_x beyond $|y| = 400$ μm (dashed contours) and truncation at $|y| = 400$ μm (solid contours). Almost identical contours were obtained using P_y [superposed on (d) as dotted curves where different from the dashed contours]. The light dashed contours give the electron temperature in kilo-electron-volts.

based on P_x that are plotted. The contours based on P_y were almost identical, as is seen in Fig. 57.11(d) where they are superposed, where different, as dotted curves.

Starting with Fig. 57.11(a), for a "standard" simulation with a Gaussian focal spot of diameter d_{90} = 400 μm, agreement with experiment is for the most part very close. As discussed above, the lack of an experimental determination of the target location relative to the grid allowed the contours to be moved in the x direction (through the transformation from x' to x) to provide the best fit. However, the contour spacing and shapes match remarkably well. A minor discrepancy is seen at the $n_c/32$ contour, where the experimental contour interval (between $n_c/16$ and $n_c/32$) seems to be smaller than predicted. Since this could be related to the choice of 0.75° assumed for θ_x at the reference point C, it is impossible in the absence of a reference shot to say whether or not this discrepancy is real. The main discrepancy is seen at the larger radii, where the experimental plasma seems to have a greater radial extent, even if the solid experimental contours are used. The greatest discrepancy is seen at radii beyond 300 μm, the largest radius in the experimental field of view. It is of interest to ascertain whether or not such a discrepancy could yield insight into physical processes such as thermal transport, and it is worth noting that a similar motivation for comparing simulated and experimental interferograms is found in Ref. 17. The following plots of Fig. 57.11 are included to show that there could be a variety of explanations for the discrepancy aside from thermal transport modeling.

The simulation of Fig. 57.11(b) assumes a flat focal spot, also of diameter 400 μm. The predicted blowoff in this case is strongly peaked in the direction of the target normal, and the match at low densities, especially around $n_c/32$, is much poorer. The reason for the different coronal shape may be readily understood from the temperature contours, shown as light dashed lines. For the flat focal spot the plasma temperature and expansion are fairly uniform in y, and the expansion velocity is initially in the $+x$ direction. Not until the combination of a rarefaction wave and a thermal wave feeds in from the edge of the spot does the plasma near the x axis see a nonzero radial pressure gradient and start to expand radially. For the Gaussian spot, radial temperature (and pressure) gradients are always present.

In Fig. 57.11(c) results are given for a simulation with a Gaussian beam of slightly bigger diameter (500 μm). Here the discrepancy at large y has almost vanished, especially for the solid experimental curves. Unfortunately the precise focal intensity distribution in the experiment was not known; thus it is entirely possible that the observed discrepancy is due primarily to an insufficiently precise knowledge of the focal spot.

Figure 57.11(d) presents the standard simulation but with a flux limiter[35] f of 0.65. (A value of 0.04 was used in the other simulations.) This led to the desired increase in the radial plasma size but also produced a more extended plasma in the x direction. One other possibility—a timing discrepancy of 0.2 ns between simulation and experiment—is investigated in Fig. 57.11(e). At the later time (1.26 ns) the predicted plasma is bigger, as expected, and has density contours comparable to those produced by the larger flux limiter. Thus, in order to make a strong statement about thermal transport, a good timing fiducial and an accurate knowledge of experimental parameters, such as the focal spot profile, are essential.

Conclusions

A new technique—grid image refractometry (GIR)—has been proposed for the determination of density profiles in underdense plasmas. The method has much in common with classical Schlieren techniques and other forms of refractometry, but includes some unique features that make it especially applicable to laser-produced plasmas where ray deflection angles can be large. GIR has significant advantages over interferometry for long-scale-length plasmas such as will be produced on the OMEGA Upgrade and, in particular, does not depend on probe-beam coherence and does not require inconveniently short probe times. (The probe duration for GIR should not exceed the time scale of plasma hydrodynamic motion, which is much greater than the fringe-blurring time.) The price paid is the loss of spatial resolution on the micron scale length, but, for the plasmas of interest, this is not particularly important. The feasibility of the method has been demonstrated by an experiment carried out on the CHROMA laser.

Even though experimental data were available just for a single shot, it has been possible to extract two-dimensional density profiles that extend up to $n_e = 10^{21}$ cm^{-3} and compare very well with hydrodynamic simulations. Few, if any, such detailed comparisons have been previously reported. For future applications to long-scale-length plasmas, it is proposed to replace the holographic system with a beam splitter and a recording system that will enable two (or more) images, corresponding to different object planes, to be recorded directly on a single shot. This should eliminate problems associated with temporal smearing of the holographic pattern.

GIR can in principle be used to investigate physical processes such as electron thermal transport, but only if an accurate knowledge of laser and target conditions is available. In addition, if a measurement were made of probe-beam attenuation across the same field of view (resulting from inverse bremsstrahlung), it would be possible to determine the electron-temperature profile in the plasma as well as the electron-density profile.

A knowledge of the density profile of long-scale-length plasmas is very important to the understanding of plasma physics issues relevant to inertial-confinement fusion. GIR seems to be a very attractive method with considerable promise for the diagnosis of millimeter-scale-length plasmas.

ACKNOWLEDGMENT

This work was supported by the U.S. Department of Energy Office of Inertial Confinement Fusion under Cooperative Agreement No. DE-FC03-92SF19460 and the University of Rochester. The support of DOE does not constitute an endorsement by DOE of the views expressed in this article. This work was also supported by the Laboratory for Laser Energetics' Summer High-School Program, which was partially funded by the National Science Foundation Grant No. RCD9055084.

REFERENCES

1. R. S. Craxton, F. S. Turner, R. Hoefen, C. Darrow, E. F. Gabl, and Gar. E. Busch, Phys. Fluids B **5**, 4419 (1993).
2. F. B. Hildebrand, *Methods of Applied Mathematics*, 2nd ed. (Prentice-Hall, NJ, 1965), p. 276.
3. C. M. Vest, Appl. Opt. **14**, 1601 (1975).
4. M. Deutsch, Appl. Phys. Lett. **42**, 237 (1983).
5. D. T. Attwood, D. W. Sweeney, J. M. Auerbach, and P. H. Y. Lee, Phys. Rev. Lett. **40**, 184 (1978).
6. A. Raven and O. Willi, Phys. Rev. Lett. **43**, 278 (1979).
7. C. B. Darrow *et al.*, Phys. Fluids B **3**, 1473 (1991).
8. W. Seka, R. S. Craxton, R. E. Bahr, D. L. Brown, D. K. Bradley, P. A. Jaanimagi, B. Yaakobi, and R. Epstein, Phys. Fluids B **4**, 432 (1992); see also Laboratory for Laser Energetics LLE Review **47**, Quarterly Report No. DOE/DP/40200-166, 1991 (unpublished), p. 109.
9. B. J. MacGowan *et al.*, Bull. Amer. Phys. Soc. **38**, 1934 (1993), paper 3E 1.
10. H. Azechi *et al.*, Phys. Rev. Lett. **39**, 1144 (1977).
11. R. E. Turner and L. M. Goldman, Phys. Rev. Lett. **44**, 400 (1980).
12. G. J. Tallents, M. D. J. Burgess, and B. Luther-Davies, Opt. Commun. **44**, 384 (1983), and Erratum **45**, 420 (1983).
13. M. D. J. Burgess, G. B. Gillman, and B. Luther-Davies, J. Appl. Phys. **54**, 1787 (1983).
14. R. Fedosejevs, M. D. J. Burgess, G. D. Enright, and M. C. Richardson, Phys. Rev. Lett. **43**, 1664 (1979).
15. Gar. E. Busch *et al.*, Rev. Sci. Instrum. **56**, 879 (1985).
16. J. A. Tarvin *et al.*, Laser Part. Beams **4**, 461 (1986).
17. M. K. Prasad, K. G. Estabrook, J. A. Harte, R. S. Craxton, R. A. Bosch, Gar. E. Busch, and J. S. Kollin, Phys. Fluids B **4**, 1569 (1992).
18. R. R. Johnson *et al.*, Phys. Rev. A **41**, 1058 (1990).
19. R. P. Drake *et al.*, Phys. Fluids **31**, 1795 (1988).
20. R. S. Craxton and R. L. McCrory, J. Appl. Phys. **56**, 108 (1984).
21. L. A. Vasil'ev, *Schlieren Methods* (Israel Program for Scientific Translations, New York, 1971).
22. V. Gurfein *et al.*, Opt. Commun. **85**, 147 (1991).
23. N. Miyanaga, Y. Kato, and C. Yamanaka, Opt. Commun. **44**, 48 (1982).
24. R. Benattar and J. Godart, Opt. Commun. **49**, 43 (1984).
25. O. Kafri, Opt. Lett. **5**, 555 (1980).
26. J. E. Trebes *et al.*, Bull. Am. Phys. Soc. **38**, 2044 (1993).
27. I. Ghozeil, in *Optical Shop Testing*, 2nd ed., edited by D. Malacara (Wiley, New York, 1992), p. 367.
28. J. A. Sell *et al.*, Appl. Phys. Lett. **55**, 2435 (1989).
29. G. Gillman, Opt. Commun. **35**, 127 (1980).
30. D. T. Attwood, IEEE J. Quantum Electron. **14**, 909 (1978).
31. P. W. Schreiber, A. M. Hunter, and D. R. Smith, Plasma Phys. **15**, 635 (1973).
32. G. Charatis *et al.*, J. Phys. (Paris) **47**, C6-89 (1986).
33. B. I. Bennett *et al.*, Los Alamos National Laboratory Report LA-7130 (1978).
34. W. F. Huebner *et al.*, Los Alamos National Laboratory Report LA-6760-M (1977).
35. R. C. Malone, R. L. McCrory, and R. L. Morse, Phys. Rev. Lett. **34**, 721 (1975).

Transport and Sound Waves in Plasmas with Light and Heavy Ions

Ion-transport coefficients are important in various aspects of plasma physics. Some of the most commonly used transport formulas have been derived by Braginskii.[1] They are obtained by assuming a fully ionized, single-ion-species plasma. Typical laboratory plasmas, however, may involve more than one species of ions. For example, in magnetic-fusion devices, high-Z impurities can be present within the DT fuel. In inertial-confinement fusion plastic materials are commonly used as ablators, which then give rise to carbon and hydrogen ions. To calculate the transport of ions in such plasmas, within the framework of single-fluid theory, it is usual to employ an average-ion model in conjunction with the Braginskii formulas. The aim of this article is to show that such a simple procedure can considerably underestimate the levels of thermal diffusion; viscosity, and joule heating for a mixture of light and heavy ions. Implications for the damping of ion-acoustic waves will be shown.

We start by recalling the formulas for the ion thermal conductivity and viscosity coefficients in an unmagnetized single-ion-species plasma. They are, respectively (in cgs units),[1]

$$\kappa_i = \gamma_i \frac{n_i T_i \tau_i}{m_i} \tag{1}$$

and

$$\eta_i = \mu_i n_i T_i \tau_i \,, \tag{2}$$

where $\gamma_i = 3.91$, $\mu_i = 0.96$, n_i is the number density, m_i is the mass, and T_i is the temperature (in ergs). The ion-ion collision time for 90° angular scattering is given by

$$\tau_i = \frac{3\sqrt{m_i}\,T_i^{3/2}}{4\sqrt{\pi}e^4 n_i \left(Z_i^2\right)^2 \ln\Lambda_i} \,, \tag{3}$$

where e is the magnitude of the electron charge and $\ln\Lambda_i$ is the Coulomb logarithm.

Let us now consider a fully ionized plasma composed of approximately equal numbers of light and heavy ions (identified by l and h, respectively). It is clear from the above equations that if $Z_h >> Z_l$, the transport will be dominated by the light species. However, since it is convenient to use a single-ion-species formalism, rather than treat the transport of each species separately, it is common to use Eqs. (1)–(3) with some appropriate average (denoted here by $\langle\,\rangle$) for m_i and Z_i. A popular approach is to use

$$\langle m_i \rangle = \left(n_l m_l + n_h m_h\right)/n_i \,,$$

$$\langle Z_i \rangle = \left(n_l Z_l + n_h Z_h\right)/n_i \,,$$

and

$$\left\langle Z_i^2 \right\rangle = \left(n_l Z_l^2 + n_h Z_h^2\right)/n_i \,,$$

where

$$n_i = n_l + n_h \,.$$

To investigate the accuracy of this averaging procedure we need to recalculate the transport coefficients. The linearized Fokker-Planck equation, written in the frame of the light-ion species with mean velocity $\mathbf{u}_l$ (obtained by expanding the distribution function as $f = f_0 + \mathbf{w}\cdot\mathbf{f}_1/w$, where $\mathbf{w} = \mathbf{v} - \mathbf{u}_l$ is the intrinsic velocity), is given by[2]

$$\left(\mathbf{C}_1^{ll} + \mathbf{C}_1^{lh}\right) = w\nabla f_0^l + \left(\frac{Z_l e}{m_l}\mathbf{E} - \frac{d\mathbf{u}_l}{dt}\right)\frac{\partial f_0^l}{\partial w} \,, \tag{4}$$

where $d/dt = \partial/\partial t + \mathbf{u}_l\cdot\nabla$, f_0 is the isotropic Maxwellian distribution, $\mathbf{f}_1$ is the anisotropic part of the distribution (responsible for the transport), $\mathbf{E}$ is the electric field, and $\mathbf{C}_1{}^{ll}$ and $\mathbf{C}_1{}^{lh}$ are the anisotropic parts of the collision operators acting on $\mathbf{f}_1$. Equation (4) has been derived with the standard assumptions of strong collisionality (which imply that $|\mathbf{f}_1| << f_0$) and

negligible contribution from electron momentum exchange. Indeed, in the absence of *l-h* collisions, Eq. (4) predicts the classical single-ion-species thermal conductivity of Eq. (1). In our case, however, $\mathbf{C}_1^{lh}/\mathbf{C}_1^{ll} \sim n_h Z_h^2/n_l Z_l^2 >> 1$ means that *l-h* collisions dominate over *l-l* collisions. Furthermore, the collision operator $\mathbf{C}_1^{lh}$ may be considerably simplified in the limit $m_h >> m_l$ to become[2]

$$\mathbf{C}_1^{lh} \approx -\frac{n_h Y_{lh}}{w^3}\left[\mathbf{f}_1^l + \left(\mathbf{u}_h - \mathbf{u}_l\right)\frac{\partial f_0^l}{\partial w}\right],$$

where

$$Y_{lh} = \frac{4\pi Z_l^2 Z_h^2 e^4 \ln \Lambda_{lh}}{m_l^2}$$

and $\mathbf{u}_h$ is the mean velocity of the h species (necessary to ensure momentum conservation).

Substituting this simplified collision operator back into Eq. (4) and expanding the right-hand side of that equation yields

$$\mathbf{f}_1^l = -\frac{w^4}{n_h Y_{lh}}\left[\left(\frac{m_l w^2}{2T_l} - \frac{5}{2}\right)\frac{\nabla T_l}{T_l}\right.$$

$$\left. + \frac{1}{p_l}\left(\nabla p_l - Z_l e n_l \mathbf{E} + n_l m_l \frac{d\mathbf{u}_l}{dt}\right)\right] f_0^l - \left(\mathbf{u}_h - \mathbf{u}_l\right)\frac{\partial f_0^l}{\partial w}. \quad (5)$$

We note that this equation is equivalent to the one used for modeling electron transport in high-Z plasmas.

Substituting Eq. (5) into the heat flow formula,

$$\mathbf{q}_l = \frac{2\pi}{3} m_l \int_0^\infty dw w^5 \mathbf{f}_1^l, \quad (6)$$

and using the velocity moment $\int dw w^3 \mathbf{f}_1{}^l$ to substitute for $\left(\nabla p_l - Z_l e n_l \mathbf{E} + n_l m_l d\mathbf{u}_l/dt\right)$, we obtain

$$\mathbf{q}_l = -\kappa_{lh}\nabla T_l + \beta_0 n_l T_l (\mathbf{u}_l - \mathbf{u}_h)$$

and the momentum exchange rate,

$$\mathbf{R}_{lh} = -\beta_0 n_l \nabla T_l - \alpha_0 \frac{n_l m_l}{\tau_{lh}}\left(\mathbf{u}_l - \mathbf{u}_h\right)$$

$$= m_l n_l \frac{d\mathbf{u}_l}{dt} + \nabla p_l + \nabla \cdot \boldsymbol{\pi}_l - Z_l e n_l \mathbf{E}. \quad (7)$$

Here the thermal conductivity is

$$\kappa_{lh} = \gamma_0 \frac{n_l T_l \tau_{lh}}{m_l}, \quad (8)$$

where

$$\tau_{lh} = \frac{3\sqrt{m_l}\, T_l^{3/2}}{4\sqrt{2\pi} e^4 n_h Z_l^2 Z_h^2 \ln \Lambda_{lh}}, \quad (9)$$

$\alpha_0 = 3\pi/32$, $\beta_0 = 3/2$, and $\gamma_0 = 128/3\pi$. The stress tensor π_l, which has been added to Eq. (7), will be subsequently evaluated. By analogy with electron-transport theory we identify α_0, β_0, and γ_0 as the resistivity, thermoelectric, and electron thermal diffusion coefficients, respectively (in the high-Z limit). (Note the extra $1/\sqrt{2}$ factor in our definition of τ_{lh}.) These results are in close agreement with the work of Hirshman,[3] who derived the thermal transport and momentum transfer coefficients numerically (via a Sonine polynomial expansion) for plasmas of arbitrary composition.

By comparing Eq. (1) with Eq. (8) we note a significant increase in the conductivity coefficient γ. Differences with regards to the mass and Z dependencies are also apparent. The ratio between the conductivities is given by

$$\frac{\kappa_{lh}}{\langle\kappa_i\rangle} = \frac{\gamma_0}{\gamma_i}\sqrt{\frac{\langle m_i\rangle}{2m_l}}\frac{\langle Z_i^2\rangle^2}{Z_l^2 Z_h^2}\frac{n_l}{n_h}\frac{\ln\Lambda_i}{\ln\Lambda_{lh}}. \quad (10)$$

If we consider a fully ionized CH plasma, where $m_l = m_p$ is the proton mass, $\langle m_i\rangle = 6.5 m_p$, $n_l = n_h$, $\langle Z_i^2\rangle = 18.5$, $Z_l^2 = 1$, and $Z_h^2 = 36$, we obtain $\kappa_{lh}/\langle\kappa_i\rangle \approx 60$. The thermal conductivity contribution from the h species is expected to be negligible since

$$q_h/q_l \sim \left(n_h/n_l\right)\left(m_l/m_h\right)^{1/2}\left(Z_l^2/Z_h^2\right) << 1.$$

Comparisons with the conductivity of a pure-H plasma (κ_l) and a pure-C plasma (κ_h) show that $\kappa_h : \kappa_{lh} : \kappa_l = 1 : 306 : 4500$.

The same type of analysis can be used to calculate the viscosity coefficient. The linearized Fokker-Planck equation describing the stress tensor contribution to the distribution function, which is now expanded as

$$f = f_0 + \mathbf{w}\cdot\mathbf{f}_1/w + \mathbf{ww}:\mathbf{f}_2/w^2 ,$$

is given by[2]

$$\mathbf{f}_2^l = \frac{w^4}{6n_h Y_{lh}}\frac{\partial f_0^l}{\partial w}\mathbf{U}_l , \tag{11}$$

where

$$\mathbf{U}_l = \nabla\mathbf{u}_l + \left(\nabla\mathbf{u}_l\right)^T - \frac{2}{3}\mathbf{I}\nabla\cdot\mathbf{u}_l$$

is the rate-of-strain tensor of the l species (superscript T denotes the transpose and $\mathbf{I}$ is the unit dyadic). From the definition of the anisotropic part of the pressure tensor,

$$\boldsymbol{\pi}_l = -\eta_{lh}\mathbf{U}_l = \frac{8\pi m_l}{15}\int_0^\infty \mathbf{f}_2^l w^4 dw , \tag{12}$$

we find that

$$\eta_{lh} = \mu_0 n_l T_l \tau_{lh} , \tag{13}$$

where $\mu_0 = 256/45\pi \approx 1.81$. Note that this value of μ_0 extends the electron viscosity given by Braginskii [i.e., $\mu_0(Z=1) = 0.73$] to the high-Z limit.

As before, we can compare Eq. (13) with the averaged version of the standard formula [Eq. (2)] to obtain

$$\frac{\eta_{lh}}{\langle\eta_i\rangle} = \frac{\mu_0}{\mu_i}\sqrt{\frac{m_l}{2\langle m_i\rangle}}\frac{\langle Z_i^2\rangle^2}{Z_l^2 Z_h^2}\frac{n_l}{n_h}\frac{\ln\Lambda_i}{\ln\Lambda_{lh}} . \tag{14}$$

Using the example of a CH plasma we then find that $\eta_{lh}/\langle\eta_i\rangle \approx 5$. The viscosity contribution from the h species is expected to be small since

$$\pi_h/\pi_l \sim \left(n_h/n_l\right)\left(m_h/m_l\right)^{1/2}\left(Z_l^2/Z_h^2\right) << 1 .$$

To illustrate the importance of these results we calculate the damping of collisional ion-acoustic waves in a CH plasma. Writing $\mathbf{u}_i = (\delta u_i, 0, 0)\exp(ikx - i\omega_i t)$ etc., the linearized single-species ion fluid equations, assuming collisionless and isothermal electrons, become

$$-\omega_i\delta n_i + n_i k\delta u_i = 0 , \tag{15}$$

$$\omega_i m_i n_i \delta u_i = kT_i\delta n_i + k\delta T_i n_i + k\delta\pi_{ixx} + k\delta\phi n_i Z_i e , \tag{16}$$

and

$$-\frac{3}{2}\omega_i n_i\delta T_i + k n_i T_i\delta u_i = -k\delta q_i . \tag{17}$$

The perturbed electric potential, assuming quasi-neutrality and neglecting Landau damping, is given by $\delta\phi = \delta n_i\, T_e/en_i$.

Equations (15)–(17) yield a cubic dispersion relation, with roots ω_i corresponding to two counter-propagating and decaying ion-acoustic waves and a zero-frequency entropy wave (e.g., Ref. 4). By requiring strong collisionality, i.e., $\omega_i\tau_i << 1$, we are able to simplify the dispersion relation and obtain the following expressions for the ion-acoustic mode:

$$\frac{\left|\mathrm{Re}(\omega_i)\right|}{k} = v_i\sqrt{\frac{5}{3} + \frac{Z_i T_e}{T_i}} \equiv c_s , \tag{18}$$

$$\frac{\mathrm{Im}(\omega_i)}{kv_i} = -\frac{2}{3}\left(\mu_i + \frac{\gamma_i}{5 + 3Z_i T_e/T_i}\right)k\lambda_i , \tag{19}$$

where $v_i = \left(T_i/m_i\right)^{1/2}$ is the ion thermal velocity, $\lambda_i = v_i\tau_i$ is its mean free path, and c_s is the sound speed.

To generalize these results to a plasma with light and heavy ions we would strictly need separate fluid equations for each species, and the resulting dispersion relation would be a sixth-order polynomial in ω. Instead, however, we can use the fact that $\left|\mathrm{Im}(\omega)\right| << \left|\mathrm{Re}(\omega)\right|$ to calculate the damping directly from the rate of entropy production. This approach,

described in detail by Braginskii,[1] is simpler than solving the dispersion relation and provides further physical insight into the damping processes.

The dissipative processes (thermal conduction, viscosity, and joule heating) are much weaker for the heavy particles than for the light, so we consider only the entropy of the light particles. We start with the entropy balance equation

$$\frac{\partial S_l}{\partial t}+\nabla\cdot\left(S_l\mathbf{u}_l+\frac{\mathbf{q}_l}{T_l}\right)$$

$$=\frac{1}{T_l}\left[-\frac{1}{2}\boldsymbol{\pi}_l:\mathbf{U}_l-\mathbf{q}_l\cdot\nabla\ln T_l+Q_{lh}\right], \qquad (20)$$

where $S_l = s_l n_l$ is the specific entropy, and (to lowest order in τ_{lh}) $Q_{lh}=-\mathbf{R}_{lh}\cdot\left(\mathbf{u}_l-\mathbf{u}_h\right)$ represents the heating of the light particles resulting from collisions with the heavy particles. To calculate the damping of a small-amplitude sound wave, we define the average over the wavelength L by example

$$\overline{S_l}=\frac{1}{L}\int_0^L S_l dz\,. \qquad (21)$$

Averaging Eq. (20) we then obtain an expression for the rate of entropy production in the wave:

$$\frac{d\overline{S_l}}{dt}=\frac{4}{3}\mu_0 n_l\tau_{lh}\overline{\left(\nabla\cdot\mathbf{u}_l\right)^2}$$

$$+\gamma_0\frac{n_l\tau_{lh}}{m_l T_l}\overline{\left|\nabla T_l\right|^2}+\alpha_0\frac{m_l n_l}{T_l\tau_{lh}}\overline{\left|\mathbf{u}_l-\mathbf{u}_h\right|^2}. \qquad (22)$$

We represent the amplitude of the wave by

$$\delta n_l/n_l=\delta n_h/n_h=\xi\sin(kx-\omega t),$$

so that to lowest order in τ_{lh} we have

$$T_l=T_h\equiv T_i,$$

$$\delta T_l/T_l=2/3\,\xi\sin\left(kx-\omega t\right),$$

and

$$\delta u_l=\delta u_h=\xi c_s\cos(kx-\omega t).$$

Using Eq. (7) to evaluate $\delta u_l-\delta u_h$ to first order in τ_{lh} then yields

$$\frac{d\overline{S_l}}{dt}=k^2 n_l\tau_{lh}\left[\frac{2}{3}\mu_0 c_s^2+\frac{2}{9}\gamma_0\frac{T_i}{m_l}+\frac{1}{2\alpha_0}\frac{T_i}{m_l}\right.$$

$$\left.\left(\frac{2\beta_0}{3}+\frac{5}{3}+\frac{Z_l T_e}{T_i}-\frac{m_l c_s^2}{T_i}\right)^2\right]\xi^2. \qquad (23)$$

The amplitude damping rate is given by

$$\mathrm{Im}(\omega)=-\frac{T_i}{2\bar{\varepsilon}}\frac{d\overline{S_l}}{dt};\qquad \bar{\varepsilon}=\frac{1}{2}n_i m_i c_s^2\xi^2\,.$$

This expression gives the rate at which the energy of the wave, ε, is degraded to heat. The resulting damping rate formula is

$$\frac{\mathrm{Im}(\omega_{lh})}{kv_l}$$

$$=-\frac{2}{3\left(5+3\langle Z_i\rangle T_e/T_i\right)}\left\{\gamma_0+\mu_0\left(\frac{m_l}{\langle m_i\rangle}\right)\left(5+3\langle Z_i\rangle T_e/T_i\right)\right.$$

$$+\left(\frac{3}{2}\right)^2\frac{1}{\alpha_0}\left[\frac{2\beta_0}{3}+\left(\frac{5}{3}+\frac{Z_l T_e}{T_i}\right)\right.$$

$$\left.\left.-\left(\frac{5}{3}+\frac{\langle Z_i\rangle T_e}{T_i}\right)\left(\frac{m_l}{\langle m_i\rangle}\right)\right]^2\right\}\left(\frac{n_l}{n_i}\right)k\lambda_{lh}\,, \qquad (24)$$

where $\lambda_{lh}=v_l\tau_{lh}$ and $v_l=\left(T_l/m_l\right)^{1/2}$. Here we can readily identify contributions due to thermal diffusion, viscosity, and joule heating by the coefficients γ_0, μ_0, and α_0, respectively.

An interesting feature of Eq. (24) is that it predicts the dominance of thermal diffusion over viscous effects for $\left(m_l/\langle m_i\rangle\right)\left(5+3\langle Z_i\rangle T_e/T_i\right)<15/2$ (i.e., $T_e/T_i<4.2$ for a

CH plasma, where $\langle Z_i \rangle = 3.5$ and $\langle m_i \rangle / m_l = 6.5$); whereas in the conventional formula the viscous damping is always dominant. More important, however, is the emergence of a joule-damping mechanism that is not present in the single-fluid model. It is easily shown for the case of CH plasma that this mechanism is dominant and at least three times larger than the thermal-diffusion mechanism. In terms of overall damping rate, a comparison between Eqs. (19) and (24), for CH, shows that

$$\frac{\mathrm{Im}(\omega_{lh})}{\mathrm{Im}(\langle \omega_i \rangle)} \approx \frac{101 + 34\,T_e/T_i + 2.77(T_e/T_i)^2}{0.86 + T_e/T_i}. \qquad (25)$$

This predicts an increase in the damping rate by at least a factor of 58.

Another interesting feature of Eq. (24) is that the joule-damping mechanism becomes independent of T_e/T_i for plasmas in which both species of ions have the same charge-to-mass ratio, so $\langle Z_i \rangle / \langle m_i \rangle = Z_l / m_l$. In such a plasma the electric field, which is the only mechanism by which the electron pressure can affect the ions, cannot drive a velocity difference in the two species, and so cannot contribute to joule heating. In this case, the viscous damping can eventually dominate for sufficiently large T_e/T_i.

In summary, the ion-transport coefficients have been calculated for a fully ionized unmagnetized plasma composed of light and heavy ions. The results show that using standard single-ion formulas with averaged ion masses and ionizations can lead to significant underestimations of the thermal conductivity, viscosity, and joule dissipation. The implications for the collisional damping of ion-acoustic waves are that joule heating and thermal diffusion can become the dominant damping mechanisms and the overall damping rate increases.

ACKNOWLEDGMENT

This work was supported by the U.S. Department of Energy Office of Inertial Confinement Fusion under Cooperative Agreement No. DE-FC03-92SF19460, the University of Rochester, and the New York State Energy Research and Development Authority. The support of DOE does not constitute an endorsement by DOE of the views expressed in this article.

REFERENCES

1. S. I. Braginskii, *Reviews of Plasma Physics* (Consultants Bureau, New York, 1965), Vol. 1, p. 205.
2. I. P. Shkarofsky, T. W. Johnston, and M. P. Bachynski, *The Particle Kinetics of Plasmas* (Addison-Wesley, Reading, MA, 1966).
3. S. P. Hirshman, Phys. Fluids **20**, 589 (1977).
4. M. D. Tracy, E. A. Williams, K. G. Estabrook, J. S. DeGroot, and S. M. Cameron, Phys. Fluids B **5**, 1430 (1993).

Three-Halves-Harmonic Radiation from Long-Scale-Length Plasmas Revisited

Introduction

Starting with the very early experiments relating to laser fusion, observations have shown a characteristic spectral emission near the 3/2 harmonic of the irradiating laser wavelength.[1] For simplicity we will name this emission "3/2 self-emission" to distinguish it from similar spectral features that may be induced by a separate probe beam. This spectral signature was immediately recognized as being related to the underlying two-plasmon-decay[2–5] (TPD) instability near quarter critical density. The detailed generation mechanism for this emission is, however, still a subject of considerable controversy and active research. This article represents another attempt to explain the detailed origin of this emission and its consequences for diagnostic applications. These conclusions can be succinctly summarized as follows: (1) The observed threshold for this 3/2 emission is not a good indicator of the threshold of the underlying TPD instability; (2) the absence of 3/2 emission is not a reliable indicator of the absence of the TPD instability; and (3) the value of the spectral features as a temperature diagnostic is very limited at best.

These conclusions are contrary to the majority of published work.[6–9] On the other hand, LLE's position on this subject has been one of caution for quite some time,[10,11] clearly de-emphasizing the diagnostic value of this signature. More recently, Meyer and Zhu[12] reported on Thomson scattering experiments on CO_2-laser-plasma interactions that showed broadening of the k-vector spectrum of TPD plasma waves well above threshold. Their conclusions are essentially similar to ours, although they did not discuss the detailed 3/2-harmonic spectra and their relevance to shorter wave interaction physics.

The continued interest in the TPD instability lies primarily in its potential for generating energetic electrons,[13] which could prove detrimental for laser fusion. The energetic electrons are produced as a consequence of the large-amplitude plasma waves generated by the TPD instability. The threshold of the TPD instability is a few times 10^{13} W/cm^2 for typical laser-fusion applications.[11] In long-scale-length plasmas this instability is apparently not influenced significantly by current laser-beam-smoothing schemes, such as smoothing by spectral dispersion (SSD).[11] Contrary results were obtained in experiments with induced spatially incoherent[14] (ISI) beams. However, these experiments were single-beam, solid-target experiments with short density scale lengths and may therefore lead to different interaction results.

Experimental Setup and Data

The experiments were carried out on the 24-beam OMEGA UV (351-nm) laser system using eight beams to explode mass-limited targets (6-μm-thick, 600-μm-diameter CH targets). Another set of eight beams was delayed by 0.6 ns and maintained the electron temperature at ≥1 keV over periods of ~1 ns. An additional interaction beam was then incident on the plasma perpendicular to the original target surface and could be timed within a few nanoseconds of the heating beams. All beams were outfitted with distributed phase plates (DPP) for increased average irradiation uniformity (ignoring the high-frequency DPP speckle pattern). The plasma produced in this way has been carefully characterized[15] and modeled using the two-dimensional hydrodynamic code *SAGE*.

Streaked 3/2-harmonic spectra were taken primarily in the backscatter direction at ~30° with respect to the interaction beam. Details of these and other data have been reported in Ref. 11. Here we would like to discuss in more detail the 3/2 self-emission, which was only perfunctorily dealt with in Ref. 11.

In Fig. 57.12 we have reproduced two typical streaked spectra. The upper streak was taken with secondary heating beams, while the lower streak was taken without secondaries. The weak signal around 1 ns is due to the primary heating beams and is of no interest in this discussion. The typical, split 3/2 emission of interest is located between 1.4 and 2.1 ns in this figure. The temporal pulse shape of the secondary heating beams is shown superposed in the upper half. (The primary heating beams have the same pulse width and peak at 1 ns but are not shown in this figure.) The dotted line superposed on

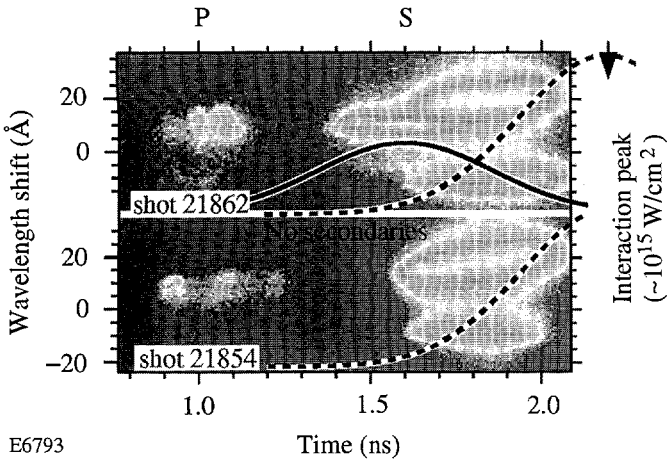

Figure 57.12
Streaked, 3/2-harmonic self-emission spectra from long-scale-length laser plasmas. Upper streak: spectrum in the presence of primary (P), secondary (S), and interaction (I) beams timed at t = 1 ns, 1.6 ns, and 2.2 ns, respectively. The intensities of the individual primary and secondary beams are ~5 to 6 × 10^{13} W/cm^2; that of the interaction beams is ~10^{15} W/cm^2. Lower streak: same as above but without secondary heating beams.

both streaks represents the normalized interaction beam intensity, which peaks at 2.2 ns. Note that the two curves are not drawn to scale; the on-target peak intensity of the interaction beam is ~10^{15} W/cm^2, while the peak intensity of each of the secondary (and primary) beams lies around 5–6 × 10^{13} W/cm^2.

There is one obvious difference between the two streaks shown in Fig. 57.12. The upper trace contains an additional spectral component that starts at ~1.4 ns, well before the onset of the main 3/2 emission, and exhibits a smaller frequency shift relative to $3\omega_0/2$. This component has been discussed in detail in Ref. 11, where it was tentatively identified as due to Thomson scattering off TPD plasmons excited by one particular secondary heating beam. In this case the interaction beam plays only the role of a Thomson probe. Separate experiments have since verified this identification. This Thomson-scattering feature is thus a very sensitive diagnostic for the TPD threshold. The threshold was found to be ~2–3 × 10^{13} W/cm^2 for the following plasma conditions near $n_c/4 : T_e \approx 1$ keV, density scale length $L_n \approx 250$ μm, λ_L = 351 nm. The theoretical TPD threshold[4] is given by

$$I_{th}^{2\omega_p} \approx 5.2\times10^{15} T_{keV} / \left(L_{n,\mu m}\lambda_{\mu m}\right)$$

$$\approx 6\times10^{13}\, W/cm^2 .$$

This intensity is ~2–3 times higher than the experimental threshold but is consistent with the intensity distribution of a typical DPP speckle pattern in which ~60% of the energy is found at intensities above the peak of the smooth Airy envelope. The latter is the generally accepted nominal beam intensity, but significant energy content is found right up to ~3 times the nominal peak intensity.

By contrast, the main 3/2-harmonic, self-emission feature exhibits larger frequency splitting (~18-Å red shift and ~12-Å blue shift) and has a threshold of a few 10^{14} W/cm^2 (see Fig. 57.12). This threshold is 5–10 times higher than the TPD threshold determined above. Thus the 3/2 self-emission threshold is not a good measure of the TPD threshold nor is the absence of 3/2 self-emission proof that the TPD instability is not excited. Here we make the usual assumption that all 3/2 emission is due to some form of Thomson scattering involving incident photons of the interaction beam and plasmons of frequency close to $\omega_0/2$, which are in some way related to the TPD instability. The problem with this assumption is the difficulty of satisfying the required phase-matching conditions.

Interpretation of Data

Reference 11 pointed out that the frequency splitting of the self-emission spectra is consistent with Thomson scattering of the interaction beam off TPD plasmons near the Landau cutoff. However, the phase-matching conditions for this scattering process are not easily satisfied, as will be discussed below. In addition, the theoretically predicted, maximum TPD growth occurs closer to $n_c/4$ with correspondingly smaller frequency splitting between the plasma waves, yet we find no evidence of these plasmons in the 3/2-harmonic self-emission spectra. However, it should be kept in mind that the growth rates drop off only very slowly with decreasing electron density.[4]

In Fig. 57.13 the TPD decay diagram is shown in k-vector space with $k_\parallel$ aligned with the density gradient prevailing in the interaction region. All TPD decay triangles terminating on a given horizontal line result in plasma waves with the same frequencies, $\omega_0/2 \pm \Delta\omega$. The TPD growth rate has its maximum along the hyperbola shown in the graph and drops to zero near the Landau cutoff, and also for $k_\perp = 0$. The growth rate[4] decreases quite slowly as one moves away from the hyperbola of maximum growth, as is also shown in Fig. 57.13 ($\gamma \approx 0.6\ \gamma_{max}$ at edge of shaded area).

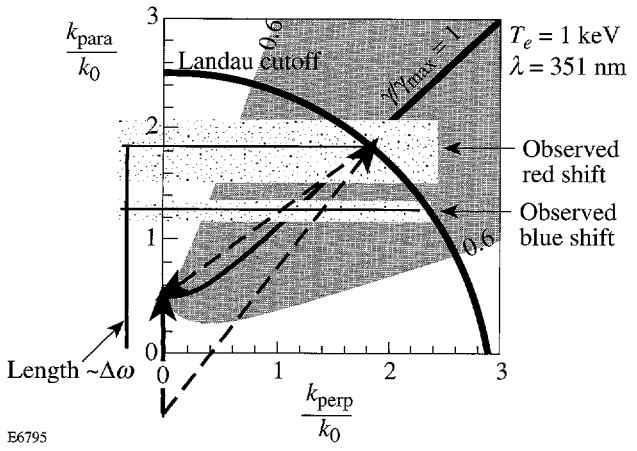

Figure 57.13
Two-plasmon decay diagram in k-space with $k_\parallel$ aligned parallel to incident beam and local density gradient. The Landau cutoff is given by $k\lambda_D = 0.3$. The frequency shifts of the two TPD daughter waves are proportional to the ordinate of the apex of the decay triangle as shown. The shaded areas correspond to the observed shifts for the red and blue components of the 3/2-harmonic self-emission.

The upper, stippled, horizontal area indicates the range of 3/2-harmonic red shifts seen in the experiments. The observed blue shifts are smaller and correspond to the lower stippled area as though the two 3/2-harmonic features originated from different decays. This difficulty can be removed as follows: First we assume that the primary TPD decays occur near the Landau cutoff and close to the maximum growth rate hyperbola. Second, to approach the phase-matching conditions for Thomson scattering involving an incident photon (wave vector k_0) and a "blue" plasmon, we must invoke a secondary electron plasma wave (EPW) decay of the "blue," i.e., longer k-vector plasmon. This results in a reduced blue-shifted secondary plasmon whose direction is parallel to that required for phase matching for Thomson scattering (see lower half of Fig. 57.14). The blue shift of this plasmon from $\omega_0/2$ also corresponds closely to that observed for the blue 3/2-harmonic feature as was already pointed out in Ref. 11. This kind of secondary decay process has been variously invoked experimentally[16,17] and theoretically[18] but was usually combined with propagation of plasmons in the density gradient. However, the importance of a threshold of these secondary decays has not been recognized.

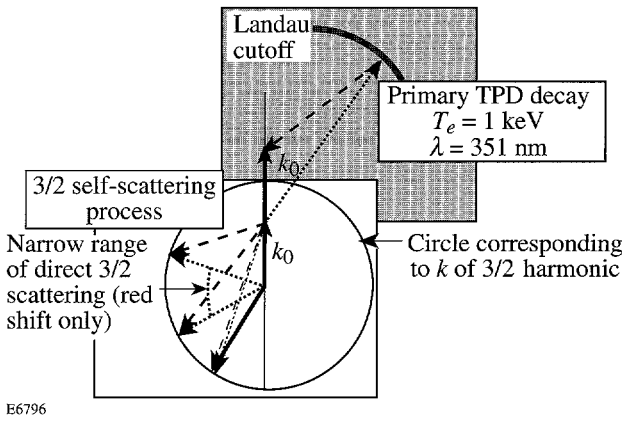

Figure 57.14
k-vector diagrams of the primary TPD decay and the secondary Thomson scattering process leading to 3/2-harmonic self-emission. The upper part of the figure shows the primary TPD decay, while the circle in the lower part represents the locus of the 3/2-harmonic em wave generated by summing an incident photon (k_0) with a plasmon. With the exception of a small range of "red" plasmons giving rise to near-90°-sidescattering, 3/2-harmonic radiation, all plasmons participating in the Thomson-scattering process must first undergo a secondary electron plasma wave decay for the "blue" plasmons or must be scattered by appropriate ion waves ("red" plasmons).

Invoking the secondary EPW decay has a number of interesting consequences: (1) It explains the higher threshold for the 3/2 self-emission compared to the TPD threshold since the plasma waves have to build up to where their intensity exceeds the threshold of the EPW decay instability. (2) The EPW decay growth rate is proportional to k and thus maximizes near the Landau cutoff. This could explain why the dominant 3/2 emission reflects TPD decays just below the Landau cutoff density. Furthermore, the decay process, while peaking in back direction, is not restricted to exact backscattering. It can thus generate the plasma waves with the proper direction for phase matching to Thomson scattering as discussed above (see Fig. 57.14). (3) Once the EPW decay instability is above threshold, ubiquitous ion waves are produced, which has been variously reported in PIC code simulations[19,20] and in experiments on 3/2-harmonic generation.[21,22]

Direct experimental evidence for the TPD instability near the Landau cutoff is shown in Fig. 57.15. The scattering configuration for this streaked spectrum is indicated at the top of the figure. One of the secondary beams was selected as the "interaction beam" while the nominal interaction beam was delayed to peak 1 ns later as indicated in the figure. The very strong Thomson signal exhibits exactly the predicted shift and is only visible in the presence of the secondary beam acting as interaction beam. (Note that the polarization was chosen to optimize this signal and that experimental constraints forced us to probe TPD decays below the maximum growth rate hyperbola. The exact decay triangle probed was located in the lower stippled area (see Fig. 57.13) and very near the Landau cutoff.

The spectral splitting of the 3/2-harmonic self-emission is of very dubious diagnostic value for estimating the coronal temperature. The above model for generating this 3/2 self-emission involves two competing effects: the spectral splitting increases with temperature for any given plasmon k-vector length $\left(\Delta\omega \sim k^2 T_e\right)$, but this effect is counterbalanced by the k-vector cutoff set by Landau damping:

$$\left(k_{\text{cutoff}} \sim 1/\lambda_D \sim T_e^{-1/2}\right).$$

Thus, one would not expect any significant temperature dependence of the 3/2 spectral splitting, which corresponds well to most of our observations. The lower streaked spectrum in Fig. 57.12 is a notable exception: here, the intense interaction beam is incident on a very cold plasma (no secondary heating beams), and very strong heating (and filamentation) is expected.

Conclusions

In this article we propose a new interpretation of the ubiquitous 3/2-harmonic emission from laser-produced plasmas. This emission is a consequence of the strongly driven TPD instability whose plasma waves (daughter waves) undergo secondary electron plasma wave decays above a certain threshold. The plasma waves produced in this process can then be Thomson scattered using again photons of the interaction beam. The resulting spectral shifts are in accord with experimental observations. On the other hand, the 3/2 self-emission threshold reflects the threshold of the EPW decay instability rather than that of the primary TPD instability. While the existence of the 3/2-harmonic emission is always associated with the TPD instability, its absence is not conclusive proof for the absence of the TPD instability. Within the framework of this model the 3/2 self-emission spectra are not a useful temperature diagnostic.

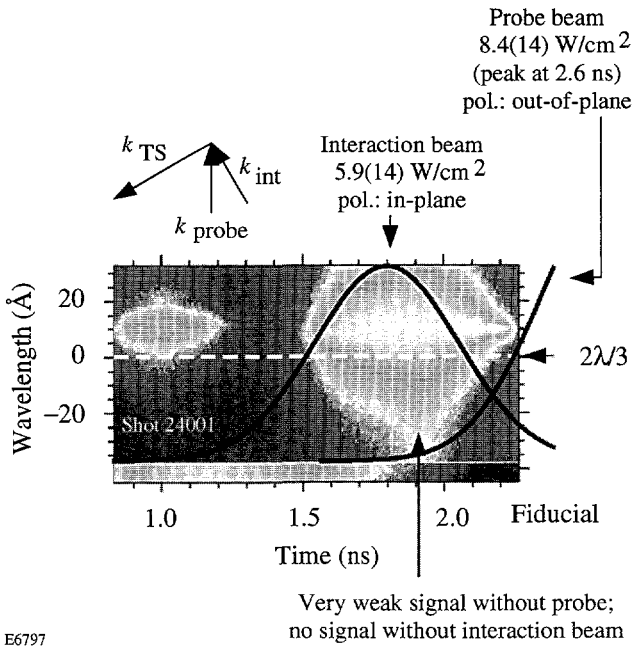

Figure 57.15
Direct evidence of TPD decay near the Landau cutoff using Thomson scattering. The TPD decay was driven by a particular secondary beam focused to ~6×10^{14} W/cm^2 (averaged over the DPP speckle pattern). The Thomson probe beam was delayed to peak at 2.6 ns to avoid any accidental 3/2-harmonic generation from the probe beam itself.

ACKNOWLEDGMENT

This work was supported by the U.S. Department of Energy Office of Inertial Confinement Fusion under Cooperative Agreement No. DE-FC03-92SF19460, the University of Rochester, and the New York State Energy Research and Development Authority. The support of DOE does not constitute an endorsement by DOE of the views expressed in this article.

REFERENCES

1. J. L. Bobin *et al.*, Phys. Rev. Lett. **30**, 594 (1973); P. Lee *et al.*, Appl. Phys. Lett. **24**, 406 (1974); H. C. Pant *et al.*, Opt. Commun. **16**, 396 (1976).
2. C. S. Liu and M. N. Rosenbluth, Phys. Fluids **19**, 967 (1976).
3. A. Simon, R. W. Short, E. A. Williams, and T. Dewandre, Phys. Fluids **26**, 3107 (1983).
4. W. L. Kruer, The *Physics of Laser Plasma Interactions* (Addison-Wesley Publ. Co., Redwood City, CA, 1988), pp. 81 ff.
5. H. A. Baldis, E. M. Campbell, and W. L. Kruer, *Handbook of Plasma Physics,* edited by N. M. Rosenbluth and R. Z. Sagdeev (Elsevier Science, Amsterdam, 1991), Vol. 3, pp. 397–408.
6. A. I. Avrov *et al.*, Sov. Phys. JETP **45**, 507 (1977); V. Yu. Bychenkov *et al.*, Beitr. Plasma Phys. **23**, 331 (1983); R. L. Berger and L. V. Powers, Phys. Fluids **28**, 2895 (1985).
7. J. Meyer, Y. Zhu, and F. L. Curzon, Phys. Fluids B **1**, 650 (1989).
8. P. E. Young *et al.*, Phys. Rev. Lett. **61,** 2766 (1988).
9. P. E. Young *et al.*, Phys. Fluids B **2,** 1228 (1990).
10. W. Seka, B. B. Afeyan, R. Boni, L. M. Goldman, R. W. Short, K. Tanaka, and T. W. Johnston, Phys. Fluids **28**, 2570 (1985).
11. W. Seka, R. E. Bahr, R. W. Short, A. Simon, R. S. Craxton, D. S. Montgomery, and A. E. Rubenchik, Phys. Fluids B **4,** 2232 (1992).
12. J. Meyer and Y. Zhu, Phys. Rev. Lett. **71,** 2915 (1993).
13. N. A. Ebrahim *et al.*, Phys. Rev. Lett. **45**, 1179 (1980); D. W. Phillion *et al.*, Phys. Rev. Lett. **49**, 1405 (1982); D. M. Villeneuve, R. L. Keck, B. B. Afeyan, W. Seka, and E. A. Williams, Phys. Fluids **27**, 721 (1984); R. L. Keck, L. M. Goldman, M. C. Richardson, W. Seka, and K. Tanaka, Phys. Fluids **27,** 2762 (1984).
14. T. A. Peyser *et al.*, Phys. Fluids B **3**, 1479 (1991).
15. W. Seka, R. S. Craxton, R. E. Bahr, D. L. Brown, D. K. Bradley, P. A. Jaanimagi, B. Yaakobi, and R. Epstein, Phys. Fluids B **4**, 432 (1992).
16. F. Amiranoff, F. Brian, and C. Labaune, Phys. Fluids **30**, 2221 (1987).
17. A similar secondary decay process was proposed for the strongly driven parametric decay instability by K. Tanaka, W. Seka, L. M. Goldman, M. C. Richardson, R. W. Short, J. M. Soures, and E. A. Williams, Phys. Fluids **27**, 2187 (1984).
18. H. C. Barr and G. A. Gardner, in the *1984 International Conference on Plasma Physics,* edited by M. Q. Tran and M. L. Sawley (Ecole Polytechnique, Lausanne, 1984), Vol II, p. 265; S. J. Karttunen, Laser and Particle Beams **3**, 157 (1985).
19. A. B. Langdon, B. F. Lasinski, and W. L. Kruer, Phys. Rev. Lett. **43**, 133 (1979).
20. D. F. DuBois and H. A. Rose, Bull. Phys. Soc. Am. **38**, 1913 (1993), paper 2Q 6.
21. P. E. Young *et al.*, Phys. Rev. Lett. **61**, 2766 (1988).
22. D. M. Villeneuve, H. A. Baldis, and C. J. Walsh, Phys. Fluids **28**, 1454 (1985); H. A. Baldis and C. J. Walsh, Phys. Scr. **T2/2** (1982); H. A. Baldis and C. J. Walsh, Phys. Rev. Lett. **47**, 1658 (1981).

OMEGA Upgrade Status Report

The completion (and acceptance by the Department of Energy) of the final design of the upgrade to the OMEGA laser system marks the beginning of the system-integration phase of the project. System integration is the manufacturing and installation of the various subassemblies that constitute the laser system. It began during this reporting period with the delivery and installation of the major structures. By the end of December, nearly all of the support structures were installed in the laser and target bays.

In November, all of the main target bay structures were installed, including the F-ASP monoliths, both end mirror structures, and the target mirror structure (TMS). During that time, the target chamber had to be installed within the TMS. To be completed are the personnel platform for the TMS and the periscope mirror assembly.

In the laser bay, nearly all of the structures were installed, including all the splitters, the amplifier and spatial filter structures for stages A through E, and the structures for the frequency converters. Left to install are four structures: one for the stage-F amplifiers and three for the stage-F spatial filters.

This issue of the LLE review continues the series begun in the last issue—the system description as excerpted from the Executive Summary provided to DOE as part of the review documentation of the OMEGA Upgrade design. This issue contains descriptions of subsystems including power conditioning, controls, optomechanical systems (both laser and target areas), and major structures.

Power Conditioning

The power-conditioning subsystem converts utility ac electrical power into the high-voltage, high-current electrical pulses used to fire the flash lamps that supply optical pump energy to the laser amplifiers. To create these pulses, large capacitors are charged to high voltage (7 kV) and then discharged through a pulse-forming network (PFN) comprising that capacitor, an inductor, and a flash-lamp pair.

The number of flash lamps used in each amplifier is dependent upon the size of the amplifier. Each PFN is connected to one, two, or five flash lamps, depending on whether it feeds a 15-cm, 20-cm, or rod amplifier, respectively. An assembly consisting of the PFN's, a charger, and the control circuitry needed to power one laser amplifier is referred to as a power-conditioning unit (PCU). This is a complete unit requiring only command instructions from the power-conditioning control computer and ac input power. A charging power supply in each PCU allows adjustment of the energy output of each amplifier; this level of control is required for balancing the power of the laser system.

In addition to the main discharge circuitry, many PCU's will have preionization and lamp check (PILC) circuits. This circuitry provides a lower energy pulse (higher voltage, lower current) that is fired 250 μs before each normal system shot (preionization). This pulse ionizes the gas in the lamp in preparation for the large current pulse that will follow. The preionization provides a near full-bore discharge that reduces the production UV line radiation that is detrimental to amplifier lifetime. In addition, the acoustic shock from the electrical discharge is reduced when a PILC is used. The PILC discharge is also used alone after a shot to check for lamp failures on that shot (lamp check). The PCU has the circuitry required to monitor each lamp during this PILC discharge and detect any that do not conduct current; faulty lamps will be replaced prior to the next shot.

To ensure safe operation, each PCU has an extensive array of hard-wired logical interlocks and self-checks. This is complemented by a local microprocessor used to monitor the interlocks and the status of various voltages and currents. This PCU control module (PCM) is based on the Neuron® Chip

from Echelon Corporation. The module contains LON (local operating network) interface circuits, a trigger input receiver, a logic power supply, and fiber-optic transceivers for communication. The PCM is housed in a steel enclosure with an eight-character alphanumeric display to indicate the status of the PCU.

Because of the high voltages present in the power-conditioning subsystem, safety was a major concern during design. The PCU's are computer controlled for normal operation, but for safety there are a number of "hard-wired" interlocks that do not rely on computers for activation. For instance, each of the enclosures is interlocked, and the capacitor is immediately discharged when the interlock is violated.

At the normal operating voltages the power-conditioning system will be capable of storing 42 MJ of electrical energy. The system is rated for even higher voltages, storing 46.2 MJ at full rated voltages. The extra capability will accommodate future needs as amplifiers (and other components) degrade and require more pump energy to obtain the nominal stage gains.

The Upgrade power-conditioning system consists of 120 disk amplifier PCU's and 97 rod amplifier PCU's. There are two types of disk amplifiers and, hence, two styles of disk PCU's. The difference is the number of individual flash-lamp circuits (PFN's) required. The 20-cm SSA (single-segment amplifier) PCU requires 16 PFN's, while the 15-cm SSA PCU requires only 12 PFN's. Other than the number of PFN's the units are identical. The PCU's will store a maximum of 368 kJ (20 cm) or 276 kJ (15 cm) at 14.8 kV.

There will be two styles of PCU's for the rod amplifiers. One type will power the stage-D and the laser driver amplifiers and will use existing OMEGA power-conditioning units with modern controls and new components. A new charging power supply will replace the 12-head chargers formerly used in the OMEGA units. These PCU's will not have PILC circuits and will store a maximum of 78 kJ at 7.5 kV. The second type of rod PCU will be used for the A, B, and C stages of rod amplifiers. These are basically a cross between the disk amplifier PCU and the stage-D rod amplifier PCU. These totally new units will also store 78 kJ at 7.5 kV (maximum voltage) and will have PILC circuits similar to the disk amplifiers.

All PCU's will require a timing signal to synchronize firing of the amplifiers. This signal will originate in the master timing system (located in the pulse-generation room) and be distributed throughout the capacitor bays to each PCU. The initiation of this signal is commanded by the power-conditioning control computer. This signal will be delayed individually at each PCU by an amount set by the power-conditioning control computer. This delay is adjusted to synchronize the peak of the amplifier gain to the arrival of the laser pulse at that amplifier. The performance of the power-conditioning system is outlined in Table 57.I.

Upgrade Control System

The Upgrade Control System (UCS) will provide operators with remote control of subsystems, displays of sensor data, and safe, automatic sequencing of key processes. The control system will also collect and record information about each shot.

1. Control System Functions

The following eight functions have been assigned to the UCS as the design of the OMEGA Upgrade system has progressed:

Table 57.I: PFN Specifications

	Disk Amps	Rod Amps
Pulse width (μs)	550	475
Linear resistance (mΩ)	120	100
Inductance (μH)	180	55
Capacitance (μF)	210	460
Charging voltage (kV)	14.1	7.3
Stored energy/PFN (kJ)	20.9	12.3
Total energy (MJ)	35.1	7.1
TOTAL ENERGY (MJ)	42.2	

1. Control of the electric power and the fluid facilities that support the beamline amplifiers
2. Routine operational alignment of the beamline optics
3. Control of the laser drivers subsystem
4. Diagnosis of the laser system's performance
5. Control of personnel access to the laser bay, target bay, capacitor bays, and the rooms under the target bay
6. Control of the vacuum system that services the spatial filters
7. Control and, where appropriate, data-acquisition support of the instruments that sense shot-event parameters
8. Control of the vacuum systems that service the target chamber and the target diagnostic instruments

These have been allocated to six top-to-bottom "functions" within the UCS:

1. The power-conditioning function will provide the power conditioning and fluid control for all of the single-pass amplifiers in the system, including those in the laser drivers subsystem.
2. The alignment function will implement beamline alignment processes, beamline energy control, and beam-to-beam timing control.
3. The laser drivers function will provide control and monitoring of the initial pulse generation and amplification processes. This includes the multipass lasers at the start of the system and the appropriate alignment and beam diagnostic elements.
4. The beamline diagnostics function will control the operation and data-acquisition functions of the instruments that measure the characteristics of the laser pulse produced by the beamlines.
5. The facility interlock function will control personnel access and the main electric power source as a function of system status.
6. The experimental system function will control the target chamber subsystems and the data-acquisition systems for the target diagnostic instruments.

An additional **seventh function**, the shot executive, is also required. This function will serve to coordinate the activities of the other functions when it is necessary for them to work together to conduct a target shot.

2. Operations Timing

The activities that make up these functions take place during the operational periods that preceed and follow the brief high-energy shot event. (Figure 57.16 illustrates this relationship.) The control system activities support maintaining the system, preparing it for the shot, and recording the shot results. The timing resolution necessary to implement these requirements is of the order of tens of seconds.

The shot executive function initiates the "pre-shot" processes that must take place in the hour before a shot, verifies that the other functions are ready for the actual shot, and initiates the "shot" preparations. Thereafter, the power-conditioning function controls the laser system to within ten seconds of the shot and then enables the key system elements to

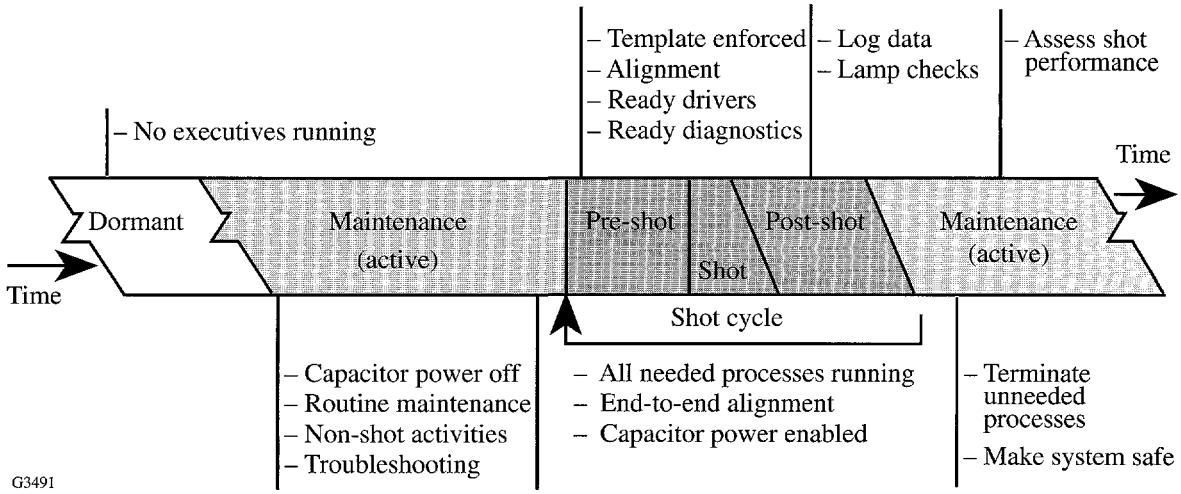

Figure 57.16
The flow (in time) of the system control operation for routine shots and maintenance. When the capacitor power supply is enabled, the system is termed active. The shot cycle is a heightened readiness state involving all of the control functions.

proceed on the basis of the electrical master timing signal. The events synchronized by the master signal include generation of the optical pulses in the laser drivers subsystem, the electrical pulses that drive the flash lamps in the laser amplifiers, and the operation of diagnostic instruments. The timing and duration requirements for the flash-lamp current are in the 100-μs range and are implemented by the electronic circuits in the PFN's. The submicrosecond characteristics of the optical pulses are achieved by electro-optical techniques.

3. General Architecture

The general hardware/software architecture that will implement each of these functions is illustrated in Fig. 57.17. Separate "executive" processes for each function will run on workstations installed in the control room. These are referred to as "host processors" and will be connected to each other and to other OMEGA Upgrade system computers via a dedicated Ethernet local area network.

Each function's executive process will provide the operator interface for the function and will exert control over and receive information from devices in the bays by communicating with one or more "intermediate" processors over the Ethernet. These intermediate computers serve to relieve the executive of routine computation and downward communication tasks. Communication between the executive processes is necessary primarily for coordination of shot-related events.

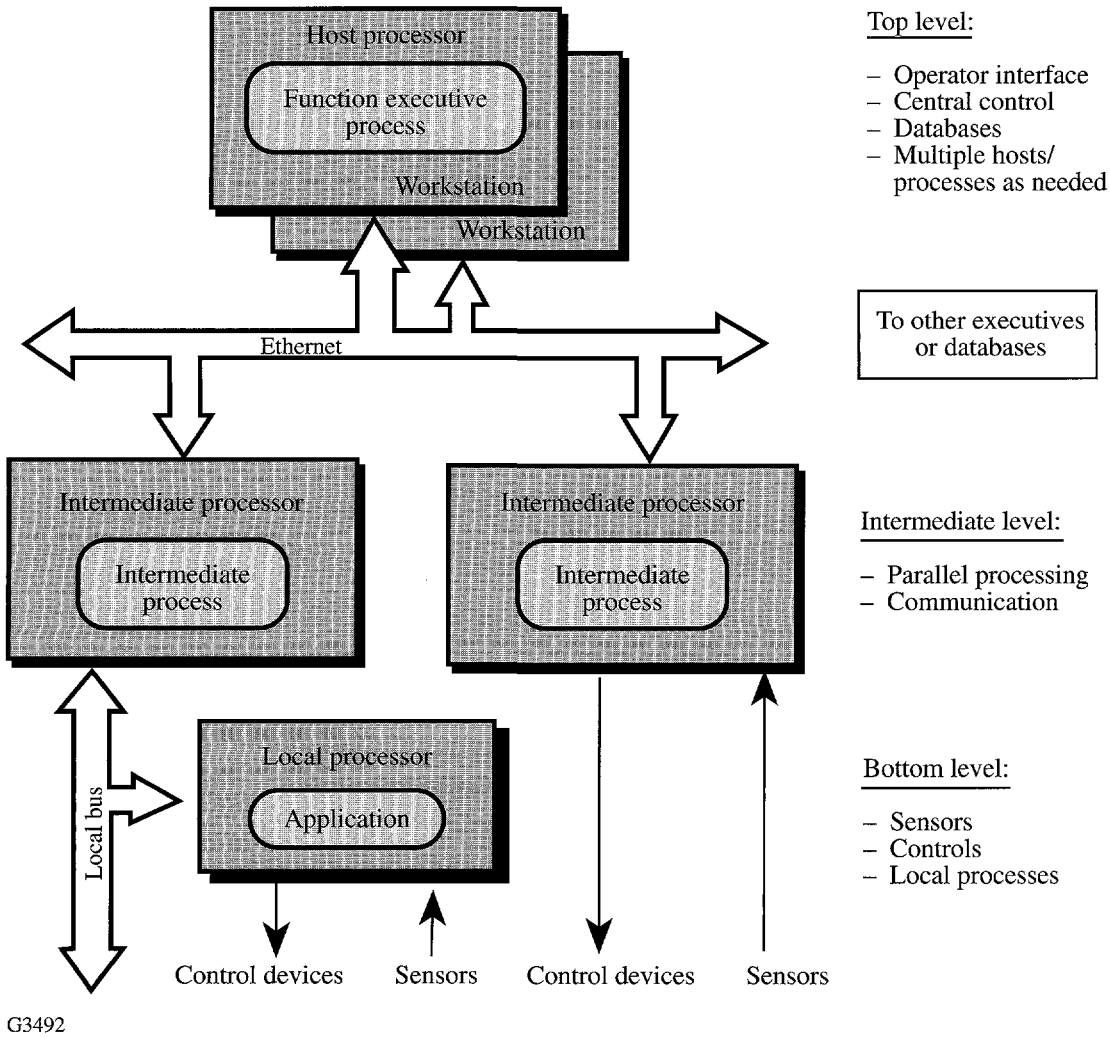

Figure 57.17
The top-level architecture of the OMEGA Upgrade control system. Three levels of computers are used to provide a system with distributed intelligence. Personnel interact with a host processor, which commands, via two local networks, numerous microprocessor-controlled devices.

At least two variations of the intermediate and bottom architectural levels will be employed in the UCS. In many situations, a third layer of computer control based on a Neuron® Device Control will be used. The Neuron is an inexpensive, single-chip, multiprocessor system that implements a local area network protocol called a local operating network (LON) and provides for control of devices and acquisition and communication of data. In the UCS, nearly 2000 Neurons will be used to integrate simple control actuators and feedback sensors under software control to produce more-sophisticated, local control devices. Neurons will also be used to acquire and digitize data from diagnostic sensors. Where the Neurons are used, the primary function of the intermediate process is to act as interpreter between the Ethernet and the LON. In this case the intermediate processor is called a LON Ethernet Network Adapter (LENA). Each LENA will service four LON's (channels), each of which will support 50 to 150 Neurons. (This configuration is illustrated on the left side of Fig. 57.17.)

Another architectural variation (illustrated on the right side of Fig. 57.17) is used to control the alignment video cameras and to acquire and process video frame data. This configuration is referred to as a digital expandable still camera (DESC). Here the intermediate process controls up to five cameras directly, rather than via a network. The DESC process also performs the digital image processing necessary to convert frames of video data into two-axis error data that is transmitted to the alignment function executive process. Similar configurations will be used to control diagnostic devices in the laser drivers, laser diagnostics, and experimental system functions.

4. Facility Interlocks

Personnel safety is of primary importance in the design of the OMEGA Upgrade System. Three major classes of hazards are addressed at a fundamental level by interlock functions built into the utilities that are part of the laboratory facility supporting the laser system. These are

- control of the power source for the high voltages inherent in the laser amplifiers;
- control of the warnings issued when the presence of alignment laser emissions could constitute an eye hazard; and
- active and passive monitoring of the location of personnel in the bays.

These and other basic facility-monitoring features are included in the following specific facility interlock subsystems:

- The electric power source for all the laser amplifiers is a commercial power substation formally designated Unit Substation #2 and commonly referred to as "the 750-kVA power source." This equipment is located at the west end of Capacitor Bay 1 on the lower level of the slab. No electric power will be available to the power-conditioning units unless a relay in the substation is closed by logic built into facility interlock hardware.
- Five laser sources and 79 beam-train shutters will be monitored to control lighted warning signs at seven locations. A voice enunciator will provide audible warnings of status changes.
- Approximately 30 surveillance video cameras will provide operators with views of the bays.
- Approximately 44 passive infrared motion sensors will alert operators to movements at times when there should be no activity.
- The open/closed status of 28 doors will be remotely sensed and monitored; 16 of these doors will also be equipped with remotely controlled locks.
- During normal operations, the identity of the occupants in each of five controlled zones will be monitored by means of a combination of badge readers and door-lock controls at the entrances.
- Bells and light beacons will warn of impending capacitor charging.
- Manual "dump buttons" are provided at numerous locations in the bays. These will directly disable the 750-kVA power and short-circuit all of the high-voltage capacitors in the system.
- The interlock logic will control grounding isolation features that ensure both personnel safety for routine operations and hardware safety during the shot events.
- The interlock logic will be able to override other controls and turn off the bay lighting.

5. Beamline Diagnostics

Acquisition of beamline diagnostic data is a major branch of the overall Upgrade control system architecture. One of the five control system executive workstations (beamline diagnostic executive) is dedicated to operating the laser diagnostics configured on the 60 beamlines located in the laser bay. These diagnostics include the following measurement systems:

- Harmonic energy detection (IR, green, and UV energy measurements)
- Full-aperture, high-flux calorimeters
- Beamline-to-beamline IR energy balance (splitting ratios, wave-plate settings)
- UV-on-target energy transport (3ω to target, beam-balance compensation)

At the highest level of the control architecture, the executive workstation first issues commands to the acquisition subsystems and then collects and processes the data for the laser system operators to evaluate. Below the executive workstation in this hierarchy are the local data-acquisition nodes that contain the specialized hardware used to interface to the laser diagnostics. These nodes reside on a combination of Versa Module Europa (VME) and Computer Automated Measurement and Control (CAMAC) platforms, depending on the application. In either case, these nodes communicate with the executive workstations through an Ethernet link. The local data-acquisition VME platform nodes contain embedded SPARC computers. These computers handle the lower-level input/output control and acquisition sequencing required to collect diagnostic data. The CAMAC platforms are interfaced to the VME platforms through high-speed, ~1.5-Mb/s bus adapters and have no local intelligence. This interface allows data to flow from CAMAC into the VME system at, or near, CAMAC backplane speeds. At the lowest level of the acquisition architecture are transient digitizing oscilloscopes and CCD (charge coupled device) camera arrays, discrete photodiodes, etc. These are used to capture electrical waveforms, two-dimensional optical data, pulsed events, etc. The oscilloscopes are interfaced to the intelligent VME nodes through dedicated general purpose interface bus (GPIB) communication lines. The CCD cameras have local video controllers and digitizing frame grabbers to buffer the images before uploading the data to the executive workstations.

Diagnosis and adjustment of the beam arrival time at the target is another critical control-system function. The responsibility for the associated tasks is shared by two of the top-level control-system functions. The beam arrival times will be measured using a photodiode at the target location and an rf interferometric technique. This system will determine the time differential between the arrival of a laser pulse at that location and the arrival of the same pulse at a reference location. The laser pulses will originate at the IR alignment table (IRAT) and be propagated through the beamlines from the stage-A splitter to the target chamber. The arrival time for each of the 60 beams is acquired sequentially. The resolution of the measurement is expected to be better than 1.5 ps.

This process must be performed as a special activity separate from normal shot operations. The alignment function will configure the IRAT and the beamlines to provide the pulses to the photodiode sensors. The experimental system function will position and control the sensor at the target location and acquire/reduce the time-differential data. The alignment function will process the timing data to determine the path adjustments required and then control the path length adjustment systems (PLAS's) to implement any required changes.

Optomechanical Systems

1. Optical System Design

The optical design of the system was constrained primarily by two factors: the need to fit the upgraded laser into the existing building and the desire to reuse as much hardware as possible (spatial filters, in particular). The top-level requirements for the total energy and the number of beams dictated the amplifier staging and the beam splitting required. Optical damage thresholds dictated the minimum beam diameters in each stage, which in turn fixed the magnification between stages. From these baselines the system was designed to incorporate image relaying as required by the implementation of SSD (smoothing by spectral dispersion) and by sound laser design practices.

Given the above, the layout of the laser system was then refined to ensure that no damage occurs from "ghost" reflections, provide equal path lengths in all beamlines, and provide an accessible and manageable system. The configuration has undergone several changes since the preliminary design. These changes were dictated by performance issues and ultimately resulted in a simpler configuration.

Once the system configuration was determined, error budgets were performed for energy, wavefront, alignment, and polarization. Each of these budgets was then distributed to the individual components in the system to formulate the requirements. For example, the wavefront budget was used to specify that the wavefront error contributed by each optical component not exceed $\lambda/10$. This value is relatively small because the disk amplifiers consume a major portion of the error budget. The pointing error in the system is driven by the requirement to point beams onto target with a precision of ~5% of the target radius. Given a minimum target radius of 300 μm and a 1.8-m-focal-length final lens, the total pointing error budget is 8.33 μrad. The distribution of this error affected the design of the alignment sensor packages, the optical mounts, and the various structures supporting the laser. It was this pointing error budget that necessitated the implementation of the epoxy/granite structures for the stage-F alignment sensor packages (ASP's), which act as the optical alignment references for the system.

The energy budget specified the fluences at various points in the system, thereby impacting the choice of substrate material, typically BK-7 or fused silica. The energy-balance constraints drove a requirement for identical beam sizes at all the frequency-conversion cells, to match the intensity and hence the conversion efficiency. This requirement forced a tight specification (±0.5%) for the focal length of the spatial filter lens. About that absolute specification, all lenses of a given type are corrected during fabrication such that all focal lengths are matched to ±0.2%.

The polarization budget suggested the contrast of the polarization required for efficient splitting and amplification. The requirements for balanced beam-to-beam frequency conversion dictated the need for Brewster-angle polarizers ahead of the FCC's. Because of the precision needed, these are required in spite of the (50:1) polarization contrast the Brewster-angle disk amplifiers provide at the end of the amplifier stages. The disk amplifiers provide a relative insensitivity to depolarization early in the system.

The resultant design is a system that fits into the existing building and maximizes the use of equipment from OMEGA. (Over 90% of existing OMEGA spatial filters were used in the upgraded system.) The system includes path-length adjustments that can provide simultaneous arrival of beam pulses at the target to within ±3 ps. Individual beams can be intentionally mistimed to ±5 ns with respect to $t = 0$. Mapping the UV beams to the spherical target chamber was performed to minimize the sensitivity to variations in performance of the individual amplifiers. This mapping (discussed under *Target Area*) uses two mirrors per beam, ensures that incident angles on the mirrors are less than 60°, maintains equal path lengths from the FCC's to the target, and fits within the existing space. The system design will deliver beams with sufficient energy, quality, and alignment accuracy to attain the ultimate goal of 1%–2% nonuniformity on target.

2. Optical Components

Optical components for the OMEGA Upgrade are being procured through several major contracts with five leading optical fabrication vendors. This section summarizes the engineering effort that led to these components being specified and purchased (at budget), with their performance meeting Upgrade requirements.

The top-level requirements for the laser performance and uniformity dictated an array of lesser requirements for appropriate beam profiles and energy levels at the target while minimizing fluences throughout the chain that could potentially damage optical components. From the requirements and configuration constraints, computer simulations of beam transport allowed determination of such parameters as fluence, B-integral, allowable wavefront and alignment error, and the required power balance.

Once the on-target error allowances were determined, optical engineers statistically apportioned the error among the components in the system. Budgets were made for the various types of error and used to establish surface finish and transmitted wavefront tolerances for each optical component. Once the fluences in the system were known, the optical material for each component could be chosen. The choice was typically between BK-7 for fluences below 2.0 J/cm^2 and fused silica for fluences above that.

Compilations of these parameters resulted in a specification control drawing (SCD) and statement of work (SOW) for each type of optical component in the Upgrade. These documents served as the basis for quotation requests from the optics vendors and as the measure of achievement for contractual obligations.

Specifications were written for the following categories of optical components:

- Spatial filter lenses
- Mirrors and beamsplitters
- Polarization control optics
- Aspheric focus lenses
- ASP optical components

The procurement cycle for each of these components required the vendor to generate plans for manufacturing, processing, cleaning, and testing of each component prior to the start of manufacturing. Source inspection, or at a minimum examination of vendor test data, has ensured that all optical components meet specifications. Typical specifications for these components (all measured at 1054 nm) are

transmitted wavefront error:	±1/10 wave
flatness (mirrors):	±1/20 wave
surface roughness:	<10 Å (rms)

3. Optical Coatings

The requirements for the OMEGA Upgrade optical coatings are discussed in the Preliminary Design Document[1] and in detail in the Optics Coating Requirements document.[2] The development of Upgrade coatings, in general, and the transport mirror coating, in particular, is described in several reports in the LLE Review.[3,4] A coating specification[5] also outlines the required tests and inspection criteria for all coated optics. A summary of the coating requirements is given in Table 57.II. The coating designations in the left column of this chart are discussed below. All the coatings have been designed, fabricated onto prototype substrates, and tested for both optical and damage specifications.

a. IR coatings. The coatings used in the IR (1054-nm) portion of the laser system comprise antireflection and reflector coatings. The substrates for the antireflection coatings are either BK-7 glass or fused silica depending on the incident fluence. The BK-7 substrates receive a vacuum-evaporated dielectric coating using an yttrium-oxide/silicon-dioxide design (1 ωAR, 1 ωAR45), while the fused silica optics are coated

Table 57.II: Coating Requirements for the OMEGA Upgrade.

Coating Designation	LC Gap	Wavelength	Incident Angle	Control Value	Reflectance		Transmittance		Max. Fluence* (J/cm^2)
					S%	P%	P%	P/S	
1ωHRSP45		1054 nm	45°	R	99.5	>99.5			5.4
1ωRSTP45		1054 nm	45°	R	>99.5	<4.0	>96		5.4
1ω99RS45		1054 nm	45°	R	99±0.5				5.4
1ω99RP45		1054 nm	45°	R		99±0.5			4.5
1ωStressAR		1054 nm	45°	R	<1.0	<0.5			5.4
1ωAR		1054 nm	0	R	<0.5	<0.5			5.6
1ωRSTP57		1054 nm	57°	T			95	500/1	5.1
1ωAR45		1054 nm	45°	R	<1.0	<0.5			5.4
LCS6.5	6.5 μ	No Optical Requirements							
LCS6.5	13 μ								
LCS9	>18 μ								
1ωARALIGN		1054 nm	0	R	<1.0	<1.0			2.9
		351 nm	0	R	>10	>10			2.9
SG1/2 ωAR		703 nm (cwl)	0	R	<1.0	<1.0			2.9
SG1 ωAR		1054 nm	0	R	<0.5	<0.5			5.4
SG3 ωAR		351 nm	0	R	<0.5	<0.5			2.9
SG3 ωAR/DPP		351 nm	0	R	<0.5	<0.5			3.6
SG3/1 ωAR		351 nm/1054	0°–8°	R	<0.5	<0.5			3.6
3ωHRSP(ANG)		351 nm	0°–60°	R	>99.5	>99.5			2.9
3ωStress		No Optical Requirements							
1/2/3 ωAR		351/527/1054	0	R	>85	>85			low power

cwl = center wavelength

*Note: Fluences assume 7-ns foot (F) pulse and 1.1-ns main (M) pulse.

with a porous-silica sol-gel (SG1ωAR). This high-damage-threshold (but delicate) coating was chosen on the basis of the fluence levels at the optics. The design may be modified after some experience on the glass development laser. The reflector coatings include high-reflectivity mirrors, partial reflectors, 45°-incidence polarizing beamsplitters, and 57°-incidence polarizers. These coatings are all based on a vacuum-evaporated dielectric coating using tantalum-oxide/silicon-dioxide designs. These materials have been extensively developed for high damage threshold and optical performance.

During initial manufacture of the reflector coating, stresses from the coating deformed the optic, causing these optics to fail optical surface figure testing. After several remedies were investigated, it was discovered that the best solution is a coating (1ωStressAR) that when applied to the back side of the optics produces similar stresses. This rear-side coating will be applied to all substrates coated with dielectric multilayers.

A coating process was developed to produce spacers of evaporated material for the liquid crystal devices in the system. These spacers provide better control of wedge tolerance (1.5 arc/s) in the assembled device, more accurate thickness of the liquid crystal layer (6.5 μm±0.5 μm), and faster assembly methods than the mylar spacers previously used.

The coating for the frequency-conversion crystals is a single-layer sol-gel design for the three wavelengths (SG1ωAR, SG1/2ωAR, and SG3ωAR). When applying these coatings, much of the effort is in the tooling and process development required for the dipping and spinning deposition processes. New polishing methods under consideration for these components also require developing cleaning methods to remove polishing oils.

b. UV optics. The UV (351-nm) transport optics are coated with a sol-gel antireflection coating (SG3ωAR) for the transmissive optics and a high-reflector coating [3ωHRSP(ANG)] for the transport mirrors. These sol-gel coatings have been designed, developed, and tested, and the production processes have been determined for all optics. For each application, the composition and design of the coatings will vary depending on the incidence angle of the beam and the orientation of the electric vector with respect to the coated surface. Optics having a low incidence angle and predominantly *s*-polarized light will use a design based on hafnium oxide/silicon dioxide. Optics that combine high incidence angle and predominately *p*-polarized light use a design containing more costly scandium-oxide/silicon-dioxide coatings. For a given angle, each design will provide the specified reflectance with the minimum number of layers to improve damage characteristics. These designs will also be modified to reduce the time-averaged electric field in the upper layers of the coatings.

A great deal of effort has gone into the design of the substrate cleaning and storage tooling, coating tooling, testing tooling, and handling tooling to ensure that no process degrades the high-quality substrate surfaces. Preliminary results from the newly installed 1.8-m coating chamber indicate that all uniformity requirements for the Upgrade optics will be met. A substantial effort went into establishing a sol-gel coating capability for the 650 optics to be coated as well as the facility needed to clean the 2000 optics for the Upgrade.

4. Optomechanical Design

Four key design constraints drove the Upgrade's optomechanical design. The first was strain-free mounting of all optical components. The mounts generally consist of three-point, 6°-of-freedom, exact-constraint designs that prevent typical mount manufacturing, assembly, and environmental tolerances from distorting the precision optical components. The second key feature is precision pointing and centering control of optical components. These include fixed mounts, manual drives, and motorized drives that typically have microinch and/or microradian accuracy and stability requirements. The third constraint is to provide an adjustment range adequate to acquire the laser beam within the optic's clear aperture. The range must be sufficient to compensate for typical fabrication and structure installation tolerances. Finally, all optical components must be packaged within the space constraints allocated by the 60-beam OMEGA Upgrade configuration. Examples of Upgrade optomechanical designs are the periscope mirror assembly (PMA), focus lens assembly (FLAS), transport mirror mount, spatial filters, and path length adjustment system (PLAS).

5. System Alignment

The alignment of the beamline segments is performed using an IR cw alignment laser and various references (typically crosshairs) located throughout the system. These references define the beam path upon which the laser system components are located. Once the system is aligned, the alignment beam propagates through the system and defines the location and direction the pulsed beam will travel during a shot. All of the optical components in the IR system are installed and aligned using this alignment beam.

End-to-end alignment of a frequency-tripled, IR laser system such as OMEGA presents a difficult alignment problem because the relatively low-power, cw IR alignment laser will not be converted to UV by the conversion crystals. This, along with the low IR reflectivity of the Upgrade's UV transport mirrors, means that a single alignment beam cannot be used to align the system from source to target.

The Upgrade alignment system therefore uses two wavelengths, unlike the previous system that was aligned from the oscillator to the target using IR light. While two wavelengths increase the system complexity, they eliminate the two disadvantages of single-wavelength alignment: the transport mirrors no longer need dual-function (IR/UV) coatings (because UV light is used to align these optics), and the focus lenses will not have to be translated after IR alignment to compensate for chromatic shift. The former dramatically improves the damage threshold of the UV coating, and the latter improves the operational accuracy of alignment. The IR portion of the laser is aligned using a 1054-nm Nd:YLF laser, together with alignment sensor packages located at the driver and stages A, C, and F within each beamline. For alignment of the UV portion of the system, a full-aperture, 351-nm cw laser is injected into the beam after the FCC's and just before the omnichromatic F-ASP's. This is done with movable mirrors located in the target bay. Co-alignment of this injected beam to the IR pulsed beam is performed using the F-ASP. An alignment sensor package located on the UV alignment table (UVAT) measures the alignment of the injected UV beams.

a. IR alignment. The following basic processes will be necessary to routinely align the IR beamlines:

1. Laser drivers and IR alignment laser injection (1 beamline segment)
2. Stage A–C pointing and centering (15 beamline segments)
3. Stage C–F pointing and centering (60 beamline segments)

Each process involves five steps: setup, image analysis, action determination, action implementation, and confirmation.

Process 1 requires the alignment laser and driver to be aligned into the A-splitter area by using an alignment sensor package in the A splitter (A-ASP). The ASP has pointing and centering references to ensure that the beam entering the stage-A splitter has the correct direction and position to propagate down the laser beamline. The driver injection is done after the alignment of the laser driver (not part of this procedure) and is necessary to propagate a driver beam into the laser chain. The backlighter driver is injected into the middle A–C segment and is aligned by the stage-A ASP. This injection is a somewhat manual process and is not part of the automated alignment routine. The following hardware is required: laser drivers, infrared alignment table (IRAT), and A-ASP.

Process 2, the alignment of the segment from the stage-A splitter to stage-C ASP, involves the alignment of the beams propagating from east to west in the laser bay and is performed using the alignment laser after it has been injected. This process is depicted in Fig. 57.18. Process 3 aligns the last portion of the IR system, the stage-C splitter to F-ASP, and is depicted in Fig. 57.19.

When all three sections are complete, the operator is assured that the centering reference at the end of the driver line has been transferred (within tolerances) to the centering fiducials at the F-ASP. This, coupled with the intermediate centering checks, ensures that the beam will not be vignetted on any optics in the laser chain. Similary, the beam pointing in all stages is checked, corrected, and verified. The final IR pointing and centering positions are recorded by the F-ASP to be used as a reference for the UV alignment process.

b. UV alignment. The periscope mirror assembly (PMA) and the F-ASP are the major elements in the UV scheme. The PMA includes the UVAT and a system that positions a set of mirrors near the face of the shield wall in front of the F-ASP's. In each position, these mirrors form a periscope that injects a UV alignment beam, which originates in the UVAT, into one of the 60 beamlines at the input end of its F-ASP. After the UV beam is correctly aligned to the fiducial in the F-ASP, it is transmitted to the target chamber and retro-reflected to a video camera that is part of the UV-ASP on the UVAT. (The beam may also be transmitted back to the UVAT via the opposing beamline that has also been accessed by the PMA.) The video signal is processed to provide position-error data that is used to drive the motorized end-mirror and target-mirror mounts to correct the pointing and centering of the beam or to adjust the focus lens in the FLAS. The PMA mirrors are then repositioned to inject the alignment beam into another beamline.

The following basic processes will be necessary to routinely align the UV optical trains to correctly deliver the shot pulse to the target:

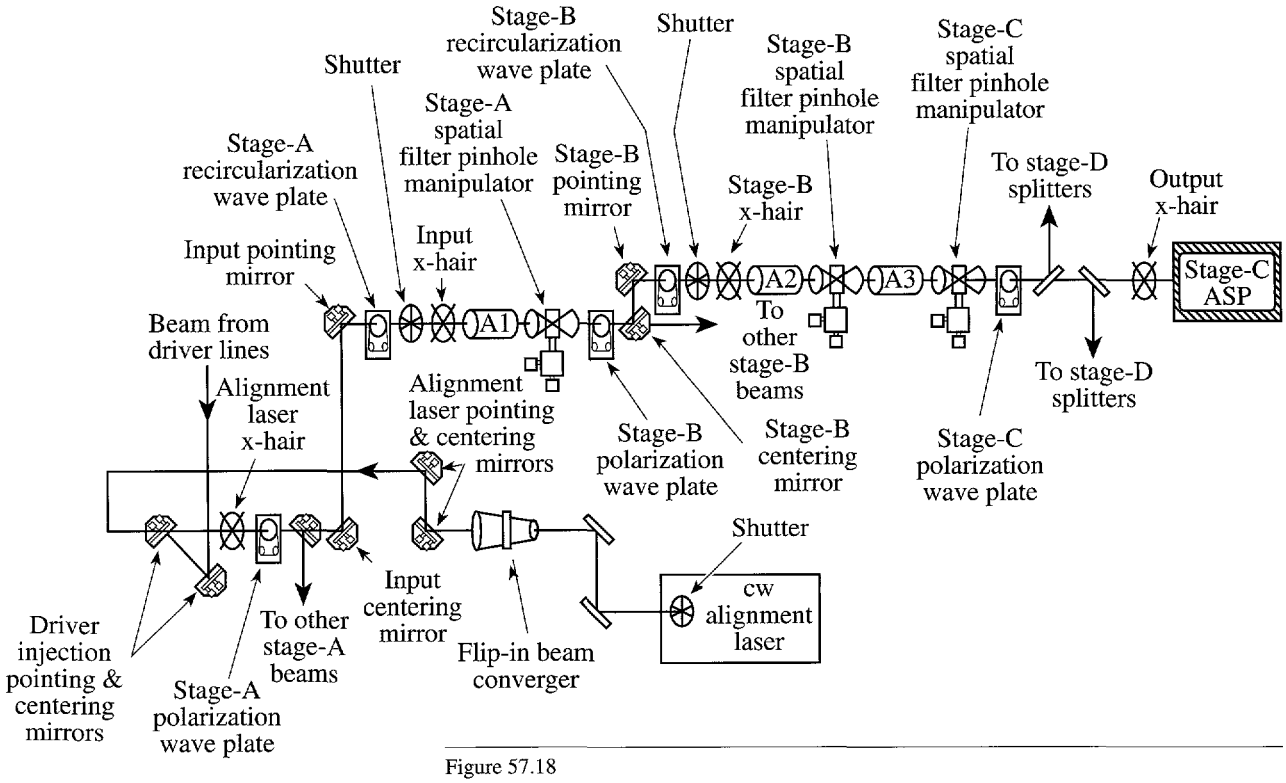

G3473

Figure 57.18
The optomechanical devices in an OMEGA Upgrade beamline from the laser driver to stage C.

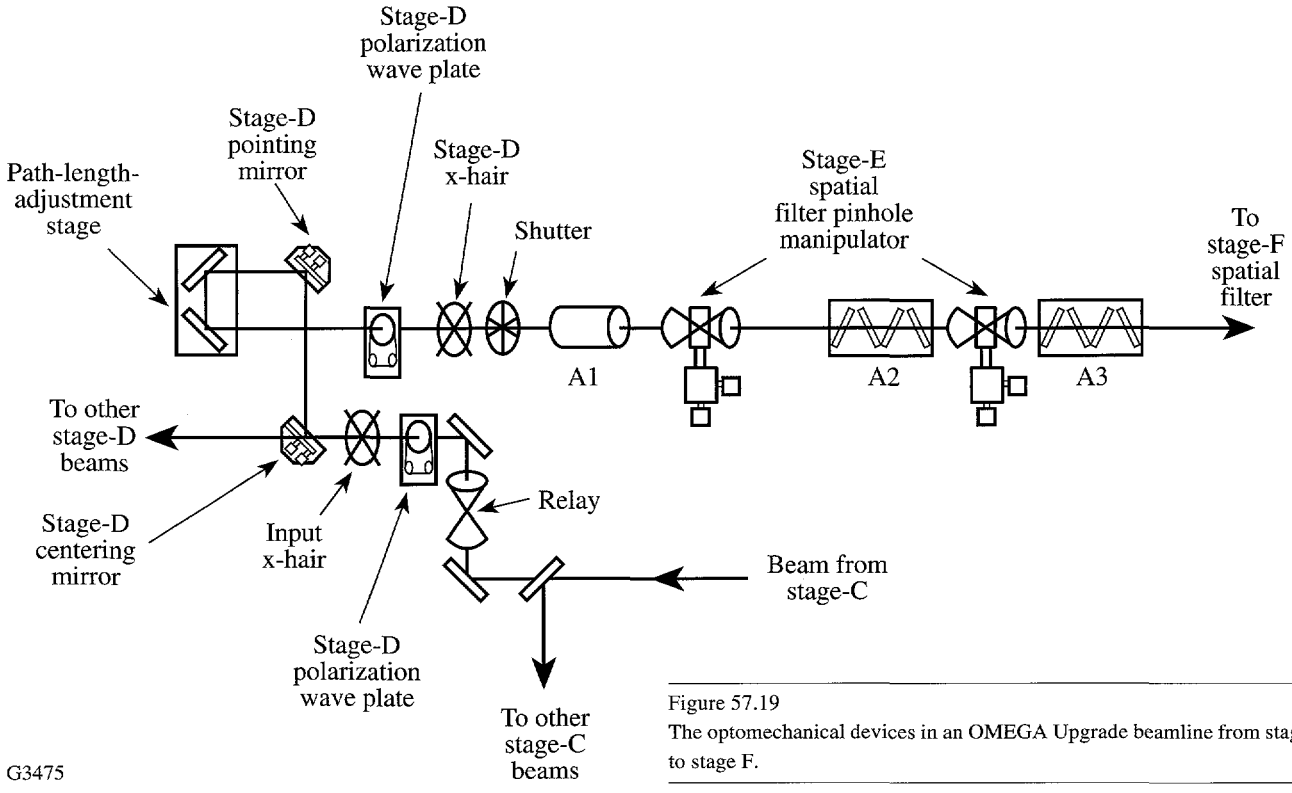

G3475

Figure 57.19
The optomechanical devices in an OMEGA Upgrade beamline from stage C to stage F.

1. UVAT laser injection
2. UV transport system pointing and centering
3. Focusing

As with IR alignment, each process involves the five steps: setup, image analysis, action determination, action implementation, and confirmation. Here each process will be performed on the 60 separate beamlines, and the set-up step includes positioning and adjusting the PMA mirrors. Figure 57.20 depicts the optical configuration to perform alignment of the UV transport system. The UV alignment system will also be used to align the 60 FCC assemblies to their respective beamlines.

c. Propagation of centering errors. During the injection alignment, the alignment table and driver fiducials are centered on the system fiducial. In the A to C split alignment, the system fiducial is centered to the A fiducial and the A to the B fiducial.

To minimize the accumulation of errors, the C split to F-ASP alignment will center the A-splitter fiducial to the D-splitter fiducial and confirm the A-splitter fiducial to the F-ASP fiducial for final IR centering.

The UV targeting will center the F-ASP fiducial to the target mirror fiducial creating a total of four stages where centering errors can occur: (1) driver to system, (2) system to cluster, (3) cluster to PMA, and (4) PMA to target mirror. The first transfer is done so that the driver line is not used for beam alignment, and the injection need not be done at the C-ASP's. The second is necessary because the system fiducial is not at an image plane and cannot be expected to have sufficient image quality for alignment past the A-split. The third transfer is necessary because targeting cannot be done in the IR. The final transfer is used to center the target mirror and the FLAS.

Wherever possible, alignment will be performed in parallel steps across the beamlines to minimize the time needed to align the entire system. It is intended to utilize the parallel structure of the control network and the image processing to minimize the time required for each alignment step. The capability to align individual or subgroups of the beamlines is still required, even though it does not use the alignment hardware to its maximum efficiency.

d. Alignment sensor packages. The alignment sensor packages (ASP's) are stable optical telescopes used to view an alignment beam propagating in a laser beamline. They monitor the alignment stability of the system by sensing the pointing of the alignment lasers, and the position of the laser beam on optical components by sensing the position of alignment fiducials (e.g., crosshairs). These fiducials can be automatically inserted into the beamline or manually attached to optomechanical assemblies such as amplifiers and spatial filters. The ASP's are also used to view the position of the

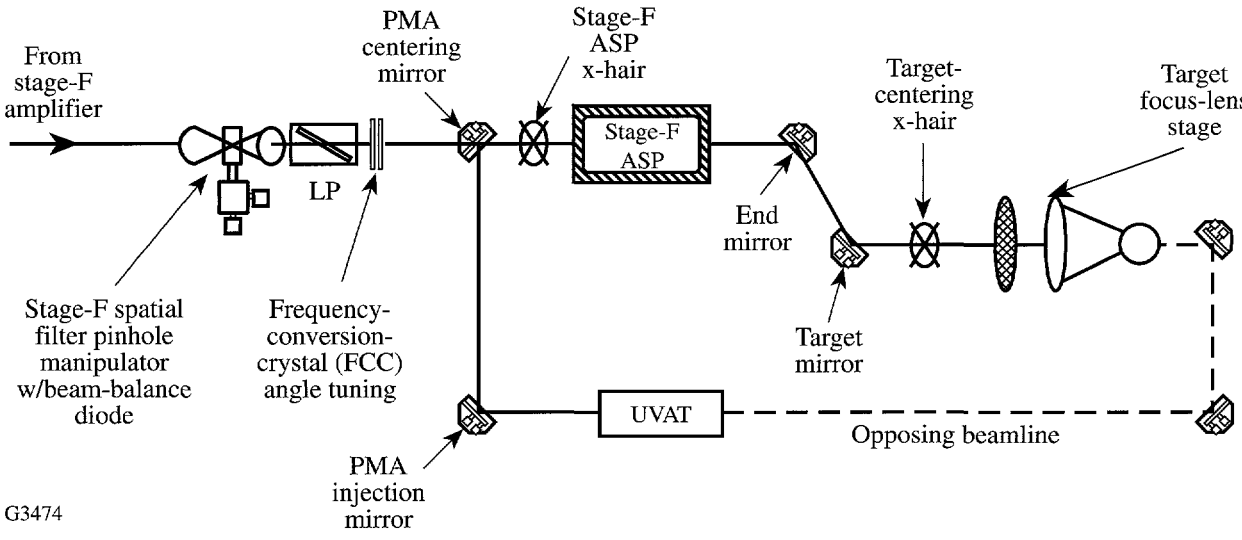

Figure 57.20
The optomechanical devices in an OMEGA Upgrade beamline from stage F to the target.

spatial filter (SF) pinholes to allow the automated alignment system to center the SF pinholes onto the beam.

The ASP's are the primary sensors for the beamline alignment system and typically reside at the ends of the beamline segments. Each ASP contains a solid-state image sensor (CCD) to view either the focus of the telescope objective (beam pointing) or the output image of the telescope, which shows the position of alignment fiducials (beam centering). Two-state devices move components within the ASP's to allow either of these functions to be performed by a single image sensor. The ASP's contain no moving or adjustable components between the entrance pupil and the point where the beam focuses on an alignment reticle. This feature provides long-term stability of the pointing reference for the beam.

To establish and maintain the beam path, the ASP's are used to view flip-in fiducials (FIF's) at the start and end of each beamline. These FIF's are surveyed into place during laser system construction and then become the reference for subsequent alignments. The ASP's locate the end fiducial relative to the image of the start fiducial to monitor beamline centering stability and maintain the beamline geometry of the laser system. Misalignments are corrected using mirrors located just before the start fiducials.

Four sets of ASP's are employed in the OMEGA laser system. A single-driver ASP resides at the end of the laser driver. A single stage-A ASP resides within the stage-A splitter. Fifteen stage-C ASP's reside at the end of the 15 beamlines that run from the B splitter to the C splitter. Sixty stage-F ASP's reside at the end of the 60 beamlines that run from the D splitter through to the FCC's. These four sets are made up of two basic types of ASP's: the driver, stage-A, and stage-C ASP's are nearly identical; the stage-F ASP is significantly different.

The driver, stage-A, and stage-C ASP's are all existing OMEGA beam diagnostic packages (BDP's) modified to sense pointing and centering with a single, solid-state detector. The top-level performance requirements for the driver, A, and C alignment sensor packages were derived from the pointing error budget, which dictated the pointing sensitivity, short-term stability, and long-term stability (drift) for these instruments. Where possible, the requirements for the driver, A-, and C-ASP's were made similar to allow common modifications to the existing BDP's and to minimize design time.

The primary function of the driver ASP is to monitor the driver alignment, particularly the coalignment of the foot and main pulses. The driver ASP must sense pointing to 1.3-μrad accuracy over a 10-mrad field of view.

The stage-A ASP monitors the injection of the driver line and IRAT beams into the laser system. It is mounted in the stage-A splitter structure and is also designed to sense pointing to 1.3 μrad over a 10-mrad field of view. This sensor must be able to diagnose beam centering (FIF position) to 0.13-mm accuracy and includes a collimation sensor to allow the collimation of the IRAT, foot-, and main-pulse drivers to be matched. This is important for the optical design (i.e., all three beams come to a common focus at the SF pinholes and at the target) as well as to maintain optimal frequency-conversion efficiency for the foot and main pulses.

The stage-C ASP monitors the alignment of the beamline segments from the B splitter to the C splitter. The stage-C ASP also must sense pointing to 1 μrad over a 10-mrad field of view and must diagnose beam centering (FIF position) and drift to 0.19-mm accuracy.

The requirements for the stage-F ASP were derived from the pointing-error budget—a systematic, top-down, allocation of the top-level pointing error of 8.33 μrad to the various components of the laser system. The driving considerations were for alignment precision (< 0.3 μrad) and pointing stability (<2.7 μrad/h). The instrument is required to meet all three of these specifications. It was also required that the F-ASP use a bare glass reflection rather than transmission through a "leaky mirror" to minimize polarization effects and maximize radiometric stability.

The precision requirement led to the choice of an effective focal length of the F-ASP objective matched to the pixel size of the detector. This, in combination with the requirement for complete absence of chromatic aberration, led to the selection of a three-mirror, off-axis, all-reflective telescope for the F-ASP objective. Although the use of a reflective telescope puts more stringent requirements on the angular stability of the optomechanical system than a refractive system would, this is compensated by the complete lack of chromatic variation of optical performance provided by an all-reflective system.

The pointing stability requirement drove the mechanical design. In general, the requirement for extreme angular stabil-

ity leads the mechanical designer to strive for symmetry in all possible aspects of the mechanical structure. The beam-to-beam spacing caused adjacent F-ASP's to be nested together in such a fashion that individual one-beam instruments would, necessarily, have been highly asymmetrical. To avoid this, ten-beam F-ASP units were designed with modular subassemblies that can be removed for off-line service as required. To further improve the stability of these instruments, the main structure was made of Harcrete™, a cast epoxy/rock composite. This material's properties include high stiffness, low thermal conductivity, excellent vibration damping, excellent dimensional stability, and the ability to be cast into complex shapes. Figure 57.21 depicts two of the cast monoliths; the one on the right is sectioned to show the optic in a single F-ASP unit. Figure 57.22 shows in detail the beam paths through one of the F-ASP's.

To avoid the problem of post-adjustment drift, the critical optical mounts were designed to be nonadjustable. Adjustable installation fixtures permit the optics to be positioned correctly and then epoxied into place, using special low-shrinkage, high-stability epoxy. The installation fixtures are then removed from the F-ASP. This scheme provides the advantages of adjustability without the associated drift problems.

The moving parts of the F-ASP are components of modular subassemblies that can be removed for off-line service. The video camera, expected to be the least reliable component of the instrument, is contained in the relay subassembly, which mounts kinematically to the F-ASP. An off-line alignment fixture adjusts and tests the relay so that it will be correctly focused and aligned when inserted into the F-ASP structure.

6. Spatial Filters

Evacuated spatial filters are used after every amplifier stage in the OMEGA Upgrade to provide image relaying and various amounts of magnification. The filter sizes depend on the beam aperture and magnification; for instance, the stage-A filter is *f*/50 and 5.6 m long, and the stage-F is *f*/22 and 10.25 m long. Aspheric lenses are used in all the large-aperture spatial filters, thereby reducing the accumulated spherical error in the system.

The spatial filters comprise five subsections: the tube weldments, the lens cells, the lens spacers, the interface package, and the pinhole manipulator. The tube weldments are 316-stainless-steel tubes with flanges and are rated for 5×10^{-6} Torr. The nominal operation pressure for the spatial filters is 2 mTorr.

The lens cells and lens spacers are mounted on each end of the weldments. The cells are one-piece annular mounts for the lens and contain two O-ring grooves for vacuum seals, one on the spacer side and the other on the lens side. The cell contains a simple, spring-loaded retainer for the lens to facilitate installation and replacement. The lens spacer is an annular aluminum cylinder used to compensate for variations in the focal length of the lenses and manufacturing tolerances of the tube weldments. Custom sizing of each spacer for a specific tube and lens pair allows the collimation of each spatial filter to be strictly maintained. The length of the spacers will be determined to ≤ 125 μm using a special fixture and collimation detector, thereby providing collimation of each spatial filter to $\lambda/4$ @ 1.054 nm.

The pinhole manipulator positions the pinhole directly at the focal point of the spatial filter, requiring adjustment in three dimensions. The pinhole manipulators from the original OMEGA system will be used on the Upgrade for stages A–D. The size and close proximity of the stage-E and F spatial filters require a new manipulator that has the slides and motors located within the spatial filter tube. The mechanical and electrical components of these manipulators are vacuum compatible.

The interface between the spatial filter and the support structure will be an air bearing that will allow the entire filter to be moved out of the beam. This will allow for the necessary removal of the spatial filters during routine alignment; quick-disconnect pneumatic fittings will make this task easier.

7. Frequency Conversion Cells

The frequency-conversion crystals (FCC's) convert the fundamental wavelength of the OMEGA laser (1054 nm) to the second- (527-nm) and third- (351-nm) harmonic wavelengths. The frequency-conversion cells have been engineered to meet the requirements established in the OMEGA Upgrade Preliminary Design Document.[1] The following describes the engineering process that led to contracts with vendors capable of supplying high-quality, frequency-conversion components.

The parameters that contribute to uniform frequency conversion were established using simulations conducted by the

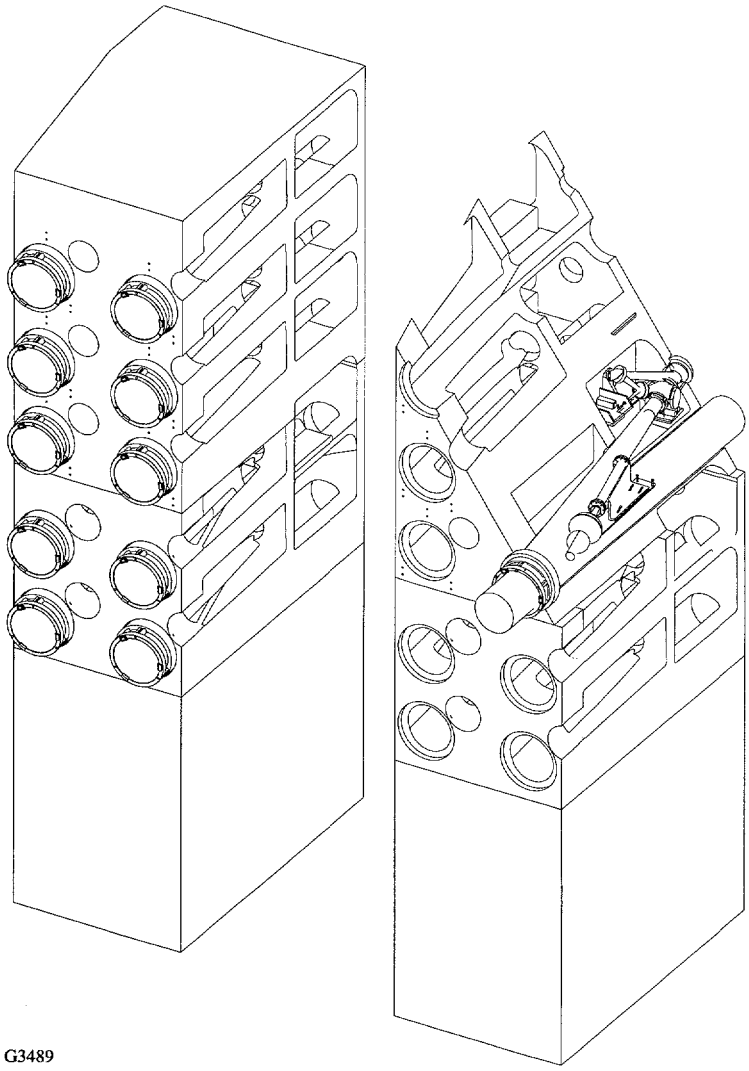

Figure 57.21
Two of the monoliths for the stage-F alignment sensor package (F-ASP), each containing ten beamlines. A section through the right structure depicts the layout of the optics for a single beamline.

code "*MIXER*."[6] To keep losses below 0.5% of the conversion efficiency at the peak of the main pulse, where the crystals are the most sensitive to errors, the following tolerances (obtained from Table 7.4 of Ref. 1 with adjustment where appropriate by the crystal thickness ratio 12:7.6) must be achieved:

Doubler misalignment	142 μrad
Doubler wavelength shift	7 Å
Doubler temperature	0.6°C
Tripler misalignment	29 μrad
Tripler wavelength shift	0.2 Å
Tripler temperature	0.1°C
Polarization angle	±0.3°
Fraction in wrong polarization	3×10^{-5}

In the preliminary design, the doubling and tripling stages each used a thicker central crystal for efficient conversion of the foot pulse surrounded by a thinner, annular crystal for efficient conversion of the main pulse. During the detailed design, a thorough investigation and reevaluation of the required pulse shapes and the associated intensity distributions at the plane of the conversion crystals led to the selection of a single-thickness crystal, which efficiently converts both main

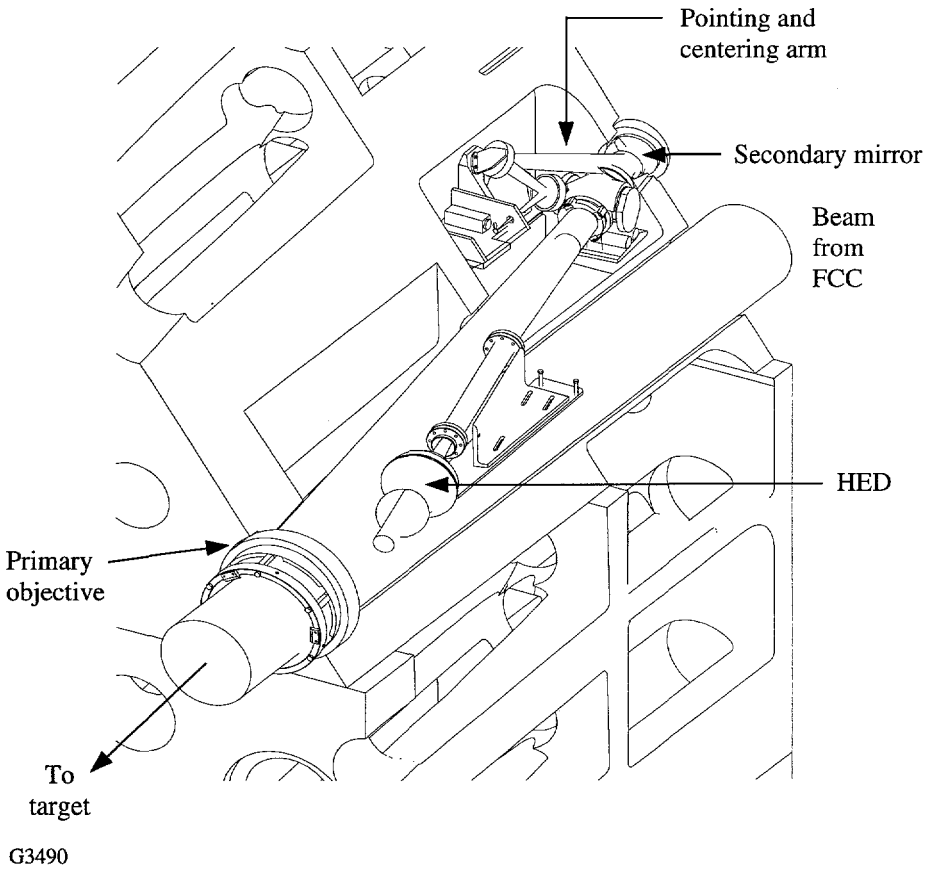

Figure 57.22
Major optical components in a stage-F alignment sensor package (F-ASP) for a single beamline.

and foot pulses and maintains the same operating parameters. This design utilizes 12-mm-thick crystals (30-cm diam) for both the doubler and tripler.

Once the crystal configuration was established, a complete specification and statement of work for the crystals was prepared using the system optical error budget. Since the crystal is a transmission optic, it should normally be subject to the same tolerances as any other optic in the system. In consideration of the different manufacturing techniques needed for these crystals, as compared with conventional optical glass elements, the error budget allocated to the FCC's was relaxed somewhat. For example, surface roughness was budgeted at 50 Å (rms) because of the difficulty in finishing KDP due to its water solubility. (However, the vendor contracted to polish the Upgrade KDP has produced a sample of KDP polished to 10-Å roughness.) The statement of work for crystals calls out the following specifications for finishing:

Transmitted wavefront error	±1/10 wave
Flatness	±1/20 wave
Surface roughness	<50 Å (rms)

The vendors were required to submit plans for manufacturing, processing, cleaning, and testing each crystal prior to the start of manufacturing. Source inspection, or at a minimum, examination of vendor test data, ensures that each crystal is produced according to specification.

Since frequency conversion is key to the efficient drive of fusion targets, the remainder of the frequency-conversion subsystem required careful design to meet the system requirements. A dielectrically coated, linear polarizer with 500:1 contrast will be placed ahead of the FCC to produce the required polarization contrast at the FCC. LLE's Optical Manufacturing section has demonstrated the ability to produce polarizers of this type. All of the optical mounts, for both the

crystals and the polarizer, will have the same stability and flexibility as the most critical optical mounts in the system. The FCC control design provides for better than 5-μrad tuning accuracy and provides for sensing of the crystal temperature, which facilitates control of the tuning angle as a function of temperature.

The FCC design includes an input window that serves two purposes: to absorb backscattered ultraviolet radiation (needed to protect the dielectric polarizer coating) and to act as a reflective alignment surface. Materials research at LLE helped determine the glass type to be used in this application; it is being manufactured to the same optical specifications as other optics.

8. Periscope Mirror Assembly

The primary function of the periscope mirror assembly (PMA) is to inject a full-aperture UV laser beam into the UV portion of the beamlines to facilitate alignment of these beams onto the target. This is necessary because the fundamental laser wavelength (1054 nm), which is used to align the IR beamlines, is not efficiently transmitted by the UV transport optics.

The 300-mm UV alignment beam originates on the UVAT and may be injected into any of the 60 OMEGA Upgrade beamlines by two sets of mobile mirrors. Two identical systems for the north and south halves of the target bay are used to reduce alignment time and, more importantly, to create a continuous optical path through opposing beams. The latter facilitates performing a multitude of alignment and calibration procedures that require reflected and transmitted UV beams. Each of the two mirror sets comprises two mirrors that move independently to inject the UVAT beam into any of the 30 beamlines located on the north or south sides of the target bay. Figure 57.23 illustrates the principal features of the PMA that services the north segment of beamlines. (The south assembly is identical.)

PMA requirements were derived from the system-level, shot-cycle time and the pointing error budget. The following key requirements have received the closest attention and have been the main drivers in the evolution of the PMA design approach:

1. Average time to position the periscope mirrors and settle transients: ≤ 15 s
2. Alignment beam coarse positioning tolerance (3 σ): pointing $\leq \pm 1.8$ mrad, centering $\leq \pm 1.0$ mm
3. Alignment beam fine pointing (1 σ) : $\leq \pm 3$ μrad
4. Alignment beam pointing stability: angular drift due to PMA effects must limit total excursion to within ± 3.0 μrad (1 σ) for a period of at least 40 s after acquiring the desired beam axis. Here, drift applies to

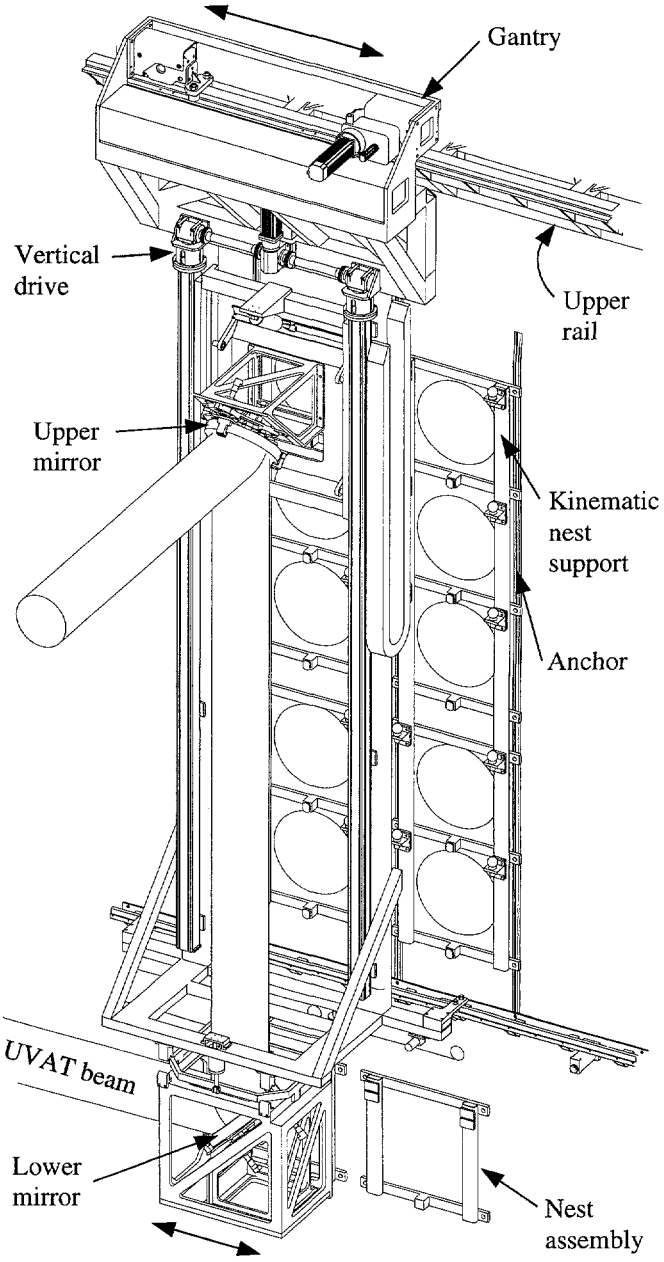

Figure 57.23
The major components for the north half of the periscope mirror assembly (PMA). The entire gantry (with the lower mirror attached) moves to each of the six columns of five beams. The upper mirror moves vertically to select a particular beamline.

beam displacements having frequency components less than 60 Hz.

Personnel safety was given highest priority followed by schedule, cost, and reliability. Also, target-bay space considerations mandated that the PMA be housed within a 1.2-m-wide corridor running along the west shield wall.

The pointing-stability requirement dictated most of this design. Based on a careful assessment of the expected shield-wall stability, kinematically ideal mounts were selected to support the periscope mirrors on the wall during alignment operations. This makes good use of the wall's great mass and intrinsic damping characteristics. Also, load paths from the periscope mirror through the mounts and into the wall were kept very short and stiff, thereby achieving high natural frequencies in spite of the large masses of the solid mirrors (5 cm × 35.5 cm × 51 cm). This avoids amplification of most wall-borne disturbances, thereby enhancing the mirror stability.

Two periscope mirror modules (PMM's), an upper and a lower, are carried by a gantry that is a major feature of each PMA system. The lower mirror directs the alignment beam to the upper mirror, which, in turn, reflects the alignment beam into the capture range of the F-ASP, i.e., into near coincidence with the desired beamline. Precision alignment with respect to the F-ASP is then accomplished by coordinated tip and tilt adjustments of both periscope mirrors using the F-ASP pointing and centering arms as references. The PMM's have built-in, two-axis micropositioners that operate under closed-loop servo control identical to those of the end and target mirrors.

A typical operational sequence for one of the gantries is as follows: Given a command from the host computer, the PMA local controller activates the horizontal drive and moves the gantry along the wall, stopping at the desired column of five beamlines. Centering and locking mechanisms are actuated to accurately position the gantry and lock it to the guide rails. While the gantry is traveling, the controller also activates a precision ball screw drive that moves the upper mirror vertically to the desired beamline. Both mirrors are then transferred to their respective kinematic nests on the shield wall and are released from mechanical contact with the gantry. This isolates the mirrors from disturbances that may otherwise be transmitted through the gantry structures. Using the F-ASP as a reference, the UV alignment beam is accurately coaligned with the primary beamline. Various alignment functions can then be performed on the UV transport system, many of which involve an ASP on the UVAT. When alignment operations at a particular beamline are complete, the mirrors are transferred back to their stowed positions aboard the gantry. The above sequence is repeated as needed for each of that gantry's 30 beamlines.

The time for repositioning at the next beamline is minimized (≤8 s) by using an efficient path through each 30-beam array. Although the array measures about 3 m by 6.7 m, maximum transport velocity and acceleration are only 23 cm/s and 15 cm/s^2, respectively. As a result, driving forces and transient disturbances are low despite the mass of the gantries (>900 kg each).

Coarse-positioning requirements will be met by surveying each kinematic nest into position using a surrogate mirror at each position in turn. The positional requirements in this case are well within the capabilities of current surveying practice.

For fine pointing, the PMM's incorporate the same design as the transport mirror mounts and TMM micro-positioners. To gain additional confidence, finite element analysis (TMM's) has been performed on those elements that differ somewhat from the TMM design. The deflection of the mirror surface figure is predicted to be less than 75 nm. A prototype is being constructed to verify mounting performance under PMA dynamic load conditions.

Many safety provisions have been factored into the PMA design: the PMA corridors will be fenced off with safety gates interlocked to PMA power; emergency stop lanyards will be installed inside the corridors; warning beacons and an audio alert will be activated during PMA transit; and mechanical sensors will be fitted on both sides of the gantries to provide emergency stops.

9. Focus Lens Assembly (FLAS)

The optomechanical requirements for the FLAS were determined by the optical design and the pointing error budget and are shown in Table 57.III.

The optical requirements for the FLAS were determined by the system requirements. The focus lens has a focal length of 1.8 m and functions at *f*/6. The lens and the separate vacuum window/blast shield produce less than a quarter-wave of aberration (at 351 nm) over a field of view (FOV) of ±2 mm. The FLAS design provides a location, just ahead of the lens, for a phase-conversion plate, expected to be a plane-parallel, fused silica component ~300 mm in diameter and 25.4 mm thick. The optical design must also ensure that damage-causing ghost

Table 57.III Summary of Requirements for Focus Lens Assembly

Centration of lens to port axis	0.25 mm
Maximum static tilt of lens	0.28 mrad
Blast-window thickness	25 mm
Focus range	10 mm
Maximum transverse motion (over focus range)	1.6 μm
Additional focal shift	+10 cm
Transverse vibration	<0.6 μm
Axial vibration	2.5 μm
Focus accuracy	25 μm
Surface deformation	<100 nm
Vacuum differential (supported by blast window)	760 Torr
Note: Positive motion is away from the chamber center.	

reflections do not fall on any optics for any focus lens position (over a range of ±10 mm).

The optical requirements were met with an aspheric singlet lens, designed to be free of spherical aberration when used in conjunction with a 25.4-mm-thick blast shield. The curvatures of the singlet were chosen to position the ghost reflections away from all optical components in the OMEGA Upgrade system. This selection of curvatures somewhat compromised the attainable FOV, as the lens shape that would maximize FOV (i.e., minimize coma) would have caused potentially damaging ghost reflections to fall on nearby optics. Despite this compromise, the FOV provided by the final design is ±4.5 mm, significantly exceeding the original requirement.

The FLAS subsystem is shown in Fig. 57.24. The left side depicts the entire assembly including the blast-shield retraction mechanism. The right side depicts a cutaway of the focus-lens barrels and shows the position of the focus lens and blast shield.

The optomechanical design of the FLAS was driven primarily by the transverse motion tolerance of 1.6 μm over the 10-cm focus range. Previous experience with OMEGA indicated that rolling bearings will not provide this accuracy. Designs incorporating flexures were found to possess insufficient stiffness to meet the requirements. The final design incorporates solid bearings consisting of polymer pads (i.e., Rulon™ or Vespel™) running against polished steel ways. Analysis shows that this design will provide sufficient stiffness and linearity of motion to satisfy the requirements.

To meet the centration requirements, as well as permit alignment of the focus axis to the center of the chamber, adjustments have been provided on the bearing pads. Datum surfaces on the end of the lens barrel will enable accurate location of the optical axis of the lens with respect to the axis of the focus motion on the mount, allowing alignment of both to the center of the chamber within tolerance.

One of the main challenges of this design was the additional requirement that the vacuum window, a 325-mm-diam × 25-mm-thick plano optic that also serves as the blast shield, be removed frequently for service. In operation, this optic will need to be changed or cleaned on a regular basis as it becomes contaminated and/or damaged. To achieve the necessary stiffness and pointing accuracy, the FLAS has to be fairly large; it nearly fills the space between the target chamber and the target mirror structure (TMS). As a result, space constraints in the vicinity of the target chamber make it impossible for one to reach in and remove the blast shield directly. A mechanism was designed that clamps and unclamps the blast-shield-to-target-chamber interface under remote control. This mechanism also transports the blast shield from the target chamber to the exterior of the TMS, where it can be grasped and removed. The mechanism works in reverse to return a blast shield from the outside face of the TMS to the target chamber, where it is correctly positioned and clamped to initiate the vacuum seal.

Major Structures Design

The major structures produced for the Upgrade include laser bay structures (23 unique designs, 74 total structures) and target bay structures (8 unique designs, 19 total structures).

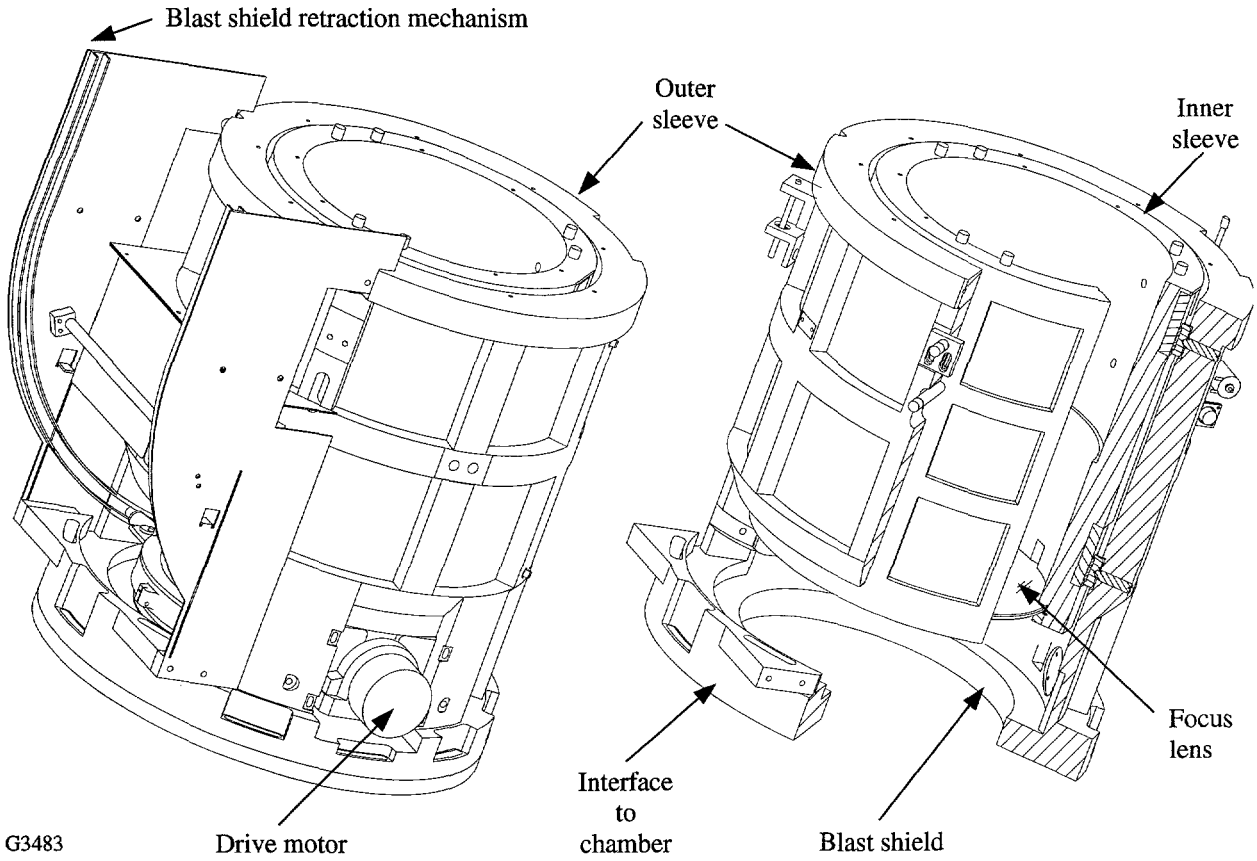

Figure 57.24
The focus lens assembly (FLAS) for the OMEGA Upgrade. On the left is the entire assembly including the blast-shield retraction mechanism. On the right is a section of the two sleeves showing the position of the focus lens and blast shield.

The key structural design requirements were

- accurately located mounting surfaces for the optical components, diagnostics, and instrumentation,
- microinch and microradian stability to the bay's thermal and vibration environments, and
- packaging and servicing of the optical components and diagnostics within the constraints of the 60-beam configuration.

The approach used to mount and accurately position the optical components is as follows: (1) The structures are typically designed to be manufactured with critical mounting surfaces located to ±3 mm relative to surveyor pads provided on the structures. (2) The structures will be surveyed into place to accuracies of ±3 mm. (3) Finally, the optical components have been typically designed to provide >±3-mm mounting adjustment and/or excess clear aperture. This adjustment range/excess clear aperture is adequate to compensate for the structure's fabrication and installation tolerances, thus assuring that the optical system can be set up and aligned.

The requirements for pointing stability are among the most challenging. For reflective optics, allowable rotations of structural mounting surfaces are ±1.5 μrad, and for refractive optics, structural deflections must be within ~0.25 μm. These goals must be met given the following environmental conditions: ±1°C temperature variations and vibration accelerations of up to 20 μg, with major peaks at 15, 20, and 30 Hz. The basic structural approach uses massive, steel space-frame structures grouted to the floor and extensive finite element analysis. An example of this space-frame approach is the target mirror structure, which uses a 3-D "soccer ball" concept to accommodate the Upgrade's 60 laser beams and provide the needed stiffness and mounting surfaces.

One notable exception to the space-frame approach is the F-ASP structure. This unique structure serves as the pointing reference for the entire laser system and, as such, has exceptional stability requirements. Its off-axis optical system has also contributed additional unique requirements to the mechanical design. The approach has been to "cast" a structure around the optical system using a structural epoxy composite, a material commonly used for machine tool bases. This material and process provide a combination of high thermal and vibration damping with the ability to accurately mold critical off-axis optical mounting surfaces into the structure.

Servicing the laser and target systems is complicated by the requirement to package the Upgrade's 60-beam laser into the facility built for the original 24-beam OMEGA system. This has resulted in structures ranging in height from 3.6 m to 9 m bordered by long aisle ways 1.2 m or less wide. One of the most difficult challenges involved servicing the disk amplifiers, which are 2 m long and weigh nearly 450 kg. Each amplifier has 32 high-voltage electrical cables, each about 13 mm thick, plus numerous cooling and nitrogen-purge lines attached. Since complete amplifiers must be replaced on a routine basis, safety, reliability, and ease of operation were essential requirements of the design. The resulting structure design is a combination of swinging doors and an overhead crane (both integral parts of the structure) for service and removal of the amplifiers (see Fig. 57.25).

A rather challenging design task was the three-level platform (see Fig. 57.26) for servicing the target mirror structure and target chamber. Key issues were to avoid obstructing the many crossing laser beam paths (see Fig. 57.29) and provide room for the diagnostics, crane-load landing areas, work areas, and storage areas. All these had to be accommodated while maintaining safe access and egress for personnel.

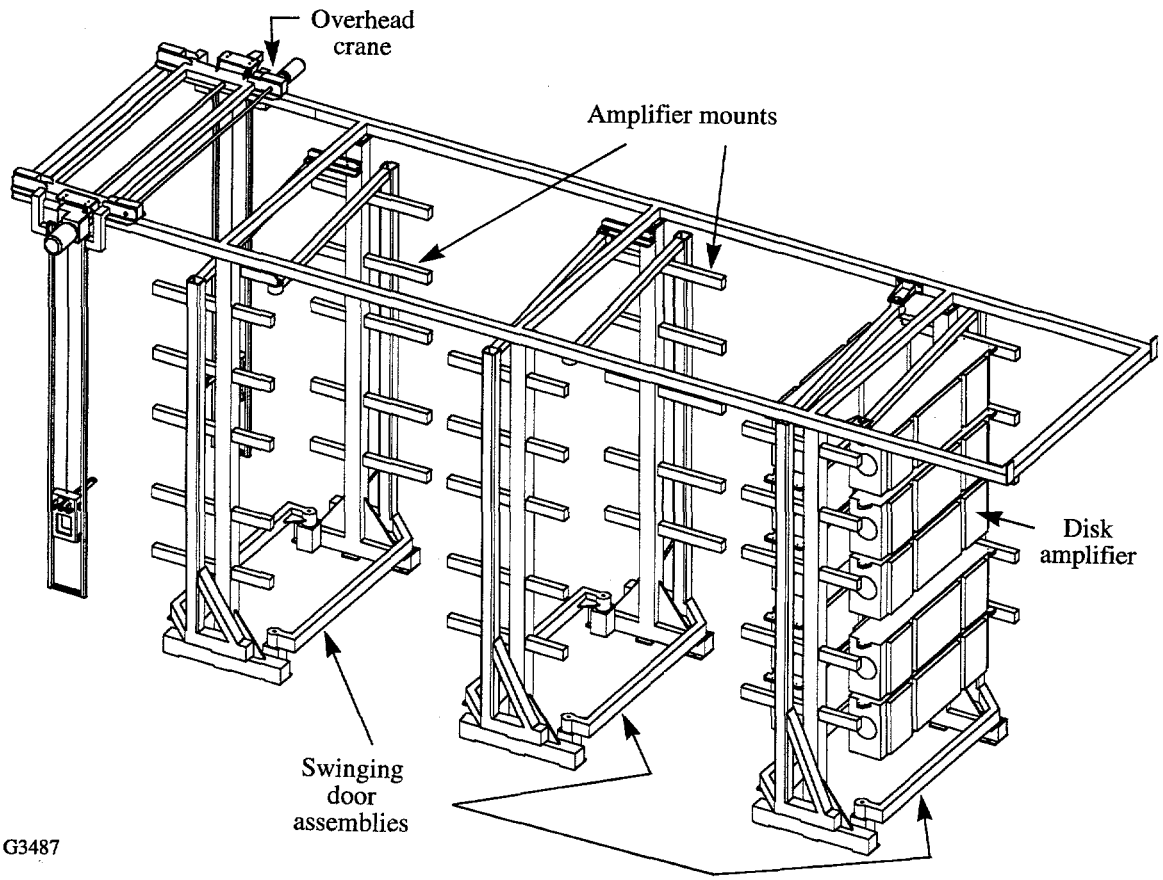

Figure 57.25
One of the four structures that support the stage-E and stage-F disk amplifiers. Each structure has six doors, each of which can swing out any or all of the five amplifiers, and a crane that lowers the amplifiers to floor level to facilitate routine maintenance.

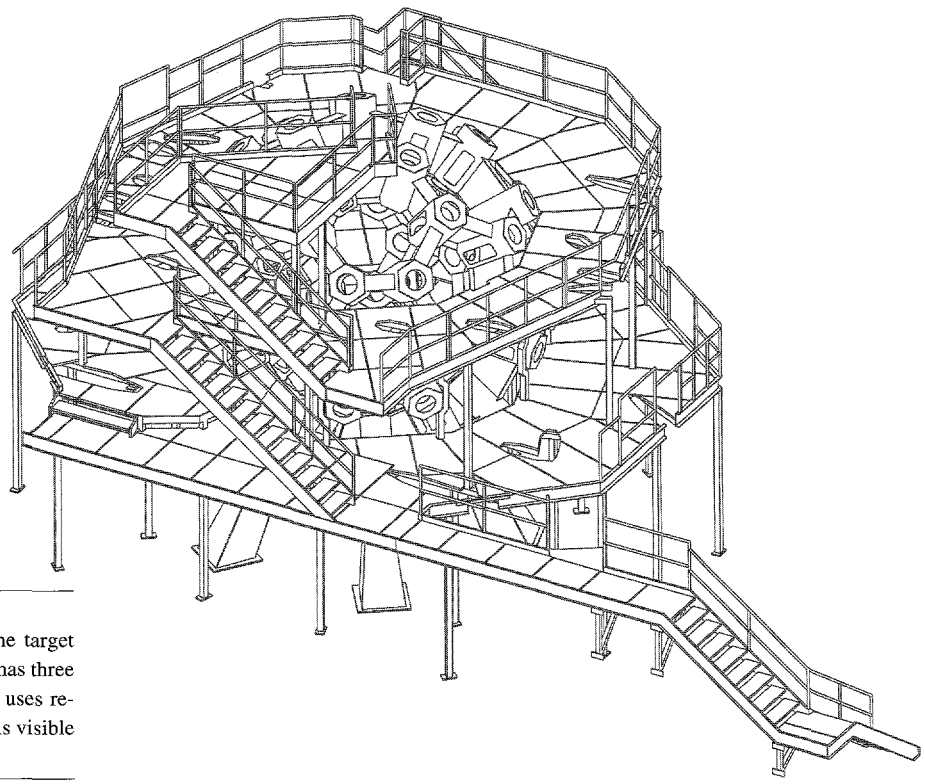

Figure 57.26
The personnel service platform for the target mirror structure (TMS). The platform has three levels, is isolated from the TMS, and uses removable grids for flooring. The TMS is visible within the platform structure.

Target Area

The layout of the target area was dominated by the requirements to deliver 60 UV beams to the target chamber and to provide access to the chamber for implementation of experimental devices on the target chamber. It is in the target bay where the use of the existing building constrained the design the most.

The target mirror structure (see Fig. 57.27) is highly modular, with five-fold rotational symmetry about the vertical axis reflecting the soccer-ball symmetry, i.e., 20 hexagons and 12 pentagons. The 60 laser beams are located at the vertices of those polygons. The laser beams are directed through hexagonal tubes that are part of the structure. The design provides for segmented personnel platforms and integrates the optical mounts with structurally rigid, hexagonal beam tubes. The target mirrors are mounted on the ends of these beam tubes. The structure has a 6-m diameter, with the target mirrors centered on a 7.2-m diameter. The beam-transport geometry is such that no angle of incidence, at either an end mirror or a target mirror, exceeds 60°. The end mirrors are held on two, separate, space-frame structures. Surrounding the TMS is a three-level personnel platform that provides access to the ports on the chamber, landing points for crane-hoisted material, and mounting points for ancillary diagnostic support systems (see Fig. 57.26).

The Upgrade's target-area design actually allows a greater free volume for the placement of diagnostic instruments than was the case on OMEGA because in the Upgrade the beams are transported to the TMS from the outside rather than between the target mirrors and the target chamber.

The UV transport system utilizes two mirrors per beam to direct the beam to the target. The two-mirror configuration was chosen for economy and to reduce the in-air path length of the UV beam. The latter was needed to ensure that the intensity-length product for the beam was below the threshold for stimulated rotational Raman scattering (SRRS).[7] Since UV light is used to align the UV transport system, the optical coatings for the transport mirrors can be optimized for UV radiation only. In the previous system the mirrors had to reflect a nominal amount of IR energy. Relaxing this requirement has allowed the design of the mirrors to provide maximum damage resistance.

The task of mapping the 60 nearly parallel beamlines to the spherical target geometry had two fundamental constraints:

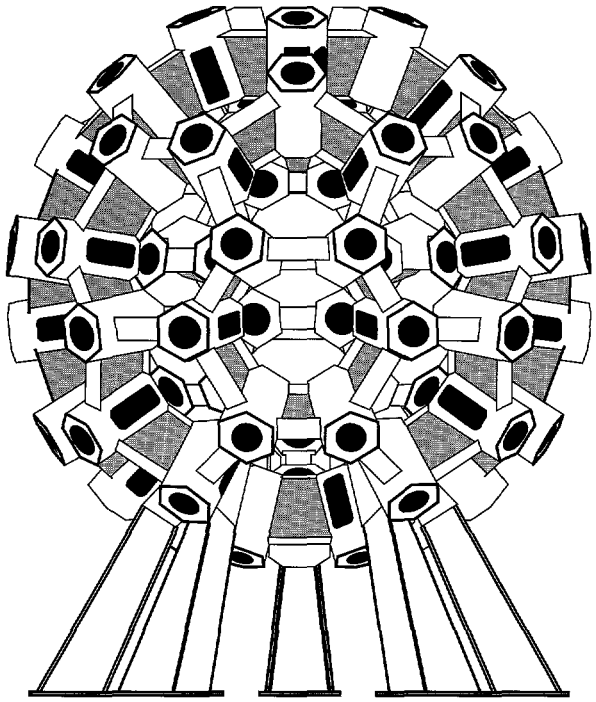

G3115

Figure 57.27
The target mirror structure (TMS) has the soccer-ball geometry defined by the beam positions. The target chamber is supported and enclosed by the TMS. Each of the 60 beams enters the TMS through the radial hexagonal tubes. The 32 diagnostic ports are located in the hexagons and pentagons of the TMS.

All 60 beams should have nearly equal path lengths, and no incident angle (on the mirrors) could be greater than 60°. Given these constraints it is a straightforward process to map a beam to a target port and then locate the end mirror along the beamline to obtain the proper path length.

For the sake of irradiation uniformity, an additional optimization was imposed upon the mapping. This entailed reducing the proximity of beams that share the same stage-A amplifiers. This is to reduce the effect any variation in the performance of a single, stage-A amplifier (distributed into 20 beams) has on target irradiation uniformity. A mapping that grouped many such beams in one area of the target would accentuate the effect a stage-A amplifier has on target performance. To mitigate this effect the beam mapping was arranged such that, for a given hexagon on the TMS, no more than three beams share the same stage-A amplifier. For the pentagons, only two such beams are allowed. Figure 57.28 is a sinusoidal projection of the beam locations indicating which beams share each of the three stage-A amplifiers.

The beam paths, as mapped by the above constraints, are shown in Fig. 57.29. The convergence of 60 beams in the existing target bay leads to a high density of beams. The need to place structures and mirror mounts in that volume without obstructing any beam is a significant design constraint. Extensive 3-D CAD models were required for nearly every design task in this area.

1. Target Chamber

Located within the TMS is the 3.3-m-diam target chamber. The chamber was fabricated to high tolerance, which allows it to be used as an alignment reference for construction of the TMS and the installation and alignment of the target mirrors and FLAS. Post-fabrication measurements indicate that the target chamber ports are positioned to better than ±75 μrad, which is a factor of 2 better than the specification.

Note: The following systems are not part of the OMEGA Upgrade Project; rather, they will be completed as part of the LLE mission. A brief description of these systems is provided for completeness.

2. Target Chamber Vacuum System

During shot operations, the target chamber will be maintained at a vacuum $<6 \times 10^{-6}$ Torr. The vacuum system is fully redundant, with a pair of three-stage, 2000-CFM roughing pumps and three closed-cycle helium cryogenic pumps. When necessary, the chamber will be vented to atmosphere with dehumidified air. The vacuum system will be controlled by a programmable-logic-controller (PLC)-based, distributed control system interfaced to the experimental-system executive computer. The main vacuum system will be capable of pumping the target chamber from atmospheric pressure to shooting vacuum ($<9 \times 10^{-6}$) in under 60 min. The redundant design of this system will support experiments with extremely long durations at high vacuum.

3. Target Positioning/Viewing

Ambient-temperature targets of all foreseeable configurations will be positioned by a multiaxis, air-locked target positioner and a multiaxis, optical target-viewing system. Each of the two target-viewing systems features a variable-magnification telescope and an actively configurable reticle. Multiple image detectors on each channel will be supported.

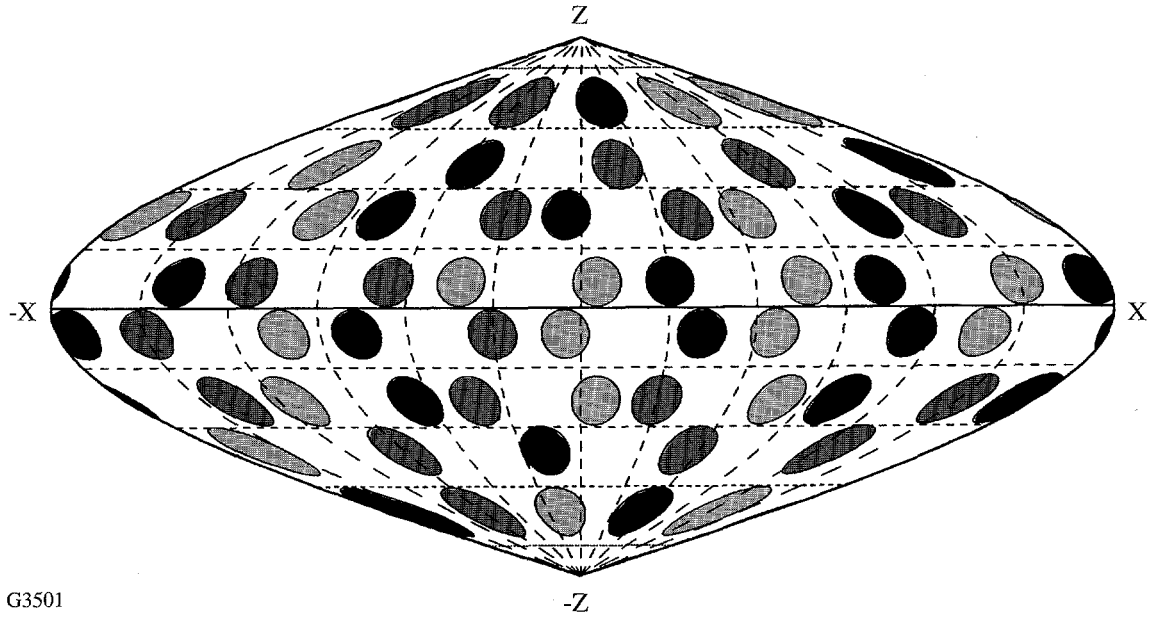

Figure 57.28
A sinusoidal projection of the beam locations on the OMEGA Upgrade target sphere. Each beam is identified by the stage-A amplifier (3 in total) from which it originates. The beam mapping was arranged so that any given TMS hexagon has at most three beams originating from the same stage-A amplifier; the pentagons have at most two beams.

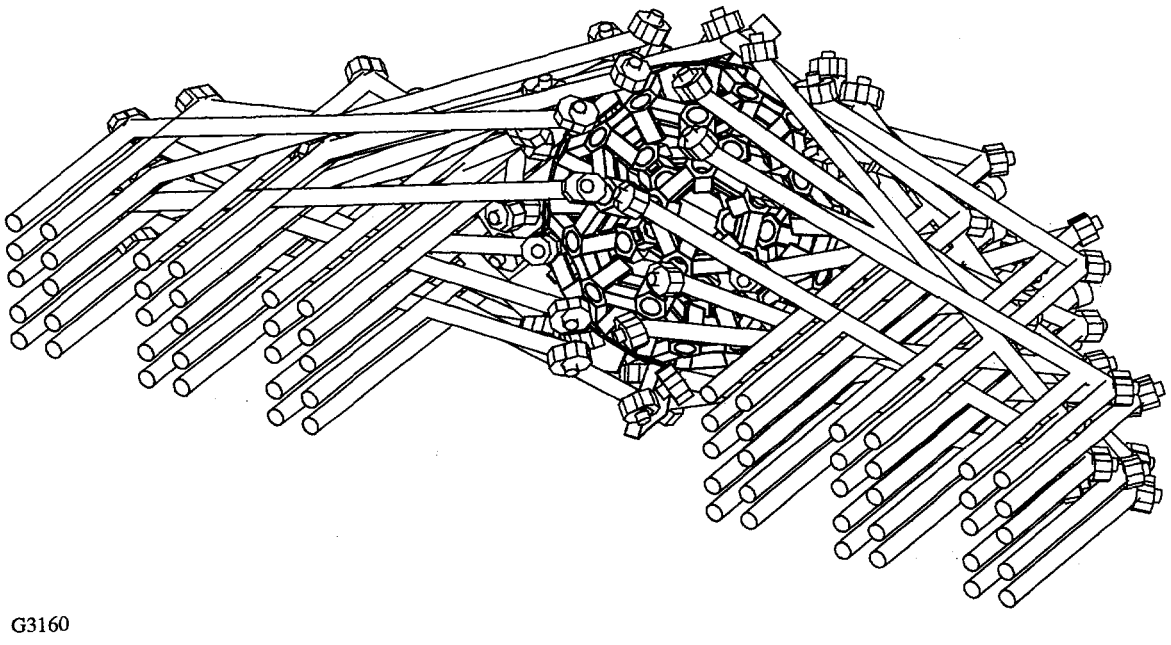

Figure 57.29
The beam paths of the UV transport system of the OMEGA Upgrade. Each beamline has two mirrors, an end mirror and a target mirror. Care was taken to ensure that all path lengths were nearly equal and that the angle of incidence on all mirrors was < 60°.

The target-viewing system will employ sophisticated image-processing techniques to provide enhanced-open-loop and automated-closed-loop target-positioner operation. The load/lock target positioner will allow selection of any target in the LLE inventory and thus will support long-duration, continuous experimental operations.

The integrated target-viewing and positioning system will allow placement of the target within a 5-μm radius of the designated center of the target chamber under either manual or automatic control.

4. Diagnostic Support Systems

Target diagnostic systems will be supported on the OMEGA Upgrade by an array of modular support systems, including mechanical interfaces, timing, vacuum, power, and control system support. The standardized interface scheme employed in the OMEGA Upgrade experimental support systems provides for simplified compatibility requirements for NLUF users and a readily reconfigurable experimental system to support future experimental programs. The diagnostics to be used on the Upgrade are not within the scope of this project. Information on these systems can be found in the LLE five-year plan.[8]

ACKNOWLEDGMENT

This work was supported by the U.S. Department of Energy Office of Inertial Confinement Fusion under Cooperative Agreement No. DE-FC03-92SF19460 and the University of Rochester. The support of DOE does not constitute an endorsement by DOE of the views expressed in this article.

REFERENCES

1. R. S. Craxton, ed., *OMEGA Upgrade Preliminary Design*, Laboratory for Laser Energetics Report DOE/DP 40200-101, University of Rochester (1989).
2. Optics Coating Requirements Document, OMEGA Upgrade No. M-AA-G-05, Rev A, 12 October 1992.
3. LLE Review **44**, 219 (1990).
4. LLE Review **51**, 139 (1992).
5. *Optical Coating Specification Document*, OMEGA Upgrade No. M-AA-G-07, 28 April 1993.
6. R. S. Craxton, IEEE J. Quantum Electron. **QE-17**, 1771 (1981).
7. M. A. Henesian, C. D. Swift, and J. R. Murray, Opt. Lett. **10**, 565 (1985).
8. Proposal for Renewal Award for Cooperative Agreement DE-FC03-85-DP402000 (US DOE/LLE, October 1991), Chaps. 3.3 and 3.4.

Target Imaging and Backlighting Diagnosis

The case of an x-ray backlighting image of a CH-shell target imploded by the OMEGA Upgrade laser system has been calculated and analyzed. The goal is to obtain information on the conditions at peak compression, where the experimental constraints due to target self-emission and required spatial resolution are maximal. Particular attention is devoted to the problem of discriminating against the target self-emission. It is shown that this can be done by obtaining a monochromatic image at a single spectral line emitted by the backlighter. Additionally, the target self-emission image has useful signatures, which can be studied with or without a backlighter. Two experimental configurations for monochromatic imaging are discussed: (a) an x-ray microscope with a flat crystal monochromator, and (b) pinhole imaging in conjunction with a curved crystal monochromator. Useful images are obtained with simple (undoped) CH-shell targets and without the need for a short-pulse backlighter beam.

The method of x-ray backlighting offers some advantages over methods employing target emission for the study of compression and stability of laser-imploded targets. One advantage of backlighting over emission imaging is the potential to delineate the interface between the pusher and the fuel. This capability is more easily realized if the compressed fuel is relatively cold near the interface (i.e., a temperature gradient exists in the fuel). Such information can, in principle, provide a direct measure of compression and evidence of any shell distortion. Emission methods can only delineate the hot core, which may consist of the fuel as well as an indeterminate section of the pusher. An additional advantage is the ability to choose a short-enough backlighting wavelength (say, $\lambda < 3$ Å) to avoid too high an opacity; with emission, the interface region is often not hot enough to emit such short wavelengths.

An important ingredient in the backlighting schemes, as discussed below, is two-dimensional monochromatic imaging; this added feature can be likewise applied to, and enhance, methods based on target emission. Monochromatic imaging can be used to probe a particular layer in the target, which is doped with a suitable material. The imaging then involves a particular atomic transition of that material that gives rise to either monochromatic emission or absorption. However, in the case of backlighting, monochromatic imaging must be used even in the absence of a doped layer to overcome the background due to target emission.

When performing backlighting imaging, the self-emission of the imaged target is normally considered a hindrance and its suppression is considered desirable. In the test case studied here the backlighting and self-emission images happen to be of comparable intensity. This is an advantageous situation because the two image components provide complementary information on the compression and implosion uniformity.

Most backlighting experiments in the past were less challenging. Typically, they used softer backlighter radiation ($\lambda > 8$ Å) than we envisage using here. Softer radiation is heavily absorbed by the shell so it can only delineate the outer surface of the shell. This kind of measurement cannot yield reliable information on the compression or stability. Softer radiation is easier to produce in copious amounts, and the requirements on spatial resolution in imaging the outer surface of the shell are more moderate. Additionally, the problem of target self-emission in those earlier experiments was much less severe because the self-emission of a low-Z polymer target is mostly very weak, except for the emission from a highly compressed core, such as predicted for OMEGA Upgrade targets.

Case Study of Experimental Parameters

We discuss the feasibility of backlighting experiments, using the *LILAC* code for simulating a candidate OMEGA Upgrade target. The target is a polymer shell of 940-μm diam and 30-μm thickness, filled with 80 atm DT gas, and imploded by a trapezoidal pulse. The pulse rises linearly over a 0.1-ns period to 13.5 TW, then remains constant for 2.2 ns, before dropping linearly over a 0.1-ns period. *LILAC* results were used for simulating the expected backlight image for this test shot. Figure 58.1 shows the density and electron-temperature

profiles predicted for this target at peak compression. The shell material has been compressed to a mean radius of ~50 μm and thickness of ~30 μm, with a density in the range of ~10–50 g/cm^3, corresponding to a $\rho\Delta r$ value of ~90 mg/cm^2. The electron temperature in the shell ranges from ~80 to ~1000 eV. Most of the backlight radiation absorption will occur within the colder, outer part of this compressed shell.

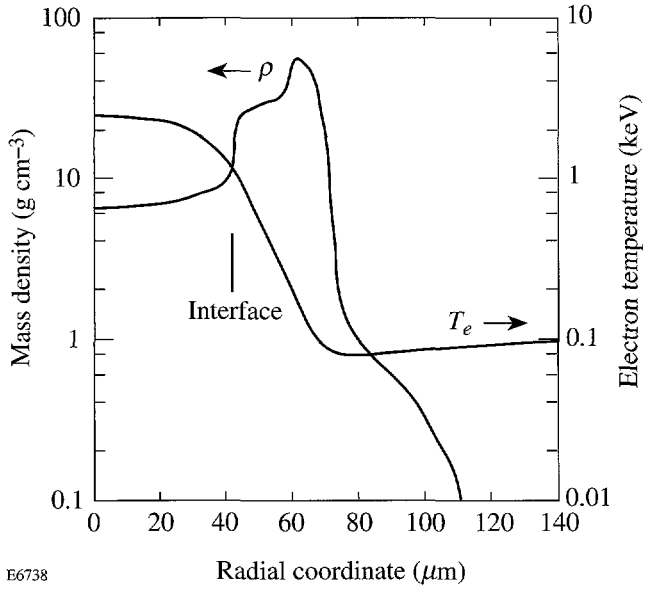

Figure 58.1
The density and electron-temperature profiles predicted by the *LILAC* code at peak compression for the case studied in this article.

Absorption Modeling

A simplified post-processor code was developed to calculate the transport of backlight radiation through the polymer target. The absorption at a wavelength λ in the CH material consists of two contributions: free-free (bremsstrahlung) and bound-free (photoionization); other absorption mechanisms (such as Compton scattering) are negligible for radiation of a few-keV photon energy. The free-free absorption coefficient at a frequency ν (in cm^{-1}) is given by

$$k_{ff} = \left(4\pi z^2 e^6 g_{ff} / 3^{3/2} hcm^2 \nu^3\right)\left(2m/\pi\kappa T\right)^{1/2} N_e N_i \,, \quad (1)$$

where g_{ff} is the free-free Gaunt factor (quantum correction). For a multispecies target, $z^2 N_e N_i$ is replaced by $N_e^2\langle z^2\rangle/\langle z\rangle$ in terms of species averages. The bound-free absorption coefficient for K-shell electrons (in cm^{-1}) in hydrogen-like ions is given by

$$k_{bf} = \left(64\pi^4 z^4 me^{10} g_{bf} / 3^{3/2} h^6 cn^5 \nu^3\right)\left(2m/\pi\kappa T\right)^{1/2} N_i \,, \quad (2)$$

where g_{bf} is the bound-free Gaunt factor, n is the principal quantum number of the absorbing level, and k_{bf} has to be calculated separately for each ionic species. For helium-like and higher ionic species, z^4 is replaced by $(z\text{-}\sigma)^4$, where σ is the Slater screening constant that equals[1] 0.3 for K-shell electrons. Neglecting the contribution to the opacity from L-shell and higher-shell electrons, the total opacity along various rays traversing the target can be now calculated, using the *LILAC*-predicted profiles of electron density and temperature through the target. To know the various N_i that go into the calculation of k_{bf} as well as into the z averages, we need first to calculate the distribution among the charge states (degrees of ionization). To calculate the charge-state distribution of carbon ions we make use of the LTE (local thermodynamic equilibrium) model. The LTE model becomes more valid as the plasma density increases and the temperature and the atomic charge Z decrease. These conditions indeed prevail within the cold, compressed part of the shell, made of low-Z polymer material. To verify the applicability of LTE we use the condition[2] given by Griem:

$$N_e > 7\times 10^{18}\left(z^7/n^{17/2}\right)\left(\kappa T/z^2 E_{\mathrm{H}}\right)^{1/2} \mathrm{cm}^{-3}, \quad (3)$$

where E_{H} is the ionization energy of hydrogen (13.59 eV) and n is the lowest principal quantum number for which the level population is still in LTE with the continuum (i.e., whose population is related to that of free electrons by the Saha equation). For a typical temperature of 150 eV within the compressed shell, which is the principal absorber of backlighting radiation, and with $Z = 6$ and $n = 1$, Eq. (3) becomes $N_e > 3.2 \times 10^{24}$ cm^{-3}. This is well below the predicted values of $N_e \geq 1 \times 10^{25}$ cm^{-3}.

We use the Saha equation to calculate the distribution of carbon ions in the C^{+4}, C^{+5}, and C^{+6} charge states, while ignoring lower ionizations (which are negligible even at the lowest existing temperature, ~80 eV). The charge-state densities are then given by the set of equations:

$$\left(N_e N^{+6}/N^{+5}\right) = \left[2Z^{+6}(T)/Z^{+5}(T)\right]\left(2\pi mkT/h^2\right)^{3/2} \exp\left[-\left(E^{+5} - \Delta E^{+5}\right)/\kappa T\right], \quad (4)$$

$$\left(N_e N^{+5}/N^{+4}\right) = \left[2Z^{+5}(T)/Z^{+4}(T)\right]\left(2\pi m\kappa T/h^2\right)^{3/2} \exp\left[-\left(E^{+4} - \Delta E^{+4}\right)/\kappa T\right], \quad (5)$$

$$N^{+4} + N^{+5} + N^{+6} = N_C, \quad (6)$$

where $Z(T)$ is the partition function, E^{+5} is the ionization energy of hydrogen-like carbon, E^{+4} that of helium-like carbon, and N_C is the total carbon ion density. The reduction in ionization energy ΔE is calculated by an approximation[3] to the theory of Stewart and Pyatt:[4]

$$\Delta E(eV) = 2.16\times10^{-7}\left(z/r_i\right)\left[\left(1+x^3\right)^{2/3} - x^2\right], \quad (7)$$

$x = r_D/r_i$, in terms of the Debye radius r_D and the interionic distance r_i:

$$r_D = \left[\kappa T/N_e\left(1+\langle z\rangle\right)\right]^{1/2}, \; r_i = \left(3\langle z\rangle/4\pi N_e\right)^{1/3}. \quad (8)$$

It should be noted that to calculate the charge distribution, we need to know $\langle z\rangle$ in Eq. (8), which calls for an iterative solution. To simplify the calculation we adopt the *LILAC* value of $\langle z\rangle$ for Eq. (8), since the reduction in ionization energy is needed only as a correction in the calculation of the charge distribution. Using the resulting densities, we can readily calculate the z averages, as well as the total bound-free opacity

$$k_{bf} = N^{+4}k_{bf,4} + N^{+5}k_{bf,5}, \quad (9)$$

where $k_{bf,4}$ is the bound-free opacity due to the helium-like carbon ion, and $k_{bf,5}$ due to the hydrogen-like carbon ion.

For the simulation we choose a backlight wavelength of 2.62 Å, corresponding to the $1s2p$–$1s^2$ line of Ti^{+20}. When irradiating a titanium backlighter target, this will be the strongest line, with a relatively low level of underlying continuum radiation.[5] We assume that the backlighter is irradiated by a single beam, identical to an OMEGA Upgrade beam with an energy of 500 J and the same pulse duration and shape as described above. We further assume a backlighter focal spot of 150-μm diam, giving rise to an irradiance of $\sim1.4\times10^{15}$ W/cm^2. This diameter is sufficiently large for imaging the core at peak compression at which time the outer shell diameter is only ~120 μm. The optimal choice of wavelength for a particular target implosion is one giving an opacity of ~1 in going through the target center at the desired time of probing. In this way the image will show the higher opacity going through the limb than through the center, thus delineating the outer as well as the inner surface of the cold pusher.

Monochromatic Absorption Images

In Fig. 58.2 we show examples of the predicted instantaneous backlighting images of the 2.62-Å line at various times during target compression. The abscissa is the lateral coordinate in the image plane, assuming unit magnification. The backlighting incident intensity is assumed to be unity. Target self-emission was not included in this calculation. The images assume that a monochromator was used for the detection; methods of monochromatization are described below. We see that titanium was a suitable choice for this target implosion; indeed, the opacity through the target center at peak compression [Fig. 58.2(e)] is ~0.9. As a result, the absorption through the target center is visibly lower than that through the limb. [The opacity through the limb in Fig. 58.2(e) is ~2.3.] The position of the minimum in the curve (maximum absorption) corresponds approximately to the fuel-shell interface; however, it is slightly larger than the interface radius. Thus, the minimum of the 2.87-ns frame [Fig. 58.2(e)] is at a radius of ~58 μm, while the interface (Fig. 58.1) is at a radius of ~45 μm. For homogeneous shells, the dip in the backlight image would correspond to a line of sight that is tangent to the fuel-shell interface; this direction corresponds to the longest chord through the target, therefore to the highest opacity. The main reason for this difference is the fact that the inner part of the shell is hot and has lower absorption (additionally, the density at this time peaks outside the interface radius). This difference yields an underestimate by a factor of ~2 in the derived compressed density. In cases where the electron-temperature profile is more centrally peaked, the absorption-profile minimum will yield a value closer to the correct density.

To minimize the smearing effect due to time integration, a framing camera can be employed behind the imaging device. In this case, only one frame can be easily accommodated because the various frames in a framing camera are recorded at various spatial directions, whereas here only one direction will yield the desired image: that given by the line connecting the main and backlighter targets. Figure 58.2 indicates that during a period of ~100 ps around peak compression (from ~2.8 to ~2.9 ns) the backlight image changes very little. Therefore, the method used to obtain time resolution need not achieve better than ~50-ps resolution (for probing peak compression).

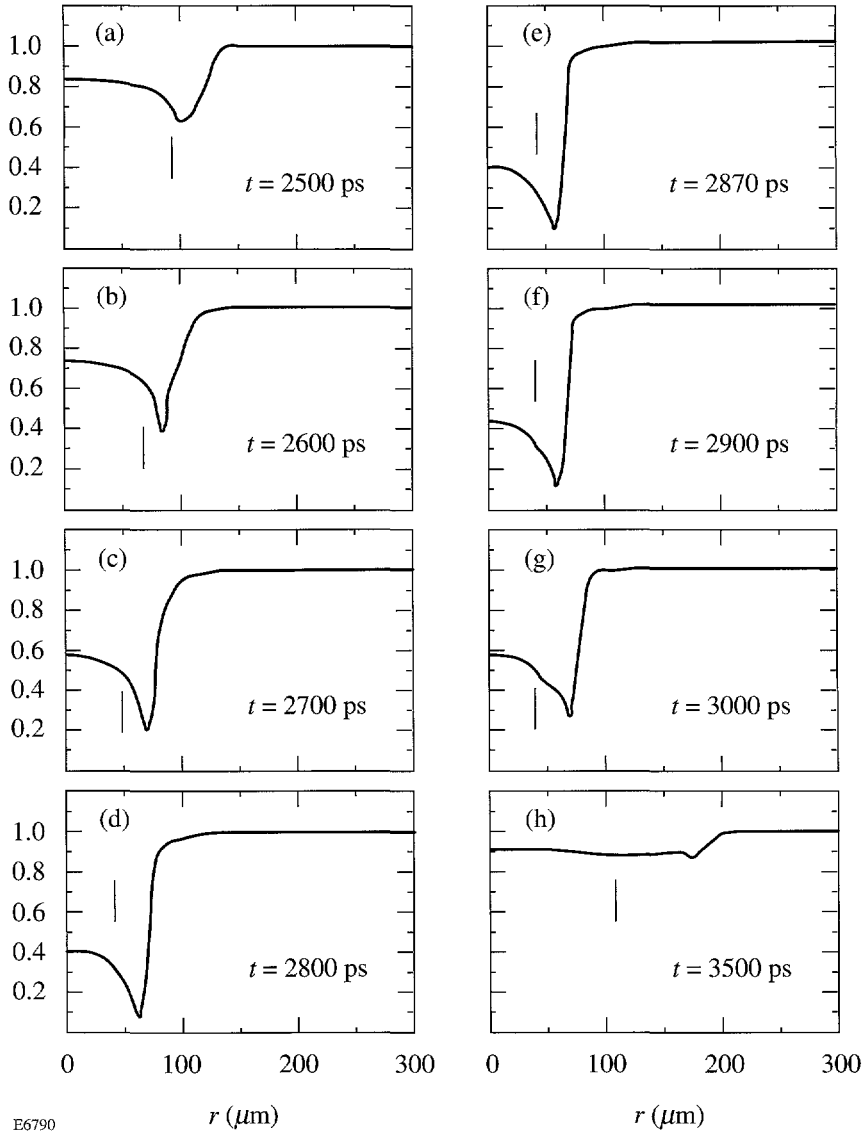

Figure 58.2
Examples of the predicted backlighting images at various times during the compression. The backlighting incident intensity was normalized to unity. Monochromatic backlighter was assumed at 2.62 Å (titanium). Target self-emission was not included. The vertical bars mark the fuel-shell interface.

Alternatively, the backlighter x-ray pulse can be shortened by using a polymer-coated Ti target, so that the Ti emission is delayed. To test this possibility we simulated the emission from a titanium target coated with varying thicknesses of polymer (CH) and irradiated with a single OMEGA Upgrade beam. The pulse shape was typical of those projected to be used in high-performance implosions: its total duration is 9 ns, it rises slowly first and then faster, until reaching a plateau of 0.3 TW from 8 to 9 ns, then dropping to zero. The total pulse energy is 0.5 kJ. This pulse shape is different than that described above, and used everywhere else in this work, and was chosen to verify x-ray pulse shortening even for this longer pulse. To simulate a backlighter disk of 150-μm diameter, irradiated at 1.4×10^{15} W/cm^2, we assumed in the simulations a spherical target of 300-μm radius, irradiated at that irradiance. We summarize the results in Fig. 58.3, showing the x-ray emission from an uncoated titanium target, as well as from a titanium target coated with an 18-μm-thick CH layer. The x-ray emission is integrated over the 4.5- to 5-keV energy band, comprising mostly the Ti^{+20} resonance line at 4.73 keV. Even with no CH coating, the x-ray pulse is considerably shorter than the incident laser pulse because the early ("foot") part of the laser pulse is too weak to yield significant x-ray radiation within this energy band. A coating of 18 μm CH further

shortens the x-ray pulse to a width of ~160 ps, while reducing the x-ray power by only a factor of ~2. Thicker coatings cause precipitous reduction in x-ray power and are thus not useful.

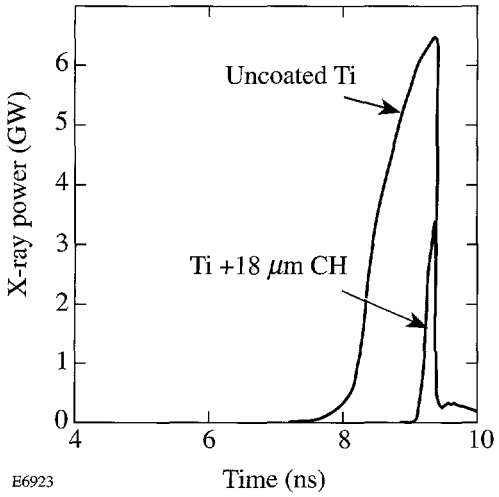

Figure 58.3
Simulated x-ray emission from an uncoated titanium target, as well as from a titanium target coated with an 18-μm-thick CH layer. The x-ray emission is integrated over the 4.5- to 5-keV energy band, comprising mostly the Ti^{+20} resonance line at 4.73 keV.

Emission Profiles

The backlighting images (such as in Fig. 58.2) should now be combined with the target self-emission profiles. We note that in LTE the local emission $\varepsilon(\nu)$ and the absorption coefficient $k(\nu)$ are related through Kirchhoff's law,[6] in terms of the blackbody function B_ν:

$$\varepsilon(\nu) = k(\nu)\,B_\nu = \left(2h\nu^3/c^2\right)k(\nu)\Big/\left[\exp\left(h\nu/\kappa T\right)-1\right], \quad (10)$$

where κ is the Boltzmann's constant. Expressing Eq. (10) in explicit units,

$$\varepsilon\left(\frac{\text{keV}}{\text{keV ns cm}^3\,\Omega}\right) = 3.13\times10^{22}\,\frac{k\left(\text{cm}^{-1}\right)\left[E(\text{keV})\right]^3}{\exp\left(E/T\right)-1}, \quad (11)$$

where Ω designates solid angle. The total spectral intensity emerging along a line of sight (in the x direction) at a distance y from the axial direction, due to both the backlighter as well as the target self-emission, is obtained by solving the radiation transport equation

$$I(\nu_0,y) = I_{BL}(\nu_0)\exp\left[-\int_{x_1}^{x_2}k(\nu_0,r)dx\right] + \int_{x_1}^{x_2}\varepsilon(\nu_0,r)\exp\left[-\int_{x}^{x_2}k(\nu_0,r')dx'\right]dx, \quad (12)$$

where $x_1 = -\left(R^2-y^2\right)^{1/2}$, $x_2 = -x_1$, $r = \left(x^2+y^2\right)^{1/2}$, $r' = \left(x'^2+y^2\right)^{1/2}$, R is the target radius, $I_{BL}(\nu_0)$ is the spectral intensity emitted by the backlighter at the line-center frequency ν_0 (i.e., at 2.62 Å), and the local emission $\varepsilon(\nu)$ is given by Eq. (11). The resulting one-dimensional profile $I(\nu_0,y)$ is in reality, of course, circularly symmetric. Since we chose $I_{BL}(\nu_0)$ to correspond to the peak of the backlighting line, the profile calculated by Eq. (12) gives the highest possible contrast between the backlighting and the self-emission images. It will be realized only if the monochromator bandwidth is not larger than the spectral width of the backlighter line. For a wider bandwidth we sample a larger fraction of the continuous self-emission, but the intensity from the backlighter (assumed to be mostly in a single spectral line) will remain about the same, thus lowering the contrast.

We next estimate the backlighting irradiance $I_{BL}(\nu_0)$ at the 2.62-Å wavelength, the $1s2p$-$1s^2$ transition of Ti^{+20}. The assumed laser irradiance on the backlighter is 1.4×10^{15} W/cm^2, or 9.4×10^{21} keV/(ns cm^2). At this irradiance, the x-ray yield for producing the Ti^{+20} line at 2.62 Å can be conservatively taken[5] to be 0.03% into unit solid angle perpendicular to the target, giving an x-ray flux of 2.8×10^{18} keV/(ns cm^2 Ω). To calculate the flux per unit photon energy, as explained above, this number has to be divided by the larger of the spectral line width and the instrumental width. The former is ~1.2 eV (see below), whereas a typical instrumental width would be ~4 eV. We finally obtain for the backlighting spectral flux at the frequency ν_0 of line center

$$I_{BL}(\nu_0) = 7.0\times10^{20}\,\frac{\text{keV}}{\text{keV}/\left(\text{ns cm}^2\ \Omega\right)}. \quad (13)$$

Using this value and the plasma profiles calculated by the *LILAC* code (Fig. 58.1) we solve Eq. (12) numerically to obtain the combined image of backlighting and self-emission. The imaging device is assumed to have unit magnification and throughput.

We show in Fig. 58.4 the combined monochromatic image (at 2.62 Å) due to backlighting and self-emission at peak compression, intercepted by a monochromator crystal of 4-eV bandwidth. The curves are normalized to the spectral intensity of the backlighter, 7.0×10^{20} keV/(keV ns cm^2 Ω). We note that the two contributions (backlighting and self-emission) are of comparable intensity in this particular case. This indicates that without the use of a monochromator crystal the self-emission will dominate the image and render the method impractical. Thus, if instead of using a monochromator we were to use a filter, the intensity of the monochromatic backlighting radiation (consisting of mostly a single spectral line) will remain about the same, but that of the continuous self-emission will greatly increase. For example, an appropriate filter for the 2.62-Å titanium line would be a 25-μm-thick titanium filter. Such a filter will produce a bandpass of an ~1-keV width (spanning the range ~4 to ~5 keV) as compared with the ~4-eV bandpass of the monochromator crystal.

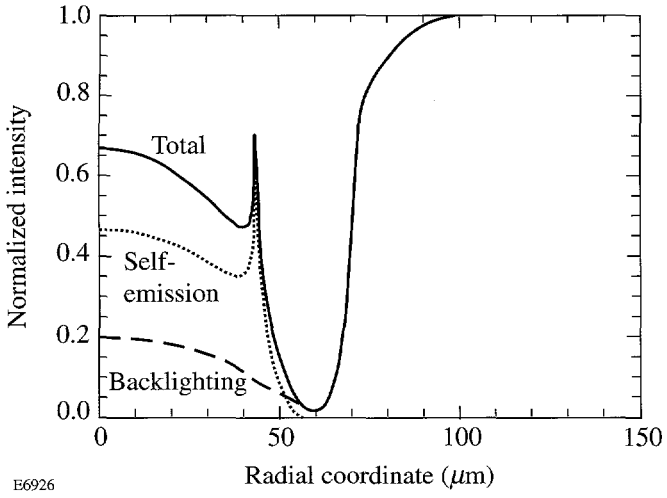

Figure 58.4
The combined image due to backlighting and self-emission at peak compression of an imploded CH shell. The image is calculated assuming a monochromatic detection at the $1s2p$–$1s^2$ line of a titanium backlighter ($\lambda = 2.62$ Å). The curves are normalized to a spectral intensity of 7.0×10^{20} keV/(keV ns cm^2 Ω).

The fact that both image components have comparable intensities makes the imaging method more powerful because information on both the cold shell as well as the interface can be simultaneously obtained. An underperforming target can be expected to show an absorption dip that is both shallower (because of a lower areal density $\rho\Delta r$ along the corresponding chord) as well as displaced to a larger radius (because of a lower compression). If the target performance greatly deviates from predictions (leading normally to a colder core), we may have to employ softer radiation to see a comparable image. Also, the two-dimensional image can show long-wavelength perturbations of the spherical symmetry.

Of particular interest is the spike seen in the self-emission image at a radial distance of ~40 μm. This spike is emitted by the innermost surface of the CH shell and is due to the so-called "limb darkening," or the fact that the depth of a line-of-sight through the rim of a shell is longer than that through its center. In the complete two-dimensional image this spike will appear as a circular ring and will closely correspond to the fuel-shell interface. It provides therefore a direct measure of the achieved compression. Because of the potential usefulness of this spike we study its characteristics in some detail. The spike, if observable, can be used also in experiments with no backlighting. The image will not be then purely monochromatic, as in Fig. 58.4, but will instead be averaged over the transmitted spectrum of the filter. Our calculations also showed that averaging the image over the transmitted spectrum of a 25-μm-thick titanium filter hardly changed the self-emission image in Fig. 58.4.

The spike in Fig. 58.4 is spatially very narrow (~3 μm wide) because only the innermost surface of the CH shell is hot enough to emit the 4.73-keV radiation contributing to the image. As Fig. 58.1 shows, that temperature is in the range ~0.6–1.0 keV. If the core in an actual experiment is colder, the spike will be too weak to be seen, unless we choose softer radiation ($E < 4.7$ keV) for the imaging. Furthermore, an excellent spatial resolution is required. In Fig. 58.5 we show the result of a convolution of the emission image of Fig. 58.4 with an imaging device of 6-μm spatial resolution (and unit magnification). The spike is still seen, but poorer resolution renders it indistinct.

Figure 58.6 shows the self-emission of the test-case target at various photon energies. The motivation is to maximize the spike visibility; therefore, the backlighting part of the image was eliminated. The contrast of the spike with respect to the central peak maximizes in the 4- to 5-keV spectral range. To understand this we turn to Eqs. (11) and (12). The factor $k(E)$ E^3 appearing in Eq. (11) is essentially independent of E. By writing the derivative dE/dT from Eq. (11) we see that at higher photon energies the contrast between the spike and the central emission falls due to the $\exp(E/T)$ factor. This is because the central core is hotter than the shell interface region, and, when E/T is smaller, the exponential term increases more slowly with increasing E. At low photon energies, ab-

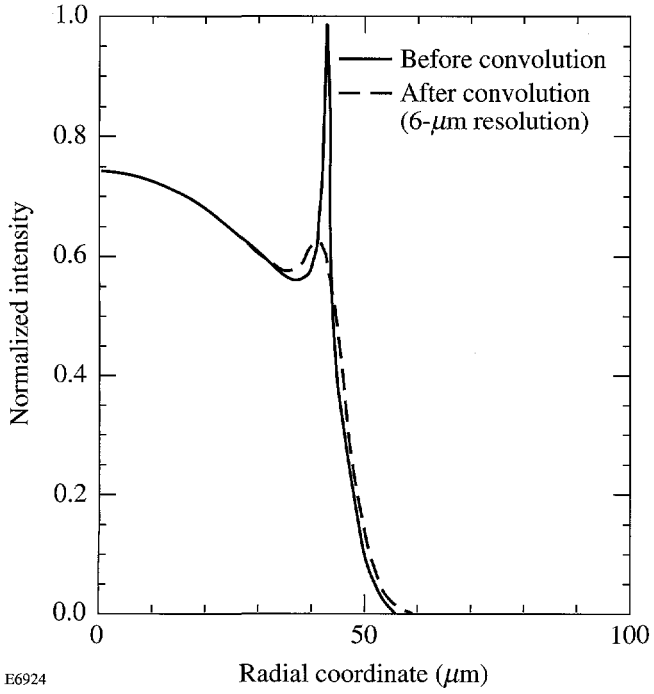

Figure 58.5
Convolution of the emission image of Fig. 58.4 with an imaging device of 6-μm spatial resolution (and unit magnification).

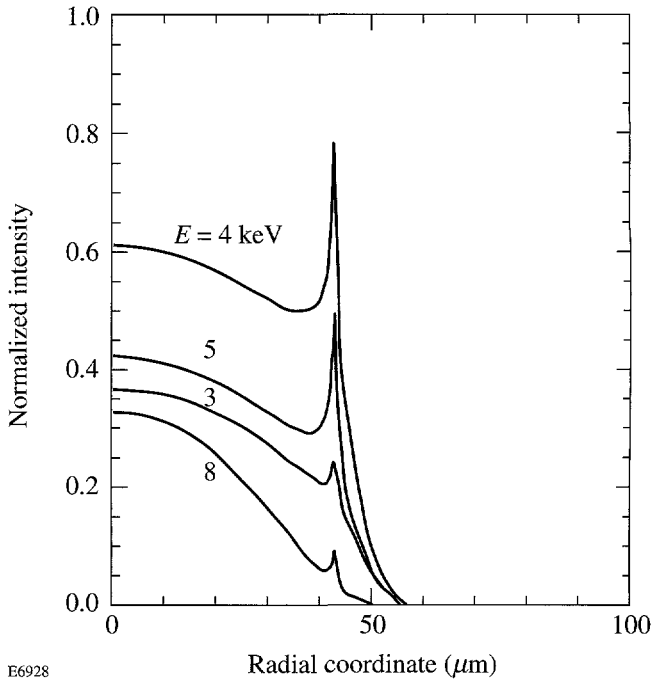

Figure 58.6
Self-emission profiles of the test-case target at various photon energies. The curves are normalized to a spectral intensity of 7.0×10^{20} keV/(keV ns cm^2 Ω).

sorption sets in and the limb-darkening effect disappears. The observed radiation from the hot part of the shell comes from the outer surface of that region and does not depend on its depth.

To maximize the spike emission it is instructive to know the relative contribution of the hydrogenic fuel and the CH shell to the emission profile. Figure 58.7 shows the emission profile of Fig. 58.4 with and without the hydrogenic fuel contribution. Even though the fuel has a lower nuclear charge than the carbon in the CH, a significant fraction of the central emission comes from the fuel because the fuel temperature is considerably higher than that in the shell. To increase the shell emission we may dope the CH shell with a higher-Z element. Irrespective of the detailed atomic physics of a high-Z dopant, its final effect is to increase the absorption coefficient and, through it, the local emission [see Eq. (11)]. To simulate doping we therefore multiply the absorption coefficient (and thereby also the emission coefficient) by a number m, which in Fig. 58.8 assumes the values 1, 2, 4, and 10. The only indeterminate information here is the quantity of a given type of dopant corresponding to each m. Figure 58.8 (calculated for a photon energy of 5 keV) shows that doping the shell cannot increase the contrast of spike to fuel emission because the opacity through the region emitting the spike is not negligible (it is of order 1). For negligible opacities, the strong Z dependence of the absorption coefficient [Eqs. (1) and (2)] when substituted into Eq. (11) will result in much higher emission. However, when opacity is not negligible, the increase in the absorption coefficient, which also appears in the exponent of the attenuation [see Eq.(12)], will dominate and limit the spike intensity to that of a blackbody emitter. Additionally, the doped cold shell will further absorb the radiation emitted at the interface region. The length corresponding to this absorption is longer than through the center; this turns a flat-topped profile, characteristic of a high-opacity emitter, into the bell-shaped profiles for the high-m cases in Fig. 58.8.

Finally, we note that if the spike is still observed in the presence of mixing (which will be the case if the mixing is modest), it would permit an estimate of the degree of mixing. Mixing will raise the fuel emission (hence, the central peak in the image) relative to the spike emission. To simulate this effect, we show in Fig. 58.9 the emission profile when the fuel absorption coefficient is multiplied by $m = 1$, 2, and 4. Since the absorption coefficient of hydrogen is purely due to inverse bremsstrahlung, which depends on Z like Z^2 [see

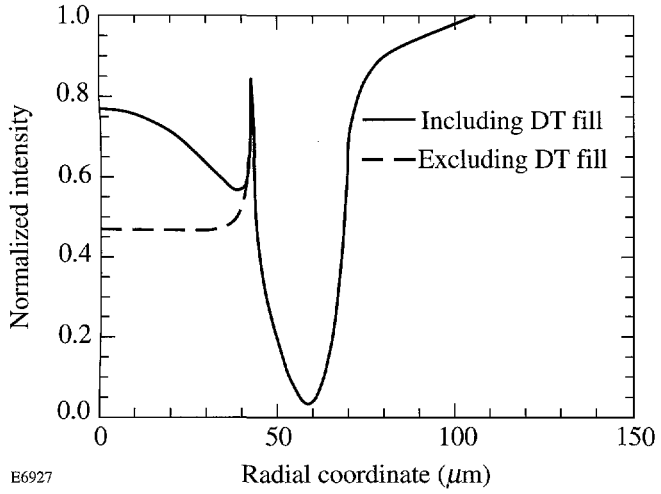

Figure 58.7
Emission profile of Fig. 58.4 with and without the hydrogenic fuel contribution.

Eq. (1)], we can estimate the amount of CH mixed into the fuel for the $m = 4$ case as 8% by atom number. Much higher levels of mixing and shell distortion will make the spike disappear and render this method inapplicable.

Image Monochromatization

To improve the absorption-image visibility we assumed above that the backlighter emission is intercepted by a monochromator crystal that is angle adjusted for peak diffraction at 2.62 Å, the backlighting wavelength. The narrow reflection window of the crystal will greatly reduce the reflected broadband self-emission but will only slightly attenuate the single backlighting line. Roughly, the energy band diffracted by the crystal will be ~1 eV, as compared with a filter transmission window of ~1 keV. Thus, without a monochromator, the peak self-emission flux will be several orders of magnitude higher than the backlighter flux.

We now discuss in more detail the effect of introducing an x-ray reflecting crystal into the detection system. A problem we need to consider is the limitation on the field of view caused by the fact that the wavelength selection by a crystal is related to directional selection. In the dispersion direction, each wavelength can only be diffracted within a narrow angular diffraction range (of the order of ~10^{-4} rad) around the Bragg angle. However, the image generated by either a pinhole camera or a microscope can have a larger divergence than the acceptance angle of the crystal, in which case the monochromatic backlighter image may be clipped. For example, a 150-μm image size that is recorded by a pinhole at a distance

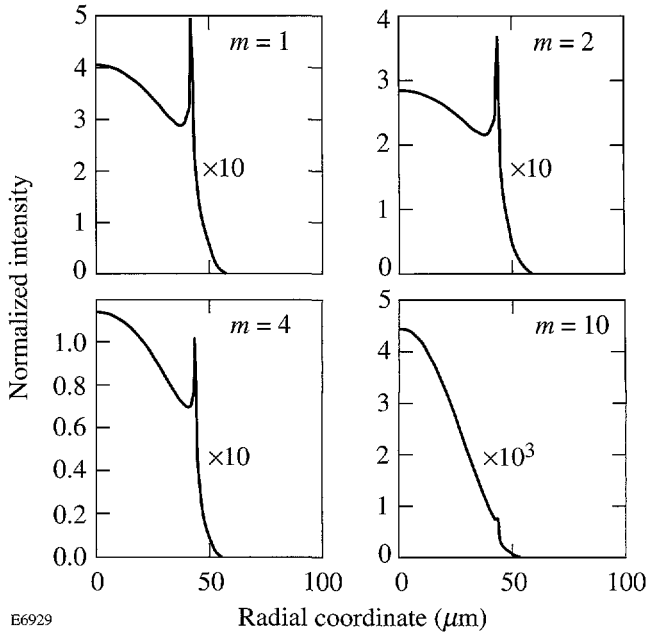

Figure 58.8
Simulation of shell doping with a high-Z additive. The absorption coefficient in the shell is multiplied by m. Detection is at 5-keV photon energy.

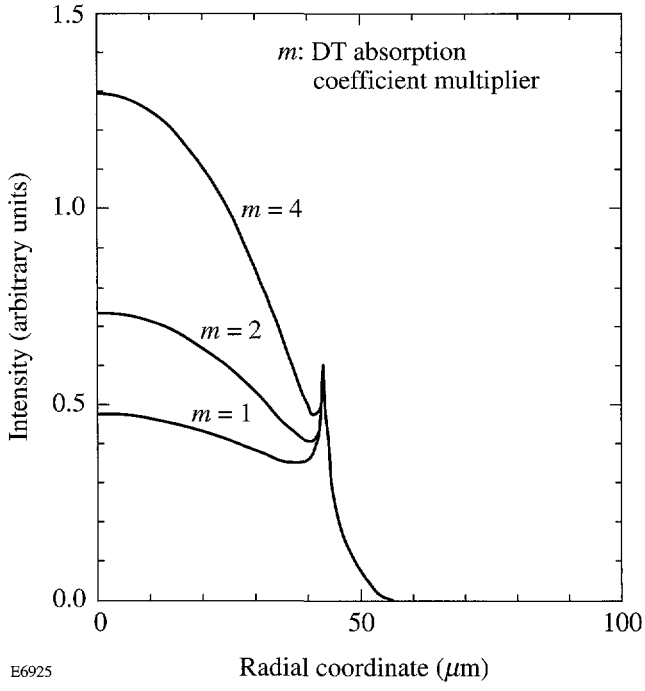

Figure 58.9
Emission profiles when the fuel absorption coefficient is multiplied by m, to simulate shell-fuel mixing. Detection is at 4.73-keV photon energy.

of 50 mm from the target corresponds to a divergence angle of 3×10^{-3} rad. Since an x-ray microscope is placed at longer distances (~200 mm), the divergence is smaller ($\sim 7 \times 10^{-4}$ rad). To minimize the clipping problem we need to maximize the crystal acceptance angle $\Delta\theta_B$ for a given linewidth $\Delta\lambda$. To see the relationship between the two, we differentiate the Bragg condition $2d\sin\theta_B = \lambda$ and obtain

$$E/\Delta E = \lambda/\Delta\lambda = \tan\theta_B/\Delta\theta_B . \qquad (14)$$

The resolving power $\lambda/\Delta\lambda$ is a slowly varying function of the Bragg angle θ_B, so to maximize $\Delta\theta_B$ we should maximize θ_B. This requires selecting a crystal whose 2d spacing is only slightly larger than the relevant wavelength, so that the diffraction angle will be close to 90°. One appropriate choice for the 2.62-Å wavelength is topaz (303), of 2d spacing 2.712 Å, giving a Bragg angle of 74.5°. However, topaz has a high resolution (~6000), which makes $\Delta\theta_B$ narrow. If we choose Ge (111) of 2d = 6.545 Å and resolution ~3000, the Bragg angle for the 2.62-Å line will be only 23.5°. Using Eq. (10) we see that the gain of a factor of ~2 in $\Delta\theta_B$, with respect to topaz (because the resolution is lower), is outweighed by a decrease of a factor of 8 in $\tan\theta_B$.

The resolving power $\lambda/\Delta\lambda$ of topaz (303) was measured[7] to be $\sim 10^4$ in the range θ_B = 10°–40°. Extrapolation to θ_B = 74° yields a resolving power of $\sim 6 \times 10^3$, which from Eq. (14) corresponds to $\Delta\theta_B = 6 \times 10^{-4}$ rad. This divergence is smaller than that of the image of either the pinhole camera (4×10^{-3}) or the microscope (1×10^{-3}). However, the clipping problem is actually less severe due to the spectral linewidth $\Delta\lambda$. For example, the Doppler width of the 2.62-Å line in a titanium plasma of ion temperature T_i = 500 eV is ΔE_l = 1.2 eV, which corresponds to $\Delta\theta_B = 9 \times 10^{-4}$ rad, about equal to the microscope image divergence. The finite spectral linewidth causes the crystal to reflect in each direction a slightly different wavelength within the linewidth. This eases the clipping problem but results in an intensity reduction of the order of 6/9 = 0.67. The field of view is still a problem for the pinhole-camera imaging, but not for microscope imaging.

The problem of limited field of view can be overcome by using a curved crystal (the Rowland circle geometry[8]), so that all rays forming the image have the same angle of incidence on the crystal. This is strictly true only for a Johansson-bent crystal. The resulting geometry is as follows: A pinhole is placed on the Rowland circle at a location corresponding to the backlighter wavelength (say, 2.62 Å). The target and the backlighter are placed outside the circle. Because of the limitation on the solid angle occupied in the target vacuum tank, only small Bragg angles are feasible. The advantage of large Bragg angles described above disappears, but the focusing geometry compensates for this. A film is placed close to the crystal because farther from the crystal the focusing due to the curvature of the crystal eliminates the imaging. We have then two options for monochromatic imaging, both shown schematically in Fig. 58.10: (a) using an x-ray microscope with a flat crystal (topaz) interposed just in front of the recording medium, and (b) pinhole imaging coupled to a curved-crystal, Rowland-circle spectrometer. In (a) the Bragg angle is large (e.g., 74.5° for topaz), whereas in (b) the Bragg angle is small (12°–18° in our present design).

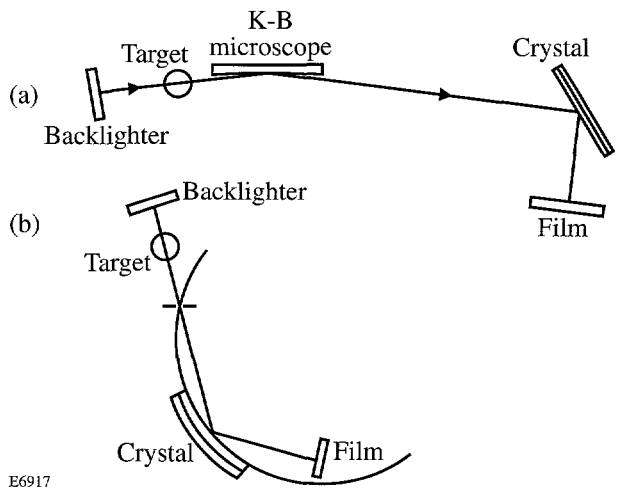

Figure 58.10
Schematic representation of two geometries for monochromatic backlighting: (a) Kirkpatrick-Baez x-ray microscope and a flat diffracting crystal; (b) pinhole imaging with a curved crystal on a Rowland circle.

The basis for imaging with a curved crystal, as stated above, is that all rays diverging from a single point on the Rowland circle and diffracted by a Johansson-type curved crystal fall on the crystal at the same Bragg angle. This assertion needs to be examined since the pinhole located on the Rowland circle [Fig. 58.10(b)] has a finite aperture. To find the divergence due to this finite size, we make use of the dispersion relation[8] of the Rowland spectrometer: $\Delta l = R\,\Delta\theta_B$, where R is the radius of curvature of the crystal (i.e., twice the radius of the Rowland circle) and $\Delta\theta_B$ is the change in the incidence angle on the crystal, corresponding to a travel Δl along the Rowland circle. A choice of R = 60 cm (corresponding to an actual spectrometer under construction at LLE) and Δl = 10 μm (corresponding to a pinhole of that diameter) yields $\Delta\theta_B = 1.67 \times 10^{-5}$ rad. This is smaller than the crystal accep-

tance angle $\Delta\theta_B = 3.5 \times 10^{-5}$ quoted above, meaning that a 10-μm-diam pinhole will not constitute the limiting factor in achieving monochromatic imaging. Instead, that limitation will be given by the imperfection of the crystal manufacturing and bending, as well as of the alignment.

We turn now to a comparison of sensitivity using both methods of imaging. A K-B microscope implemented at LLE[9] has a solid-angular aperture of 3×10^{-7}. For measuring the 4.73-keV titanium line, a gold coating is appropriate, having a reflection efficiency of ~0.3 over the range ~3.0–5.5 keV. The effective throughput (product of the angular aperture and the efficiency) is 9×10^{-8}. For the case of the pinhole-crystal method, a 10-μm-diam pinhole at 50 mm from the target, as assumed above, yields a solid-angular aperture of 4×10^{-8}, smaller than the aperture for the case of a K-B microscope. This is an additional advantage (in addition to the ease of aligning) in using a microscope-crystal combination, as opposed to using a pinhole with a curved crystal. It should be noted that there is no sensitivity gain due to the curvature of the crystal in the latter case because the film is placed very close to the crystal [Fig. 58.10(b)], before any significant focusing occurs. As explained above, such focusing would eliminate the imaging.

The effect of the monochromator bandwidth in reducing the continuum radiation participating in the image was already included (assuming a bandpass of 4 eV). We now calculate the crystal attenuation of the backlighting image for the experimental arrangement shown in Fig. 58.10(a). As it turns out, the results for the arrangement in Fig. 58.10(b) for a particular configuration are very similar.[10] The attenuation of the backlight image due to diffraction off a crystal monochromator is only by a factor of 2–5 because the beam forming the image is quasi-collimated when falling on the crystal.

We estimated above a resolving power of $\sim 6 \times 10^3$ for the topaz crystal at 2.62 Å; this corresponds to an energy window of $\Delta E_c = 0.79$ eV. This happens to be smaller than the generic 4-eV bandwidth assumed in the calculations above. We first note that the divergence of the beam focused by the microscope and incident on the crystal is smaller than the angular reflection curve. If the crystal angle is properly tuned, all rays are approximately incident at the angle of the peak in the reflectivity curve. However, the actual reflectivity is not simply given by the peak reflectivity because of the finite spectral width of the 2.62-Å line. The reflection as a function of wavelength is simply related to the angular reflection curve through the Bragg relation. This curve is approximately a Gaussian with peak reflectivity $R_{\max}$ and width ΔE_c. The spectral line shape can also be taken as a Gaussian of width ΔE_l. The effective crystal reflectivity will be lower than $R_{\max}$ because only rays of wavelength close to line center fulfill exactly the Bragg diffraction condition; the effective reflectivity is then given by the integral (assuming that the angle of incidence is the Bragg angle of peak reflectivity for the line-center wavelength):

$$R = \left(R_{\max}/\Delta E_l\sqrt{\pi}\right)\int_{-\infty}^{\infty}\exp\left[-\left(\Delta E/\Delta E_l\right)^2\right]$$

$$\exp\left[-\left(\Delta E/\Delta E_c\right)^2\right]dE = R_{\max}\Delta E_t/\Delta E_l\,, \qquad (15)$$

where $\Delta E_t^{-2} = \Delta E_l^{-2} + \Delta E_c^{-2}$. For increasing ΔE, both the incident intensity (first Gaussian) is decreasing as well as the reflectivity (second Gaussian) because the detuning from line center is then larger. ΔE_t should not be construed as a total width; in fact ΔE_t is smaller than either ΔE_l or ΔE_c. As expected, when $\Delta E_l << \Delta E_c$, $R \approx R_{\max}$. In the opposite case, when $\Delta E_l >> \Delta E_c$, $R \approx R_{\max}\,\Delta E_c/\Delta E_l$. In either case, the reflected intensity drops as we go to larger Bragg angles because (1) the peak reflectivity $R_{\max}$ drops for increasing θ_B and (2) ΔE_c also drops for increasing θ_B. Since the resolving power $E/\Delta E$ is usually almost constant as θ_B changes, it means that ΔE_c changes like $\sim 1/\sin\theta_B$. In the case of flat-crystal diffraction we are compelled to pay the price of reduced intensity to ensure a large enough field of view (by going to large Bragg angles, where $\Delta\theta_B$ is larger, even though ΔE_c is smaller). When using a curved crystal (Rowland spectrometer), the field-of-view problem is overcome because of the property of Rowland circle focusing, namely, that all rays diverging from a point on the circle fall on a Johansson-bent crystal at the same angle, enabling us to take advantage of the higher reflectivity at small Bragg angles. On the other hand, small Bragg angles are also mandated by the geometric constraints of the target vacuum chamber.

For the case of the topaz crystal, it was estimated earlier that $\Delta E_c = 0.79$ eV and $\Delta E_l = 1.2$ eV, yielding $R = (0.66/1.2)$ $R_{\max} = 0.55\ R_{\max}$. To estimate $R_{\max}$, we extrapolate the data for the integrated reflectivity of topaz to 74° and find R_{int} $\sim 2 \times 10^{-4}$. Using the relationship $R_{\text{int}} \approx \Delta\theta_B \times R_{\max}$ and the value of $\Delta\theta_B$ estimated above, we find $R_{\max} = 0.33$ and,

finally, the effective reflectivity $R = 0.18$. This attenuation is the price we have to pay for using a monochromator crystal for reducing the contribution of target self-emission.

Conclusions

The expected backlighting and self-emission images of a particular CH target to be imploded on the OMEGA Upgrade are calculated for a variety of experimental parameters. The goal is to image the shell at peak compression with opacity of the order of 1. In this case, the image should delineate the inner surface of the imploded shell (or at least its colder portion), thus providing useful information on the compression and the symmetry. It is shown that to overcome the problem of target self-emission, the image has to be monochromatized with a diffracting crystal, and that the resulting attenuation of the backlighting image is not severe (by a factor of ~5). For the target studied, the two image components are then comparable in intensity, and both provide useful information on target behavior. Two experimental configurations for monochromatic imaging are described: (a) using a microscope and a flat crystal, and (b) using pinhole imaging and a curved crystal in the Rowland geometry. Useful images are obtained with simple (undoped) CH-shell targets and without the need for a short-pulse backlighter beam.

A particularly interesting feature is the appearance in the self-emission of a circular spike that closely delineates the fuel-shell interface but requires high spatial resolution to be observed. The optimization of its appearance is studied. Finally, it is shown that mixing of shell material into the fuel at up to ~10% by atom number might be diagnosable by the spike.

ACKNOWLEDGMENT

This work was supported by the U.S. Department of Energy Office of Inertial Confinement Fusion under Cooperative Agreement No. DE-FC03-92SF19460, the University of Rochester, and the New York State Energy Research and Development Authority. The support of DOE does not constitute an endorsement by DOE of the views expressed in this article.

REFERENCES

1. H. A. Bethe and E. E. Salpeter, in *Quantum Mechanics of One- and Two-Electron Atoms* (Academic Press, New York, 1957), p. 295.
2. H. R. Griem, in *Plasma Spectroscopy* (McGraw-Hill, New York, 1964), p. 148, Eq. [6-55].
3. R. W. Lee, B. L. Whitten, and R. E. Stout II, J. Quant. Spectrosc. Radiat. Transfer **32**, 91 (1984).
4. J. C. Stewart and K. D. Pyatt, Jr., Astrophys. J. **144**, 1203 (1966).
5. B. Yaakobi, P. Bourke, Y. Conturie, J. Delettrez, J. M. Forsyth, R. D. Frankel, L. M. Goldman, R. L. McCrory, W. Seka, J. M. Soures, A. J. Burek, and R. E. Deslattes, Opt. Commun. **38**, 196 (1981); D. L. Matthews *et al.*, J. Appl. Phys. **54**, 4260 (1983).
6. H. R. Griem, *Plasma Spectroscopy* (McGraw Hill, New York, 1964), Eq. (7-6).
7. K. Gisselberg, Ark. Fys. **30**, 359 (1965).
8. B. Yaakobi, T. Boehly, and P. Audebert, Rev. Sci. Instrum. **61**, 1915 (1990).
9. Laboratory for Laser Energetics LLE Review **46**, NTIS document No. DOE/DP/40200-156, 1991 (unpublished), p. 91.
10. B. Yaakobi, F. J. Marshall, R. Epstein, and Q.Su, "Monochromatic Backlighting as a Laser-Fusion Diagnostic," to appear in the Journal of X-Ray Science and Technology.

Effect of Electron Collisions on Ion-Acoustic Waves and Heat Flow

Introduction

The damping rate of ion-acoustic waves in plasma plays an important role in establishing the threshold for the onset of stimulated Brillouin scattering, ion-temperature-gradient instability, current-driven ion-acoustic instability, and other drift-wave microinstabilities. The effect of electron-ion (*e-i*) collisions on the ion-acoustic damping rate has been recently investigated by analytically solving the electron Fokker-Planck (FP) equation for a Lorentz plasma (i.e., neglecting *e-e* collisions) with cold ions and arbitrary $k\lambda_{ei}$ (where k is the wave number and λ_{ei} is the *e-i* mean free path).[1] It was shown that, as *e-i* collisions are introduced, the damping rate γ rises monotonically above the collisionless Landau limit γ_Λ, reaches a peak at $k\lambda_{ei} \sim \left(Zm_e/m_i\right)^{1/2}$ (where Z is the charge number and m is the mass), and then decreases to zero as $k\lambda_{ei} \rightarrow 0$ with the damping rate γ_{fluid} predicted by fluid theory.

The main purpose of this article is to assess the contributions from both *e-e* and *e-i* collisions on the damping of the ion-acoustic waves. Results are based on numerical simulations using a code (*SPRING*) that solves the linearized electron FP and cold-ion fluid equations. We are able to explore a wide range of values of $k\lambda_{ei}$ and Z by expanding the electron-distribution function in an arbitrary number of Legendre modes, and by using the *exact* form of the Rosenbluth[2] potentials (neglecting terms of the order of m_e/m_i). In the high-Z limit, where *e-e* collisions can be ignored, the analytic Lorentz-plasma results of Epperlein *et al.*[1] are recovered. For low-Z plasmas, *e-e* collisions become significant and promote a reduction in the damping near $k\lambda_{ei} = 1$, though γ still remains larger than γ_L and γ_{fluid}. The approximation of isotropic Rosenbluth potentials is also investigated and found to yield sufficiently accurate values of γ (error <10%). A further useful approximation that involves adjusting the *e-i* collision frequency to simulate the strength of *e-e* collisions is shown to be similarly accurate. Although finite ion-temperature effects have been neglected in the current analysis, their contribution to γ has been investigated by Randall[3] and more recently by Tracy *et al.*,[4] who calculated the ion-acoustic eigenfrequency ω for arbitrary $k\lambda_{ii}$ (where λ_{ii} is the *i-i* mean free path) and isothermal electrons.

It is also of interest to calculate the effective (or generalized) thermal conductivity κ based on the perturbed distribution function and compare it to the classical Spitzer-Härm (SH)[5] conductivity κ_{SH}. Not only does this give insight into electron kinetic effects, but it can also provide a way of incorporating kinetic effects into fluid equations. This idea has been successfully used in the context of electron heat transport in laser-produced plasmas[6] and more recently in the context of drift-wave microinstabilities in tokamak plasmas.[7,8] In particular, generalized thermal conductivities have been calculated by Hammett and Perkins[7] (κ_{HP}) for collisionless plasmas, and by Chang and Callen[8] for arbitrary $k\lambda_{ei}$, ω, and Z.

The results for κ calculated here are shown to reproduce the analytic results of Epperlein *et al.*[1] obtained in the Lorentz plasma approximation. In the collisional limit ($k\lambda_{ei} << 1$) κ approaches κ_{SH}, and in the collisionless limit ($k\lambda_{ei} >> 1$) it approaches κ_{HP}. We find, however, significant discrepancies with the results of Chang and Callen. They underestimate κ by factors ranging from 2.4 (at $Z = 1$) to 7.1 (as $Z \rightarrow \infty$) in the collisional limit.

The introduction of a spatially modulated inverse-bremsstrahlung heating source has also been recently shown to significantly reduce the effectiveness of heat conduction when $k\lambda_{ei} >> 1$.[9] A simple analytic formula for $\kappa_{\text{IB}}/\kappa_{\text{SH}}$ as a function of $k\lambda_{ei}$ has been proposed, based on simulations with an approximate form of the FP equation. Here we are able to assess the accuracy of the κ_{IB} formula and show that the reduction in conductivity (relative κ_{SH}) for $k\lambda_{ei} >> 1$ is indeed larger than for the undriven case, with freely propagating sound waves.

In the following sections, we describe the electron FP and cold-ion fluid equations and the numerical scheme (*SPRING* code) adopted for their solution; finally, our results are presented and summarized.

Electron Fokker-Planck and Cold-Ion Fluid Equations

Our model consists of a quasi-neutral homogeneous background plasma with fully ionized ions. The full electron FP operator is used, with the exception of *e-i* energy-exchange terms (which provide contributions of the order of $m_e/m_i << 1$). Adopting a perturbation of the electron distribution function of the form

$$f(x,\mathbf{v},t) = F_0(v) + \sum_{l=0}^{L} f_l(v,t)\,P_l(\mu)\exp(ikx), \qquad (1)$$

where $\mu = v_x/v$ and $P_l(\mu)$ is the lth Legendre mode, the linearized electron FP equation (defined in the rest frame of the ions) becomes[10]

$$\frac{\partial f_0}{\partial t} + \frac{ikv}{3} f_1 - \frac{iku_i}{3} v\frac{\partial F_0}{\partial v} = C_{ee}^i(F_0, f_0) + C_{ee}^i(f_0, F_0), \quad (2)$$

$$\frac{\partial f_1}{\partial t} + ikvf_0 + ikv\frac{2}{5}f_2 - \left(\frac{|e|E}{m_e} + \frac{\partial u_i}{\partial t}\right)\frac{\partial F_0}{\partial v}$$

$$= -\nu_{ei} f_1 + C_{ee}^i(F_0, f_1) + C_{ee}^a(F_0, f_1), \qquad (3)$$

$$\frac{\partial f_2}{\partial t} + \frac{2}{3}ikvf_1 + \frac{3}{7}ikvf_3 - \frac{2}{3}iku_i v\frac{\partial F_0}{\partial v}$$

$$= -3\nu_{ei} f_2 + C_{ee}^i(F_0, f_2) + C_{ee}^a(F_0, f_2), \qquad (4)$$

and

$$\frac{\partial f_l}{\partial t} + \frac{l}{2l-1}ikvf_{l-1} + \frac{l+1}{2l+3}ikvf_{l+1}$$

$$= -\frac{l(l+1)}{2}\nu_{ei} f_l + C_{ee}^i(F_0, f_l) + C_{ee}^a(F_0, f_l) \qquad (5)$$

for $l > 2$. The ion velocity u_i and electric field E are first order in the perturbation, and

$$F_0(v) = N_e\left(2\pi v_t^2\right)^{-3/2}\exp\left(-v^2/2v_t^2\right)$$

is an equilibrium Maxwellian, where N_e is the background electron number density, $v_t = \left(T_e/m_e\right)^{1/2}$ is the electron thermal velocity, and T_e is the electron temperature (in energy units). The velocity-dependent *e-i* collision frequency is given by

$$\nu_{ei}(v) = 4\pi N_e Z\left(e^2/m_e\right)^2 \ln\Lambda/v^3,$$

where e is the electron charge and $\ln\Lambda$ is the Coulomb logarithm (assumed the same for both electrons and ions). The terms C_{ee}^i and C_{ee}^a (defined in the Appendix) represent the isotropic and anisotropic parts of the *e-e* collision operator, respectively. Since the latter involves integration over the perturbed distribution function, it is usually neglected in FP calculations.[11] The validity of such approximation is the subject of "Approximations to the Fokker-Planck Equation" on p. 72.

The linearized cold-ion continuity and momentum equations are

$$\frac{\partial n_i}{\partial t} + ikN_i u_i = 0, \qquad (6)$$

and

$$N_i m_i \frac{\partial u_i}{\partial t} = ZN_i|e|E + R_{ie}, \qquad (7)$$

where $R_{ie} = \left(4\pi m_e/3\right)\int dv v^3 \nu_{ei} f_1$ is the *i-e* momentum exchange rate, n_i is the perturbed ion number density, and N_i is its background value. The perturbed electric field is calculated via Poisson's equation,

$$ikE = 4\pi|e|\left(Zn_i - n_e\right), \qquad (8)$$

where the perturbed electron number density is $n_e = 4\pi\int_0^\infty v^2 f_0 dv$.

Numerical Scheme (*SPRING* code)

A computer code (*SPRING*) has been written to solve Eqs. (2)–(8). It uses a "time-splitting" scheme with the following stages:

$$\frac{\partial f_1}{\partial t} = \left(\frac{|e|E}{m_e} + \frac{\partial u_i}{\partial t}\right)\frac{\partial F_0}{\partial v} \qquad \text{(acceleration)},$$

$$\frac{\partial f_0}{\partial t} = \frac{iku_i}{3} v \frac{\partial F_0}{\partial v} \qquad \text{(compression)},$$

$$\frac{\partial f_2}{\partial t} = \frac{2}{3} iku_i \mathrm{v} \frac{\partial F_0}{\partial \mathrm{v}} \qquad \text{(viscosity)},$$

$$\frac{\partial f_0}{\partial t} = C_{ee}^i(F_0, f_0) + C_{ee}^i(f_0, F_0)$$

$$\frac{\partial f_l}{\partial t} = C_{ee}^i(F_0, f_l) + C_{ee}^a(F_0, f_l) \qquad (e\text{-}e \text{ collision}),$$

and

$$\frac{\partial f_l}{\partial t} = -\frac{l}{2l-1} ikvf_{l-1} - \frac{l+1}{2l+3} ikvf_{l+1} - \frac{l(l+1)}{2} \nu_{ei} f_l$$

(advection and e-i angular scattering),

where $l > 0$. The acceleration, compression, and viscosity stages are advanced explicitly in time. In the e-e collision stage, the isotropic collision operators (which are differential operators) are evaluated implicitly using the Chang-Cooper[12] scheme, whereas the anisotropic operators (which are integral operators) are evaluated explicitly. In the advection-scattering stage, f_l is solved implicitly at each velocity group, using the boundary condition that $f_{-1} = f_{L+1} = 0$. The distribution function is defined on a velocity mesh with constant spacing of typically $\Delta v = 0.125\, v_t$ between $v = 0$ and $6v_t$.

After advancing the distribution function in time, with a fixed time step Δt, the ion-fluid equations are solved explicitly. However, solving Poisson's equation explicitly to calculate E can lead to numerical instabilities when $\Delta t\, \omega_p > 1$ [where $\omega_p = \left(4\pi N_e e^2/m_e\right)^{1/2}$ is the plasma frequency]. To avoid this problem we use an implicit-moment method,[13] which involves taking density and momentum moments of the FP equation and substituting back into the ion continuity and Poisson's equations. An approximation to the electric field at a time $(t + \Delta t)$ can then be obtained from

$$ikE(t+\Delta t) = \frac{4\pi|e|}{\left(1+\omega_p^2\Delta t^2\right)}\left\{Zn_i(t) - n_e(t) + ik\Delta t N_e \left[v_e(t) + ik\Delta t p(t)/N_e m_e - \Delta t R_{ie}(t)/N_e m_e\right]\right\}, \quad (9)$$

where $p = \left(4\pi m_e/3\right)\int dv v^4 f_0$ and $v_e = \left(4\pi/3N_e\right)\int dv v^3 f_1$. Since we are interested in low-frequency phenomena, such as sound waves, Eq. (9) allows us to use time steps larger than ω_p^{-1}.

The sound-wave eigenfrequencies are determined by appropriately initializing the dependent variables and monitoring their temporal evolution over several wave periods. In the past, simulations of this kind (involving the ion FP equation) have suffered from the occurrence of spurious transients that required complicated procedures to filter out the correct eigenfrequencies.[3] This problem appears to be associated with the fact that the "exact" perturbed eigenfunctions f_l are not known *a priori*. Rather than trying to guess f_l, a more satisfactory approach is to start with $f_l = n_i = 0$ and $u_i = 1$. The variables then typically converge to the appropriate eigenmodes within a few sound-wave periods. (An alternative approach based on eigenvalue analysis has also been proposed by Tracy *et al.*[4])

SPRING Simulation Results

The code *SPRING* provides ion-acoustic damping rates γ/kc_s for different values of $k\lambda_{ei}$, $k\lambda_D$, Z, and A, where

$$\lambda_{ei} = 3T_e^2 \Big/ \left[4(2\pi)^{1/2} N_e Z e^4 \ln\Lambda\right],$$

$\lambda_D = v_t/\omega_p$ is the Debye length, A is the atomic mass, and $c_s = \left(ZT_e/m_i\right)^{1/2}$ is the isothermal sound speed. The code also calculates an effective thermal conductivity defined by $\kappa \equiv -q_{\mathrm{FP}}/ikT_{\mathrm{FP}}$, where

$$q_{\mathrm{FP}} = \left(2\pi m_e/3\right)\int dv\, v^5 f_1$$

is the electron heat flow and

$$T_{FP} = (4\pi m_e / N_e) \int dv \left(v^4/3 - v^2 v_t^{\,2} \right) f_0$$

is the temperature. Since we are primarily concerned with collisional effects, we choose $\lambda_D << k^{-1}$; also, for simplicity, we take $A = 2Z$.

1. Damping rate γ

The first test of *SPRING* involves neglecting *e-e* collisions altogether. This is equivalent to using the Lorentz plasma approximation, or high-Z limit, since $\nu_{ei}/\nu_{ee} \sim Z$. In this instance Eqs. (2)–(8) can be solved analytically by the method of continued fractions (see Ref. 1), and the results are plotted as curve *d* in Fig. 58.11. The code is found to reproduce these damping rates very accurately throughout the whole range of $k\lambda_{ei}$. (In practice, this requires using $Z >> 10^4$.)

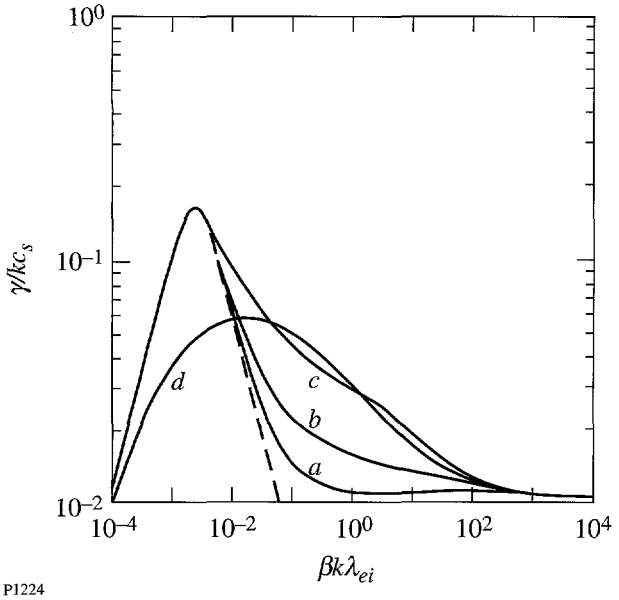

Figure 58.11
Plots of the damping rate of ion-acoustic waves γ/kc_s as functions of $\beta k\lambda_{ei}$, where c_s is the isothermal sound speed, k is the perturbation wave number, λ_{ei} is the electron-ion mean free path, and β is a scaling factor ($\beta = 0.24$, 0.68, 0.92, and 1 for $Z = 1$, 8, 64, and ∞, respectively). Solid curves represent *SPRING* simulations with (a) $Z=1$, (b) $Z = 8$, (c) $Z = 64$, and (d) $Z = \infty$. The dashed curve refers to the fluid result.

To test the accuracy of the numerical implementation of the *e-e* operators we first consider the collisional case ($k\lambda_{ei} << 1$) with $Z = 1$. In this limit the Legendre expansion [Eq. (1)] can be truncated at $l = 1$, and f_0 approaches a perturbed Maxwellian. Since this is also the fluid limit, a sound-wave dispersion relation can be derived using the standard fluid equations (neglecting viscosity effects) with the Spitzer-Härm thermal conductivity $\kappa_{SH} = \gamma_0(Z) N_e v_t \lambda_{ei}$, where the Z-dependent, thermal-conductivity coefficient is approximately given by $\gamma_0(Z) \approx 3.20(0.24 + Z)/(1 + 0.24Z)$ and $\gamma_0(\infty) = 128/3\pi$. The resultant dispersion relation (using $\partial/\partial t = -i\omega$) is found to be

$$\left(\frac{\omega}{kc_s} \right)^2 = \frac{2}{3 + i\left(\frac{\omega}{kc_s} \right) 3r} + 1 , \qquad (10)$$

where r is the ratio of the thermal diffusion rate $\left(2k^2\kappa_{SH}/3N_e\right)$ to the sound transit rate (kc_s) across k^{-1}. Since $r = 2\gamma_0 k\lambda_{ei} \left(m_i/Zm_e\right)^{1/2}/3$, it has been found convenient to plot γ/kc_s as a function of $\beta k\lambda_{ei}$, where

$$\beta = (A/2Z)^{1/2} \gamma_0(Z)/\gamma_0(\infty)$$

is a scaling factor of order unity. The damping rates based on Eq. (10) are plotted in Fig. 58.11 (dashed curve). *SPRING* simulation results are found to be in good agreement with these as $k\lambda_{ei} \to 0$.

Let us now consider the more interesting case of finite Z and $k\lambda_{ei}$. The results are shown in Fig. 58.11 (solid curves *a–c*) for $Z = 1$, 8, and 64. Starting from the large $k\lambda_{ei}$ limit, we note that the dominant collisional contribution comes from *e-i* collisions. [Here, a large number of Legendre modes are necessary to accurately model the damping (e.g., typically $L = 20$ for $\beta k\lambda_{ei} = 10^2$).] In the intermediate regime of $\beta k\lambda_{ei} \sim 1$ we find the peculiar result that *e-e* collisions actually reduce the damping rate. The reason for this becomes apparent if we consider the nature of the electron collisional process. As shown by Epperlein *et al.*[1] elastic scattering between electrons and ions gives rise to both sound-wave damping, through thermal diffusion, and sound-wave "undamping," through disruption of the Landau wave-particle interaction. However, the main collisional contribution between electrons is energy exchange, which acts to drive f_0 toward a perturbed Maxwellian. Hence, introducing *e-e* collisions can actually reduce the damping rate by bringing it closer to the fluid limit. Since $\nu_{ei}/\nu_{ee} \sim Z$, this effect is strongest for low-Z plasmas. (Although γ does not fall below γ_L for $\beta k\lambda_{ei} > 0.01$, if we artificially reduce the value of Z, we can effectively extend the "fluid limit" to larger values of $k\lambda_{ei}$ and thereby allow γ to be less than γ_L.)

To a lesser extent, *e-e* collisions also affect the anisotropic parts of the electron distribution function (i.e., $f_1, f_2, \ldots$). For example, the *e-e* collision terms on the RHS of Eq. (3) are responsible for reducing the thermal conductivity, thus giving rise to the Z-dependent thermal coefficient γ_0 in the fluid limit.

2. Approximations to the Fokker-Planck equation

The *e-e* collision operator for $l > 0$ (see Appendix) can be separated into an isotropic part $C_{ee}^{i}(F_0 f_l)$, which involves derivative operations on f_l, and an anisotropic part $C_{ee}^{a}(F_0 f_l)$, which involves integral operations on f_l. Since the latter is more difficult to implement numerically, it is usually neglected in electron FP calculations. Here we investigate the implications of neglecting both $C_{ee}^{a}(F_0 f_l)$ and $C_{ee}^{i}(F_0 f_l)$ for $l > 0$ and how we can simulate their effects by appropriately adjusting the value of ν_{ei}. We also briefly explore the possibility of using a generalized collision frequency to simulate the contribution from an infinite Legendre-mode expansion.

The effect of neglecting *e-e* collisions altogether (the so-called Lorentz approximation) has already been demonstrated in Fig. 58.11. There we see that apart from the weakly collisional regime $\beta k\lambda_{ei} >> 1$, where electron collisions play a relatively minor role in the sound-wave damping, or the strongly collisional regime $\left(\beta k\lambda_{ei} << 10^{-4}\right)$, where the thermal diffusion rate is much less than sound transit rate, it is not reasonable to neglect *e-e* collisions for $Z < 64$. This is especially true near the maximum value of γ/kc_s, at $\beta k\lambda_{ei} \approx 0.002$, where even for $Z = 64$ the Lorentz approximation leads to large errors.

The first approximation we consider uses isotropic Rosenbluth potentials only (i.e., setting $C_{ee}^{a} = 0$). Figure 58.12 shows a comparison of the damping rate (open circles) with the more accurate calculation discussed in the previous section. We note that the largest errors occur over the range $10^{-1} < \beta k\lambda_{ei} < 10^{1}$ with an overall maximum of about 10%. Since the relative contribution from *e-e* collisions is most significant for low Z, the worst possible case occurs with $Z = 1$.

The second approximation neglects *e-e* collisions altogether for $l > 0$ (i.e., setting $C_{ee}^{i} = C_{ee}^{a} = 0$ for $l > 0$). To offset this more drastic approximation we introduce a modified collision frequency $\nu_{ei}^{*} = \left[\gamma_0(\infty)/\gamma_0(Z)\right]\nu_{ei}$. The new factor $\left[\gamma_0(\infty)/\gamma_0(Z)\right] \approx (Z + 4.2)/(Z + 0.24)$ has the effect of giving the correct (SH) thermal conductivity in the collisional limit. A plot of the corresponding damping rate for $Z = 1$ (the crosses in Fig. 58.12) shows that, once again, the errors are larger at intermediate values of $\beta k\lambda_{ei}$ with a maximum of about 10%. As in the previous case, this low-Z example provides the worst possible case.

The advantage of neglecting *e-e* collisions for $l > 0$ (through the introduction of ν_{ei}^{*}) is that Eqs. (3)–(5) become algebraic in v, allowing for much faster numerical solution of the coupled equations.

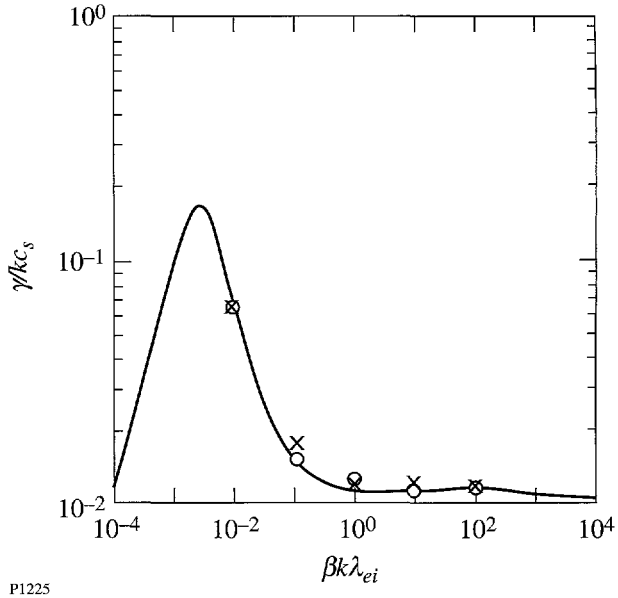

Figure 58.12
Plots of the damping rate of ion-acoustic waves γ/kc_s as functions of $\beta k\lambda_{ei}$ for $Z = 1$ (as in Fig. 58.11). Results using isotropic Rosenbluth potentials are displayed as open circles, whereas those using ν_{ei}^{*} are displayed as crosses.

Provided we are only interested in low-frequency waves [such that $\omega << \nu_{ei}(v_t)$], we can now go a step further and use the techniques of Ref. 1 to reduce Eqs. (3)–(5) to a single equation,

$$ikvf_0 - \left[\frac{|e|E}{m_e} + \frac{\partial u_i}{\partial t} + \left(\nu^* - \nu_{ei}^*\right)u_i\right]\frac{\partial F_0}{\partial v} = -\nu^* f_1 . \quad (11)$$

Here, $\nu^*(k) = \nu_{ei}^*\left[1 + \left(\pi kv/6\nu_{ei}^*\right)^2\right]^{1/2}$ is the low-frequency-generalized collision frequency proposed by Epperlein *et al.*,[1] which incorporates the contribution from all Legendre modes with $l > 1$. By substituting Eq. (11) into Eq. (2), we are left with a single differential equation for f_0, which is easier to solve than the original set of coupled equations. However, a discussion of the numerical methods involved is outside the scope of this article.

3. Effective thermal conductivity κ

Figure 58.13 plots (a) $|\kappa/\kappa_{SH}|$ and (b) arg(κ) as functions of $\beta k\lambda_{ei}$ for $Z = 1$, 8, 64, and ∞ (solid curves). The dashed curve shows the results of Hammett and Perkins (for a collisionless plasma).

When neglecting *e-e* collisions (Lorentz plasma approximation), our results agree with the analytic solutions of Ref. 1. In the collisional limit $(k\lambda_{ei} << 1)$, we have $\kappa = \kappa_{SH}$, whereas in the collisionless limit $(k\lambda_{ei} >> 1)$, we have $\kappa = \kappa_{HP} = 3(2/\pi)^{1/2} N_e v_t/|k|$ [see dashed curve HP in Fig. 58.13(a)]. (The formula for κ_{HP} is 1.5 times larger than the one used by Hammett and Perkins since ours is defined in terms of the isotropic temperature T_{FP}.) Comparing our results with those of Chang and Callen,[8] however, we find considerable discrepancy in the $k\lambda_{ei} << 1$ limit. Although the authors point out in their paper that they underestimate the thermal conductivity by a factor of 2.4 for $Z = 1$, this factor actually rises up to 7.1 for $Z >> 1$.

Two mechanisms can be identified that reduce the heat flow below the SH limit, q_{SH}. The first one is caused by a departure of f_0 from the perturbed Maxwellian.[14] When the mean free path of heat-carrying electrons (with velocities close to 3.6 v_t) becomes greater than k^{-1}, their spatial gradient in configuration space is reduced. Since these relatively collisionless electrons cannot thermalize instantaneously with thermal electron population (as required by fluid theory), the heat flow is reduced below q_{SH}. The reduction in heat flow is therefore governed by the balance between the thermal-diffusion rate and the *e-e* thermalization rate [as given by the collision term in Eq. (2)]. In the Lorentz plasma approximation, where *e-e* collisions are neglected altogether, there is no effective coupling between different electron-energy groups, as illustrated by the large phase shift between q_{FP} and T_{FP} in Fig. 58.13(b). As seen in Figs. 58.13(a) and 58.13(b), the departure from fluid theory then becomes significant when $r \sim k\lambda_{ei}(m_i/Zm_e)^{1/2} > 1$, i.e., when the thermal-diffusion time becomes less than the hydrodynamic time. As *e-e* collisions are introduced (identified by the finite-Z curves), f_0 is driven closer to a perturbed Maxwellian and the onset of kinetic effects is shifted to larger values of $k\lambda_{ei}$. The phase difference between q_{FP} and T_{FP} is also considerably reduced by the introduction of *e-e* collisions and becomes negligible for $Z = 1$ [see Fig. 58.13(b)].

Regardless of the *e-e* thermalization strength, the electron heat flow cannot exceed the "free-streaming," or collision-

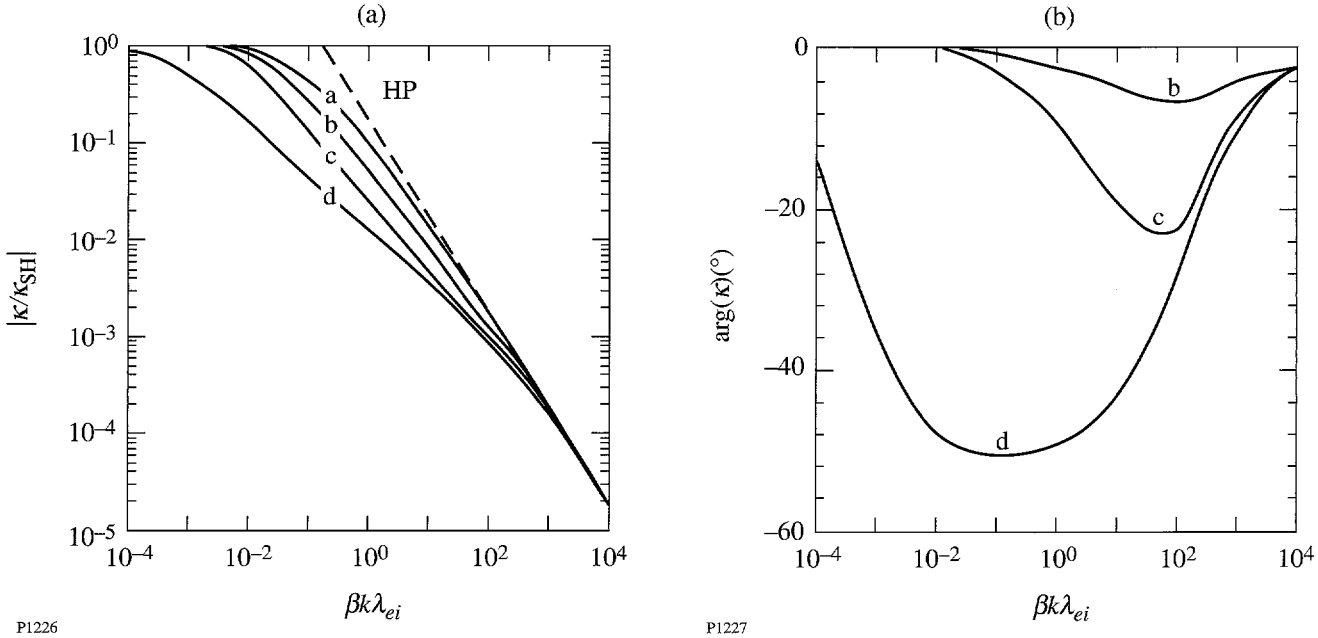

Figure 58.13
Plots of (a) $|\kappa/\kappa_{SH}|$ and (b) arg(κ) as functions of $\beta k\lambda_{ei}$, where κ and κ_{SH} are the effective and Spitzer-Härm thermal conductivities, respectively. As in Fig. 58.11, the solid curves refer to *SPRING* simulation results with (a) $Z = 1$, (b) $Z = 8$, (c) $Z = 64$, and (d) $Z = \infty$ [for $Z = 1$, arg(κ) <<1]. Here the dashed curve refers to the model of Hammett and Perkins.

less, limit as calculated by Hammett and Perkins,[7] i.e., $q_{HP} = -(ik/|k|)3(2/\pi)^{1/2} N_e T_{FP} v_t$. This gives us the second mechanism for the reduction of κ, with the upper limit shown by the plot of $\kappa_{HP}/\kappa_{SH} = 9(2\pi)^{1/2}(A/2Z)^{1/2}/(128\beta k\lambda_{ei})$ (dashed curve) in Fig. 58.13(a).

Other processes can also affect the electron thermal conductivity. Inverse-bremsstrahlung heating, for example, preferentially heats low-velocity electrons, which in turn modifies f_0 and leads to even further reduction of κ.[9] Such a phenomenon has been recently investigated and shown to have a significant impact on both filamentation[9] and stimulated Brillouin scattering[15] in laser-produced plasmas. The corresponding values of κ have been calculated using the nonlinear FP code *SPARK*; the following analytical fit to the simulation results has been proposed:[9]

$$\frac{\kappa_{IB}}{\kappa_{SH}} = \frac{1}{1+(30k\lambda_e)^{4/3}}, \qquad (12)$$

where $\lambda_e = \eta T^2/\left[4\pi N_e e^4 Z^{1/2} \ln\Lambda\right]$ is the electron delocalization length and $\eta = \left[\gamma_0(Z)/\gamma_0(\infty)\right]^{1/2}$. (As observed in Ref. 9, certain care is needed in defining Z for multispecies ions.) The resulting dashed curve (IB) for $Z = 1$ is plotted in Fig. 58.14 as a function of $\beta k\lambda_{ei}$. Although the original simulation results were based on a two-Legendre-mode expansion for the distribution function (i.e., $L = 1$), the contribution from higher-order modes have been investigated by Epperlein and Short[6] [using a generalized collision frequency ν^* of the type discussed in "Approximations to the Fokker-Planck equation"] and found to be negligible.

Here, we are able to check on the accuracy of Eq. (12) by using *SPRING* with an inverse-bremsstrahlung heating source of the type[16]

$$\frac{1}{v^2}\frac{\partial}{\partial v}\left(\frac{g}{v}\frac{\partial f_0}{\partial v}\right)$$

inserted on the right-hand side of Eq. (2), where

$$g = \left[1+(\nu_{ei}/\omega_0)^2\right]^{-1}$$

and ω_0 is the light-wave frequency. The code is then run until the distribution function reaches a steady state. In this case, ion motion does not play a significant role. The corresponding values of κ/κ_{SH} (also for $Z = 1$) have been calculated for range of $bk\lambda_{ei}$ and displayed as circles in Fig. 58.14. As shown, the simple analytic fit [Eq. (12)] can accurately reproduce the more accurate *SPRING* simulation results. For comparison, the values of κ for an undriven plasma [curve Z = 1 in Fig. 58.13(a)] has also been plotted in Fig. 58.14.

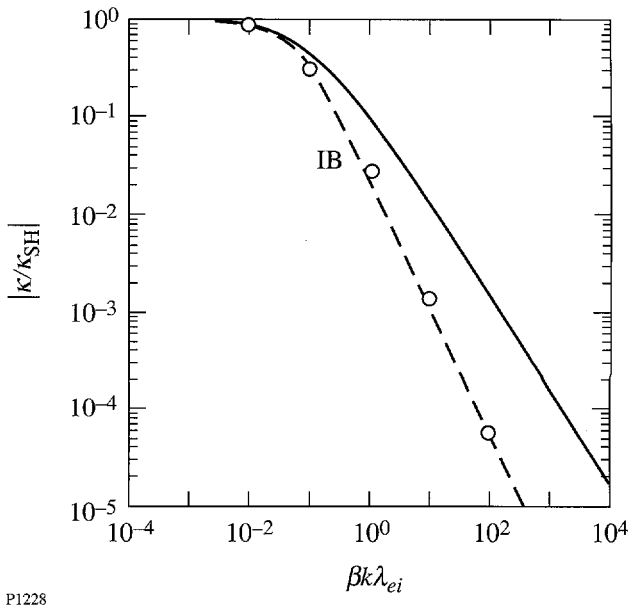

Figure 58.14
Plot of κ/κ_{SH} as a function of $\beta k\lambda_{ei}$ for $Z = 1$ (as in Fig. 58.13). Here the dashed curve refers to the analytic formula for κ_{IB} (from Ref. 9), and circles represent *SPRING* simulation results with an inverse-bremsstrahlung heating source.

Summary

The effect of electron collisionality on the damping of ion-acoustic waves has been investigated by numerically solving the electron FP and cold-ion-fluid equations. The code (*SPRING*) developed for this purpose reproduces the analytic results previously obtained for a Lorentz plasma (i.e., without *e-e* collisions).

The introduction of *e-e* collisions shows that the Lorentz approximation is inadequate near the peak of the damping rate at $k\lambda_{ei} \sim (Zm_e/m_i)^{1/2}$. For $k\lambda_{ei} > (Zm_e/m_i)^{1/2}$ and $Z < 64$, *e-e* collisions reduce the damping rate below the Lorentz value, though it still remains higher than the γ_{fluid} and γ_L.

A convenient approximation that involves adjusting the *e-i* collision frequency to model the contribution from *e-e* collisions for $l > 1$ has been found to yield errors of up to 10% in the damping rate. A further generalization of the *e-i* collision

frequency that simulates the contribution from all Legendre modes with $l > 1$ has also been discussed.

Calculations of the effective thermal conductivity κ for a Lorentz plasma have shown significant reduction from the Spitzer-Härm value κ_{SH} for $k\lambda_{ei} > 10^{-4}$. However, even for Z as high as 64, *e-e* collisions extend the validity of the fluid approximation for up to $k\lambda_{ei} \sim 10^{-2}$. In the limit as $k\lambda_{ei} \to \infty$, κ approaches the value $3(2/\pi)^{1/2} N_e v_t / k$ predicted by Hammett and Perkins.

Heating the plasma with a spatially modulated inverse-bremsstrahlung heating source, and solving for the steady-state distribution function, has been shown to further reduce κ. The accuracy of a simple analytic formula previously derived for κ_{IB} has been verified for up to $k\lambda_{ei} \sim 10^{2}$.

ACKNOWLEDGMENT

The author acknowledges many useful discussions with Robert W. Short, Albert Simon, and Mark D. Tracy. This work was supported by the U.S. Department of Energy Office of Inertial Confinement Fusion under Cooperative Agreement No. DE-FC03-92SF19460, the University of Rochester, and the New York State Energy Research and Development Authority. The support of DOE does not constitute an endorsement by DOE of the views expressed in this article.

APPENDIX: THE ELECTRON-ELECTRON COLLISION OPERATOR

The isotropic and anisotropic parts of the collision operator are given by[2,10]

$$C_{ee}^{i}(f_0, f_l) = \nu_{ee} v \frac{\partial}{\partial v}\left[f_l I_0^0 + \frac{v}{3}\frac{\partial f_l}{\partial v}\left(I_2^0 + J_{-1}^0\right)\right]$$

and

$$C_{ee}^{a}(f_0, f_l)$$

$$= \nu_{ee}\left\{ 4\pi v^3 f_l f_0 + \frac{l(l+1)}{6} f_l\left(-3I_0^0 + I_2^0 - 2J_{-1}^0\right)\right.$$

$$+\frac{v^2}{2(2l+1)}\frac{\partial^2 f_0}{\partial v^2}\left[\frac{(l+2)(l+1)}{2l+3}\left(I_{l+2}^l + J_{-1-l}^l\right)\right.$$

$$\left.-\frac{l(l-1)}{2l-1}\left(I_l^l + J_{1-l}^l\right)\right]$$

$$\left.+\frac{v}{2(2l+1)}\frac{\partial f_0}{\partial v}\left[-\frac{(l+1)(l+2)}{(2l+3)} I_{l+2}^l - \frac{\left(l^2-l-4\right)}{(2l+3)} J_{-1-l}^l\right.\right.$$

$$\left.\left.+\frac{\left(l^2+3l-2\right)}{(2l-1)} + \frac{l(l-1)}{(2l-1)} J_{1-l}^l\right]\right\},$$

where

$$I_m^n = \frac{4\pi}{v^m}\int_0^v f_n w^{2+m} dw,\ J_m^n = \frac{4\pi}{v^m}\int_v^\infty f_n w^{2+m} dw$$

and $\nu_{ee}(v) = 4\pi N_e\left(e^2/m_e\right)^2 \ln\Lambda / v^3$ is the velocity-dependent *e-e* collision frequency. Here we note that $C_{ee}^{i}(f_0, f_0) = C_{ee}^{a}(f_0, f_0)$.

REFERENCES

1. E. M. Epperlein, R. W. Short, and A. Simon, Phys. Rev. Lett. **69**, 1765 (1992).
2. M. N. Rosenbluth, W. M. MacDonald, and D. L. Judd, Phys. Rev. **107**, 1 (1957).
3. C. J. Randall, Phys. Fluids **25**, 2231 (1982).
4. M. D. Tracy, E. A. Williams, K. G. Estabrook, J. S. DeGroot, and S. M. Cameron, Phys. Fluids B **5**, 1430 (1993).
5. L. Spitzer, Jr. and R. Härm, Phys. Rev. **89**, 977 (1953).
6. E. M. Epperlein and R. W. Short, Phys. Fluids B **3**, 3092 (1991).
7. G. W. Hammett and F. W. Perkins, Phys. Rev. Lett. **64**, 3019 (1990).
8. Z. Chang and J. D. Callen, Phys. Fluids B **4**, 1167 (1992); Phys. Fluids B **4**, 1182 (1992)
9. E. M. Epperlein, Phys. Rev. Lett. **65**, 2145 (1990); E. M. Epperlein and R. W. Short, Phys. Fluids B **4**, 2211 (1992).
10. I. P. Shkarofsky, T. W. Johnston, and M. A. Bachynski, *The Particle Kinetics of Plasmas* (Addison-Wesley, Reading, MA, 1966); T. W. Johnston, J. Math. Phys. **7**, 1453 (1966).
11. E. M. Epperlein, *Laser and Particle Beams* **12**, 257 (1994).
12. J. S. Chang and G. Cooper, J. Comput. Phys. **6**, 1 (1970).
13. R. J. Mason, J. Comput. Phys. **41**, 233 (1981).
14. A. R. Bell, Phys. Fluids **26**, 279 (1983).
15. R. W. Short and E. M. Epperlein, Phys. Rev. Lett. **68**, 3307 (1992); H. A. Rose and D. F. DuBois, Phys. Fluids B **4**, 1394 (1992); E. M. Epperlein and R. W. Short, Phys. Fluids B **4**, 4190 (1992); H. A. Rose and D. F. DuBois, Phys. Fluids B **4**, 4192 (1992).
16. A. B. Langdon, Phys. Rev. Lett. **44**, 575 (1980).

Particle-in-Cell Code Simulations of the Interaction of Gaussian Ultrashort Laser Pulses with Targets of Varying Initial Scale Lengths

Introduction

Since the advent of ultrashort laser pulses[1] there has been interest in the interaction of such pulses with solid targets. Several new modes of laser-plasma interaction at high intensities ($I\lambda^2 > 10^{16}$ W/cm^2 μm^2) have been identified, the most important being "vacuum heating,"[2] which dominates over resonance absorption when scale lengths are very short. These new absorption mechanisms, as well as nonlinear resonance absorption (wave breaking), are usually studied with a PIC (particle-in-cell) code. In one series of published results from PIC simulations, the interaction of p-polarized light with a plasma over a wide range of irradiances and scale lengths is described.[3] The range covered in these simulations included the transition from resonance absorption to vacuum heating. The simulations were carried out for a constant pulse, and few details were provided on the behavior of the fields and of the plasma. Other published results of PIC simulations[4] have concentrated on the effect of the radiation pressure on the motion of the ions at intensities in excess of 10^{18} W/cm^2 μm^2. Above this intensity the interaction enters another regime in which relativistic effects become important. We will not deal with the relativistic regime in this article. Incidentally, Vlasov codes have also recently been developed to study these nonlinear absorption mechanisms.[5]

Here, we present simulations in which a 100-fs Gaussian pulse interacts with preformed plasmas of varying scale lengths. These calculations simulate many of the actual experimental conditions in which laser pulses are preceded by either a long ASE pulse or a pedestal due to imperfect pulse expansion and recompression in chirp-pulsed amplification schemes. These simulations, carried out at an irradiance of 10^{16} W/cm^2 μm^2, near the irradiances reached in many experiments, include ion motion. A set of simulations was carried out with electron-ion collisions included. We find that observables like the absorption fraction, the fast-electron and fast-ion energy, and the production of harmonics depend strongly on the scale length of the initial profile.

The calculations were carried out with the 1 1/2-D relativistic PIC code *EUTERPE*.[6] Electron scattering due to collisions with the ions is included using a Monte Carlo rotator at the end of each time step.[7] To treat p-polarized oblique incidence, simulations are done by transforming to a reference frame moving in the transverse direction with velocity $v_d = c \sin\theta$, where θ is the angle of incidence.[3] This method suffers from two limitations: First, it does not model rippling of the critical surface, which becomes significant above 10^{18} W/cm^2 μm^2 and leads to a more complex angular distribution of the incident laser light. Second, at large angles, the maximum density, which transforms as $n_e/n_c = \gamma^{-3}(n_e/n_c)'$, where

$$\gamma = \left[1 - \left(\frac{v_d}{c}\right)^2\right]^{-1/2} = \sec\theta,$$

becomes very large, which forces the time step to be very small and the number of particles to be large in order to obtain reasonable results. Most of the runs were done with 50,000 particles and with a mesh size of 500–1000 grid points. The absorption fraction, defined as the internal energy in the plasma divided by the cumulative input energy, is calculated in two ways: In the first way, the internal energy in the plasma is obtained as the sum of the kinetic energy over all the particles minus the initial internal energy of the plasma. In the second way, the internal energy is calculated by subtracting the electromagnetic energy in the box from the time-integrated Poynting vector at the left (input) boundary. Ideally, these two methods should yield the same absorption fraction.

Transition from Resonance Absorption to Vacuum Heating

In vacuum heating,[2] the longitudinal electric field does not penetrate into the plasma because of the steep density gradient but reaches its maximum value in the vacuum near the plasma

boundary. When electrons penetrate into the vacuum with the right timing, they are accelerated outward by the large longitudinal electric field. They are then turned around by the oscillating field and the electrostatic potential and penetrate into the solid with velocity $v \approx v_{osc}$ where they deposit their energy. Vacuum heating becomes the dominant absorption mechanism when the oscillatory orbit of the electrons in the laser field becomes large compared to the scale length. This can occur for either very steep density gradient or very large laser intensity.

We will discuss the transition from resonance absorption to vacuum heating for the nonrelativistic intensity regime, $I\lambda^2 < 10^{18}$ W/cm^2 μm^2. We are especially interested in finding "observables," experimental and numerical, that lead to the definition of the regime. Experimental observables include the absorption fraction, the fast electron spectrum (deduced from hard x rays, K_α emission, and electron spectrometry), and the harmonic emission. Numerical observables include the experimental observables, the electron phase space, the electron trajectories, and the longitudinal electric field profile. Velocities are normalized to the velocity of light, positions to c/ω_0, and time to ω_0^{-1}, where ω_0 is the laser frequency.

The difference between resonance absorption and vacuum heating can be readily seen by plotting the electron trajectories (orbits) for two extreme scale lengths: $L/\lambda = 1$ and $L/\lambda = 0.001$, where λ is the laser wavelength. In Fig. 58.15(a), in which are plotted the trajectories of selected electrons (every 1000th) near the critical surface for a constant irradiance of 5×10^{16} W/cm^2 μm^2, an incident angle of 30°, and $L/\lambda = 1$, we observe the growth of the electron plasma wave until wave breaking starts at about 60 ω_0^{-1}. Wave breaking tends to occur in a random fashion in the resonance region when electron orbits cross. The electron trajectories for vacuum heating, shown in Fig. 58.15(b), show a very different behavior. In this case the conditions are a constant irradiance of 10^{18} W/cm^2 μm^2, an incident angle of 30°, and $L/\lambda = 0.001$. Starting with the first period of the laser, and for each successive period ($T = 2\pi$), electrons are pulled out into the vacuum and returned to the solid with velocities near v_{osc}. Interesting structures can also be observed: the successive long and short orbits into the vacuum every two laser periods and the smaller orbits with a "period" of one-half a laser period.

The difference in the longitudinal electric field profile for the two cases is shown in Fig. 58.16 along with the electron density profile. The electric field shown here, and in all subsequent graphs, is the oscillating field averaged over a period of the laser field normalized to the incident longitudinal electric field. In the resonance absorption case [Fig. 58.16(a)] the resonant field at the critical surface is large compared to the incident field and creates a "hole" in the density profile due to the ponderomotive force. In the vacuum heating case,

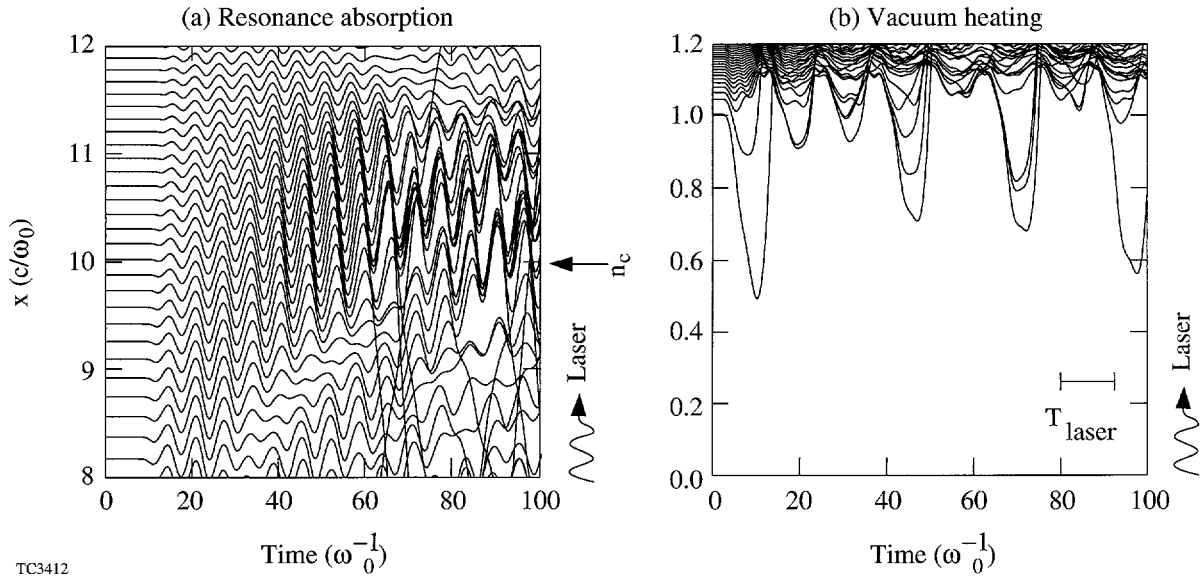

Figure 58.15
Electron trajectories for the two regimes: (a) resonance absorption; (b) vacuum heating. In both cases the laser is incident from the bottom. Only a sample of all the electrons is shown. Conditions are (a) $I\lambda^2 = 10^{16}$ W/cm^2 μm^2 and p-polarized light incident at 30°, $L/\lambda = 1.0$ linear, cold plasma without collisions, and stationary ions; (b) $I\lambda^2 = 10^{18}$ W/cm^2 μm^2 and p-polarized light incident at 30°, $L/\lambda = 0.001$ linear, cold plasma without collisions, and stationary ions.

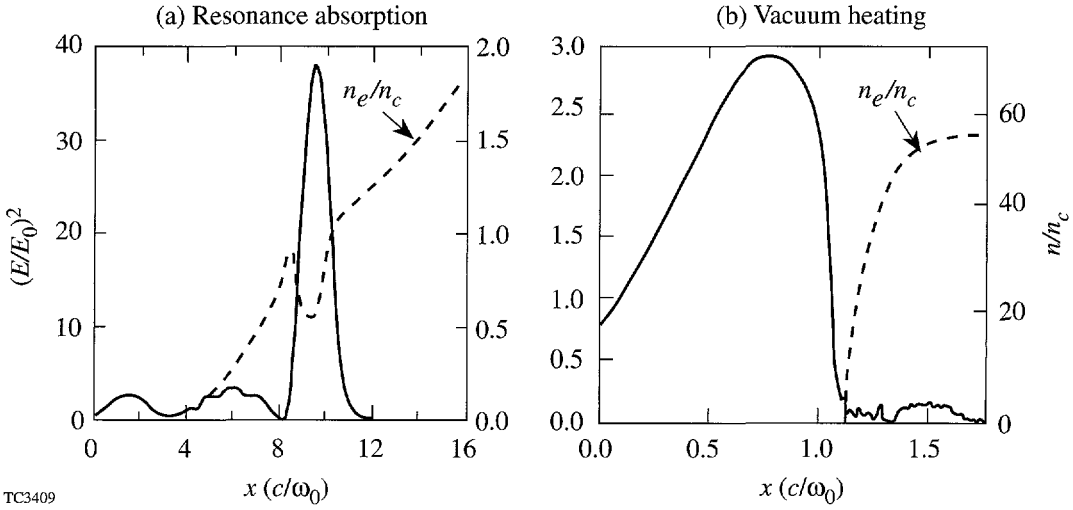

Figure 58.16
Period-averaged oscillating longitudinal electric field and electron density profile for the two cases in Fig. 58.15. The electric field is normalized to the incident longitudinal field.

the field does not penetrate into the plasma and displays the swelling expected near the surface of a conductor. The peak value of the field in the vacuum heating case is much lower than that in the resonance absorption case. As will be discussed below, this leads to much lower hot-electron energies for the same irradiance.

The transition from one regime to the other is complex, yet it is necessary to understand the changes that are occurring during this transition because many experiments are carried out under these conditions. The most straightforward way to study this transition is to vary the ion density profile, holding the irradiance fixed. In this way we avoid the added complexity that would arise from changes in such quantities as the absorption fraction and the electron maximum energy due to changes in the irradiance.

Interaction with Gaussian Pulses

Most, if not all, PIC simulations are carried out with a temporal irradiance characterized by a rising portion followed by a constant intensity up to some time limited by either computer time, by "numerical heating" due to the statistical nature of the problem, or by numerical instabilities in the code. These irradiation conditions approximate reasonably well those at the peak of pulses with pulse duration larger than tens of picoseconds; this may not be the case in ultrashort pulse laser interactions. With the advent of lasers with pulse duration of about 100 fs, it is now possible with present day computing power to simulate the interaction of an entire pulse with a plasma. Of course, PIC codes cannot simulate realistically high-density plasma in which electrons are described by Thomas-Fermi statistics and ions by short-range interaction. Atomic physics processes such as ionization and radiation are not included in PIC codes, although some effort is being made to include ionization.[7]

In this section we present the results of the study of the interaction of a 100-fs Gaussian pulse (full-width at half-maximum) with plasmas of varying initial electron and ion density scale lengths. The initial scale length is varied in order to simulate many present day experiments in which a prepulse creates a plasma in front of the solid surface before the arrival of the main pulse. Simulations with a Gaussian pulse can model more realistically than constant pulses the production of fast ions and the effect of the temporal variation of the irradiance on the absorption fraction, on the production of fast electrons and ions and of harmonics, and on the distortion of the density profiles due to the ponderomotive force. The simulations include ion motion and, in some cases, electron-ion collisions. In the collisionless case the ions have a charge of unity and a mass of 3600 m_e. In the collisional case, the simulations are specialized to fully ionized aluminum ($Z = 13$) and a laser wavelength of 620 nm [the wavelength of a CPM (chirped pulse modulated) dye laser]. The irradiance is started and stopped at 1% of the peak power, taken to be 10^{16} W/cm^2 μm^2. The simulations were carried out at a 30° angle of incidence and included 50,000 particles.

Four linear density profiles were used: $L/\lambda = 0.001$, 0.01, 0.1, 1.0. The following experimental diagnostics are displayed

for these four cases: the energy spectrum of the electrons that entered the solid (those reaching the high-density boundary), the energy spectrum of all the ions at the end of the pulse, and the cumulative absorption fraction as a function of time. The effect of the initial density profile on the electric field near or in the plasma and on the ion density profile at the end of the pulse will also be discussed.

We first discuss changes in the longitudinal electric field profile due to variations in the initial scale length, as displayed in Fig. 58.17. At the two extremes, $L/\lambda = 0.001$ and $L/\lambda = 1.0$, the electric field shows the behavior expected from vacuum heating and resonant absorption respectively. As the scale length is decreased from $L/\lambda = 1.0$, we observe the gradual change from the the single resonant peak to the wave swelling outside the steep plasma profile. Conditions at $L/\lambda = 0.1$ are complex: the resonant field is split and a resonance at $2\ n_c$ can be observed. At that scale length the resonant peak occurs near the edge of the plasma: the width of the resonant region is equal to or larger than the scale length and the orbits of the thermal electrons in that region can extend into the vacuum. As the gradient steepens to $L/\lambda = 0.01$, some field swelling in the vacuum interfaces can now be observed along with a resonance peak at the edge of the plasma and small multi-resonances in the overdense plasma. At the steepest gradient the field is confined to the vacuum and all resonances have disappeared.

The effect of the ponderomotive force due to the electromagnetic field on the ion density profile is shown in Fig. 58.18 at a time near the end of the pulse. The dashed line indicates the initial density profile. In the shortest scale length case, $L/\lambda = 0.001$, the pressure from the reflected laser beam is not large enough to move back the density profile during the pulse duration. Ions below the critical surface have expanded into the vacuum due to two effects: the pressure of the heated thermal electrons that have expanded into the vacuum and the electrostatic potential from electrons pulled into the vacuum by the vacuum heating absorption process. At such a short scale length the density gradient at the critical surface is not steepened, but lengthened due to the expansion. The medium-scale-length cases, $L/\lambda = 0.01$ and 0.1, show a slight deformation of the ion density profile. This effect is caused by the ponderomotive pressure of the resonant field situated at the edge of the plasma, not by the pressure of the reflected

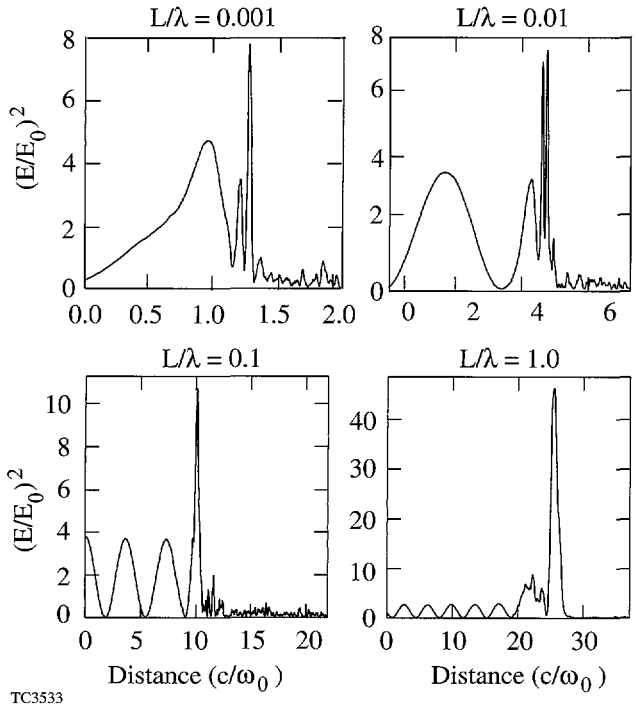

Figure 58.17
Period-averaged oscillating longitudinal electric field in the transition from resonance absorption to vacuum heating at the peak of the Gaussian pulse (400 ω_0^{-1}). Laser conditions are $I\lambda^2 = 10^{16}$ W/cm^2 μm^2 and p-polarized light incident at 30°; the initial density profiles are linear, and collisions are not included.

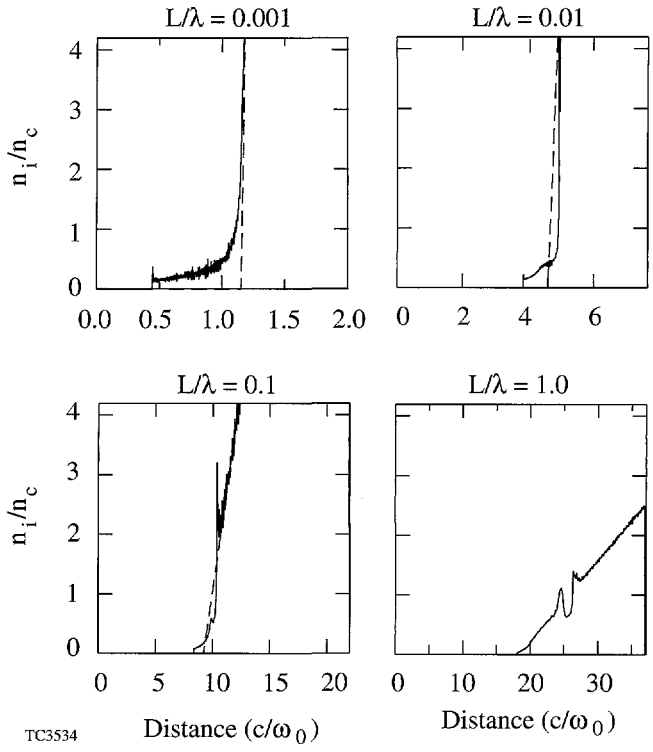

Figure 58.18
Ion density profile at the end of the pulse for the conditions in Fig. 58.17. The dashed curve is the initial density profile.

light. At the peak of the pulse the profile steepening is slight and should not affect the resonant absorption process. At the end of the pulse the profile for the case $L/\lambda = 0.1$ was steepened to $L/\lambda = 0.025$. Profile modification is more evident in the long-scale-length case because the resonant field is larger than at shorter scale lengths. At the peak of the pulse a small plateau is created, and the local scale length at the critical surface is about 0.5 λ. By the end of the pulse a hole about 0.5 n_c deep has been dug into the ion density profile by the resonant electric field.

One of observables strongly affected by variations in the scale length is the harmonic emission, plotted in Fig. 58.19. For the case $L/\lambda = 1$ we observe the harmonic emission expected from resonance absorption: an exponentially decreasing series of harmonics. For $L/\lambda = 0.1$, the harmonic series is very noisy and is cut off above $n = 2$. The case $L/\lambda = 0.01$ is very interesting in that the emission occurs at half-harmonics: 3/2 and 5/2; we have found no explanation for this behavior. At the steepest gradient, very weak harmonics are observed at $n = 3$ and 4, but none at $n = 2$. The low harmonic level is probably due to the low absorption efficiency of the vacuum heating mechanism at this intensity. At higher intensities the entire range of harmonics can be observed.

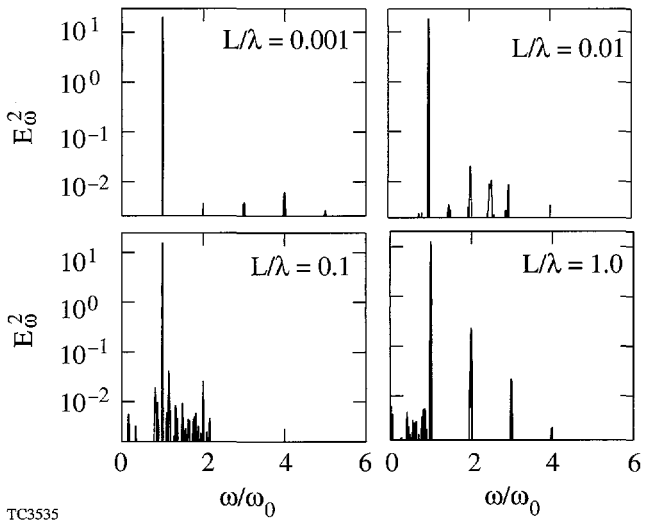

Figure 58.19
Power spectrum of the reflected light for the conditions in Fig. 58.17. Note the half-harmonics produced in the case $L/\lambda = 0.01$.

The spectra of the electrons that have left the computational box at the high-density end for the four cases are shown in Fig. 58.20. These are electrons that create observable bremsstrahlung hard x rays and K_α emission from the solid target. The maximum energy of the electrons decreases with scale length, in agreement with the decreasing peak values of the electric field observed in Fig. 58.17. It is not straightforward to obtain a temperature from the spectra because the electron distribution is not Maxwellian, especially for the short-scale-length cases. One reason is that vacuum heating tends to produce beams of electrons rather than a distribution; the other reason is that the spectra are cumulative over a range of intensity, therefore over a range of temperatures. For $L/\lambda = 0.1$ and $L/\lambda = 1.0$, the distributions are nearly Maxwellian with temperatures of 22 keV and 35 keV respectively. For $L/\lambda = 0.001$ and $L/\lambda = 0.01$ the slopes of the main body of the distribution yield 6 keV and 10 keV, respectively.

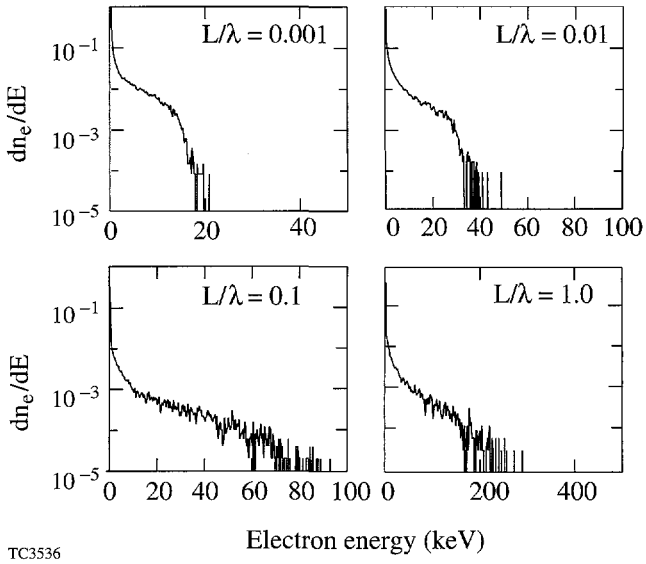

Figure 58.20
Cumulative distribution of the electrons entering the solid (leaving at the right-hand-side boundary) for the conditions in Fig. 58.17.

The ions spectra for the four cases, another experimental diagnostic, are shown in Fig. 58.21. The spectra contain the main body of the ion distribution at low energy and the distribution of the fast ions accelerated by the hot electrons. From $L/\lambda = 0.001$ to $L/\lambda = 0.01$, as expected the peak ion energy increases with scale length as did the hot-electron distribution. The increase is small between $L/\lambda = 0.01$ and $L/\lambda = 0.1$, and the peak energy is actually lower for $L/\lambda = 1$ than for $L/\lambda = 0.1$, despite the fact that the fast-electron energy increases sharply in that range of scale length. Two effects may be responsible for the scaling of the fastest ion energy: not enough time to accelerate the ions to their maximum velocity because of the short pulse duration; the

accelerating electrostatic potential, given roughly by T_h/L, where T_h is the hot-electron temperature, is lower in the long-scale-length cases.

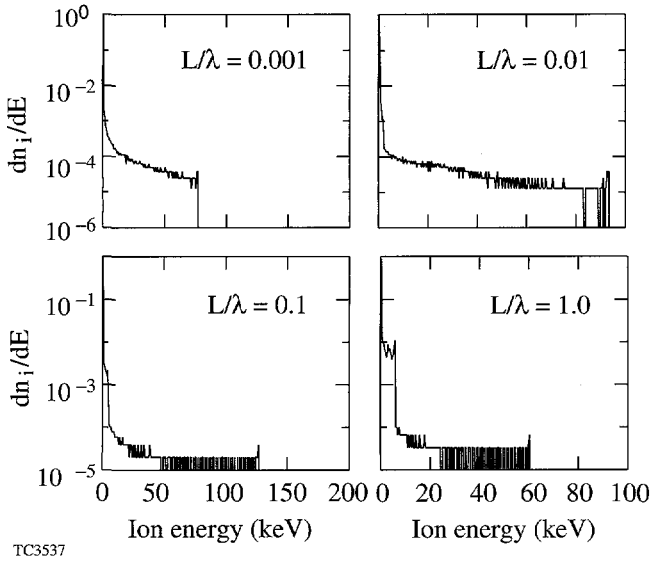

Figure 58.21
Total ion spectrum at the end of the pulse for the cases in Fig. 58.17. The energetic ions are the fast ions accelerated into the vacuum.

The cumulative absorption fraction as a function of time is plotted in Fig. 58.22 for the four cases. The peak of the pulse is at 400 ω_0^{-1}. In these graphs, the absorption fraction is defined as the time-integrated Poynting vector at the vacuum boundary minus the electromagnetic energy in the computing box, divided by the time-integrated input laser energy at the vacuum boundary. The "hash" in the line is due to the time-varying value of the electromagnetic energy in the box. The final absorption fraction is low at the short scale lengths (about 10%) and increases with scale length as the resonance absorption regime becomes dominant. Adding collisions ($Z = 13$) has little effect on these results: the absorption fraction is slightly larger early in the pulse but is slightly lower near the peak of the pulse because collisions decrease slightly the resonant field. At this intensity vacuum heating is a very inefficient absorption process.

The results of the simulations are summarized in Fig. 58.23 where the absorption fraction and the maximum electron and ion energy are plotted as a function of the scale length. The absorption remains very low for $L/\lambda < 0.01$ and increases for increasing scale length to the large values associated with resonance absorption. The electron peak energy scales roughly as $(L/\lambda)^{0.4}$, except through the vacuum heating range where it would be expected to depend only on the laser intensity through v_{osc}. These results, and the behavior of the longitudinal electric field, point to the existence of three regions as discussed in Ref. 3: the vacuum heating region below $L/\lambda = 0.01$; a region in which the oscillatory orbit of the electrons is about the distance between the critical surface and the vacuum/plasma interface; and a resonance absorption region above $L/\lambda = 0.03$, where the resonance occurs inside the plasma and the oscillating electrons never reach the vacuum. The second region is very complex. The resonance structure of the electric field splits for some values of L/λ, while harmonic resonances appear in the overdense plasma. A detailed study of the electron orbits shows that the electrons near the plasma/vacuum interface can be accelerated into the vacuum without undergoing wave breaking, while electrons slightly deeper in the plasma, but still in the resonance region, are accelerated by wave breaking. The different regimes can be seen as plateaus in the absorption fraction separated by transition regions. Similar results, but slightly shifted to higher scale lengths, were obtained for an irradiance of 10^{17} W/cm^2 μm^2: The transition to vacuum heating occurs now for $L/\lambda \approx 0.03$ as compared to $L/\lambda \approx 0.01$ for the lower irradiance case.

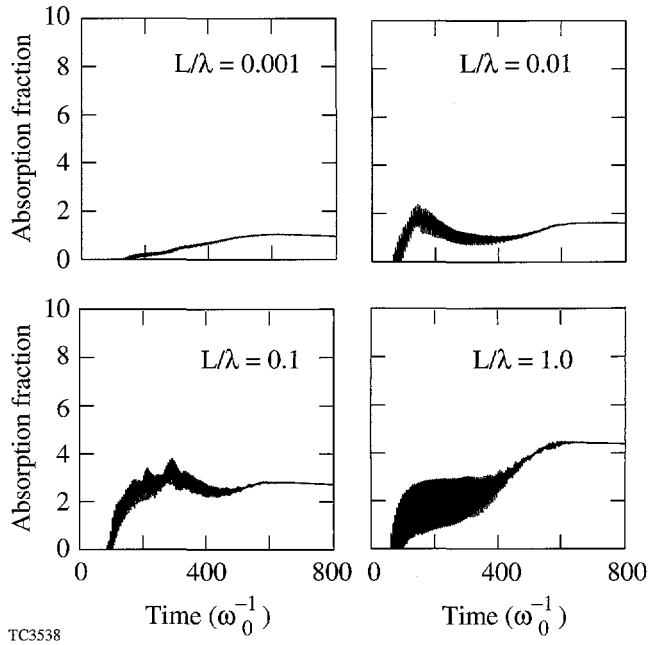

Figure 58.22
Cumulative absorption fractions for the conditions in Fig. 58.17. The "hash" in the line is due to the time-varying value of the electromagnetic energy in the box.

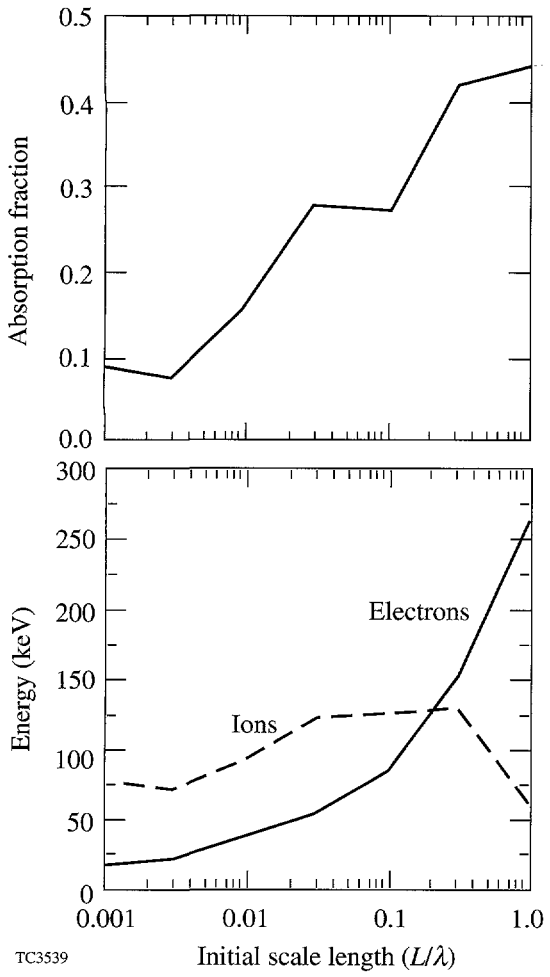

Figure 58.23
Summary of the results from the simulations of the transition from vacuum heating to resonant absorption for conditions in Fig. 58.17.

Conclusions

The transition from the resonance absorption regime to the vacuum heating regime in short-pulse laser-plasma interaction has been studied using the 1 1/2-D PIC code *EUTERPE*. Laser conditions were a 100-fs Gaussian pulse with $I\lambda^2 = 10^{16}$ W/cm^2 μm^2 and p-polarized light incident at 30°. The transition was observed by varying the density scale length over the range $L/\lambda = 0.001$ to 1.0.

We observed that vacuum heating occurred for $L/\lambda < 0.01$. This is a very steep scale length that can be obtained only with very short pulses (about 100 fs) in the absence of any prepulse energy on the target. For $0.3 > L/\lambda > 0.01$ the resonant region remains at the edge of the plasma. In this transition regime the behavior of the resonant field becomes complex as the orbits of the resonant electron extend into the vacuum. For $L/\lambda > 0.3$, the resonance region moves into the plasma, and the "classic" resonance absorption regime is recovered. The peak resonant longitudinal electric field, the peak electron energy, and the absorption fraction increase with increasing scale length. Harmonic production above the second harmonic disappears in the transition regime. Adding collisions with $Z = 13$ has little effect on these results.

ACKNOWLEDGMENT

This work was supported by the Laboratoire pour l'Utilisation des Lasers Intenses and the Laboratoire de Physique des Milieux Ionisés, Ecole Polytechnique, Palaiseau, France and by the Centre d'Etude de Limeil-Valenton du Commissariat à l'Energie Atomique, Villeneuve-St-Georges, France. This work was also supported by the U.S. Department of Energy Office of Inertial Confinement Fusion under Cooperative Agreement No. DE-FC03-92SF19460, the University of Rochester, and the New York State Energy Research and Development Authority. The support of DOE does not constitute an endorsement by DOE of the views expressed in this article.

REFERENCES

1. P. Main and G. Mourou, Opt. Lett. **13**, 467 (1988).
2. F. Brunel, Phys. Rev. Lett. **59**, 52 (1987).
3. P. Gibbon and A. R. Bell, Phys. Rev. Lett. **68**, 1535 (1992).
4. For example, J. Denavit, Phys. Rev. Lett. **69**, 3052 (1992).
5. H. Rhul and P. Mulser, presented at the *23rd Annual Anomalous Absorption Conference*, Wintergreen, VA, 21–25 June 1993, paper 2O3.
6. G. Bonnaud and G. Reisse, Nucl. Fusion **26**, 633 (1986).
7. J. M. Wallace *et al.*, Phys. Fluids **3**, 2337 (1991).

Characterization of Thick Cryogenic Fuel Layers: Compensation for the Lens Effect Using Convergent Beam Interferometry

Historically, the fuel content and fuel-layer uniformity of cryogenic targets have been characterized interferometrically using plane-wave illumination.[1–6] This technique has the sensitivity necessary to detect a deviation from sphericity of the fuel layer's inside surface as small as a few percent of its total thickness. In the past at LLE, the targets examined were typically 250-μm-diam glass capsules with wall thicknesses of a few micrometers that were filled with enough fuel to produce a condensed fuel layer less than 10 μm in thickness. Future OMEGA Upgrade cryogenic targets will consist of polymer capsules several tens of micrometers thick with diameters ranging from 700–1100 μm. These will be filled with condensed D_2 or DT fuel with a thickness of up to 100 μm.

A capsule with a thick cryogenic layer condensed on its interior behaves as a strong negative lens, which has several adverse effects on its interferogram when created with plane-wave illumination. Computer simulations of typical interferograms are shown in Fig. 58.24. The highly divergent and spherically aberrated wavefront created by the target cannot be effectively collected and imaged using optics with convenient numerical apertures, resulting in loss of information near the perimeter of the target's image. In addition, when this highly curved wavefront interferes with a planar reference wavefront, an interferogram with a fringe spatial frequency that increases radially to very high values near the perimeter of the target's image is produced. Since the phase, and therefore

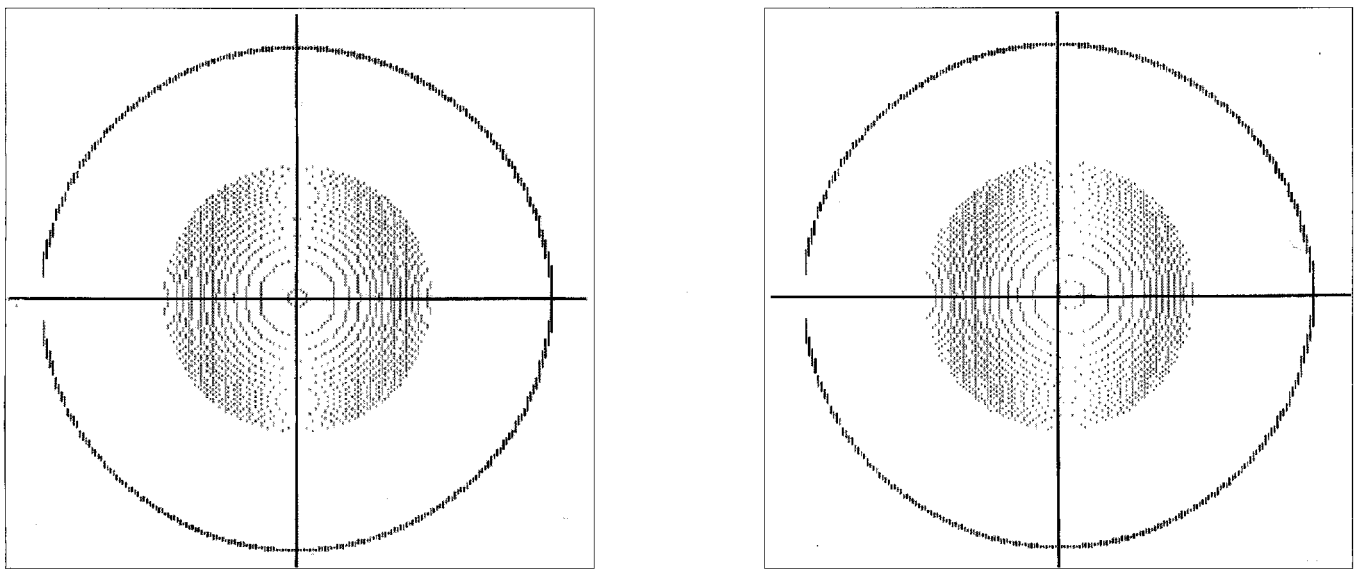

T1083

Figure 58.24
Computer-generated interferograms of a 10-μm-thick polystyrene capsule with a diameter of 1120 μm that contains 100 μm of condensed fuel. These were created with the assumptions that both the object and reference beams consisted of planar wavefronts with a 514-nm wavelength, and *f*/6 optics were used to image the target. All of the surfaces in (a) are perfectly concentric with one another, whereas (b) displays a 5% fuel nonconcentricity, i.e., the center of the spherical inner surface of the condensed fuel layer has been displaced to the right in the figure by 5% of its total thickness. Obviously, a 5% nonconcentricity can be easily detected, but higher-order nonuniformities are much more difficult to detect due to the very high fringe frequency. In addition, information regarding the state of the fuel near the perimeter of the target's image has been lost due to refraction of the object beam outside of the imaging optics' finite collection aperture.

thickness, resolution resulting from the analysis of an interferogram is inversely proportional to the number of detector elements per fringe, the phase sensitivity is reduced dramatically when the fringe frequency approaches the Nyquist limit of the detector. As the fringe frequency nears the frequency of pixels in the CCD array, aliasing occurs and the fringes become unresolved. Evidence of this is the Moiré patterns exhibited in the theoretical interferograms of Fig. 58.24, where the fringes are beating with their array locations instead of CCD detector elements.

There are several requirements of a cryogenic-target interferometer that are applicable to OMEGA Upgrade target experiments. First, it should be sensitive to high-order fuel nonuniformities, not only nonconcentricity of the inner and outer fuel-layer surfaces. It should also be suitable for a wide range of capsule/fuel-layer dimensions. It should be simple to implement, optically stable, and amenable to computerized wavefront-measuring techniques (i.e., phase-shifting interferometry) to obtain the most accurate quantitative information possible. Finally, it should be compact and versatile enough to be adapted to *in-situ* fuel-layer characterization both in laboratory and target chamber experiments.

To realize these requirements, an interferometer has been developed that illuminates the target with a wavefront that is convergent to a point near the target's rear focal point, thus causing a nearly planar wavefront to emerge from it. A comparison between the emergent wavefront with plane-wave and convergent-beam illumination is shown in Fig. 58.25. With convergent-beam illumination, when the transmitted wavefront interferes with a planar reference wavefront, a low-fringe-frequency interferogram of the target is produced that can be analyzed with a better phase resolution.

When imaged on axis, the wavefront emerging from the target with plane-wave illumination departs from a plane with two major components: a diverging spherical element designated as x_1 in Fig. 58.26 and a spherical aberration contribution designated as x_2. In Fig. 58.26, f_{tgt} is the effective focal length of the target as measured from the capsule's equatorial plane (i.e., the y-axis), examples of which are given as a function of fuel-layer thickness for a 10-μm-thick polystyrene capsule in Fig. 58.27. For $(r/f_{tgt})^2 << 1$, where r is the inner radius of the condensed fuel layer, x_1 can be approximated as parabolic: $x_1 = \left(r^2/2f_{tgt}\right)y^2$, while x_2 depends on y to the fourth power as $x_2 = W_{040}y^4$. The optical system collects and images this transmitted wavefront and the capsule. Since the perimeter of the target's image is normally in focus in an interferogram, the emergent wavefront is imaged as if projected back into the equatorial plane of the target; hence y is the normalized pupil function and is given by the ratio of the distance from the center of the target's image to the inner radius of the fuel layer r. Therefore, if x_1 is eliminated by illuminating the target with a wavefront converging to a point behind it, a distance f_{tgt} away from its center, only the spherically aberrant component of the transmitted wavefront remains. This flattens the wavefront emerging from the target, with only the curvature due to the spherical aberration term left. By using convergent-beam illumination, not only is more light collected from regions near the perimeter of the target, but the interferogram consists of fewer rings that are concentrated near the perimeter of the target's image, decreasing the maximum fringe frequency to a value well below the Nyquist limit of the detector array.

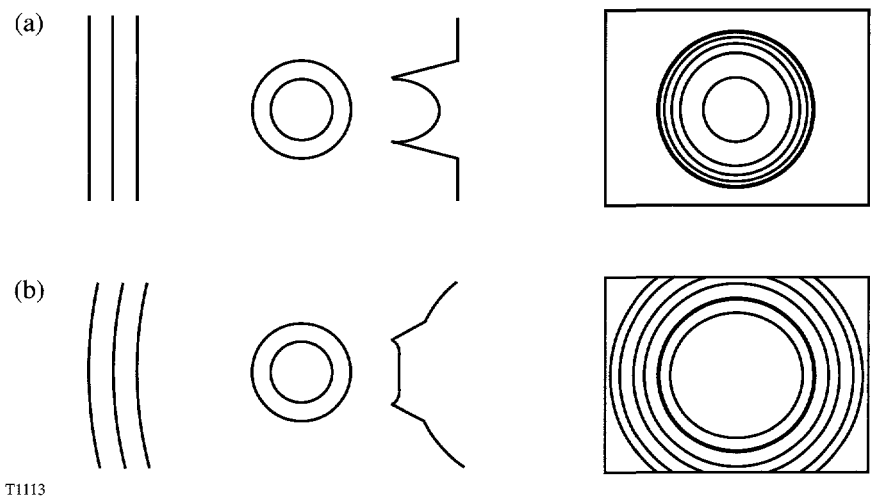

Figure 58.25
An illustration of the wavefront that emerges from a capsule filled with a thick condensed fuel layer when both plane-wave and convergent-beam illumination are used, along with hypothetical interferograms that are produced when the transmitted wavefront interferes with a planar reference wavefront. It is apparent in (a) that a relatively small portion of the highly divergent wavefront can be effectively collected and imaged. However, in (b), not only is the transmitted wavefront flattened, but the light surrounding the capsule can also be readily collected and imaged.

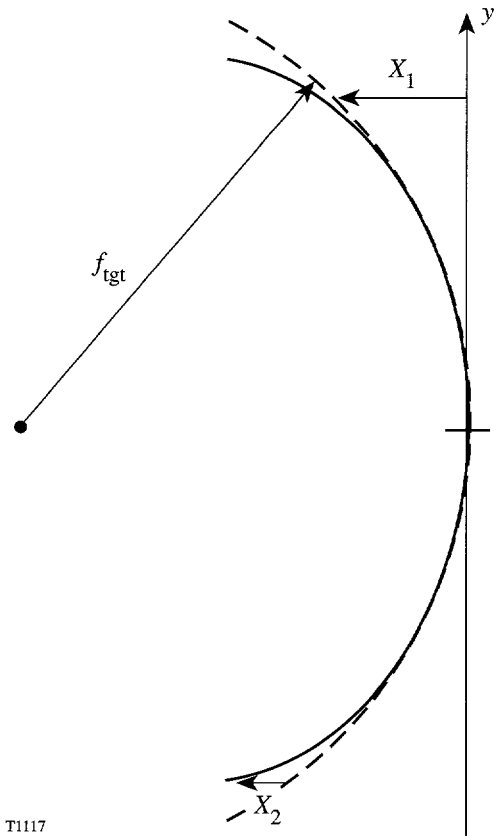

Figure 58.26
An illustration of the wavefront emerging from a cryogenic target when it is illuminated with a planar wavefront. The emergent wavefront is normally imaged as if projected back into the equatorial plane of the target, making the y-axis lie along a major diameter of the spherical inner surface of the condensed fuel layer. The transmitted wavefront contains two major components: a diverging spherical constituent designated as x_1 and a spherical aberration term designated as x_2, and f_{tgt} is the effective focal length of the target.

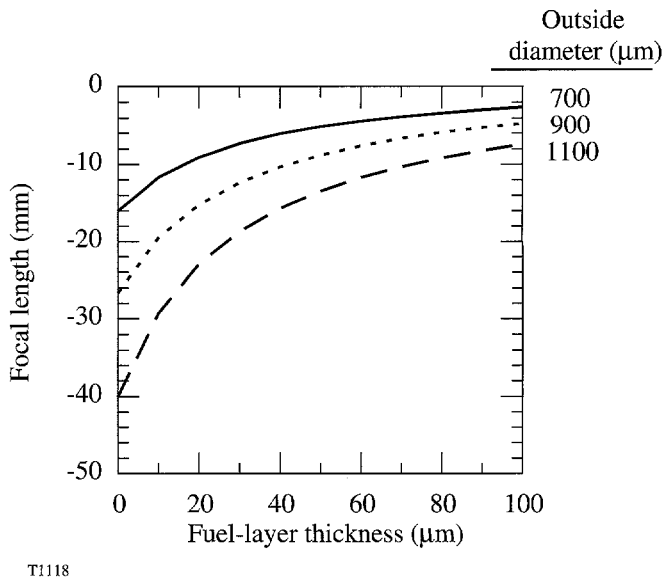

Figure 58.27
The effective focal length f_{tgt} of cryogenic targets as a function of condensed fuel-layer thickness. A 10-μm-thick polystyrene capsule was assumed for the various outside diameters shown. Paraxial rays were traced through hypothetical targets to find their focal lengths, which are measured from their equatorial plane.

The values for $r^2/2f_{tgt}$ and W_{040} in Fig. 58.28 were calculated by tracing paraxial rays through a hypothetical cryogenic target to find its focal length and applying third-order aberration theory to determine the spherical aberration component. The values shown are for the emerging wavefront projected back into the equatorial plane of the target and denote the maximum values these quantities take, i.e., for $y = 1$. The number of fringes present in an interferogram between the center of a target's image and a point along its radius can readily be determined from Fig. 58.28 by summing x_1 and x_2 for a given y and dividing by the wavelength of the light used to create it. For example, a 10-μm-thick polystyrene capsule with a diameter of 1100 μm containing 100 μm of condensed fuel would have 39 fringes between its center and the inside of the fuel layer when planar wavefronts with a 0.5-μm wavelength are utilized to create its interferogram. Eliminating the spherical component of the emerging wavefront by illuminating the same target with a beam of light converging to its focal point 6.8 μm behind it produces only 13 fringes, which are mainly concentrated toward the perimeter of the image. Hence, a greater sensitivity to nonconcentricities and higher-order nonuniformities in the fuel layer can be achieved.

The optical system used to create an interferogram of a cryogenic target with convergent-beam illumination is shown in Fig. 58.29. (The properties of the light sources and components of the initial beamsplitting system shown in Fig. 58.30 will be discussed in detail later since their use will become more apparent following a description of the imaging system.) The light is delivered to the interferometer using two single-mode optical fibers, one for the object arm and another for the reference arm. The optical fibers serve several purposes. They vibrationally and optically isolate the laser source from the structural and optical components of the interferometer. In addition, the optical fiber's flexibility makes relative placement of the light source and the interferometer unrestrictive. Transmitting only the lowest-order mode, the optical fibers also serve to spatially filter the light emitted by the laser source.

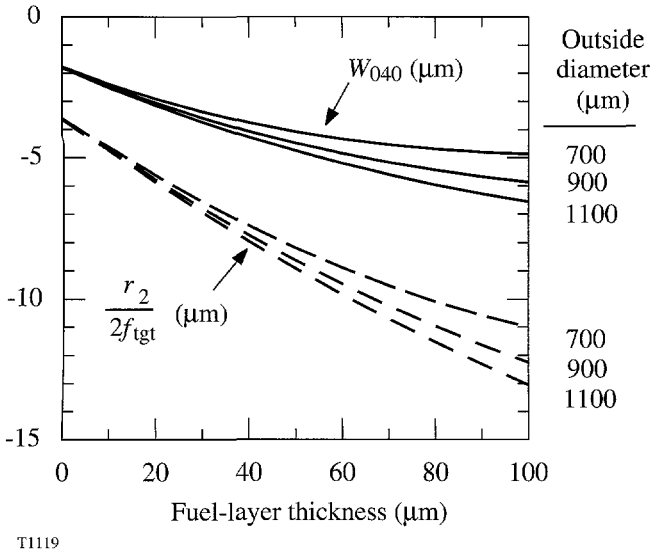

Figure 58.28
The values for $r^2/2f_{tgt}$ and W_{040} for cryogenic targets as a function of condensed fuel-layer thickness. Again a 10-μm-thick polystyrene capsule was assumed for the outside diameters shown. Third-order aberration theory was used to determine W_{040}. The values shown are for the emerging wavefront projected back into the equatorial plane of the target and denote the maximum values these quantities take, i.e., for $y = 1$.

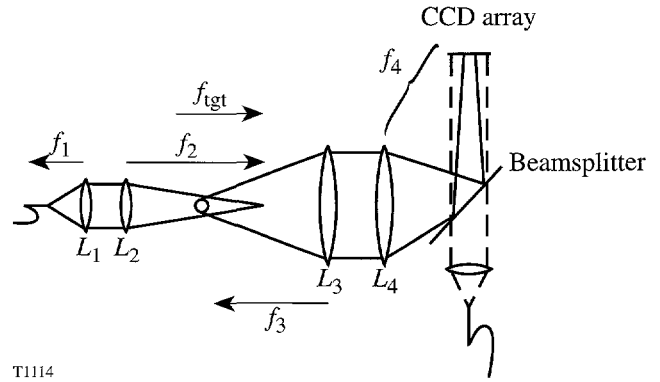

Figure 58.29
A schematic of the optical system used to create an interferogram of a cryogenic target with convergent-beam illumination The optics that control the point of focus of the convergent beam and those that image the target are shown. The dotted line denotes the collimated reference beam.

The light emerging from the optical fiber in the object arm is first collimated with lens L_1 and is focused to a point with L_2. All lenses in the interferometer are achromatic doublets corrected for infinite conjugates. All imaging takes place close to the optical axis of the interferometer, so the use of these lenses minimizes spherical aberration. Since the light between L_1 and L_2 is collimated, only the position of L_2 is adjusted to locate the focus of the convergent beam at the rear focal point of the cryogenic target.

The target is imaged onto a CCD array by the optical relay system composed of lenses L_3 and L_4. The ratio of the focal lengths of these lenses, f_4/f_3, determines the magnification of the imaging system. In some instances, the working distance between the target and L_3 (i.e., f_3) is required to be large, such as the case of imaging in the OMEGA Upgrade target chamber. For large magnifications, the required value of f_4 may then exceed the physical dimensions of the space allotted to this target diagnostic. In this case, f_4 can be made equal to f_3, and a microscope objective lens can be used to further image the intermediate unity-magnification image of the target onto the CCD array.

The light emerging from the optical fiber in the reference arm of the interferometer is collimated, and the reference beam is combined with the object beam using a 50/50 beamsplitter. The partially reflective coating on the parallel-plate beamsplitter faces L_4 so that no aberration is introduced into the object beam by passage through a thick plate. Since the reference beam is collimated, its passage through the plate does not affect the planar reference wavefronts except to displace them laterally with respect to the optical axis of the collimating lens. The direction of propagation between the object and reference beams (i.e., the tilt) is controlled by rotating the reference beam's collimating lens about an axis perpendicular to its optical axis. Both the object and reference beams have a Gaussian, and therefore nonuniform, intensity profile upon emerging from the single-mode optical fiber. The centroid of the intensity distribution of the interferogram produced on the CCD array can also be positioned by translating the collimating lens in a direction perpendicular to its optical axis.

As the position of the focal point of L_2 is translated longitudinally with respect to the target's position, the irradiance of the object beam at the target (and its image) varies dramatically. The individual irradiances of the object and reference beams at the CCD array must be equal to produce interference fringes with the maximum possible contrast. Hence, to obtain high-contrast interferograms for a wide range of cryogenic target dimensions, the ratio of the power launched into the two fibers must be continuously variable. Referring to Fig. 58.30, this is accomplished using a polarizing beamsplitter in conjunction with linearly polarized laser light and a half-wave plate that can be rotated about its cylindrical axis. As the half-wave plate is rotated, the power ratio of the object beam to the reference beam varies continuously between 0 and 1.

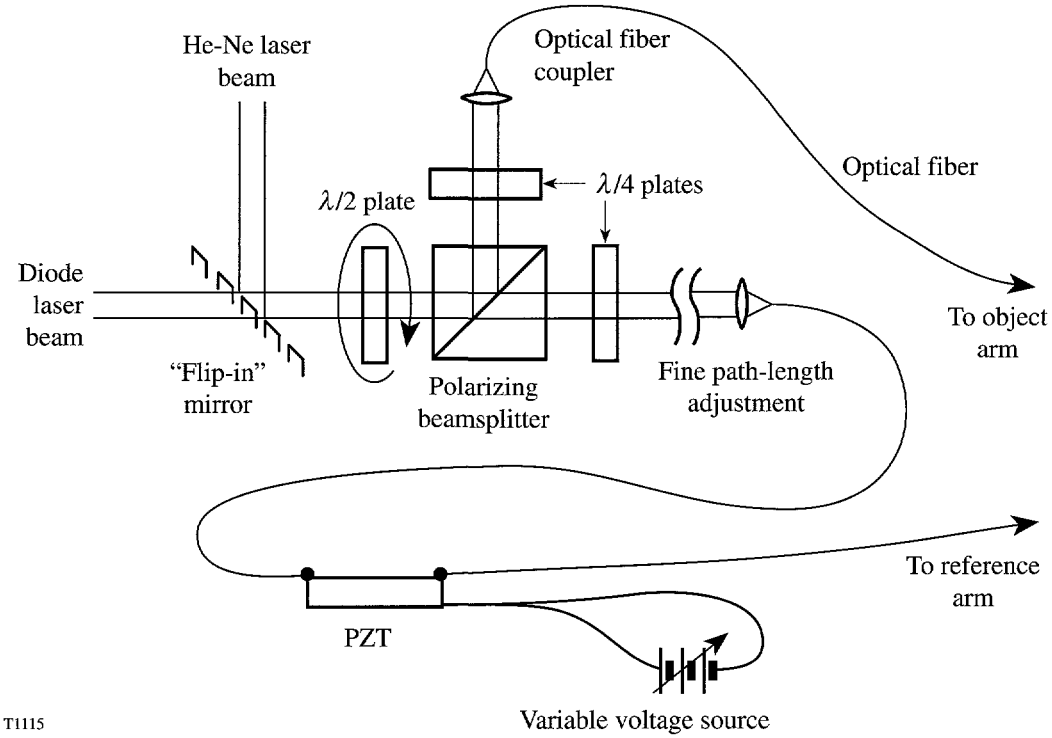

Figure 58.30
A schematic of the optical system that divides the source of radiation into the object and reference beams. Variable wavefront division is possible using the half-wave plate and the polarizing beamsplitter. Polarization-preserving fiber is unnecessary if quarter-wave plates are used to circularly polarize the light launched into the single-mode optical fibers, thereby reducing the detrimental effects that the variable bending conditions of the fiber have on the interferogram.

When linearly polarized light propagates through an optical fiber that is not polarization preserving, the polarization direction of the light emerging from the fiber depends on the bending conditions of the fiber between the source and its termination. The contrast of an interference pattern also depends on the relative angle between the polarization directions of the two beams that produce it. To stabilize the interferogram's contrast, quarter-wave plates are used to launch circularly polarized light (with the same handedness) into each fiber. Although some ellipticity is introduced into the light's polarization during propagation through the fiber, the contrast remains relatively constant as the fibers' bending conditions change.

An interferogram created with long-coherence-length light generally contains a significant amount of low-contrast noise due to interference between reflections from the various optical surfaces. To reduce this noise, a source of short-coherence-length light can be utilized. However, this makes the alignment and optical-path balance between the object and reference beams more critical. GaAlAs gain-guided laser diodes operate with numerous longitudinal modes resonating simultaneously, producing radiation with a bandwidth of several nanometers. This translates to a coherence length of only a few millimeters. To aid in alignment, the optical system is first aligned using a long-coherence-length source such as a He-Ne laser. When the maximum contrast of the interference fringes has been obtained by trimming the length of the optical fibers and adjusting the spacing between the polarizing beamsplitter and the optical-fiber coupler in the reference arm, the "flip-in" mirror in Fig. 58.30 can be removed and the laser diode becomes the light source. Fine path-length adjustment is accomplished by careful positioning of the optical-fiber coupler in the reference arm, which is mounted on a precision slide. A broadband polarizing beamsplitter and liquid-crystal wave plates that have an equal retardance for two wavelengths[7] are used so the contrast of the interferogram is not altered when the light sources are interchanged.

Phase sensitivities of the order of a few hundredths of a fringe can be achieved using phase-shifting techniques.[8–10] This involves sequentially acquiring multiple interferograms, each with a known phase offset between them caused by introducing a slight path-length change in one of the interferometer's arms. The phase of each point in the interferogram, modulo 2π, is then obtained by performing simple

mathematical operations on the set of interferograms. One advantage of phase-shifting methods is that the phase resolution depends primarily on the dynamic range of the CCD array (and the contrast of the interferogram) and, to a lesser degree, on the dimensions of individual pixels, as is the case with fringe-finding techniques.

An elegant method of introducing a controlled phase step into one of the interferometer's arms is to slightly elongate the optical fiber in that arm. This method introduces a path-length change alone and does not affect the tilt between the object and reference wavefronts, which can often be disturbed when an optical element such as a mirror or lens is displaced to introduce the same phase shift. A piezoelectric element to stretch the fiber and its associated electronics is commercially available in a single, compact unit.[11] The device is driven with a 0- to 10-V signal, which is compatible with typical digital-to-analog converters. The total phase shift introduced with respect to the maximum applied voltage can be selected by varying the total length of the fiber cemented to the piezoelectric element.

Typical interferograms produced with both plane-wave and convergent-beam illumination are shown in Fig. 58.31. To date, a laser diode has not been purchased, although suitable candidates have been identified. Therefore, both images in Fig. 58.31 were produced with a He-Ne laser. At this time, both large-diameter capsules and the methods to produce uniform, thick condensed fuel layers in them remain to be fully developed. Hence, tests were performed on room-temperature capsules with effective focal lengths comparable to those calculated for OMEGA Upgrade–sized capsules containing thick cryogenic fuel layers. Figure 58.31(a) was obtained by removing L_2 and adjusting the half-wave plate to produce maximum fringe contrast. In Fig. 58.31(b), L_2 was replaced and its position was adjusted until the center of the target's image was nearly uniform in intensity. Note that the f-number of L_2 must be chosen to sufficiently overfill the target's image so that the curvature of the object wavefront passing around the capsule can be accurately determined, as described below.

The interferogram shown in Fig. 58.31(b) is analyzed in the following manner to obtain information about the thickness and uniformity of the condensed fuel layer. First the center of the target's image is located while blocking the reference beam. The reference beam is restored, and phase-shifting techniques are utilized to map the phase of the wavefront as a function of position within the image, modulo 2π. The phase of the wavefront is "unwrapped" so that continuous surfaces representing the wavefront inside and outside the target's image are obtained. The discontinuity between the wavefront transmitted through the capsule and that passing around it occurs near the circumference of the capsule, where there is a substantial step in the object wavefront's phase and there may be a dark area due to light being refracted outside the aperture of L_3.

The wavefront within the interior of the capsule is then fitted to a set of polynomials that are orthonormal over a unit circle, such as Zernike polynomials.[12,13] The center and radius of curvature of the wavefront surrounding the target's image is then determined. Although the background rings should be made concentric with the center of the target's image, the lateral displacement between the centroid of the target's circumference and the center of curvature of the wavefront surrounding the target's image determines the magnitude and direction of the residual tilt between the object and reference wavefronts. The difference in curvature of the wavefronts transmitted through and passing around the target is used to determine the thickness of the fuel layer, accounting for the contribution due to the empty capsule. The coefficients of the higher-order polynomials reveal the thickness and lateral dimensions of the nonuniformities present in the condensed fuel layer.

Although the analysis of the interferogram produced is significantly more complicated, the interferometer described above has several advantages over optical systems that illuminate the target with planar wavefronts. By illuminating the target with a beam converging to its rear focal point, the wavefront emerging from the target is flattened, with only the curvature due to the spherical aberration term remaining. More light is collected from regions near the perimeter of the target, and the interferogram consists of a set of rings that are concentrated near the perimeter of the target's image. This enhances the phase sensitivity, and therefore the sensitivity to thickness variations, that can be achieved with a specific CCD array.

In addition, this interferometer incorporates several unique features. The location of the convergent beam's focal point can be continuously adjusted to compensate for a wide range of capsule/fuel-layer dimensions. Stretching the optical fiber in the reference arm provides phase-shifting capabilities without translating optical components. The use of relatively short-coherence-length light suppresses interference from spurious reflections within the optical system, thereby reducing noise in the interferogram.

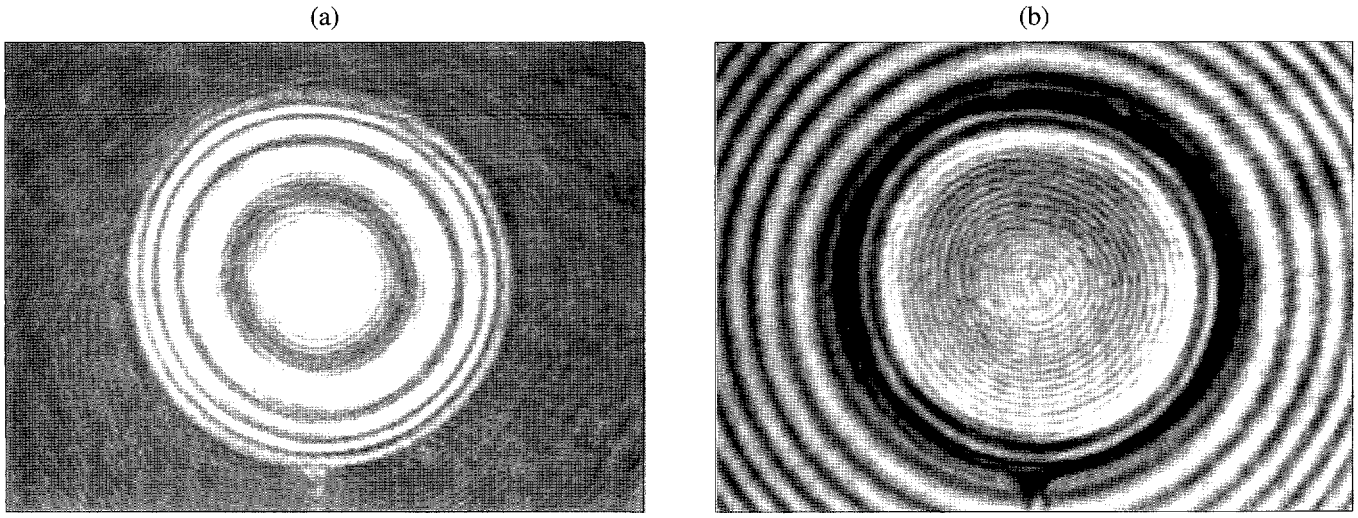

Figure 58.31
Actual interferograms of a 3.3-μm-thick glass capsule with a diameter of 270 μm. This capsule has the same focal length (−8.0 mm) as the target used to generate the interferograms in Fig. 58.24; however, W_{040} for the capsule in these images is only −0.55 μm instead of −6.5 μm for the comparable cryogenic target. The capsule was illuminated by a He-Ne beam and imaged by *f*/3.5 optics. In (a), L_2 was removed and the half-wave plate adjusted to produce maximum fringe contrast. L_2 was replaced in (b) and its position was adjusted until the center of the capsule's image was nearly uniform in intensity. Note the low-contrast noise in each due to interference between the reflections from the various optical surfaces and the relatively long coherence length of the light used.

ACKNOWLEDGMENT

This work was supported by the U.S. Department of Energy Office of Inertial Confinement Fusion under Cooperative Agreement No. DE-FC03-92SF19460, the University of Rochester, and the New York State Energy Research and Development Authority. The support of DOE does not constitute an endorsement by DOE of the views expressed in this article.

REFERENCES

1. J. A. Tarvin *et al*, in *Interferometry* (SPIE, San Diego, CA, 1979), Vol. 192, pp. 239–243.
2. T. P. Bernat, D. H. Darling, and J. J. Sanchez, J. Vac. Sci. Technol. **20**, 1362 (1982).
3. K. Kim, L. Mok, and M. J. Erlenborn, J. Vac. Sci. Technol. A **3**, 1196 (1985).
4. K. Kim and D. L. Krahn, J. Appl. Phys. **61**, 2729 (1987).
5. T. R. Pattinson and W. J. Felmlee, J. Vac. Sci. Technol. A **6**, 1882 (1988).
6. H. J. Kong, M. D. Wittman, and H. Kim, Appl. Phys. Lett. **55**, 2274 (1989).
7. Meadowlark Optics, 7460 Weld County Road 1, Longmont, CO 80504-9470.
8. K. Creath, in *Surface Characterization and Testing*, edited by K. Creath (SPIE, Bellingham, WA, 1986), Vol. 680, pp. 19–28.
9. K. Kinnstaetter, A. W. Lohmann, J. Schwider, and N. Streibl, Appl. Opt. **27**, 5082 (1988).
10. K. Creath, in *Progress in Optics XXVI*, edited by E. Wolf (Elsevier Science Publishers, 1988), pp. 349–393.
11. Canadian Instrumentation and Reseach Limited, 5035 North Service Road, Unit B7/8, Burlington, Ontario, Canada L7L 5V2.
12. M. Born and E. Wolf, *Principles of Optics*, 6th ed. (Pergamon, Oxford, 1980), pp. 464–468.
13. D. Malacara, ed., *Optical Shop Testing* (John Wiley & Sons, New York, 1978), pp. 489–505.

Compact, Multijoule-Output, Nd:Glass, Large-Aperture Ring Amplifier

A high-gain, large-aperture ring amplifier (LARA) has been developed with a 37-mm clear aperture that delivers output energies of >15 J in a 1-ns pulse at a wavelength of 1.053 μm. The compact ring amplifier fits entirely on a 4' × 10' table and is the main component of the OMEGA Upgrade driver line. The key elements of the ring cavity are a flash-lamp-pumped, 40-mm-diam Nd:glass amplifier rod, a telephoto lens vacuum spatial filter, and a Pockels cell that optically switches the pulse to be amplified in and out of the ring cavity.

System Optical Configuration

The standard optical configuration for the LARA amplifier is shown in Fig. 58.32. A pulse originating from a regenerative amplifier passes through an apodizer before entering LARA. The apodizer modifies the beam profile in order to produce a prescribed near-field intensity distribution after amplification. A typical apodizer and its corresponding annular beam are shown in Fig. 58.33. The apodizer pattern (Fig. 58.33) is one of carefully shaped teeth protruding into the transmission region. The radially varying teeth width determines the radially varying transmission function. Although this concept is not new,[1] the fabrication technique used is new. The apodizer is manufactured by depositing a thin, opaque layer of chrome on one side of a plane-parallel BK7 substrate. The plane-parallel substrate minimizes pointing changes when the apodizer is inserted into the beam. Using standard lithographic techniques, the apodizer is etched into the chrome layer. The teeth in the apodizer are at high spatial frequency and are removed by the spatial filter in LARA, leaving behind the low-frequency, radial intensity modulation. Different apodizers can be used to produce different beam profiles after amplification in LARA. Annular, flat-topped, and a variety of other beam profiles have been produced in this fashion. After passing through the apodizer, the pulse is switched into LARA for amplification by reflection off the input polarizer.

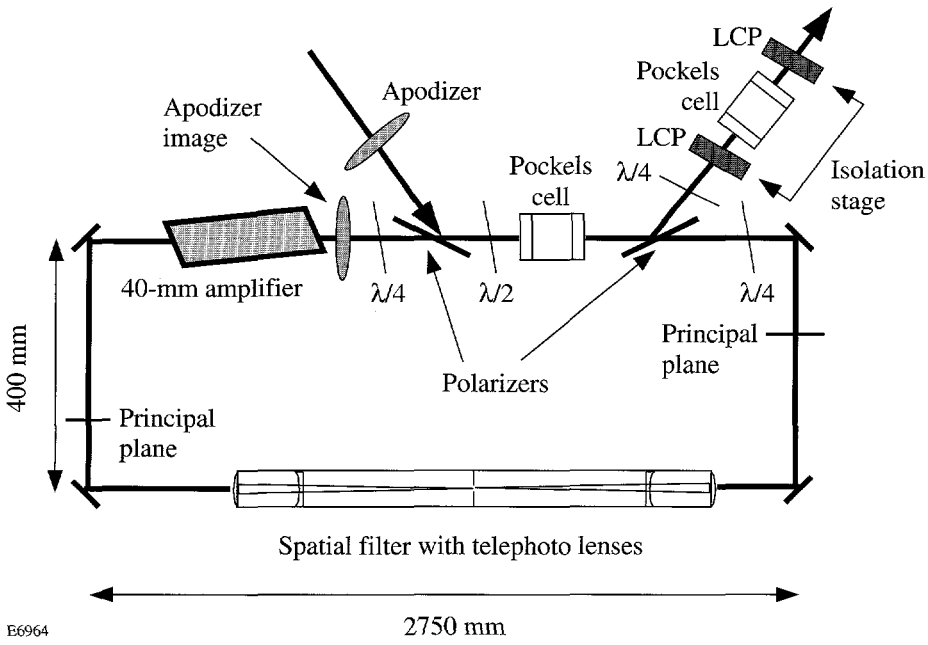

Figure 58.32
Standard LARA design with apodizer image at the output beam inside the cavity.

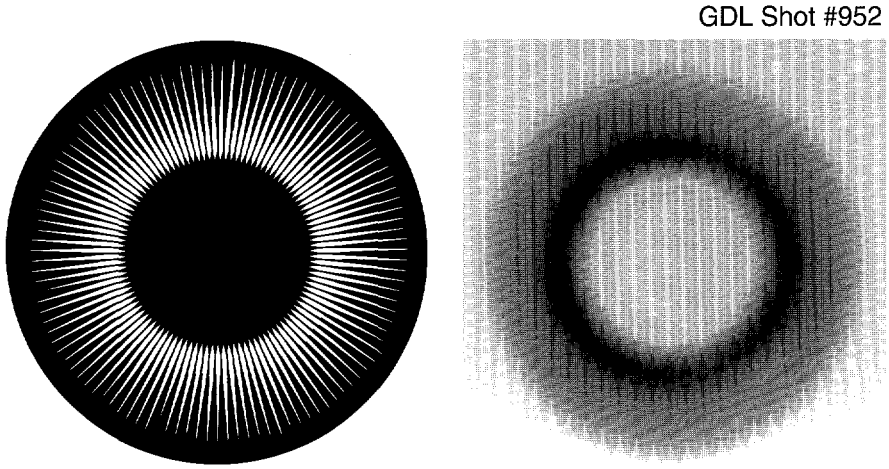

Figure 58.33
Cerated apodizer used to produce annular beam from LARA (left) with corresponding near-field output from LARA (right).

The polarization of a pulse inside LARA is controlled by the combination of two polarizers: a half-wave plate and a Pockels cell as shown in Fig. 58.32. With the Pockels cell off, *s*-polarized light enters LARA by reflection off the input polarizer. The half-wave plate changes the light to *p*-polarization, which is transmitted by the output polarizer. After one round trip, the light is again changed back to *s*-polarization by the half-wave plate and is reflected out of LARA by the output polarizer. Under an ideal situation where the polarizers have infinite contrast between transmitted *p*-polarized and reflected *s*-polarized light, a pulse can travel at most one round trip before being reflected out of LARA by one of the polarizers. This design feature limits the amount of amplified spontaneous emission (ASE) that can build up inside LARA.

If more than one amplification pass is desired, the Pockels cell can be pulsed to its half-wave voltage during the first round trip of an injected pulse. When the pulse passes through the polarizer section again, it experiences a full-wave rotation from the half-wave plate and pulsed Pockels cell and is transmitted by the output polarizer. After the pulse passes the Pockels cell for a final round trip, the Pockels cell is turned off, and the pulse is subsequently reflected out of LARA off the output polarizer. In this fashion, multiple round trips in LARA can be made by turning the Pockels cell on for multiples of the round-trip cavity time (22 ns). For example, four round trips occur when the Pockels cell is turned on for 66 ns.

Polarization control is also used for purposes other than containing the pulse in the LARA cavity. The addition of two quarter-wave plates, as shown in Fig. 58.32, changes *p*-polarized light to circular polarization while passing through the amplifier rod and spatial filter. The effects of radial birefringence are mitigated by passing circularly polarized light through the amplifier rod. Also, backreflected beams from near-normal surfaces in the cavity such as the spatial filter lenses are reflected out of LARA from the polarizers because of a half-wave rotation from double passing the quarter-wave plates. This prevents damage due to ghost reflections by directing the ghost energy out of LARA before it is amplified.

A vacuum spatial filter with telephoto lenses is placed inside LARA to provide 1:1 imaging in the cavity, provide spatial beam cleanup after each amplification pass, increase the threshold for "self-lasing" of the cavity, and cancel odd-order wavefront aberrations for an even number of round trips. A typical ring cavity design with 1:1 imaging would use a two-lens relay, with one lens at each principal plane in Fig. 58.32 and focal lengths equal to one-fourth of the round trip cavity distance. At the high energies of LARA, a vacuum relay is required to eliminate breakdown at the focus of the lenses. For a 1:1 imaged cavity the principal planes must lie in opposing legs of the ring and cause difficulties in the design of a vacuum relay. Therefore a relay with telephoto lenses is placed in one leg of the ring. The effective focal length of the telephoto lenses is equal to one-fourth the cavity round-trip distance, but the principal planes are displaced from the lens positions allowing the relay to lie in one leg of the ring.

Spatial amplitude noise from each amplification pass is filtered by placing a pinhole at the focus of the vacuum relay. The pinhole also reduces ASE in LARA by limiting the range

of pointing angles that can propagate inside LARA. Since the spatial filter causes an image inversion when traversed, odd-order aberrations in LARA, such as coma, will be eliminated provided an even number of round trips are made.

After amplification, the pulse is switched out of LARA by reflection off the output polarizer and passes through a quarter-wave plate and an isolation stage. The isolation stage consists of two liquid crystal polarizers (LCP) of opposite handedness surrounding a Pockels cell. The isolation stage is used to improve the contrast between the amplified pulse out of LARA and any pre- or post-pulses. The isolation stage also protects LARA from light propagating back through the isolation stage.

One of the drawbacks of the present LARA design (Fig. 58.32) is the 1:1 imaging of the cavity that places the image of the input apodizer inside LARA. At times, space constraints do not allow for proper image relaying of the apodizer through the output of LARA. An alternative LARA design that overcomes this difficulty is shown in Fig. 58.34. Here, the image of the apodizer in the output beam falls outside the LARA cavity, which simplifies image relay into the rest of the amplifier chain.

System Characterization

Several features of the LARA amplifier are investigated: holdoff, gain versus bank energy, near field, interferometry, and prepulse contrast. Unless otherwise stated, the results presented are for a four-pass LARA in the configuration shown in Fig. 58.32. Since the amplifying medium in the LARA cavity is a flash-lamp-pumped, 40-mm-diam Nd:glass amplifier rod, a maximum repetition rate of one shot per 5 min is used for system characterization.

The holdoff voltage of the ring amplifier cavity is defined as the voltage to which the amplifier can be fired before self-lasing of the ring occurs. Self-lasing of the ring occurs when the round trip gain for ASE exceeds the round-trip losses with the Pockels cell in the "off" state. Below the self-lasing threshold, any ASE traveling around the ring can accumulate only over one round trip before being reflected from the cavity. The self-lasing threshold is primarily determined by the practical limitations set by the finite contrast of the polarizers and the Pockels cell, as well as nonideal wave plates, the size of the spatial filter pinhole, and the birefringence of optical components between the input and output polarizers. Since there are more optical components between the polarizers in the cavity configuration in Fig. 58.34, a lower self-lasing

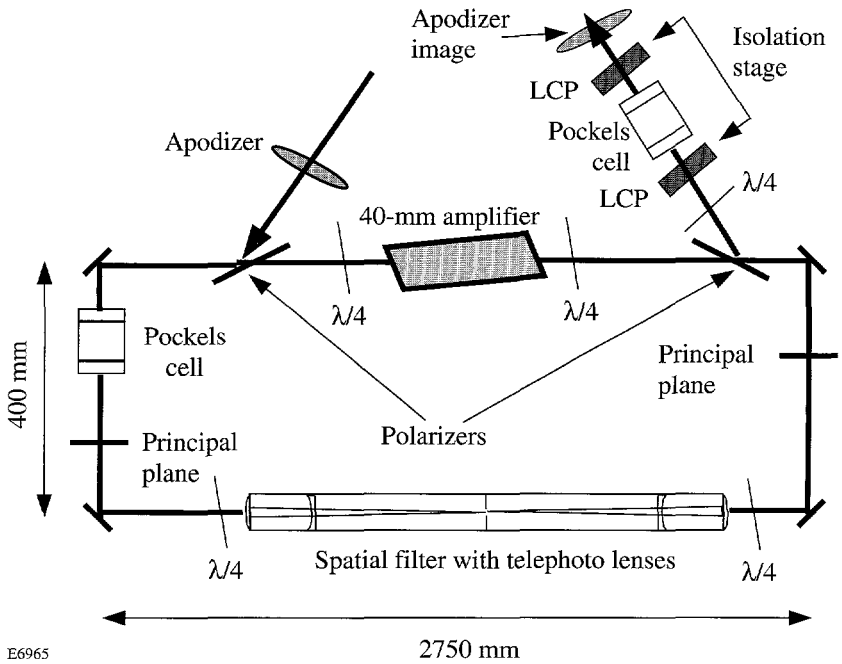

Figure 58.34
Alternative LARA design with apodizer image of the output beam outside the cavity.

threshold or holdoff voltage is both expected and observed. Holdoff voltages as high as 6.4 kV, with a corresponding single-pass, small-signal gain of $G_{ss} \approx 19$, have been measured for the cavity in Fig. 58.32, while holdoff voltages for Fig. 58.34 are around 6.0 kV ($G_{ss} \approx 16$). Since the gain bandwidth of Nd:glass[2] is ~200 Å, the optical elements of the LARA cavity must not provide only for high contrast at the 1.053-μm amplification wavelength, but also for wavelengths to either side. Thus, we observed a higher self-lasing threshold for zero-order wave plates than for multiple-order wave plates. It should also be kept in mind that incorrectly set wave plates in the cavity can result in catastrophic self-lasing with resulting damage to optical components.

The onset of self-lasing is easily diagnosed with the fluorescence traces from the amplifier rod. Figure 58.35 shows photodiode-recorded fluorescence traces of a LARA under normal operating and under self-lasing conditions without pulse injection. Self-lasing manifests itself in the familiar spikes superimposed on a usually smooth fluorescence trace. More dramatic self-lasing can be detected by placing burn paper outside of LARA facing the input and output polarizers.

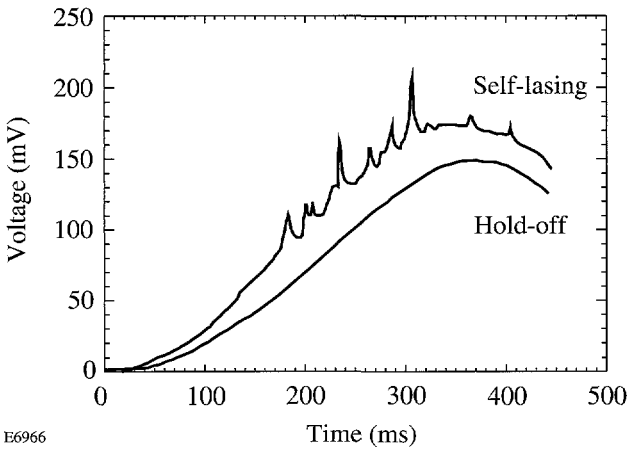

Figure 58.35
The fluorescence traces from a LARA amplifier exhibiting self-lasing (top trace) and under normal hold-off conditions (bottom trace).

The total small-signal gain of the LARA system as a function of flash-lamp bank energy for three and four round trips is shown in Fig. 58.36. With four round trips, total gains of $\geq 10^5$ have been achieved at bank energies of 6 kV without noticeable degradation in beam quality. Figure 58.37 shows the output beam profile for a full-aperture, 13.7-J LARA shot with 140-μJ input energy. The azimuthally averaged lineout shows the 37-mm beam diameter with an intensity distribution

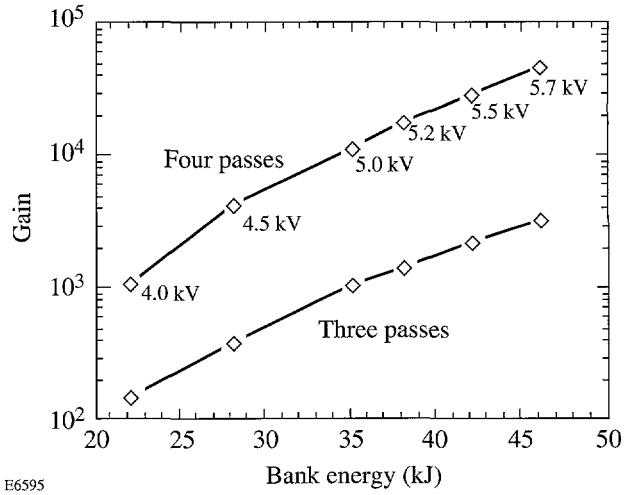

Figure 58.36
Total gain of LARA as a function of flash-lamp bank energy for three- and four-pass configurations.

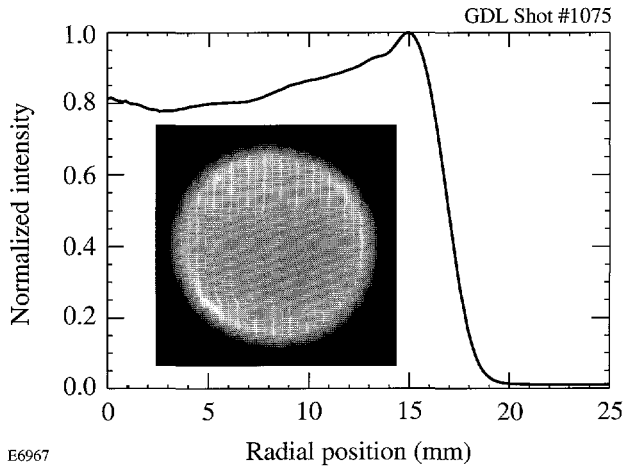

Figure 58.37
Near field of 13.7-J shot from LARA with azimuthally averaged lineout.

peaked at the edges of the beam due to the radial gain in the 40-mm amplifier rod. The peaked edges were expected because the apodizer used with this test was not designed to produce a flattop beam at total small-signal gains of $\geq 10^5$. An appropriately designed apodizer can easily produce a flattop profile at this energy.

The wavefront quality of LARA at full aperture and high energy has been investigated with a self-referencing Mach-Zehnder interferometer.[3] Figure 58.38 shows a reduced interferogram of the LARA output at 17.8 J. The background phase error of the interferometer error is removed from the

measurement using a separately recorded wavefront of the input beam without passing through LARA. The peak-to-valley wavefront distortion of an amplified full-aperture beam after four round trips is approximately 1 wave (see Fig. 58.37). Half of this wavefront distortion is directly attributable to the LARA Pockels cell. In the OMEGA Upgrade driver-line application, the aperture diameter is 20 mm and the corresponding peak-to-valley wavefront distortion is a very satisfactory ~0.25 waves.

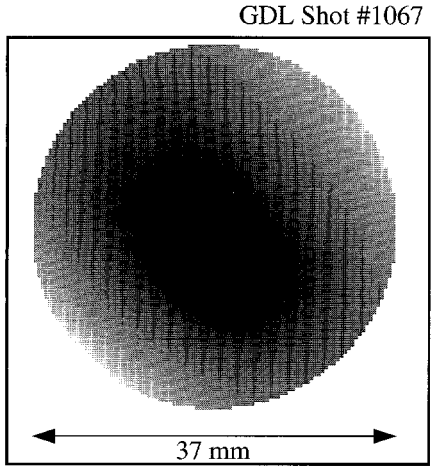

Figure 58.38
Interferogram of 17.8-J shot from LARA (interferometer error subtracted); peak-to-valley wavefront error = 0.970±0.138 waves, rms error = 0.255±0.307 waves.

One interesting characteristic of LARA is its 'first-shot syndrome,' which manifests itself as a degradation of wavefront quality for the first shot of the day. Figure 58.39 shows the peak-to-valley wavefront error over a 37-mm aperture obtained for a series of shots on a typical day. The peak-to-valley wavefront quality of the first shot of the day with a "cold" amplifier rod is shown by the circle in Fig. 58.39. The series of data points below this circle shows a reduced peak-to-valley distortion for all subsequent shots taken at various intervals between 7 and 20 min. There is a ≥0.5-wave peak-to-valley reduction from the first shot of the day to all subsequent shots. The 'first-shot syndrome' is not well understood, but similar observations have been made previously on the 24-beam OMEGA system. As a practical precaution, the first shot of the day for LARA will not be allowed to propagate down the main amplifier chains of the OMEGA Upgrade.

For the OMEGA Upgrade, the required prepulse energy contrast on target is $>10^9$, which translates to a prepulse contrast for LARA of $>10^4$. Prepulses on the LARA output are due to leakage of a small percentage of the circulating pulse within LARA during each round trip. Without firing the LARA amplifier, the measured prepulse contrast is $\sim 4 \times 10^3$. Under amplified conditions the prepulse contrast is enhanced (multiplied) by the single-pass small-signal gain of the LARA amplifier (typically $G_{ss} \approx 10$) since the prepulse is due to the circulating main pulse during the next-to-last round trip inside LARA. Thus, the LARA prepulse contrast is $\geq 4 \times 10^4$, which is well within the OMEGA Upgrade requirements.

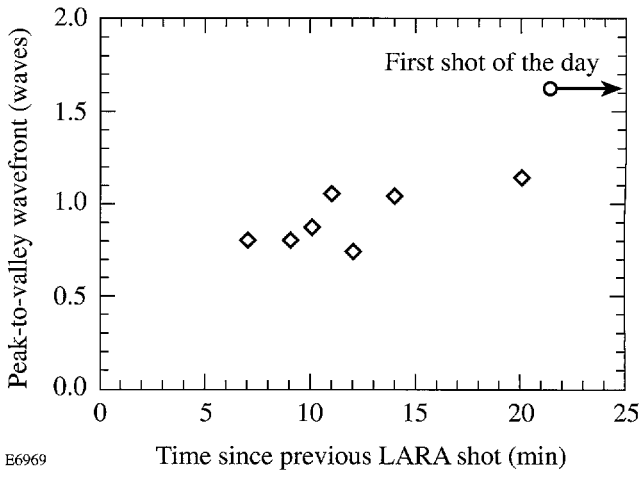

Figure 58.39
The peak-to-valley wavefront quality of LARA output at full aperture for the first shot of the day (circle) and subsequent cycled shots (diamonds).

Conclusions

A high-gain, large-aperture ring amplifier (LARA) has been developed with a 37-mm clear aperture that delivers output energies of >15 J in a 1-ns pulse at a wavelength of 1.053 μm. The compact ring amplifier fits entirely on a 4' × 10' table and is the main component of the OMEGA Upgrade driver. The key elements of the ring cavity are a flash-lamp-pumped, 40-mm Nd:glass amplifier rod, a telephoto lens vacuum spatial filter, and a Pockels cell that injects the input pulse and ejects the output pulse from the ring cavity. LARA produces a high-energy output beam with excellent wave-front quality and near-field beam profile. LARA output beam profiles can be tailored by an input apodizer. At full aperture (37 mm), a four-pass LARA introduces ~1-wave peak-to-valley distortion on the wavefront quality of the beam. At the 20-mm aperture used by the OMEGA Upgrade, the peak-to-valley distortion is only ~0.25 waves. Excluding the first LARA shot of each day, a consistent wavefront quality is maintained for all shots. The prepulse contrast of LARA output is typically $>10^4$, which meets the OMEGA Upgrade specifications.

ACKNOWLEDGMENT

We would like to acknowledge the invaluable contributions of many LLE co-workers: D. Bancroft, W. Beich, D. Brown, C. Cotton, J. H. Kelly, C. K. Merle, R. G. Roides, W. Seka, M. D. Skeldon, M. Tedrow, K. Thorp, M. D. Tracy, and I. Will. Their efforts are greatly appreciated. This work was supported by the U.S. Department of Energy Office of Inertial Confinement Fusion under Cooperative Agreement No. DE-FC03-92SF19460, the University of Rochester, and the New York State Energy Research and Development Authority. The support of DOE does not constitute an endorsement by DOE of the views expressed in this article.

REFERENCES

1. J. Auerbach and J. Lawson, Lawrence Livermore National Laboratory (private communication).

2. S. E. Stokowski, R. A. Saroyan, and M. J. Weber, Lawrence Livermore National Laboratory Report, M-95, Rev. 2, Vol. 1 (1981).

3. Laboratory for Laser Energetics LLE Review **31**, NTIS document No. DOE/DP/40200-47, 1987 (unpublished), p. 114.

Atomic Force Microscopy Observation of Water-Induced Morphological Changes in Y_2O_3 Monolayer Coatings

Environmental stability studies for thin-film coating materials employed on the upgraded OMEGA laser system are essential for defining acceptable air humidity levels and their control, as well as for facilitating proper thin-film coating design of long-term-use OMEGA laser optics. Moisture penetration into porous, dielectric thin-film coatings causes generally undesirable changes in the film's optical performance parameters—a fact that has been well known for some time now.[1,2] The major effects previously observed and studied in this regard are shifts in the transmission characteristics of narrow-band filters,[3,4] caused by the replacement of air with a 1.3-index medium inside the pores; enhanced absorption in the IR water band;[5] and changing mechanical stress (either compressive or tensile)[6] that renders difficult maintaining stringent wavefront-error requirements on reflective components. Thermal annealing,[7] ion bombardment, and, more generally, preparing coatings with dense-packing structure are among the methods devised in combating water effects in dielectric films.

In addition to these macroscopic effects, certain narrow-band filters also showed microscopic morphology modifications upon water penetration. These changes took the form of circular patches that remained unaffected even by a 4-h vacuum treatment of the dielectric filter stack at 200°C.[3] To our knowledge, no detailed, submicron resolution studies of such patterns were performed to date, and no fundamental insight into the growth mechanism of such patterns exists.

In this work, Y_2O_3 monolayer coatings, grown by Alpine Research Optics Inc., Boulder, CO, were used to examine AFM-resolution morphological changes caused by both a standard laboratory environment and artificial, accelerated testing in 100% relative humidity and also by droplet seeding.

Experimental Method

BK-7 glass substrates served as support for electron-beam-evaporated, 1-μm-thick, single-layer Y_2O_3 coatings. During evaporation, substrates were held at 300°C. After shipment, samples were stored in conventional, unsealed containers. In as-received condition, the films showed no evidence of moisture penetration; however, after 2-months' exposure to a fluctuating-humidity laboratory environment, reaching sporadic humidity episodes with up to 90% relative humidity, first signs of water-penetration-induced morphology changes were observed. After an additional two months, steady-state, moisture-penetration patterns developed.

Sample microscopy was carried out on a Nanoscope III (Digital Instruments, Inc.) Atomic Force Microscope using several probes, depending on sample average-surface-roughness conditions. On smooth areas with peak-to-valley variations <500 nm and lacking steep structural features, standard silicon nitride (Si_3N_4) probes proved adequate. For steep-height-gradient situations, etched silicon probes of high aspect ratio were necessary to avoid "surface-probe convolution" imaging. The Y_2O_3 surface proved to be quite stable even after hard engagement of the probe tip, and no special measures seemed necessary to prevent surface modification by the probe. A challenge did arise from the "stickiness" of the probes to water-modified sample areas, which we attributed to excessive electrostatic charging. Adjustments to the microscope feedback loop and reducing the scanning speed were successful countermeasures in this case. Microscope resolution was limited by residual system vibration noise that remained after isolation of the entire AFM/optical microscope monitor assembly on commercial vibration-isolation mounts. Cleaved-mica reference surfaces were readily imaged at atomic-scale resolution in this microscope-mounting configuration.

Artificial seeding of sample surfaces with de-ionized, distilled H_2O (18 MΩ/cm) was accomplished using a micropipette dispenser with 40-nl resolution. In the standard laboratory environment, such small water volumes evaporate from the sample surface within tens of seconds.

Moisture-Penetration Patterns

Resolving the earlier-reported, circularly symmetrical, water-penetration islands at increased resolution, one finds each island to contain a pronounced, central, pyramidal feature (occasionally split into twins or a closely packed multitude of

pyramids). Typical examples of such features are depicted in Figs. 59.1(a)–59.1(c). Their height above the adjacent film surface reaches 3 μm, and lateral extensions of up to 10 μm have been encountered. These pyramids are surrounded by a pronounced concentric-ring pattern varying in diameter from 10 to 100 μm [Figs. 59.2(a)–59.2(d)] and in width from 5 to 30 μm. We surmise that variations in ring sizes represent various developmental stages in ring formation.

When the features are small, i.e., at the early stages of the process, the concentric ring is not yet clearly isolated from the central feature and contains a high density of tiny pyramids [Fig. 59.2(a)]. Upon further development, the ring separates from the central feature, leaving a concentric region with two distinct spatial and structural characteristics [Figs. 59.2(b) and 59.2(c)]. At the same time, small pyramids in the central region merge into the larger, micron-scale central pyramid [Figs. 59.1(b) and 59.1(c)].

Analyzing the region between the central pyramid and the ring, one finds the following radial subdivision: In the immediate vicinity of the central pyramid a patchwork of islands

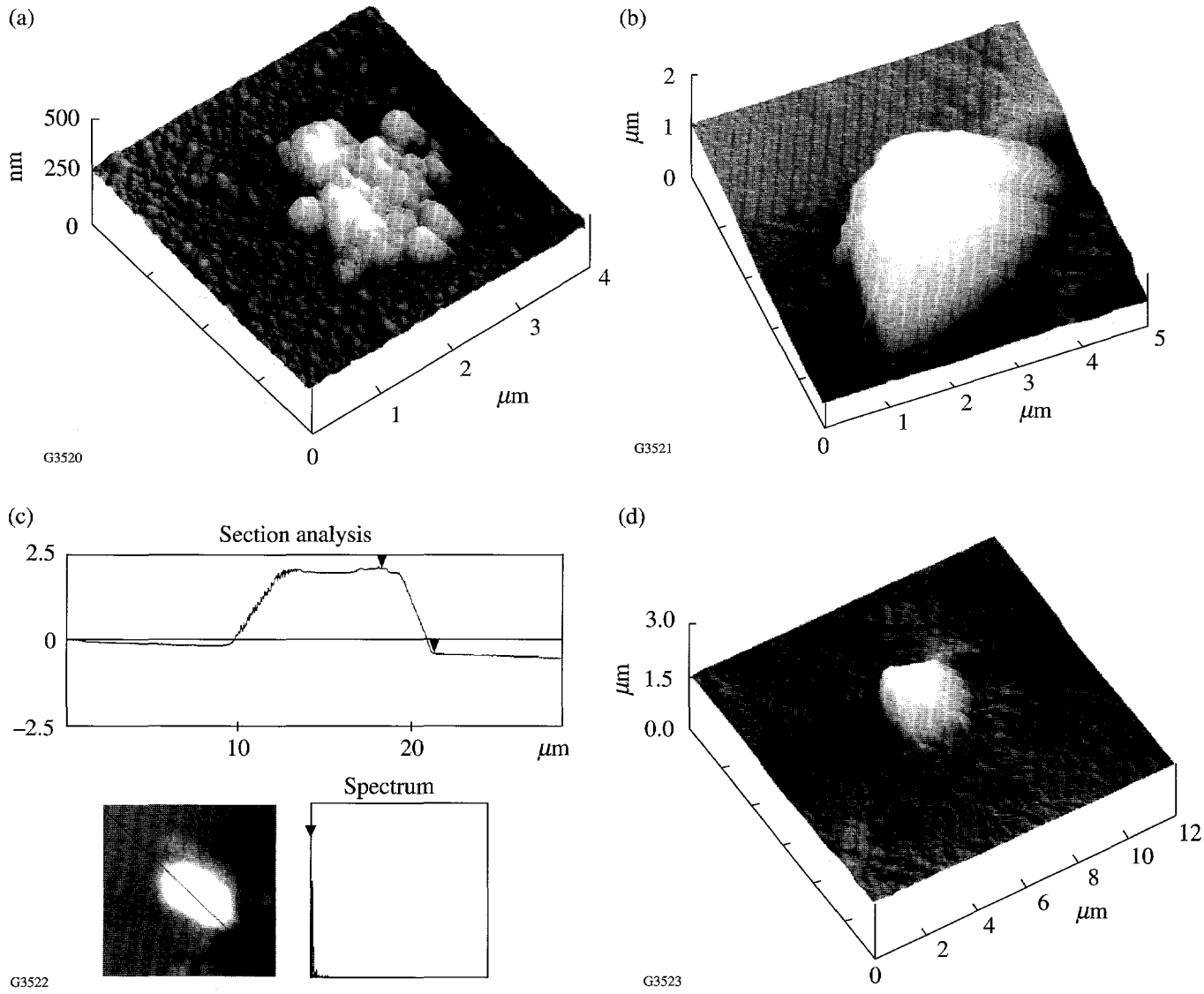

Figure 59.1
(a) Early developmental stage of a water-penetration-island central feature; small pyramids have already formed but have not yet merged. (b) Monolithic pyramidal structure with 5-μm base and 1-μm height typically found in the center of well-developed water-penetration islands. (c) Cross-sectional scan through a fully developed, 10-μm base pyramid. (d) Lower magnification view of pyramid in (b), allowing view of surrounding zone.

exists that differ from one another in both rms roughness and average height [Fig. 59.1(d)], while near the inner edge of the ring is a zone where the columnar film structure is undergoing coalescence. A similar zone of columnar coalescence is also found around the outer edge of the ring. In fact, columnar coalescence appears to be a global film process that we observed with a reduced time constant in unaffected film areas as well. At this time, the difference in rate constants between coalescence in water-penetration island areas and coalescence in "unaffected" areas appears to be a factor of 2 to 3.

Near the central pyramid, the island topography [Fig. 59.1(d)] comprises up to 100-nm height variations among islands, with rather-smooth-surface islands always being depressed in height relative to rough-surface islands. Figure 59.3(d) shows a head-on view of the columnar structure in one of the smooth

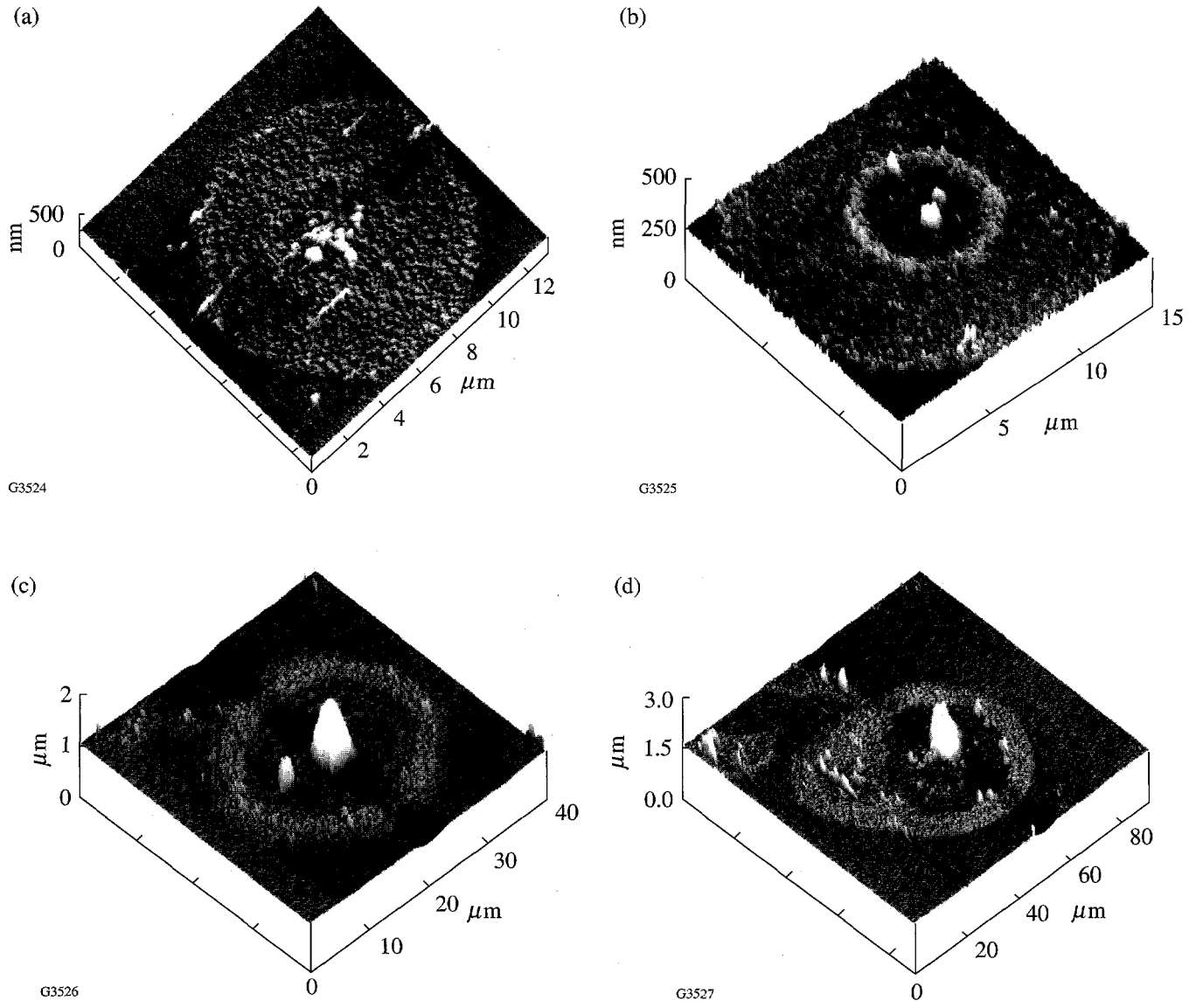

Figure 59.2
(a) View of the early stage of pattern formation: the ring (12-μm outer diameter) has not yet separated from the central feature. (b) View of ring separation in progress: the central feature is clearly developed, and a "dead-zone" between ring and central feature has evolved (18-μm) ring diameter. (c) Steady-state pattern of fully developed central pyramid, ring, and intermediate zone, which contains randomly distributed, rough, and very smooth patches with height variations of up to 100 nm. (d) Very-large, >60-μm-diam, water-penetration pattern with asymmetric shape resulting from the merger of two adjacent patterns at different developmental stages.

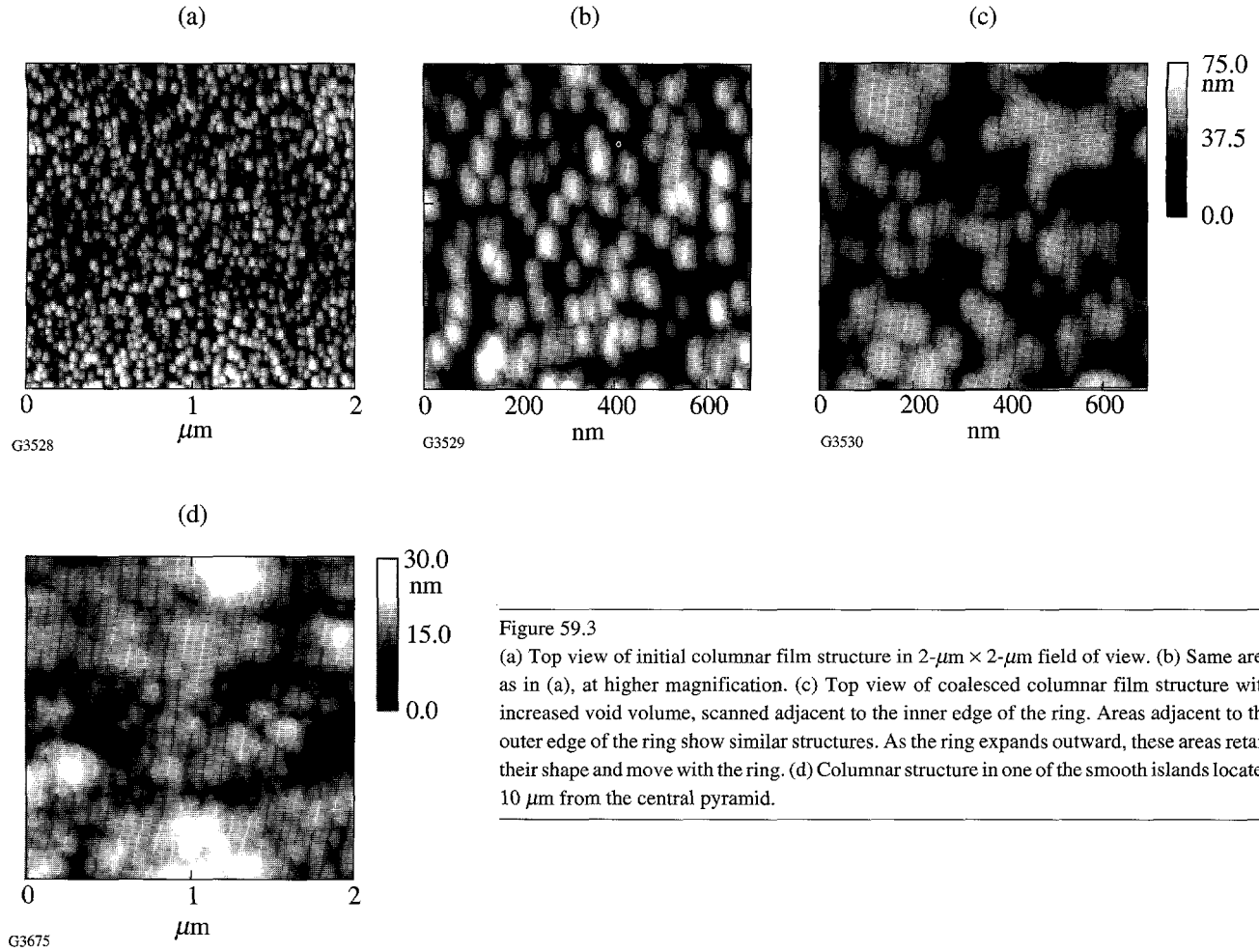

Figure 59.3
(a) Top view of initial columnar film structure in 2-μm × 2-μm field of view. (b) Same area as in (a), at higher magnification. (c) Top view of coalesced columnar film structure with increased void volume, scanned adjacent to the inner edge of the ring. Areas adjacent to the outer edge of the ring show similar structures. As the ring expands outward, these areas retain their shape and move with the ring. (d) Columnar structure in one of the smooth islands located 10 μm from the central pyramid.

islands located 10 μm from the central pyramid. Although columnar structure still exists, the columns' spatial frequencies have changed relative to the initial spatial frequencies shown in Fig. 59.3(a) at identical magnification and in Fig. 59.3(b) in a 700-nm × 700-nm "close-up" of a film area unaffected by water (the scanned, unaffected area is >1 mm away from the center of the water-penetration island). The lower spatial frequency of the columns is accompanied by a reduction in rms roughness to below 4 nm.

Figure 59.3(c) depicts a 700-nm × 700-nm top view of film columns and voids in the zone adjacent to the inner edge of the ring. Here, voids have widened because of columns that coalesced into coarser structures. The rms surface roughness remains unaffected by this coalescence [8.9 nm in the area of Fig. 59.3(c) versus 9 nm in the initial film].

The ring itself exhibits a very rough granular structure with average grain size varying between 300 and 400 nm (Fig. 59.4). The internal structure and/or porosity of these grains is yet unresolved.

The central pyramidal structures are monolithic with many, varying-size steps (1- to 100-nm scale) decorating the surfaces (Fig. 59.5). Until now, it was not possible to unambiguously determine the crystalline structure and, by implication, the solid-state phase of the yttrium-oxide complex making up the pyramids. This critical determination was hampered by signal-to-noise limits and by probe-tip geometry restrictions. The arrival of "oxide-sharp Si_3N_4" tips is expected to facilitate unraveling this important information that permits identifying the physico-chemical transport mechanism underlying the topographical patterns shown here.

Forced-Humidity Tests

When observing moisture-penetration results from a regular laboratory environment, one needs to remain aware of contaminants in the air that potentially shift the neutral water-

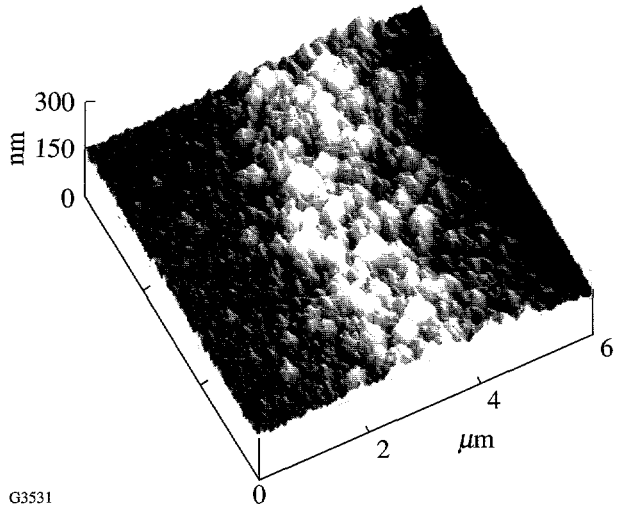

Figure 59.4
View of the 300- to 400-nm average grain size of a portion of the highly granular, well-developed ring.

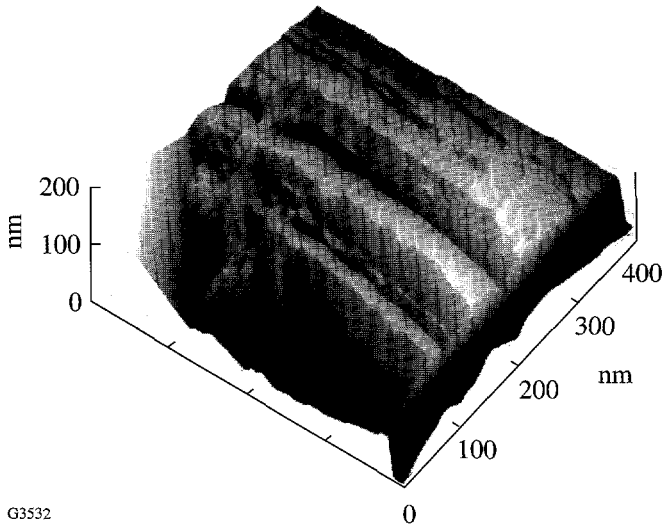

Figure 59.5
View of planar dislocation steps along the trapezoidal surface of a central pyramid. The translational regularity is indicative of the pyramid's crystallinity.

vapor pH to the basic or acidic side. In order to explore to what extent pure water drives these morphological changes, an artificial, 100%-relative-humidity condition was set up, and, independently, seeding of films by microdroplets was carried out. Samples left the humidity environment only during periods of testing. After 50 cumulative hours of exposure to 100% humidity, the first, nascent water-penetration marks became observable in a form familiar to regular laboratory effects (Fig. 59.6). This proved that water alone can promote Y_2O_3 morphological changes. The question then arose as to whether forced filling of the film pores would accelerate the mass transport such that changes driven by vapor-phase concentration over periods of months could become observable within hours or minutes.

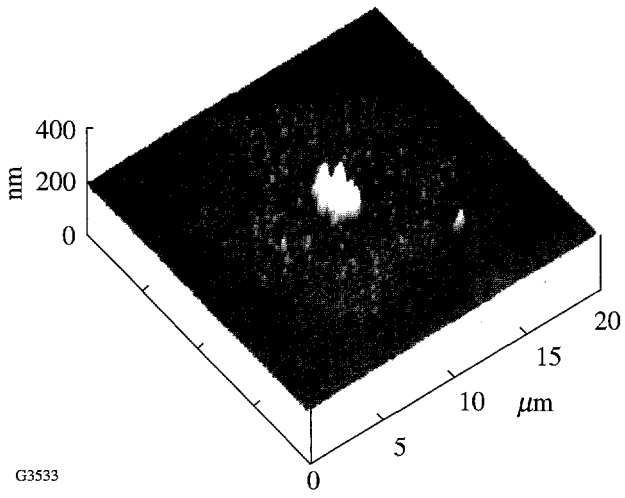

Figure 59.6
Moisture-penetration pattern in Y_2O_3 developing under 100%-relative-humidity, 50-h exposure.

After dowsing with 300-nl droplets, which each covered 0.35 to 0.60 mm^2, pyramidal pattern growth set in within 24 h [Figs. 59.7(a) and 59.7(b)] and continued for several weeks until an equilibrium pattern was established; however, ring structures failed to evolve. Instead, a high density of pyramids (of the order of 1 per 10 μm^2) was found, with film material between pyramids remaining [Fig. 59.7(c)] largely unmodified. Both the pattern-initiation sites and the transport mechanism for ring growth and expansion are therefore much likely different under vapor-phase conditions from mechanisms of fluid-phase chemistry active in forced seeding.

Conclusion

Long-term morphological changes induced by water penetration in Y_2O_3 monolayer films exhibit a pattern evolution that greatly influences atomic-force microscopy observations of such film surfaces. The finding that such films tend to uncontrollably change while one is watching them now has a rational basis. Growth patterns include distinct pyramidal features that either roughen the film during the early phase of growth kinetics or aggregate with time, leaving behind circular islands within which the typical dielectric-film, co-

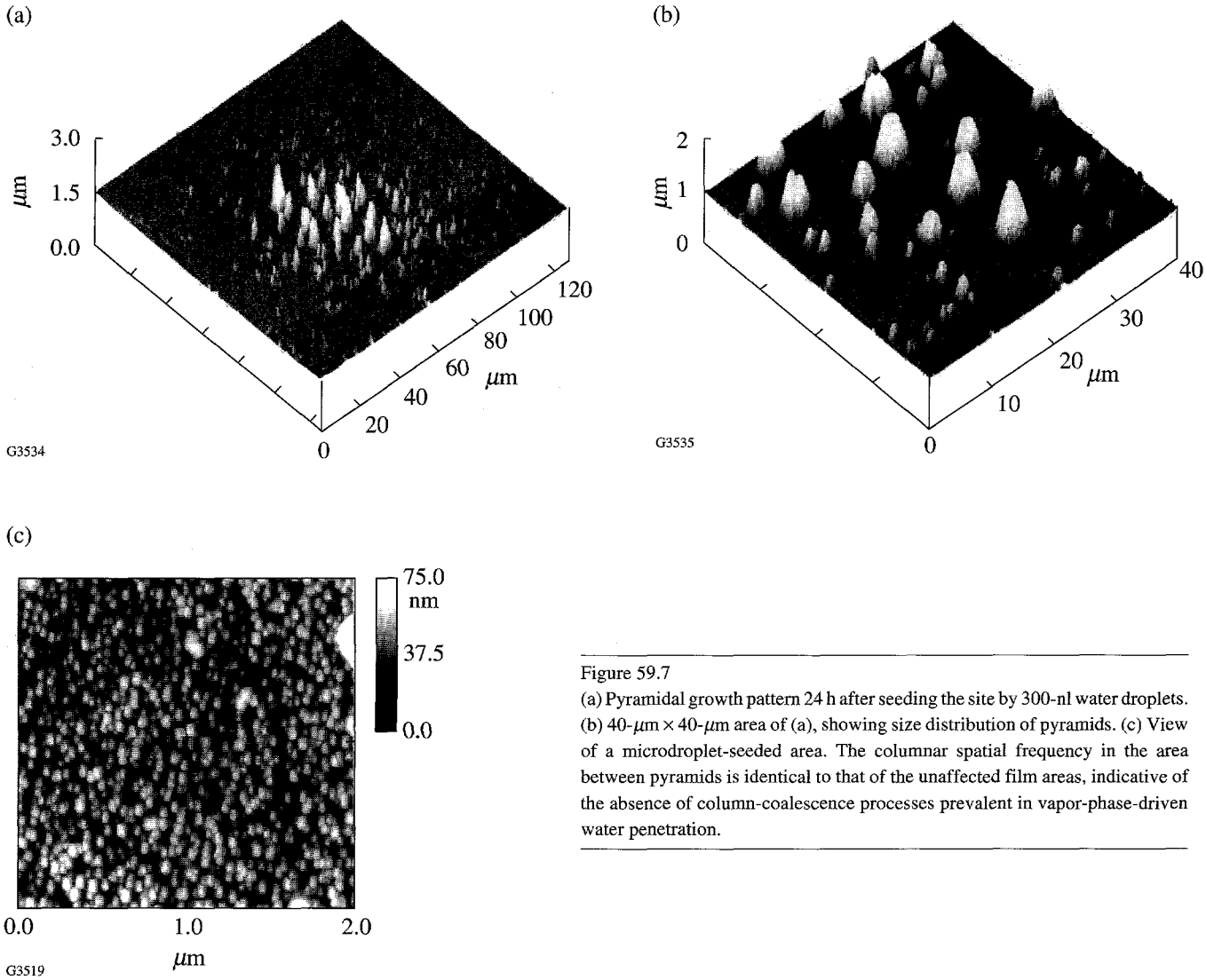

Figure 59.7
(a) Pyramidal growth pattern 24 h after seeding the site by 300-nl water droplets. (b) 40-μm × 40-μm area of (a), showing size distribution of pyramids. (c) View of a microdroplet-seeded area. The columnar spatial frequency in the area between pyramids is identical to that of the unaffected film areas, indicative of the absence of column-coalescence processes prevalent in vapor-phase-driven water penetration.

lumnar-growth structures have been irreversibly modified. The underlying mechanism for this redistribution of material is most intriguing but remains unresolved, pending further improvements in our experiment. It is already clear, however, that no additives to water are needed to promote the process. From an end-user concern, it is important to screen whether (and which, if any) additives, such as surfactants or solvents used in cleaning and maintenance of laser systems and infrastructures, further enhance film degradation through mechanisms evidenced here.

ACKNOWLEDGMENT

This work was supported by the U.S. Department of Energy Office of Inertial Confinement Fusion under Cooperative Agreement No. DE-FC03-92SF19460 and the University of Rochester. The support of DOE does not constitute an endorsement by DOE of the views expressed in this article. This work was carried out on equipment of the Center for Optics Manufacturing (COM). The COM is a DOD Center of Excellence by the U.S. Army Material Command.

REFERENCES

1. H. K. Pulker and E. Jung, Thin Solid Films **9**, 57 (1971).
2. S. Ogura and H. A. Mcleod, Thin Solid Films **34**, 371 (1976).
3. H. A. Mcleod and D. Richmond, Thin Solid Films **37**, 163 (1976).
4. N. E. Holm and O. Christensen, Thin Solid Films **67**, 239 (1980).
5. T. M. Donovan and P. A. Temple, in *Laser-Induced Damage in Optical Materials: 1979* (SPIE, Bellingham, WA, 1980), Vol. 568, pp. 237–246.
6. H. Sankur and W. Gunning, J. Appl. Phys. **66**, 807 (1989).
7. S. G. Saxe *et al.*, Appl. Opt. **23**, 3633 (1984).

Observation of Longitudinal Acceleration of Electrons Born in a High-Intensity Laser Focus

We have measured the energy and angular distributions of electrons born in and ponderomotively accelerated from a high-intensity laser focus. The angular distribution relative to the $\vec{k}$ of the laser shows the first observation of electrons ejected with momentum in the $\vec{k}$ direction. This forward acceleration comes from the conservation of momentum in the photon field.

At very-high laser intensities, a free electron's oscillatory motion in a laser field becomes anharmonic. A detailed, theoretical examination of electron trajectories and emitted harmonic radiation was conducted by Sarachik and Schappert in 1970.[1] They parameterized the nonlinear electromagnetic wave effects by q (sometimes called η),

$$q^2 = 2\frac{e^2\langle A^2\rangle}{m_0^2c^4}, \tag{1}$$

where c is the speed of light, e and m_0 are the electron charge and rest mass, respectively, ω is the laser frequency, and $\langle A^2\rangle$ is the time average of the square of the vector potential of the laser. When $q < 1$, it is related to the ponderomotive potential (average quiver energy) of the laser, by $\Phi_{\text{pond}} = q^2mc^2/4$. When q approaches 1, a significant drift of the electron in the direction of field propagation arises. This drift, first predicted quantum mechanically in 1964 by Brown and Kibble[2] and classically by Eberly and Sleeper[3] in 1968, is second order in q.

In a laser focus, even at small q, an electron feels a force along the gradient of the ponderomotive potential. At moderate intensities, an electron born in a cylindrically symmetric laser focus with **k** in the z direction, is radially accelerated out of the focus.[4,5] An electron gains the full ponderomotive energy if the laser pulse duration τ_L is longer than the time it takes the electron to escape from the laser focus, τ_{esc}. If the laser pulse duration is sufficiently long, the electron's final kinetic energy for linear polarization is equal to its initial energy plus the ponderomotive potential at which it was born.[6] For circular polarization, the electron's final energy is twice its ponderomotive potential due to the conservation of angular momentum in the laser field.[7,8] An electron that is incident on a laser focus can be scattered off the ponderomotive potential, and, in the case of the standing wave, the electron can be Bragg scattered—the Kapitza-Dirac effect.[9] These effects were observed by Bucksbaum *et al.*[10,11] These and all other ponderomotive experiments have examined first-order effects in q and have been conducted with $q << 1$.

References 1–3 assumed that a free electron was initially at rest before the interaction with a plane-wave laser field. In our experiments an electron is released via ionization into the presence of an already intense electromagnetic field. The measurement of electrons with energies exceeding the minimum required for ionization has been labeled above threshold ionization (ATI) and reviewed recently by Freeman and Bucksbaum.[12] Electrons created by ionization are typically released with a few electron volts of energy, which can be considered to be at rest when the ponderomotive potential is much larger. This was observed in experiments by Corkum *et al.*,[7] where $q \sim 0.01$ and the electrons were observed in the radial direction due to their initial drift velocity. Free-electron interactions with laser pulses where q approaches 1 are examined in this experiment. This allows examination of second-order effects in q and, in particular, the predicted longitudinal drift.

The longitudinal drift of an electron was shown by Corkum *et al.*[13] to arise from the absorbed longitudinal momentum that accompanies the energy absorption from the focused laser field. The longitudinal momentum p_z is related to the perpendicular momentum by[13]

$$p_z = \frac{p_\perp^2}{2m_0c}. \tag{2}$$

The perpendicular momentum is related to the total energy by $p_\perp = m_0c\sqrt{2(\gamma-1)}$.[13] Electrons leave the laser focus at an

angle θ with respect to the k vector of the laser given by

$$\theta = \tan^{-1}\sqrt{\frac{2}{\gamma - 1}}. \tag{3}$$

The perpendicular momentum arises from two sources: the conservation of canonical angular momentum[1,14] and the ponderomotive acceleration out of the focus.[2,3]

The longitudinal drift arising from the conservation of angular momentum can be derived from the Hamilton-Jacobi method of Sarachik and Schappert[1] or directly from the invariance of the canonical momentum and energy.[14] If the electron is assumed to be born at $t = 0$ in a field that is uniform in the transverse direction, the electron drift velocity in the nonrelativistic limit, after the laser pulse has passed, is

$$\vec{v}_D = \frac{e}{mc}\vec{A}(0) + \frac{\vec{k}}{|k|}\frac{e^2A^2(0)}{2m^2c^3}. \tag{4}$$

The first term in Eq. (4) represents the transverse drift associated with the conservation of canonical angular momentum; the second term is the associated longitudinal drift. Equation (4) agrees with Eq. (2). If the electron is assumed to be born at the peak of the field, then $A(0) = 0$ for linear polarization, while $|A(0)| = c|E(0)|/\omega$ for circular polarization, where $E(0)$ is the electric field at the time the electron is born.

Reiss[15] and Delone and Krainov[16] have performed detailed calculations of the initial momenta of electrons produced due to the ionization of atoms in strong fields. Both found that for circular polarization the electrons had a forward momentum that was consistent with Eq. (4).

A second radial drift is associated with ponderomotive acceleration out of the laser focus.[2,3] In the weakly relativistic limit, $q < 1$, the radial ponderomotive energy is given by

$$\Phi_p = \frac{e^2\langle A^2\rangle}{2mc^2} = \frac{e^2\langle E^2\rangle}{2m\omega^2}, \tag{5}$$

where $\langle A^2\rangle$ is the temporal average of the square of the vector potential at the time of ionization. Thus for weakly relativistic conditions, an electron born in the focus of a laser pulse will have a final perpendicular velocity

$$v_{\perp r}(\infty) = \left\{\frac{2}{m}\left[\left(\frac{eA(0)}{\sqrt{2}mc^2}\right)^2 + \Phi_{\text{pond}}\right]\right\}^{\frac{1}{2}}\hat{r}. \tag{6}$$

In the above analysis, it is assumed that the laser pulse duration is long enough that the electrons can turn all of the ponderomotive energy into directed kinetic energy.[6] We can combine Eq. (6) with Eqs. (2) and (4) to determine the final drift velocity for circular polarization when $\tau_{\text{esc}} << \tau_L$,

$$\vec{v}_D(\infty) = \sqrt{2}v_{\text{osc}}\hat{r} + \frac{v_{\text{osc}}^2}{c}\hat{z}, \tag{7}$$

and for linear polarization,

$$\vec{v}_D(\infty) = \frac{v_{\text{osc}}}{\sqrt{2}}\hat{r} + \frac{v_{\text{osc}}^2}{4c}\hat{z}. \tag{8}$$

The quiver velocity v_{osc} is defined in terms of the peak electric field (field at ionization),

$$v_{\text{osc}} = \frac{|eE(0)|}{m\omega}. \tag{9}$$

The drift of the electrons is shown schematically in Fig. 59.8.

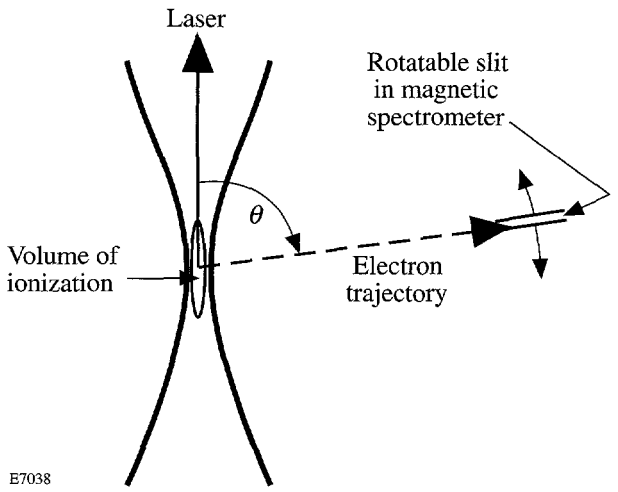

Figure 59.8
Experimental setup showing the position of the magnet gap in the spectrometer in relation to the laser focus, a typical electron trajectory, and the definition of θ. The volume of ionization refers to the volume in which the intensity exceeds the threshold intensity of ionization for a particular charge state and is not to scale.

These results have been confirmed by a fully relativistic Monte Carlo simulation of the electron dynamics. The simulation involved propagating a circularly polarized, Gaussian temporal and spatial profile laser pulse over a few thousand atoms placed at random positions within a laser focus. The laser parameters were based on measurements of the corresponding parameters of our laser system. Electrons were released into the field at the intensity necessary for Coulomb barrier suppression ionization (BSI),[17]

$$E = \frac{\varepsilon_{\text{ion}}^2}{4Z}, \tag{10}$$

where ε_{ion} is the ionization potential and Z is the ionic charge with zero initial velocity. The fully relativistic equation of motion

$$\dot{\vec{p}} = -e\vec{E} - \frac{e}{\gamma mc}\vec{p} \times \vec{B} \tag{11}$$

for the electron trajectories was solved for each electron, and the electrons' positions and velocities after exiting the focus were stored. These electron trajectories, which agreed with Eq. (7), were then convolved with the spectrometer characteristics to give the expected observed energy and angular distributions.

The experiment consisted of creating free electrons via ionization in the laser focus and measuring the ejected electron distributions as a function of energy and angle from the beam axis.

We have constructed a magnetic spectrometer to measure the energy and angular distributions of electrons emitted from a high-intensity laser focus. The spectrometer consists of a magnet for steering the electrons, a scintillator for detection of the electrons, and a photo-multiplier-tube (PMT) for detection of photons created in the scintillator.

The steering magnet is a 10-cm-square piece of high-purity iron with a 6-cm-square cut from the center. A 2-mm gap was cut in one side of the iron, and coils of wire were wrapped around the other three sides of the iron to create an electromagnet. A 100-ms square-topped pulse of voltage is applied across the coils of the magnet resulting in a magnetic field in the gap. The electromagnet is fired 80 ms before the laser pulse, allowing the magnetic field in the gap to be in a steady state by the time electrons are ionized in the laser focus. Residual fields or hysteresis effects on the iron core of the magnet are minimized by degaussing after every firing of the magnet using a slowly diminishing ac current. This technique allows magnetic fields in the gap from 50 to 6000 G to be reliably formed with less than 5% fluctuation from shot to shot.

The magnet is placed above the laser focus with the 2-mm gap aligned with the focus, allowing a line of sight to be traced from the focus through the gap in the magnet. Electrons emitted from the laser focus toward the gap in the magnet enter the gap and are curved by the magnetic field. Electrons with energies giving a gyro-radius of approximately 1.5 cm in the applied magnetic field travel through the gap and strike the scintillator where ultraviolet photons are emitted. The photon flux is then measured using the PMT, and the electrical signal is read by an analog-to-digital converter, which gives a number of counts proportional to the electron number and energy. Peak signal-to-noise ratios of 1000 to 1 are obtained with this setup. The direct line of sight from the focus to scintillator is blocked by 3 cm of aluminum shielding. Aluminum sheet metal is used elsewhere as shielding so that the only possible noise source is stray light through the gap in the magnet.

The energy window of the spectrometer is varied by changing the magnetic field in the gap of the steering magnet. A calibration has been performed using an electron gun producing electrons of known energy. The electron gun was placed at the laser focus and aimed toward the gap in the steering magnet. The magnetic field in the gap was varied by adjusting the voltage applied across the coils of the electromagnet allowing a measurement of the applied voltage versus electron energy. The calibration showed an energy window of $\Delta E/E \sim 0.3$ FWHM. Monte Carlo predictions of the calibration curve are in excellent agreement with the measured calibration.

The angular distribution of electrons in θ (relative to the k of the laser) is measured by rotating the entire spectrometer, which is cylindrically shaped. The central axis of this cylinder passes through the laser focus at 90° to the laser axis. The gap in the magnet is offset from the central axis of the spectrometer and is always aligned so that a clear line of sight can be traced from anywhere on this central axis through the gap in the magnet (see Fig. 59.8).

An angular resolution of ±2° is achieved with this setup. This uncertainty comes from two sources: The first is the geometric angular resolution due to the gap in the magnet. The gap is 2 mm wide, which corresponds to an angular spread of

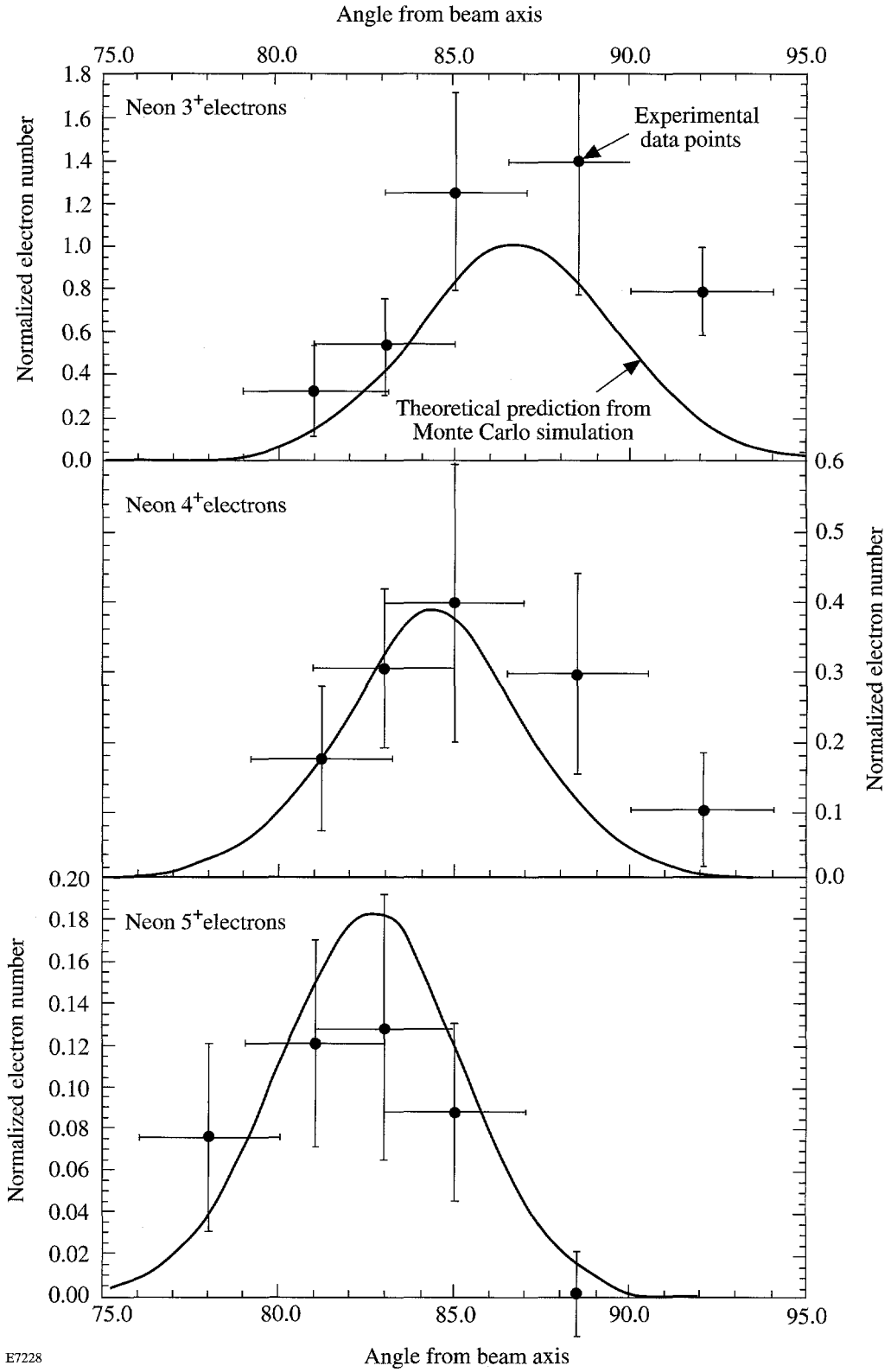

Figure 59.9
Observed experimental angular distribution data points for electrons ionized from the 3^+, 4^+, and 5^+ charge states of neon. The solid curve represents the expected angular distribution for each charge state from the theoretical Monte Carlo simulation of the electron dynamics.

±1° for electrons traveling from the laser focus. The second is due to an asymmetry in the magnetic field of the magnet in the spectrometer. A slight tilt found in the magnetic field deflected electrons by 5°±1° from their original ejection angle. This angle was determined from the detection angle of the Ne^{3+} electron peak on one side of the laser focus compared to its position on the opposite side of the focus. The symmetry of the focus requires that this peak occur at the same angle from the k vector of the laser on both sides of the focus. This was used to determine the angle of electron deflection due to the tilt in the field. This determination is accurate to ±1° and, when combined with the geometric resolving power of the gap, gives a total uncertainty in the angle of ±2°.

The experiments were performed with a 1.05-μm, 1-ps laser system using chirped-pulse amplification (CPA), which is described elsewhere.[18] The experiment discussed in this article was conducted in neon at a pressure of 5×10^{-4} Torr. The laser was focused with $f/6$ optics producing a 5-μm ($1/e^2$ radius) focal spot and a peak laser intensity of approximately 5×10^{17} W/cm^2 ($q \sim 0.5$). Circular polarization was used to avoid possible asymmetries in the electron angular distribution in the plane of polarization upon ionization due to non-zero initial velocities of the electrons along the electric field.[7]

Helium was ionized to confirm the expected ponderomotive energies associated with the BSI threshold intensities. This was accomplished by measuring the energy spectrum of helium and assuming that the highest energy electron peak was from He^{2+}. The energy of this peak was 3.0 kV, which is in agreement with the approximate expected value of 3.5 kV based on BSI in circular polarization and subsequent acceleration of the electron by the ponderomotive potential. Ne^{3+} is created at approximately the same intensity as He^{2+},[17] which was used to determine the electron peaks in the neon spectrum. Energies of the electrons ionized from the 3^+, 4^+, 5^+, and 6^+ charge states of neon were in agreement with the expected ponderomotive energies associated with their corresponding BSI threshold intensities.

Figure 59.9 shows the measured data values of the angular distribution of the 3^+, 4^+, and 5^+ electrons of neon and their expected theoretical positions based on the Monte Carlo simulation. The angular spread in the electron distributions is due primarily to the intensity distribution of the laser focus. The ponderomotive force is linearly related to the gradient of the intensity distribution, which is not always perpendicular to the beam axis in a focused Gaussian beam. As a result some electrons have a small component of ponderomotive acceleration along the beam axis. This acceleration is symmetric about 90° to the beam axis due to the symmetry of a Gaussian beam as it passes through focus and cannot explain any forward shift of the peak of the electron distribution. A normalized electron number is used on the y axis since we do not have an absolute calibration of the number of electrons striking the scintillator in the experiment. A single normalization constant was used in a least-squares fit between the Monte Carlo simulation and experimental data for all three charge states.

Figure 59.10 shows the angle of peak electron number for the 3^+, 4^+, and 5^+ neon charge states measured as a function of electron energy. The points found from the Monte Carlo simulation are in good agreement with the angular distribution predicted in Eq. (3). The experimental points are in good agreement with both of these predicted values. From this we conclude that a nonsymmetric forward acceleration of the electrons has been observed, consistent with the forward drift found in Refs. 1–3.

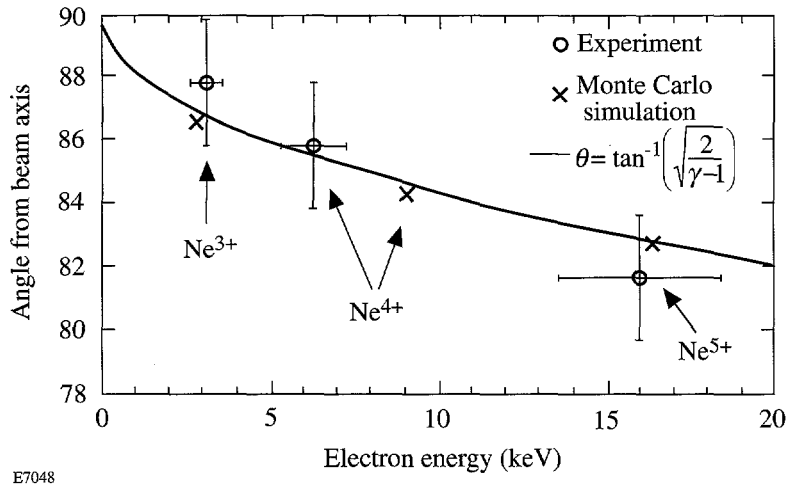

Figure 59.10
Angle of peak electron number for the 3^+, 4^+, and 5^+ electrons of neon from the theoretical Monte Carlo simulation of the electron dynamics and the observed experimental data points. The solid curve is the theoretical prediction of Eq. (4).

We have made the first observations of a forward acceleration of electrons in a high-intensity laser focus. Good agreement is shown between the forward shifted angle of the fully relativistic theoretical predictions and the data obtained.

ACKNOWLEDGMENT

The author's gratefully acknowledge conversations with J. H. Eberly. This work was supported by the U.S. Department of Energy Office of Basic Energy Sciences, Division of Chemical Sciences. Additional support was provided by the U.S. Department of Energy Office of Inertial Confinement Fusion under Cooperative Agreement No. DE-FC03-92SF19460, the University of Rochester, and the New York State Energy Research and Development Authority. The support of DOE does not constitute an endorsement by DOE of the views expressed in this article.

REFERENCES

1. E. S. Sarachik and G. T. Schappert, Phys. Rev. D **1**, 2738 (1970).
2. L. S. Brown and T. W. B. Kibble, Phys. Rev. **133**, A705 (1964).
3. J. H. Eberly and A. Sleeper, Phys. Rev. **176**, 1570 (1968).
4. H. A. H. Boot, S. A. Self, and R. B. R-Shersby-Harvie, J. Elect. Control **4**, 434 (1958).
5. T. W. B. Kibble, Phys. Rev. **150**, 1060 (1966).
6. R. R. Freeman *et al.*, Phys. Rev. Lett. **59**, 1092 (1987).
7. P. B. Corkum, N. H. Burnett, and F. Brunel, Phys. Rev. Lett. **62**, 1259 (1989).
8. P. H. Bucksbaum *et al.*, Phys. Rev. A **41**, 4119 (1990).
9. P. L. Kapitza and P. A. M. Dirac, Proc. Cambridge Philos. Soc. **29**, 297 (1933).
10. P. H. Bucksbaum, M. Bashkansky, and T. J. McIlrath, Phys. Rev. Lett. **58**, 349 (1987).
11. P. H. Bucksbaum, D. W. Schumacher, and M. Bashkansky, Phys. Rev. Lett. **61**, 1182 (1988).
12. R. R. Freeman and P. H. Bucksbaum, J. Phys. B: At. Mol. Opt. Phys. **24**, 325 (1991).
13. P. B. Corkum, N. H. Burnett, and F. Brunel, in *Atoms in Intense Fields*, edited by M. Gavrila (Academic Press, New York, 1992), pp. 109–137.
14. W. B. Mori and T. Katsouleas, Phys. Rev. Lett. **69**, 3495 (1992).
15. H. R. Reiss, J. Opt. Soc. Am. B **7**, 574 (1990).
16. N. B. Delone and V. P. Krainov, J. Opt. Soc. Am. B **8**, 1207 (1991).
17. S. Augst, D. Strickland, D. D. Meyerhofer, S. L. Chin, and J. H. Eberly, Phys. Rev. Lett. **63**, 2212 (1989).
18. Y.-H. Chuang, D. D. Meyerhofer, S. Augst, H. Chen, J. Peatross, and S. Uchida, J. Opt. Soc. Am. B **8**, 1226 (1991).

Spatial Intensity Nonuniformities of an OMEGA Beam due to Nonlinear Beam Propagation

Several applications require that a laser beam maintain a high degree of wavefront quality after propagating a long distance through air. In particular, laser drivers for inertial confinement fusion use intense laser beams that propagate tens of meters through air to a fusion target. Many amplification stages are required in the system to reach the energy levels required for each beam. Good beam quality is essential throughout the system to prevent the onset of nonlinear effects that can lead to optical damage or wavefront degradation. To maintain beam quality, spatial filters are used between amplification stages to remove high-spatial-frequency modulation impressed onto the beams by random or fixed phase distortions in the beam paths. Despite the use of spatial filters, the wavefront quality of a high-energy laser can be degraded, and nonlinear optical effects can occur in the system.

Forward stimulated rotational Raman scattering (SRRS) can be generated when intense laser fields propagate through air[1–3] due to the N_2 molecules in the interaction path. This unwanted Raman radiation can degrade the spatial as well as the temporal characteristics of the beam. In addition, when a high-energy laser is focused into a spatial filter, the residual material remaining in the spatial filter can act as a nonlinear medium to again degrade the beam quality.

It is well known that for Raman scattering the coupling between the Raman Stokes and anti-Stokes radiation in a dispersive medium leads to the generation of conical emission.[4] The Stokes and anti-Stokes radiation is emitted at angles to the optical axis due to phase matching and is azimuthally symmetric about the optical axis. If the cylindrical symmetry of the pump wave is broken, then another phase-matched four-wave-mixing process can break the azimuthal symmetry of the conical emission, and a transverse modulational instability can occur. This instability manifests itself as preferential gain at six angles uniformly spaced around the cone, resulting in six intensity peaks around the cone resembling a hexagonal intensity distribution in the far field. Evidence of this four-wave-mixing convective instability was first reported by Tan-No *et al.*[5] in 1980. Since then several other observations have been reported along with several theoretical analyses.[5–13] The majority of the work in this field has been performed with counter-propagating pump beams in a nonlinear medium. A notable exception is the work of Pender and Hesselink,[9] who observed this instability with a single forward pump wave as in the experiments performed with the OMEGA laser to be discussed here.

Two separate experiments were performed with the OMEGA laser that show evidence of this transverse modulational instability. In the first experiment a beam underwent free propagation through air, and the instability was observed in the presence of SRRS. In the second experiment a 1-kJ laser was focused into a vacuum spatial filter having a 50-μm residual fill pressure, and the instability was observed in the near field after the spatial filter. These experiments illustrate that in order to determine the details of the spatial structure of an intense beam propagating in a nonlinear medium, this four-wave-mixing transverse modulational instability must be considered.

Experiments

Two separate experiments that exhibit transverse modulational instabilities were performed. In one experiment, the generation of SRRS in air was studied to determine the effects of SRRS on the propagation of OMEGA Upgrade beams as they propagate through air to a target. In another experiment the requirements on the final fill pressure for high-energy spatial filters was studied.

In the first experiment[2] a third-harmonic beam at 351-nm wavelength 600-ps full-width at half-maximum (FWHM) from the OMEGA laser was down collimated to approximately a 5-cm beam diameter and propagated over a 35-m path length in air. The near-field beam intensity profile was recorded on film at the beginning and end of the beam path. The spectral content of the beam was also recorded on film at the end of the air path using a 1-m spectrometer. The film was

developed, digitized with a microdensitometer, and converted to intensity exposure by using the appropriate film-density, log-intensity calibration for the film and for the experimental conditions used.

The spectrum, displayed in Fig. 59.11, clearly shows the generation of Stokes and anti-Stokes radiation from the SRRS process in air. For this experiment approximately 1% of the laser energy was converted to SRRS.

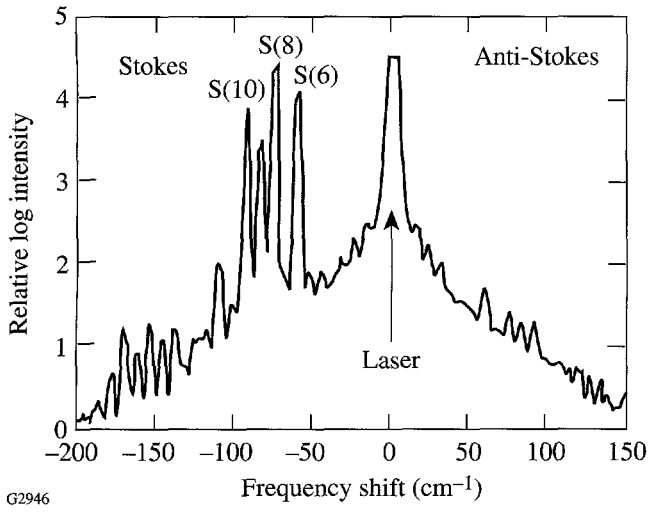

Figure 59.11
Raman spectrum showing several of the *S* transitions of nitrogen in air. The pump laser saturated the film at a frequency shift equal to zero.

The intensity distribution at the end of the 35-m air path is shown on a log scale in Fig. 59.12, where strong intensity modulation can be seen. To determine the spatial frequency content of the beam at the end of the air path, a two-dimensional FFT was calculated from the measured intensity distribution. To highlight the features in the FFT, the central portion of the FFT (containing the near dc spatial components) was blocked, and the FFT was plotted on a log scale, as shown in Fig. 59.13. Although the FFT is symmetric about positive and negative frequencies, it clearly shows evidence of the hexagonal pattern in the far field associated with the transverse modulational instability.

In the second experiment a beam with 1 kJ of energy, 700-ps FWHM, and a 1054-nm wavelength was focused into a spatial filter. The spatial filter input and output beam diameters were 18 cm, and the *f* number of the spatial filter was equal to 14. In an attempt to determine the maximum fill pressure allowed for this spatial filter with these beam param-

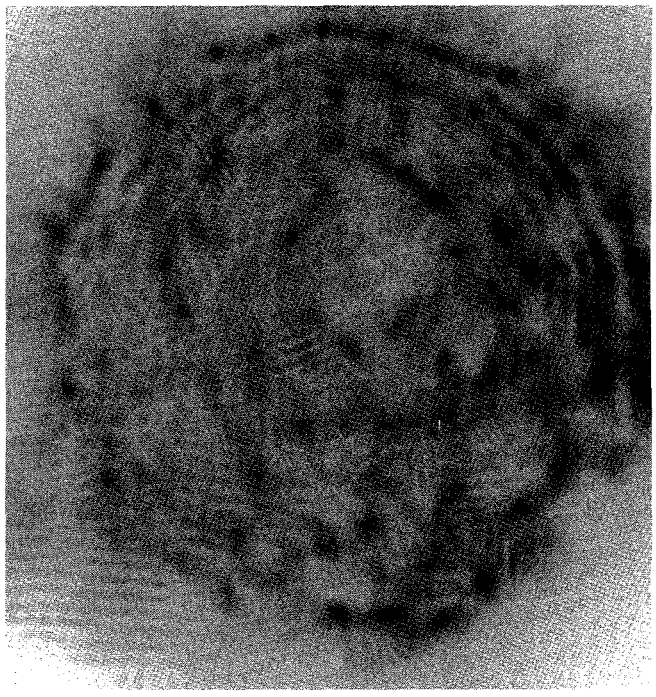

Figure 59.12
Near-field intensity distribution of the beam after propagating 35 m in air, plotted on a log scale.

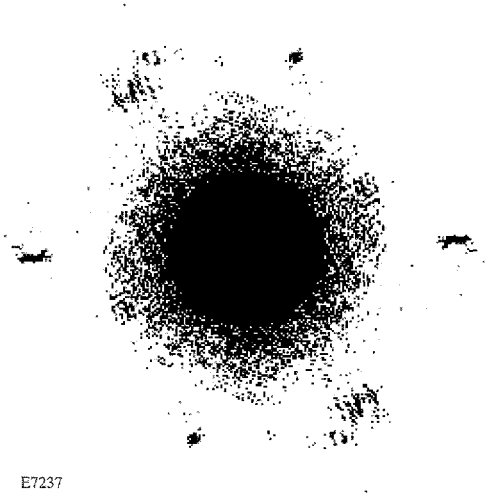

Figure 59.13
FFT of the near-field intensity distribution of the beam after propagating 35 m in air. The central portion of the FFT containing the low spatial frequencies was blocked, and the remaining FFT was plotted on a log scale. The hexagonal intensity distribution surrounding the central spot can be seen and is caused by the transverse modulational instability.

eters, the fill pressure was varied, and the beam intensity distribution after the spatial filter was recorded on film. The film was again digitized and intensity converted. The input beam to the spatial filter was slightly astigmatic. The intensity modulation on the beam exiting the spatial filter with a 50-μm residual fill pressure (the highest pressure used in the experiments) is shown in Fig. 59.14. To enhance the intensity modulational features on the image of the beam, a constant intensity (equal to 80% of the maximum intensity) was subtracted from the digitized near-field intensity distribution of the beam. The results are shown in Fig. 59.14. In this figure a hexagonal intensity distribution can be seen at the approximate center of the distribution centered on the cross with a diameter approximately equal to the beam radius. Additional modulation at the edges of the intensity distribution can also be seen. For this experiment, no measurements were made of the spectral content of the beam.

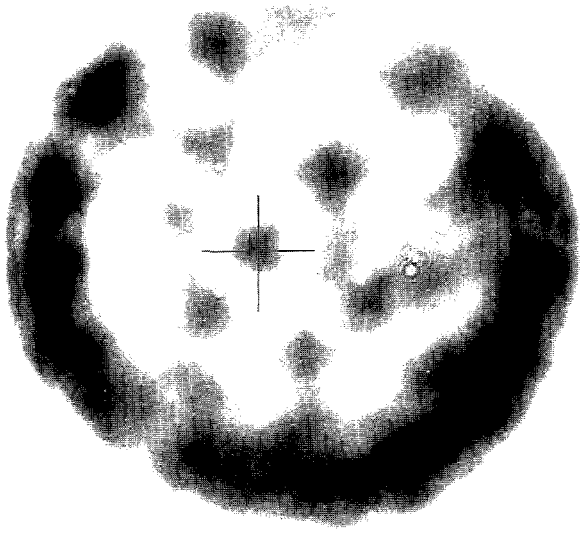

E7238

Figure 59.14
Near-field intensity distribution of a 1-kJ beam at 1054-nm wavelength after propagating through a spatial filter with a 50-μm residual fill pressure. To help illustrate the modulation, 80% of the beam intensity was subtracted from the image. The hexagonal intensity distribution caused by the transverse modulational instability can be seen centered on the cross with a diameter approximately equal to the beam radius.

The above experiments show evidence of a transverse modulational instability with a high-energy laser. The observed hexagonal intensity distributions are characteristic of a four-wave-mixing interaction that can be understood through simple modeling using the plane-wave approximation.

Theory and Discussion

Stokes and anti-Stokes SRRS will be generated when an intense laser beam propagates over a long path in air. Appreciable amounts of this radiation are created when the product of the laser intensity times the interaction length exceeds a minimum threshold. In a dispersive medium, the coupling between the Stokes and anti-Stokes fields leads to conical emission. If the pump laser is not cylindrically symmetric, then the coupling between the Stokes and anti-Stokes fields can lead to the observed transverse modulational instability.

To see the origin of this transverse modulational instability we follow the analysis of Pender and Hesselink[9] and begin with the wave equation in a Raman active medium:

$$\nabla^2 E - \frac{n^2}{c^2}\frac{\partial^2 E}{\partial t^2} = \frac{4\pi}{c^2}\frac{\partial^2 P^{NL}}{\partial t^2}, \tag{1}$$

where the nonlinear polarization is given by

$$P^{NL} = \chi^{(3)} E^3 . \tag{2}$$

We assume that the seven waves making up the hexagonal intensity distribution (the six waves uniformly spaced around the cone plus one on axis) are all linearly polarized, have the same frequency (such as all Stokes frequencies), and propagate in the near forward direction (i.e., no counterpropagating beams). For clarity the seven waves are shown in Fig. 59.15. In the plane wave approximation we assume that the total electric field E is given by the sum of the laser field and a sum over seven Stokes and seven anti-Stokes fields. With these assumptions, the total electric field in the medium is given by

$$E = E_L e^{-i(\omega_L t + \mathbf{k}_L \cdot \mathbf{z})} + \sum_{j=0}^{6} E_{Sj} e^{-i(\omega_S t + \mathbf{k}_{Sj} \cdot \mathbf{z})} + \sum_{j=0}^{6} E_{Aj} e^{-i(\omega_A t + \mathbf{k}_{Aj} \cdot \mathbf{z})} + cc, \tag{3}$$

where the subscripted E's are the amplitudes of waves with frequency ω and wave vector $\mathbf{k}$, and the subscripts L, S, and A denote the laser, Stokes, and anti-Stokes fields, respectively. If we cube this total electric field, substitute into the optical wave Eq. (1) with the appropriate nonlinear polarization [Eq. (2)], and make the standard assumptions in steady state, we get for a typical Stokes field ($S1$ in Fig. 59.15, for example)

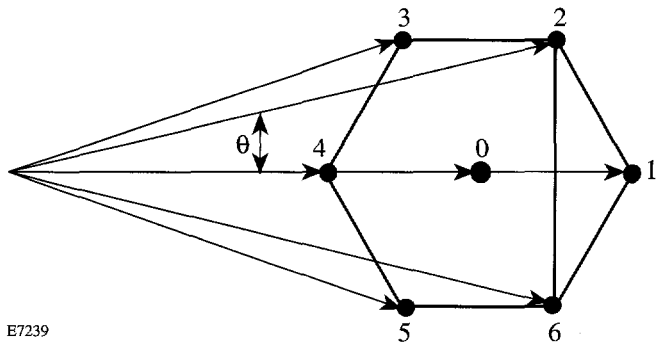

Figure 59.15
Diagram of the seven beams making up the hexagonal intensity distribution characteristic of the transverse modulational instability.

$$\frac{\partial E_{S1}}{\partial z} = -i\gamma\left\{|E_L|^2 + \sum_{j=0}^{6}|E_{Aj}|^2 + \sum_{j=0}^{6}|E_{Sj}|^2 - \frac{1}{2}|E_{S1}|^2\right\}E_{S1}$$

$$-i\frac{\gamma}{2}E_L^2E_{A4}^*\exp[-i\Delta k_{A4}z]$$

$$-i\frac{\gamma}{2}E_{S0}^*E_{S2}E_{S6}\exp[+i\Delta kz]$$

$$-i\frac{\gamma}{2}E_{S0}\left(E_{S2}E_{S3}^* + E_{S6}E_{S5}^*\right)\exp[-i\Delta kz]$$

$$-i\frac{\gamma}{2}E_{S4}^*E_{S0}^2\exp[-i2\Delta kz]$$

$$-i\frac{\gamma}{2}E_{S4}^*\left(E_{S2}E_{S5} + E_{S3}E_{S6}\right) \qquad (4)$$

with $\Delta k_{Aj} = \left(2\mathbf{k}_L - \mathbf{k}_{S1} - \mathbf{k}_{Aj}\right)\cdot\mathbf{z}$ and $\Delta k = k(1-\cos\theta)$ and where θ is the cone angle for Stokes and anti-Stokes coupling and γ is the coupling coefficient. This equation describes the evolution of one of the Stokes waves (wave $S1$) in the medium and has many contributions that will be discussed further to provide insight into the nature of the instability.

The first term on the right in Eq. (4) contains the intensity-induced refractive index terms and gives rise to ordinary stimulated scattering. The second term on the right is the Raman Stokes and anti-Stokes coupling term that can be completely phased matched $\left(\Delta k_{Aj} = 0\right)$, even in a dispersive medium. In a dispersive medium phase matching occurs when the Stokes and anti-Stokes fields propagate at some angle to the optical axis giving rise to conical emission. (This second term has azimuthal symmetry and is present for any choice of Stokes wave around the cone.)

The third and fourth terms are largely responsible for the transverse modulational instability. The third term on the right is a near-phase-matched, four-wave-mixing term and gives rise to loss for $S1$, i.e., one photon is absorbed from each of beams $S0$ and $S1$ and reemitted into beams $S2$ and $S6$. Near complete phase matching for this process occurs and can be seen from Fig. 59.15 since a line drawn through $S2$ and $S6$ and a line drawn through $S0$ and $S1$ bisect one another. (A small phase mismatch Δkz exists due to the off-axis propagation of the waves involved. Perfect phase matching would occur only for all waves propagating in the forward direction; however, the additional gain provided in this off-axis direction by ordinary conical emission outweighs the loss due to this phase mismatch.) In a similar manner, the fourth term on the right contains two near-phase-matched (by the same argument given for the third term), four-wave-mixing terms. These contributions give rise to additional gain for $S1$ at the expense of the pair of waves $S2$ and $S3$ and the pair $S5$ and $S6$. Hence, hexagonal position $S1$ has two gain contributions [Eq. (4), term (4)] and one loss contribution [Eq. (4), term (3)] resulting in net gain due to the four-wave-mixing process associated with the transverse modulational instability. This implies that if Stokes wave $S1$ is present, it will lead to the efficient generation of the other Stokes waves around the hexagon since we can rotate the cone by 60° and repeat the argument. The location of $S1$ along the cone, however, is arbitrary, and for an azimuthally symmetric pump laser we would expect ordinary conical emission. If, on the other hand, the pump laser is not perfectly symmetric about the optic axis, then the Stokes wave at $S1$ may experience higher gain than the other waves around the cone, which will initiate the instability leading to the formation of the hexagonal intensity distribution.

The fifth and sixth terms on the right are terms that contribute to uniform gain around the cone and, hence, do not contribute to the instability.

Equation (4) was derived assuming that only seven Stokes waves were present. For analytical purposes Pender and Hesselink assumed 13 waves in their analysis (12 waves uniformly spaced around the cone plus one on axis). In their numerical analysis they show that for uniform seeding of all 13 waves only ordinary conical emission results. If, on the other hand, one of the waves on the cone is seeded with a

higher intensity then the others, this wave and the other five waves making up the corresponding hexagonal intensity distribution see higher gain than the remaining six around the cone. In fact, the six waves that do not see gain actually experience loss, implying that, in this case, energy is redistributed around the cone favoring the hexagonal pattern formation. Equation (4) is in the same form as that of Pender and Hesselink, and, hence, their results are expected to apply here. Thus, it is plausible to expect a transverse modulational instability to occur in the presence of stimulated Raman scattering as was observed in the experiments discussed above.

Conclusions

Transverse modulational instabilities have been observed in an OMEGA beam in two separate experiments. In one experiment a collimated beam with 351-nm wavelength propagated through air, and the instability was observed in the presence of stimulated rotational Raman scattering. In the second experiment, the instability was observed when a 1-kJ laser pulse with 1054-nm wavelength was focused into a spatial filter having a 50-μm residual pressure. In both experiments, the transverse modulational instability took the form of a hexagonal intensity distribution in the far field of the interaction region.

A qualitative analysis of the instability can be performed in the plane-wave approximation. The instability is due to a phase-matched, four-wave-mixing interaction involving the Raman Stokes and anti-Stokes fields in the medium. The data and analysis agree well with similar work in the field. A complete analysis of the beam intensity modulation on a high-energy laser should include the effects of this transverse modulational instability.

ACKNOWLEDGMENT

The author thanks J. Kelly, K. Thorp, and M. Tedrow for experimental results that lead to Fig. 59.14 and to R. Bahr for his work on the SRRS experiment. This work was supported by the U.S. Department of Energy Office of Inertial Confinement Fusion under Cooperative Agreement No. DE-FC03-92SF19460, the University of Rochester, and the New York State Energy Research and Development Authority. The support of DOE does not constitute an endorsement by DOE of the views expressed in this article.

REFERENCES

1. M. A. Henesian, C. D. Swift, and J. R. Murray, Opt. Lett. **10**, 565 (1985).
2. M. D. Skeldon and R. E. Bahr, Opt. Lett. **16**, 366 (1991).
3. Laboratory for Laser Energetics LLE Review **52**, NTIS document No. DOE/DP/40200-229, 1992 (unpublished), p. 211.
4. N. Bloembergen, *Nonlinear Optics* (The Benjamin/Cummings Publishing Co., Inc., MA, 1982).
5. N. Tan-No, T. Hoshimiya, and H. Inaba, IEEE J. Quantum Electron. **16**, 147 (1980).
6. G. Grynberg, Opt. Commun. **66**, 321 (1988).
7. G. Grynberg *et al.*, Opt. Commun. **67**, 363 (1988).
8. A. L. Gaeta, M. D. Skeldon, R. W. Boyd, and P. Narum, J. Opt. Soc. Am. B **6**, 1709 (1989).
9. J. Pender and L. Hesselink, J. Opt. Soc. Am. B **7**, 1361 (1990).
10. R. Chang *et al.*, Opt. Commun. **88**, 167 (1992).
11. J. B. Geddes, J. V. Moloney, and R. Indik, Opt. Commun. **90**, 117 (1992).
12. J. Y. Courtois and G. Grynberg, Opt. Commun. **87**, 186 (1992).
13. M. Tamburrini *et al.*, Opt. Lett. **18**, 855 (1993).

Calculated X-Ray Backlighting Images of Mixed Imploded Targets

Shell-core mixing, which can occur during the deceleration phase of a laser-driven implosion, is believed to be the major limitation on target performance. This mixing is brought about by a hydrodynamic instability during the deceleration phase, which is seeded by instability generated during the acceleration phase due to laser and target nonuniformities.[1] The image of the x-ray emission from the shell (enhanced by high-Z doping) was used in recent experiments to diagnose this effect.[2] Because of the limb effect, this emission appears in the image in the form of a ring; mixing causes this emission ring to move toward smaller radii. However, the difference in the image characteristics between mixed targets and unmixed targets, which compress to a smaller radius, is subtle: in the former case, the outward drop in intensity is slower. Thus, a smaller compression and mixing tend to cancel each other's effect on the position of the ring in the image.

We show here that when backlighting imaging is used in the experiment, that uncertainty can be largely removed. An important ingredient of such imaging is the ability to record simultaneously the backlighting image as well as the image due to the target self-emission. We showed earlier[3,4] that to achieve this requirement, the image has to be monochromatized by a diffracting crystal because self-emission from predicted OMEGA Upgrade targets was shown to completely overwhelm the intensity of any backlighting radiation. However, if most of the backlighter radiation is comprised in a single spectral line to which the monochromator is tuned, the two image components can be made to have comparable intensities.

An absorption ring appears in the image, outside the ring due to target self-emission, when the proper backlighter conditions are chosen. The results of this work show that, whereas the emission ring indeed moves to smaller radii when mixing is introduced, the backlighting absorption ring is virtually unaffected. Thus, the relative position of the two rings constitutes a mixing signature. In other words, the absorption ring delineates the colder part of the shell and is a true signature of the compression, whereas the emission ring reflects the shell material motion due to mixing.

We calculate here the combined backlighting and self-emission image of a particular simulated target implosion on the OMEGA Upgrade laser. For this test case, *LILAC* results were used for the expected temperature and density profiles of the unmixed target. A post-processor code was developed[4] to calculate the transport of backlight radiation through the target, as well as the self-emission of the target itself (and its transport). A simplified procedure is used to simulate the mixing, and the radiation transport equation is then solved for the unmixed as well as the mixed targets. The total calculated image has two components that are measured simultaneously: the one due to the backlighting, and the other due to target self-emission. The former is calculated assuming a certain incident flux level, based on experiments; the latter is directly calculated from the *LILAC* profiles, using the radiation transport code developed here.

The target is a polymer shell of 940-μm diameter and 30-μm thickness, filled with 80 atm DT gas, and imploded by a trapezoidal pulse. The pulse rises linearly over a 0.1-ns period to 13.5 TW, then remains constant for 2.2 ns, before dropping linearly over a 0.1-ns period. Figure 59.16 shows the density and electron-temperature profiles predicted for this target at peak compression. The shell material has been compressed to a mean radius of ~50 μm and thickness of ~30 μm, with a density in the range of ~10 to 50 g/cm^3, corresponding to a $\rho\Delta r$ value of ~90 mg/cm^2. The electron temperature in the shell ranges from ~80 to ~800 eV. Most of the backlight radiation absorption will occur within the colder, outer part of this compressed shell.

Modeling of Target Mixing

We follow a procedure suggested by Landen *et al.*[2] for choosing the size of the spatial region over which mixing occurs during the deceleration (or burn) phase of the implosion. It is implicitly assumed that the instability during the acceleration phase is not severe enough to disrupt the shell, but it only seeds the instability due to the deceleration. Figure 59.17 describes the procedure. The $R_i(t)$ curve represents the motion of the fuel-shell interface. The free-fall line $R_{ff}(t)$ is a constant-velocity trajectory tangent to the $R_i(t)$ curve

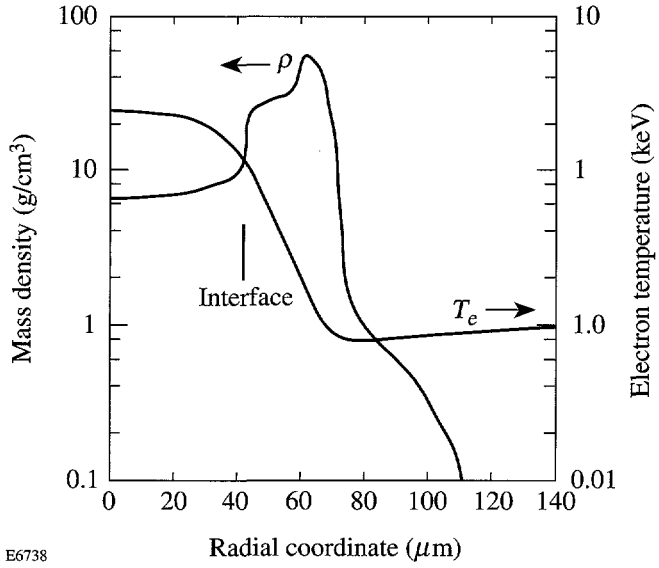

Figure 59.16
The density and electron-temperature profiles predicted by the *LILAC* code at peak compression for the case studied in this article.

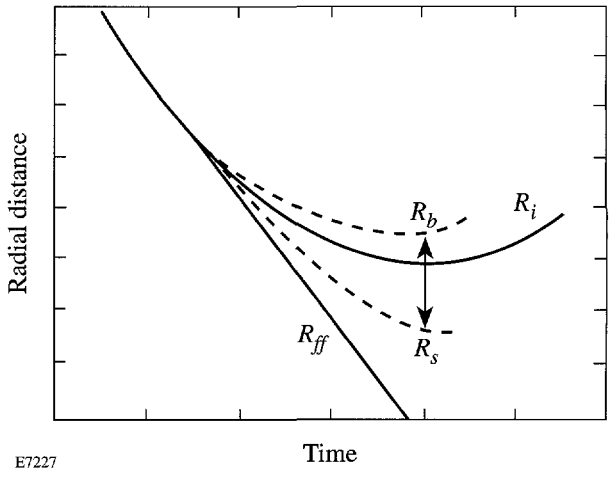

Figure 59.17
Schematic description of trajectories defining the mixed region [according to Eq. (1)]. R_i is the shell-fuel interface, R_{ff} the free-fall line, R_s the edge of the spikes region, and R_b the edge of the bubbles region. The mixed region extends from R_s to R_b.

at a time when the implosion velocity is maximal. A mixed region of F% means that the deepest penetration of shell material into the fuel region spans F% of the distance between the $R_i(t)$ curve and the free-fall line. Comparison with implosion experiments[2] on NOVA yielded a value of F ~20%; we show here results of calculations using this value and higher degrees of mixing. Simulations of Rayleigh-Taylor unstable implosions[5] show that in the nonlinear regime of the instability the shell (the heavier fluid) penetrates into the fuel (the lighter fluid) in the form of spikes. In between the spikes the fuel penetrates into the shell region in the form of bubbles whose penetration span is typically half that of the penetration of the spikes. We refer to the region comprised between $R_s(t)$ and $R_b(t)$ as the mixed region. In Fig. 59.17 the curves delineating the extreme positions of the spikes $R_s(t)$ and the bubbles $R_b(t)$ are shown schematically. Theory shows that for Atwood number 1 the amplitude of the spikes (measured from the unperturbed interface position) is twice that of the bubbles.[6] More specifically, for $F = 0.2$ the trajectories $R_s(t)$ and $R_b(t)$ will be given by

$$R_i(t) - R_s(t) = 0.2\left[R_i(t) - R_{ff}(t)\right],$$
$$R_b(t) - R_i(t) = 0.1\left[R_i(t) - R_{ff}(t)\right]. \quad (1)$$

The $R_i(t)$ curve for the test case analyzed here was plotted, and the parameters of the mixed region [$R_s(t)$ and $R_b(t)$] were determined as a function of time. At peak compression, the interface position with no mixing was $R_i = 42.7\ \mu$m, whereas the parameters of the mixed region for two particular values of F were

$$\text{for } F = 0.2: \quad R_s = 34.5\,\mu m, \quad R_b = 45.5\,\mu m$$
$$\text{for } F = 0.4: \quad R_s = 26.6\,\mu m, \quad R_b = 50.0\,\mu m. \quad (2)$$

Once the mixed region boundaries are thus determined, the procedure for the actual mixing must be determined. The manner in which the material is assumed mixed within the mixed region is somewhat arbitrary. We choose a simple prescription where the mixing is not uniform but rather decays with distance. The choice is made separately for the density of carbon ions (hence the density of shell material) and for the density of fuel ions. Using these choices, other parameters are calculated: the fraction of carbon ions out of the total ion density, the average charge $\langle z \rangle$, the total electron density, and the temperature. Figure 59.18 shows the mixing choices for the shell material and fuel (and some resulting distributions) for the test case, at peak compression (2.9 ns). Figure 59.18(a) shows the density N_C of carbon ions (atomic absorption calculations are done for C and H separately). The unmixed density curve is taken from *LILAC* runs, such as in Fig. 59.16. The

mixed curve for N_C is assumed to start from zero at R_s and to extend linearly with distance up to R_b. The slope of the curve is determined by the requirement that the mixing conserves mass (or the number of ions). As seen, this results in a jump at the $r = R_b$ position. This is not surprising if we note that the mixed profiles, such as the $N_C(R)$ curve in Fig. 59.18(a), represent lateral averages over the varying spike-bubble structure of the unstable region. The smearing, implicit in our assumption that the curves depend only on r, results in a sharp drop in laterally averaged density when crossing from the unmixed to the bubbles region.

Figure 59.18(b) shows the choice for the mixed profile of the fuel, N_F, using a slightly different prescription than that applied to the shell; N_F stands for the total density of D and T ions. The mixed curve is assumed to start from 0 at $r = R_b$ and to extend linearly inward up to the point where it meets the unmixed curve. Again, the slope of the curve is determined by the requirement that the mixing conserves mass. Because of the spike in the unmixed fuel profile near the interface, extending the linear profile all the way to $r = R_s$ would cause a transfer of fuel material from the spike inward, not only outward. Because of the choice made here, part of the fuel in the mixed region remains unaffected by the mixing (the fuel comprised between $r = 26.6$ and $r = 36.0$ μm).

To check how reasonable the resulting profiles are, we calculate the carbon fraction, defined as

$$f_C = N_C/(N_F + N_C + N_H). \quad (3)$$

Figure 59.18(c) shows that f_C is reasonably smooth and indeed reaches the correct boundary conditions: 0.5 at $r = R_b$

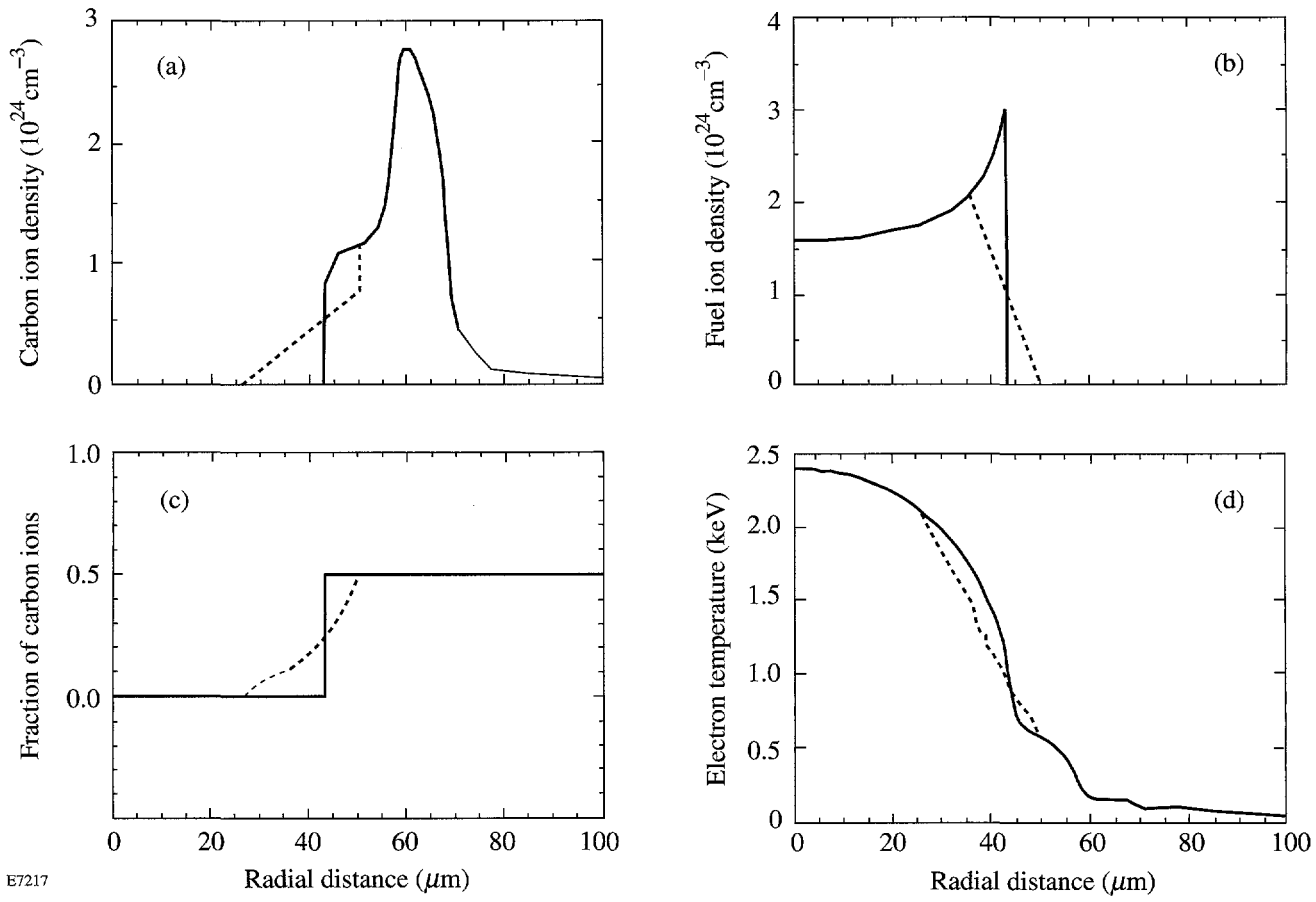

Figure 59.18
Radial profiles in the unmixed (—) and mixed (- - -) target, for $F = 0.4$ mixing: (a) the chosen distribution of carbon ion density (half the CH ion density), (b) the chosen distribution of fuel ions (half of which is D, half T), (c) the calculated distribution of the fraction of carbon ions among all hydrogenic ions (H, D, and T), and (d) the calculated distribution of the electron temperature. The shell-fuel interface position with no mixing is at 42.7 μm.

and 0 at $r = R_s$. A similar behavior is seen by the profile of the average charge.

We next calculate the effect of mixing on the temperature and electron density. We assume that the radial ordering of any two shell elements that moved into the fuel is the same as they had before moving, and likewise for fuel elements. We further assume that both CH or fuel material carry their own temperature as they move to new locations, where their temperature is then averaged with the local temperature (of material that has not moved). For example, the innermost shell cell in the unmixed target is assumed to map onto a region in the mixed target extending from $r = R_s$ outward, until the total mass in that cell is exhausted; a similar transfer holds for all consecutive shell cells within the mixed region. For the fuel, the outermost cell in the unmixed target maps in the mixed target onto the region extending from $r = R_b$ inward, etc. Once the temperatures of the fuel and shell elements in each zone are determined, the final temperature is given by the average of the two, weighted by the corresponding densities. The same applies to both the electron and ion temperatures. The unmixed and mixed electron temperature profiles at peak compression are shown in Fig. 59.18(d). Obviously, colder shell material lowered the temperature of the fuel region it migrated to, whereas hotter fuel material raised the temperature of the shell region it migrated to. Updating the electron density is similar to updating the temperature. The average charge $\langle z \rangle$ in each unmixed shell zone maps onto the corresponding mixed zones as before; the final electron density is given by $N_e = 2\langle z \rangle N_C + N_F$.

The modeling of target mixing, where a given shell layer is doped with a high-Z dopant, follows the same procedure as outlined above. Namely, the dopant material follows the CH element in which it was embedded initially, and the percentage of doping remains the same. The modeling used here does not include self-consistent feedback, i.e., the effect of mixing in one time step upon the hydrodynamics and radiation physics in subsequent steps. The limitations resulting from this simplification will be further discussed below.

Backlighting and Self-Emission Images of Unmixed Targets

Next we study the ability to diagnose mixing through its effect on target images due to both self-emission and backlighting. The problem of backlighting, including that of doped targets, has been studied previously.[4] In Fig. 59.19 we show an image of a doped but unmixed target, at $\lambda = 1.48$ Å (the helium-like resonance line of Cu^{+27}), and then show how it changes when mixing is introduced. The total image is due to both self-emission and backlighting (for distances $\gtrsim 45$ μm the self-emission is negligible, and the total image is due to backlighting). The two vertical bars mark the boundaries of the doped region (the left bar also marks the interface). The curves in Fig. 59.19 assume diffraction off a crystal of 4-eV bandwidth (rocking-curve width). As seen, the two image components have comparable intensity, which will be shown below to be essential for the diagnostic method. Without monochromatization, the self-emission will overwhelm the backlighting image and render the method impractical. Thus, if instead of using a monochromator we were to use a filter, the intensity of the monochromatic backlighting radiation (consisting mostly of a single spectral line) will remain about the same. However, the intensity of the continuous self-emission will greatly increase because the filter bandpass will be ~1 keV, as compared to the crystal bandpass of ~4 eV. The spike at $r = 43$ μm is emitted by the shell's inner surface. It exists because the CH shell has a higher Z than the fuel, but only the inner surface of the shell is hot enough to emit at short wavelengths. With no mixing the spike is too narrow to be easily measurable.

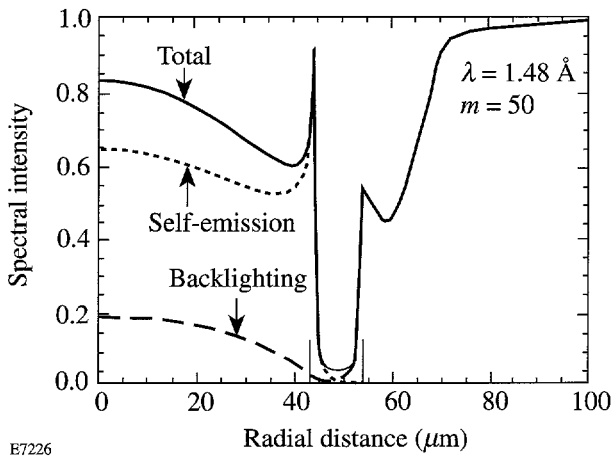

Figure 59.19
The total image due to self-emission and backlighting at $E = 8.39$ keV ($\lambda = 1.48$ Å), with no mixing. The curves are normalized to a spectral intensity of 1.4×10^{20} keV/(keV ns cm^2 Ω), the assumed backlighter x-ray flux at this wavelength. For distances $\gtrsim 45$ μm the self-emission is negligible, and the total image is due to backlighting. The two vertical bars mark the boundaries of the doped region (the left bar is also the interface).

The curves in Fig. 59.19 are normalized to a spectral intensity of 1.4×10^{20} keV/(keV ns cm^2 Ω), the assumed backlighter x-ray flux at this wavelength. This spectral flux level is based on x-ray yield experiments[7] using the helium-like resonance line of Cu^{+27} ($\lambda = 1.48$ Å). The image in

Fig. 59.19 is of a doped target, where the inner 2.4 μm have been doped with a high-Z dopant. The motivation for doping is to create a narrower region of absorption so that the delineation of the dense, cold part of the shell be done with greater definition. The initial thickness of the doped layer was chosen so that its width at peak compression (with no mixing) will be resolvable by the imaging instrument. In Fig. 59.19, the width of the absorption ring due to the high-Z dopant (around $r \sim 50$ μm) is about $\Delta r = 8.6$ μm, well within the resolving capability of our x-ray microscopes. Additionally, the outer absorption ring (around $r \sim 58$ μm) is due to absorption in the undoped CH shell. It corresponds to the maximum in the shell density (see Fig. 59.16). On moving to smaller radii, the absorption in the CH decreases partly because of a decrease in the shell density, but mainly because of a rise in the temperature. Figure 59.19 shows clearly the benefit of doping the target: it reduces significantly the width of the absorption region. It also explains the choice of backlighting wavelength: for the absorption in the doped part of the shell to be dominant, the wavelength must be short enough so that the CH absorption is small (see Fig. 59.22 for an image of an undoped target at a longer backlighting wavelength).

Doping was modeled here in a simplified way—by multiplying the total absorption coefficient of the undoped target by a factor m ($m = 50$ in Fig. 59.19). The total calculated absorption coefficient includes bound-free and free-free absorptions.[4] Irrespective of the detailed atomic physics of a high-Z dopant, its final effect is to increase the absorption coefficient and, through it, the local emission (which was related to the absorption coefficient through the Kirchhoff's law). To simulate doping we therefore multiply the absorption coefficient (and thereby also the emission coefficient) by a number m. The only information that is indeterminate here is the quantity of a given type of dopant corresponding to each m.

Calculations with different thicknesses of the doped layer show that the initial thickness of 2.4 μm for the test shot considered here is about optimal. For thinner doped layers the resulting absorption dip may be difficult to resolve, at least in the absence of severe mixing. For thicker doped layers, the outer part of the doped layer is at a low temperature during peak compression. Thus, the temperature where the doped layer absorbs most in Fig. 59.19 is around 400 eV, whereas a thicker doped layer will extend the absorption to regions of temperatures down to ~100 eV, where the absorption is much higher. Such increased absorption causes severe attenuation of the self-emission, particularly from the region near the interface, thus obliterating the sharp rise in intensity seen at $r \sim 45$ μm.

In order to estimate the amount of doping corresponding to a given m we must apply a non-LTE collisional-radiative model to a given high-Z dopant. If the doping is not negligibly small, we must also recompute the hydrodynamic evolution of the doped target. Instead, we make a rough estimate of the doping level corresponding to $m = 50$ if the chosen dopant is chlorine. It has been shown[4] that most of the shell absorption in carbon is due to the bound-free (photo-ionization) process; this is certainly true for any higher-Z dopant. For most of the shell the chlorine ions will be ionized to the helium-like state so that their average Z will be ~15. Since the bound-free absorption coefficient depends on Z like Z^4 (for a given ion density), we estimate that to achieve $m = 50$, the density of chlorine ions should be about the same as that of carbon ions. Higher-Z doping elements will require a lower doping level for the same value of m. Also, a lower value of m can be acceptable if a smaller absorption dip can be tolerated.

Backlighting and Self-Emission Images of Mixed Targets

We now apply the mixing procedure as described earlier to the test target at peak compression and then apply the radiation transport post-processor to calculate the backlighting and self-emission images.

Figures 59.20 and 59.21 show the combined image with and without mixing. The degree of mixing in Fig. 59.20 is $F = 0.2$; in Fig. 59.21 it is $F = 0.4$. The unmixed image is from Fig. 59.19. As mentioned above, comparison with experiments reported previously agreed with a value of $F = 0.2$. Mixing has two effects on the image: (a) the spike of self-emission greatly broadens spatially and moves toward the target center, and (b) its intensity increases dramatically. Both of these effects are caused by CH material moving into higher-temperature regions within the fuel. For $F = 0.2$ the spike moves from $r = 44$ μm to $r = 37$ μm, and its peak intensity increases by about a factor of 12.5. For $F = 0.4$ the spike moves from $r = 44$ μm to $r = 32$ μm, and its peak intensity increases by about a factor of 40. The spike in these two cases broadens to a width of about 5 μm and 9 μm, respectively. The predicted increase in intensity is easily measurable, but the shifts and broadenings are still within the capabilities of the OMEGA Upgrade diagnostics.

The most striking feature in Figs. 59.20 and 59.21 is the fact that the absorption dip is hardly affected by the introduction of mixing. Thus, the measured separation between the emission peak and absorption dip (both of which appear as rings in the two-dimensional image) is a convenient signature of the degree of mixing. As stressed above, the calculations performed here do not account for the feedback effect of the mixing on the

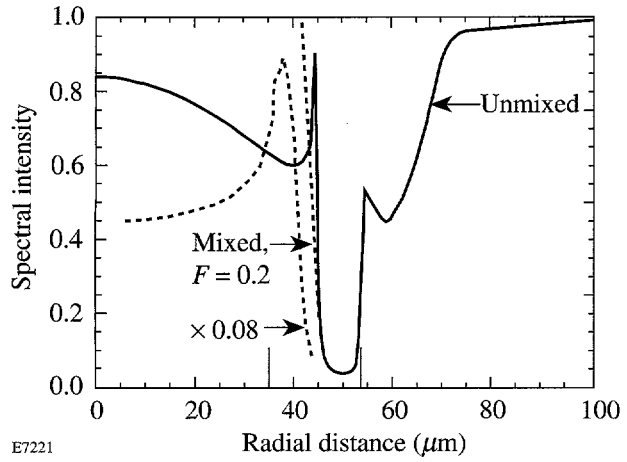

Figure 59.20
The total image at λ = 1.48 Å due to self-emission and backlighting for unmixed and mixed targets (with a degree of mixing $F = 0.2$). The unmixed image is from Fig. 59.19. The curves are normalized to a spectral intensity of 1.4×10^{20} keV/(keV ns cm^2 Ω). The two vertical bars mark the boundaries of the doped region (in the mixed target). The shell-fuel interface position with no mixing is at 42.7 μm.

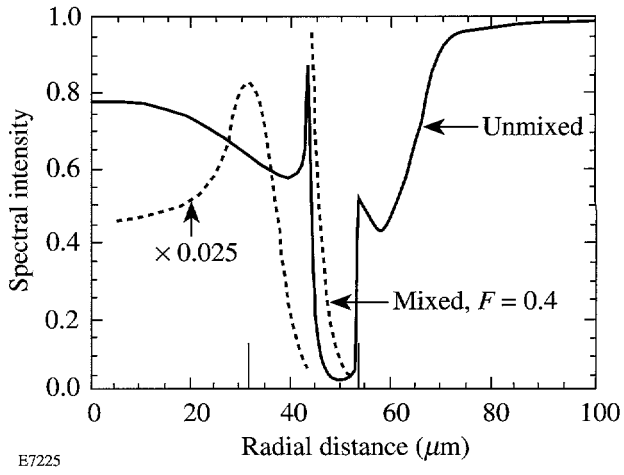

Figure 59.21
The total image at λ = 1.48 Å due to self-emission and backlighting for unmixed and mixed targets (with a degree of mixing $F = 0.4$). The unmixed image is from Fig. 59.19. The curves are normalized to a spectral intensity of 1.4×10^{20} keV/(keV ns cm^2 Ω). The two vertical bars mark the boundaries of the doped region (in the mixed target). The shell-fuel interface position with no mixing is at 42.7 μm.

hydrodynamic and thermodynamic target evolution. The main effect of such a feedback is expected to be the lowering of the temperature in the fuel region due to radiation cooling by the high-Z contaminant (which includes CH material and any dopant assumed in the initial target). This cooling will reduce the intensity of the emission peak. However, the general statement will still be valid, that the absorption dip is a signature of the position of the compressed shell, whereas the emission peak is a measure of the penetration of shell material into the fuel. *Thus, a very useful comparison of experiment and theoretical predictions can be obtained if the imaging includes a backlighting component in addition to the self-emission image.*

Finally, we discuss the effect of mixing on the backlighting image of undoped targets. Since, as we have seen earlier, the absorption of 1.48-Å radiation in the test target with no doping is very small, we increase the backlighting wavelength to 2.62 Å (the wavelength of the helium-like resonance line of Ti^{+20}). Figure 59.22 shows the combined backlighting and self-emission images for two degrees of mixing, $F = 0.2$ and $F = 0.4$. The spectral flux is normalized to that expected[7,8] from a titanium backlighter: 7.0×10^{20} keV/(keV ns cm^2 Ω). Undoped targets give rise to a broader, less-well-defined absorption peak. However, the target fabrication is simpler, and, due to the longer wavelength, the intensity is higher. Comparing Fig. 59.22 to Figs. 59.20 and 59.21 shows that the position of the emission peaks for a given F value is almost the same for the two different wavelengths. However, the increase in intensity is not as dramatic as with the shorter wavelength. As recalled, the increase in intensity of the self-emission is due to shell material moving into higher temperature regions in the core. The intensity is governed by factors of the type $\exp[-(E/kT)]$, where E is the photon energy. Thus, when E is higher (as is the case in Figs. 59.20 and 59.21), the intensity increases faster with increasing temperature.

The fact that the peak position is about the same for the two wavelengths (for the same level of mixing) supports the contention that a fully consistent calculation of the mixed target evolution should result in a similar shift of the emission peak. Radiation cooling will certainly reduce the emission peak intensity, but the peak position will depend primarily on the length of mixing and less on the temperature. The peak appears roughly at the position of maximum penetration of the shell material into the fuel because the temperature there is maximal over the penetration depth. We have calculated images such as in Figs. 59.20–59.22 for increasing F values, up to the maximum of F ~0.7; at that value of F the free-fall line (see Fig. 59.17) reaches the target center by the time of peak compression. In all these cases the absorption dip position and depth remain about the same. This means that the observation of significant deviations from the predicted characteristics of the absorption ring is evidence of more severe instability, such

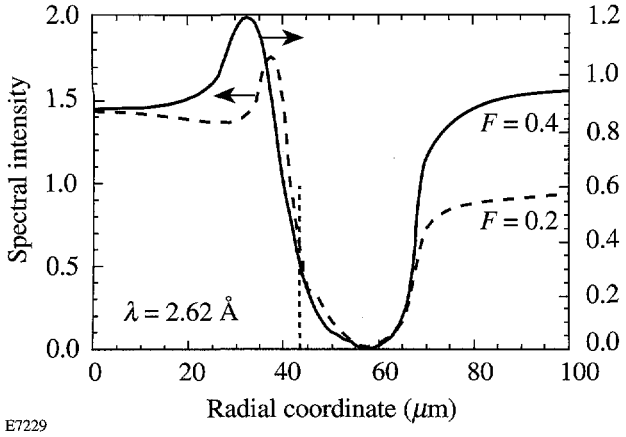

Figure 59.22
The combined backlighting and self-emission image of the test target with no doping, at $\lambda = 2.62$ Å, and two degrees of mixing: $F = 0.2$ and $F = 0.4$. The curves are normalized to a spectral intensity of 7.0×10^{20} keV/(keV ns cm^2 Ω). The vertical dashed bar marks the position the shell-fuel interface would have without mixing.

as shell disruption on the way in, due to initial nonuniformity. Finally, the measured absorption depth (i.e., the attenuation of backlighting radiation) can be used for comparison with predictions. This attenuation depends both on the shell temperature and the shell $\rho\Delta r$. The position of the absorption ring can be used to deduce the fuel compression and the presence of low-order nonuniformity of the compressed core.

ACKNOWLEDGMENT

This work was supported by the U.S. Department of Energy Office of Inertial Confinement Fusion under Cooperative Agreement No. DE-FC03-92SF19460, the University of Rochester, and the New York State Energy Research and Development Authority. The support of DOE does not constitute an endorsement by DOE of the views expressed in this article.

REFERENCES

1. J. D. Lindl, R. L. McCrory, and E. M. Campbell, Phys. Today **45**, 32 (1992).
2. O. L. Landen, W. K. Levedahl, and T. R. Dittrich, Bull. Am. Phys. Soc. **38**, 2083 (1993).
3. B. Yaakobi, F. J. Marshall, Q. Su, and R. Epstein, to appear in the Journal of X-Ray Science and Technology.
4. Laboratory for Laser Energetics LLE Review **58**, NTIS document No. DOE/SF/19460-17, 1994 (unpublished), p. 57.
5. C. P Verdon, R. L. McCrory, R. L. Morse, G. R. Baker, D. I. Meiron, and S. A. Orszak, Phys. Fluids **25**, 1653 (1982).
6. D. L. Youngs, Physica **12D**, 32 (1984); S. W. Haan, Phys. Rev. A **39**, 5812 (1989); N. Freed, D. Ofer, D. Shvarts, and S. A. Orszag, Phys. Fluids A **3**, 912 (1991).
7. B. Yaakobi, P. Bourke, Y. Conturie, J. Delettrez, J. M. Forsyth, R. D. Frankel, L. M. Goldman, R. L. McCrory, W. Seka, J. M. Soures, A. J. Burek, and R. E. Deslattes, Opt. Commun. **38**, 196 (1981).
8. D. L. Matthews *et al.*, J. Appl. Phys. **54**, 4260 (1983).

Evaluation of Cosmic Rays for Use in the Monitoring of the MEDUSA Scintillator–Photomultiplier Diagnostic Array

Current and planned ICF implosion experiments require the detailed measurement of physical conditions on the imploded core. Glass and plastic shells filled with D_2 open a window into the core by measuring the ratio of the various fusion reactions occurring during the implosion.[1] The number of each reaction is measured by characterization of the energy spectrum for the penetrating reaction products (either neutrons or protons). The measurement of the neutron energy spectrum around the 3-MeV neutron from the $d(d,He^3)n$ reaction and around the 14-MeV neutron from the $d(t,He^4)n$ reaction has evolved into the most used nuclear core diagnostic.

For a target filled with D_2, the $d(t,He^4)n$ fusion reaction is a secondary process and will generate about 10^{-3} times less neutrons than the primary D_2 reaction, $d(d,He^3)n$. Large area detectors that measure the neutron energy spectrum by the time-of-flight (TOF) method have become the standard for determination of the details of the 14-MeV neutron spectrum.[2] Adaptations of this instrument are being built to also measure the neutron spectrum from the various primary fusion reactions with high energy resolution.[3] The Laboratory for Laser Energetics at the University of Rochester is building such a detector for implosion experiments planned for the OMEGA Upgrade. This diagnostic, a multi-element detector using a scintillator array (MEDUSA),[4] will be used to study the details of the neutron energy spectrum around the 14-MeV neutron emitted from the $d(t,He^4)n$ secondary reaction.

MEDUSA

The MEDUSA diagnostic consists of 960 separate scintillator-photomultiplier detectors arranged in an array with 32 columns and 30 rows. This array is located in a separate instrumentation room 19 m from the center of the target chamber. At this distance the time-of-flight for the 14-MeV neutrons will be 370 ns after their creation. The center of the target chamber is about 9.3 m above the center of the instrument. This requires that the array be tilted at an angle of 26° relative to the vertical so that the detector plane is normal to the line connecting the center of the array with the center of the target chamber. The active area of the array is 3.87 m^2, resulting in a subtended solid angle of 0.011 sterad. Each element of this array is constructed from a solid block of NE 110 scintillator 6.35 cm high × 6.25 cm wide × 7.62 cm deep. A Thorn EMI 9257B photomultiplier is attached to the rear of the scintillator block. A schematic for each of the individual detection channels is shown in Fig. 59.23.

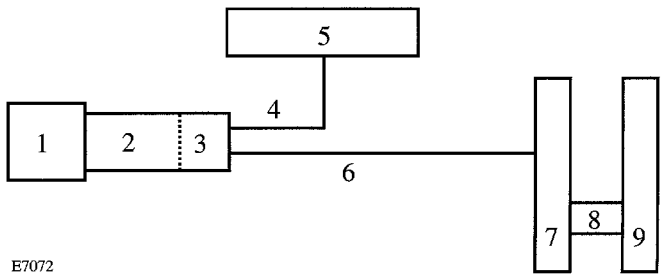

Figure 59.23
Schematic of each MEDUSA scintillator-photomultiplier channel.

Each MEDUSA channel (Fig. 59.23) consists of nine separate components, giving a total of 8640 components for the whole diagnostic array. All such large arrays require that all of these individual pieces continue to work during the lifetime of the instrument. The large neutron scintillator array (LaNSA) at the Lawrence Livermore National Laboratory[2] uses radioactive sources placed in each channel to monitor individual channel performance. LaNSA is a horizontal array at the bottom of a deep well, which makes the use of naturally occurring ionizing radiation difficult. The LLE MEDUSA array is nearly vertical and, as such, is a prime candidate for the use of cosmic rays as a source of ionizing radiation to monitor channel performance. The calculation of the counting rates and signal levels will determine if this technique will work.

Cosmic Rays

The flux of cosmic rays incident onto the surface of the earth is known to be 110 particles/(m^2 str s),[5] about 73% [80 particles/(m^2 str s)] of which are penetrating particles. Most of the particles at the earth's surface are muons. Muons are

generated from the decay of pions created when a high-energy particle in space interacts with a nucleus in the earth's atmosphere. The muons have sufficient energy to be classified as minimum ionizing particles, which are particles that have energies greater than or equal to the energy of a particle at the minimum of the *dE/dx* ionization loss curve. Counting rates for the detectors in the MEDUSA array are calculated to be 2.9 particles/h for a single column of 30 scintillator-photomultiplier channels. This gives a total counting rate of 93.2 particles/h for all 32 columns in the diagnostic array. An overnight run of 16 h will result in 50 counts for each detector—enough counts to determine the status of all components in the diagnostic.

A minimum ionizing particle passing through a NE 110 scintillator has an energy loss (*dE/dx*) of 2.0 MeV/cm. The minimum path length of a cosmic ray detected by the MEDUSA scintillator-photomultiplier channel is 6.35 cm, resulting in a total energy deposition from the cosmic ray of 12.7 MeV. This is very well matched to the maximum energy deposited by a neutron of 13.7 MeV. Since there is sufficient signal to detect a neutron, there will be enough signal to detect a cosmic ray.

A test on a small subarray will determine if both a sufficient count rate and signal level exist to detect cosmic rays in the MEDUSA diagnostic array.

Cosmic Ray Tests

A smaller subarray of detectors was constructed to simulate the larger MEDUSA diagnostic. A schematic of this setup is shown in Fig. 59.24. It is constructed from a 4 × 4 array of MEDUSA scintillator-photomultiplier channels and two separate trigger counters. The trigger counters are used to establish the presence of a cosmic ray that has passed through the detectors in the subarray. Sixteen detectors were used from the MEDUSA diagnostic for the test so that the test was conducted with a sample of detectors used in the primary array. The trigger counters are scintillator-photomultiplier detectors constructed for a high-energy physics experiment conducted at the Fermi National Accelerator Laboratory in the 1970's and 1980's. The scintillator in the trigger counters is NE 111, 8.89 cm long × 7.62 cm deep × 1.27 cm thick. An Amperex 56 AVP is used as the photomultiplier. The voltages required by the trigger counters were 1750 V and 2200 V. The size of the trigger counters allowed tests to be conducted on four of the 16 subarray detectors during a single data-acquisition session.

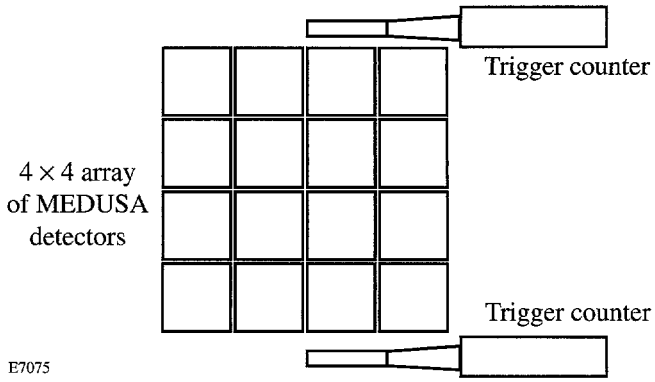

Figure 59.24
Schematic of the subarray used to test the cosmic-ray count rate concept for monitoring the MEDUSA diagnostic.

The trigger counters and the subarray detectors were connected to the electronics shown schematically in Fig. 59.25. The trigger counters were connected to a discriminator located in a NIM bin with the threshold set to 100 mV. The discriminator outputs were used as inputs for a coincidence logic unit. This logic unit gave an output when both discriminators detected a pulse above threshold to establish the presence of a particle passing through both trigger counters. The output of the logic unit was used as the start trigger for a time-to-digital converter (TDC) and as a gate signal for the charge-to-digital converter (QDC). The MEDUSA scintillator-photomultiplier outputs are fed into a CAMAC discriminator and a CAMAC QDC. The discriminators have computer-selectable thresholds. Outputs from the CAMAC discriminator were used as the stop triggers for the TDC. CAMAC scalars counted outputs from the trigger counter discriminators, logic unit, TDC start trigger, and MEDUSA channel discriminator. The CAMAC crate was controlled with an IEEE 488 interfaced controller connected to a Macintosh computer using National Instruments' Lab View as the data-acquisition software. This electronics and software configuration allowed a great deal of flexibility in the tests conducted with this subarray.

Three primary tests were conducted with the 4 × 4 subarray of MEDUSA detectors: (1) determination of the count rate as a function of the discriminator threshold; (2) measurement of the charge distribution as a result of cosmic rays depositing energy in the scintillators; and (3) studying the temporal histogram from the CAMAC TDC stop trigger generated when a cosmic ray is detected by the MEDUSA scintillator-

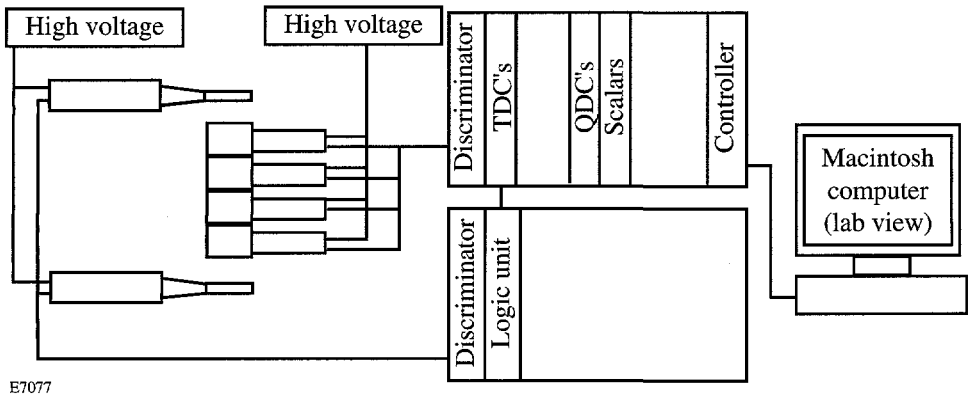

Figure 59.25
Schematic of the electronics used to test the cosmic-ray monitoring concept on the MEDUSA subarray.

photomultiplier channel. The output signal uniformity of the four channels tested is an indication of the expected performance for the whole array during a cosmic-ray test sequence. The results from the above measurements are shown in Figs. 59.26–59.28.

Data from the counter threshold measurement is shown in Fig. 59.26. The number of counts in 1000 s is plotted as a function of the CAMAC discriminator threshold. Four of the MEDUSA subarray detectors are plotted on the same graph. The minimum discriminator threshold is 20 mV, and the maximum threshold is 1020 mV. The first important observation is that all four detectors show nearly identical performance. There are two regions evident in the threshold data. The region below 50 mV is dominated by the noise from the scintillator-photomultiplier detector. These data are fit by an exponential, and the function can be integrated to determine the probability for a noise count during the active time of a neutron spectral measurement. All four channels show a 5% probability that there will be a noise trigger in all 960 detectors for a 1-μs diagnostic time window for a discriminator threshold of 17 mV. These data are being used to determine the thresholds for all 960 MEDUSA channels.

The results from the charge distribution test are shown in Fig. 59.27. As in the previous data, it is evident that all four counters have a nearly identical charge spectrum from cosmic ray energy deposition. There is a well-defined peak that is well separated from any noise. All four detectors show a peak at around 400 counts, corresponding to an integrated charge of 100 pC. The signal was attenuated by 2 before it was connected to the QDC. The total integrated charge from the detector is 200 pC. It was shown previously that a cosmic-ray event simulates a 13.7-MeV neutron that deposits 12.7 MeV in the scintillator. The data from the charge spectrum imply that a 13.7-MeV neutron will yield a total output charge of 216 pC.

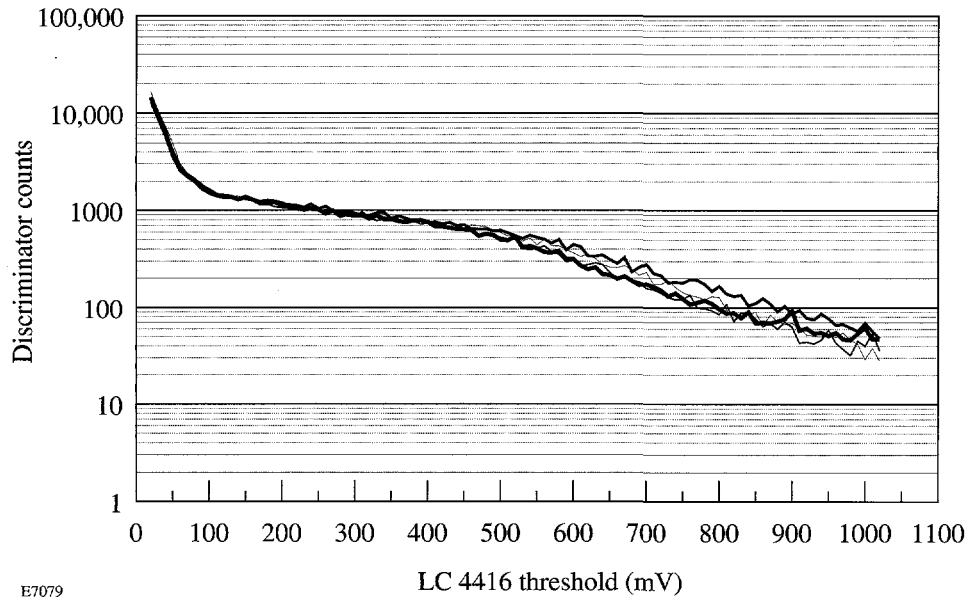

Figure 59.26
Plot of the number of counts from the discriminator verses the discriminator threshold for the MEDUSA channel subarray.

The uniformity of the spectrum from each of the four detectors will allow the cosmic-ray data to correlate to the calibration data from the nuclear fusion product source used to check selected detectors.[6] The cosmic-ray data will thus be able to serve not only as a monitor of the performance of each channel but also as a check of the energy calibration for the detectors.

The TDC data, plotted in Fig. 59.28, are nearly identical for each of the channels, as was the case in the two previous tests. All four channels show a peak around 20 ns. This time is determined by the added delay in each channel to insure that the stop triggers arrive after the start triggers. The width [full-width at half-maximum (FWHM)] for all of the channels is less than 0.5 ns, which is equivalent to one count of the TDC output. The consistency of these data indicates that it will be possible to use the cosmic ray data to check the performance of the TDC's used on the MEDUSA diagnostic.

Summary

The results from the initial tests to determine the utility of using cosmic rays to monitor the performance of the MEDUSA detectors indicate that this source of ionizing radiation is quite suitable. All tests imply that the data from the cosmic-ray monitoring sessions can be used to not only monitor the channels but also check their calibrations. The calculated counting rate for the subarray was 392 particles/h; the measured rate was 349 particles/h. MEDUSA's calculated counting rate of 93.2 particles/h should be close to the actual

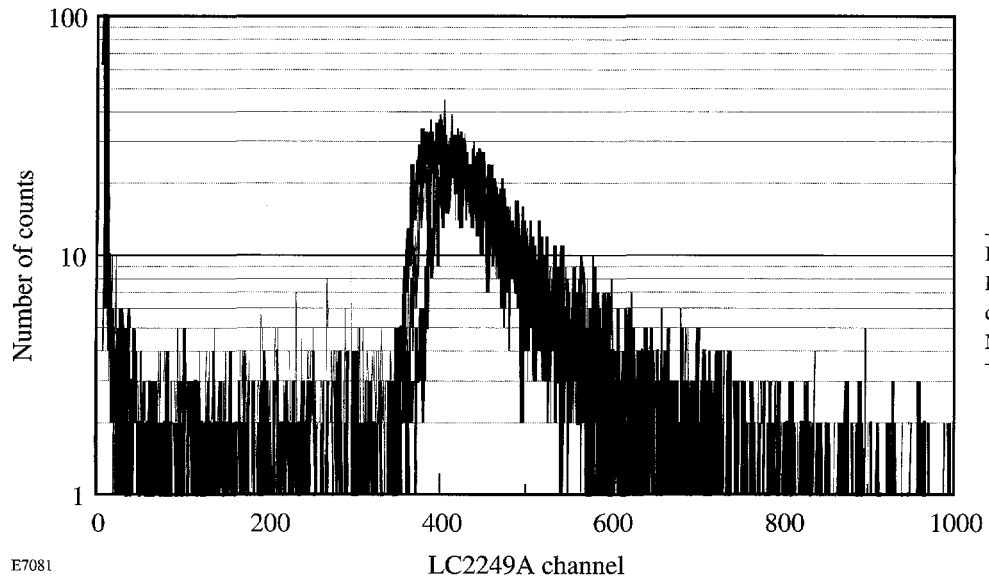

Figure 59.27
Pulse-height spectrum from the CAMAC charge-to-digital converter connected to the MEDUSA channel subarray.

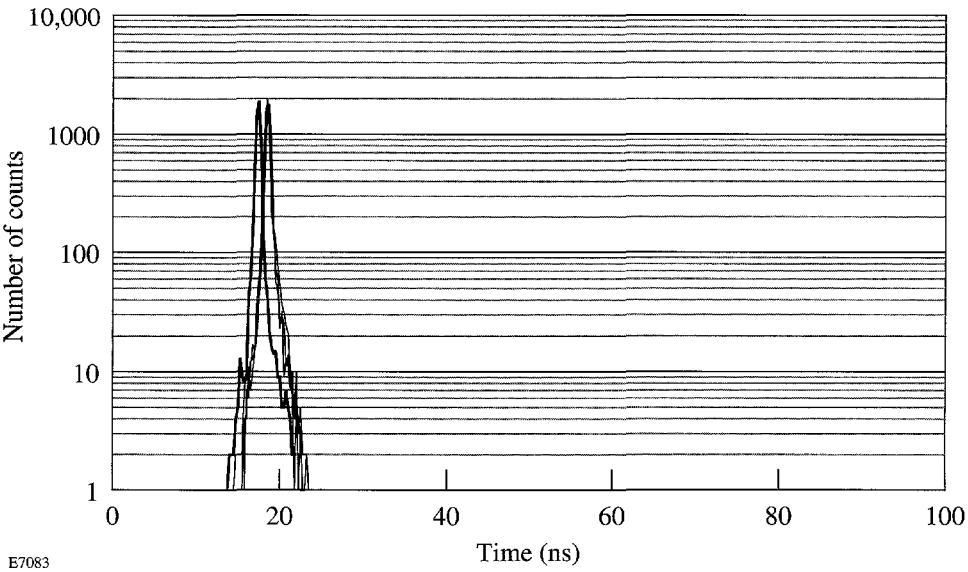

Figure 59.28
Temporal count spectrum from the CAMAC time-to-digital converter connected to the MEDUSA channel subarray.

counting rate when the full detector is completed and ready for testing. There is excellent agreement with the expected signal levels and temporal stop trigger jitter. Radiation sources or optically coupled sources should not be required to monitor the individual channels. To test the MEDUSA diagnostic, only a data-acquisition routine will be required to collect and analyze cosmic-ray events when the detector is not needed to acquire data from an ICF implosion.

ACKNOWLEDGMENT

This work was supported by the U.S. Department of Energy Office of Inertial Confinement Fusion under Cooperative Agreement No. DE-FC03-92SF19460 and the University of Rochester. The support of DOE does not constitute an endorsement by DOE of the views expressed in this article.

REFERENCES

1. T. E. Blue and D. B. Harris, Nucl. Sci. Eng. **77**, 463 (1981).
2. M. D. Cable, S. P. Hatchett, and M. B. Nelson, Rev. Sci. Instrum. **63**, 4823 (1992).
3. R. E. Chrien, presented at the *APS 10th High-Temperature Plasma Diagnostics Conference*, Rochester, NY, 8–12 May 1994.
4. R. L. Kremens and M. A. Russotto, presented at the *APS 33rd Annual Meeting of the Division of Plasma Physics*, Tampa, FL, 4–8 November 1991.
5. M. Aguilar-Benitez *et al.*, in the *Particle Properties Data Booklet*, from the *Review of Particle Properties*, Physical Review **D45**, Part 2 (June 1992).
6. S. Padalino, B. Emerling, P. King, M. Rodgers, and R. Kremens, presented at the *APS 10th High-Temperature Plasma Diagnostics Conference*, Rochester, NY, 8–12 May 1994.

Highly Efficient Second-Harmonic Generation of Ultra-Intense Nd:Glass Laser Pulses

Major advances in laser technology at LLE have included the demonstration of high-efficiency frequency doubling and tripling of fusion lasers[1] and the development of short-pulse, chirped-pulse-amplification (CPA) lasers.[2] These technologies were combined a few years ago with the demonstration of 75% efficient frequency doubling of 1.6-ps laser pulses on the CPA T^3 (table-top terawatt) system at LLE, in collaboration with the Australian National University (ANU).[3] Excellent agreement with simulations demonstrated that "standard" frequency conversion theory also applies in the picosecond regime, at intensities up to a few GW/cm^2.

This article reports a more recent collaboration with the University of Michigan. In an extensive series of experiments, 500-fs, 1053-nm laser pulses were converted to the second harmonic in KDP crystals at intensities up to 400 GW/cm^2, with efficiencies of ~80%, without any obvious damage to the crystals. This result extends the regime of validity of the theory nearly two orders of magnitude higher in intensity. Further, the results provide evidence that, at these intensities, it is necessary to include self- and cross-phase modulation in the theory. Most significant, though, may be the extension of the available wavelength range of CPA systems used for ultra-intense laser-matter interaction experiments.

CPA lasers have been successfully used to generate peak laser powers in the infrared well beyond the terawatt regime.[4–7] When focused, these lasers can produce intensities exceeding 10^{18} W/cm^2, giving access to new regimes of laser-matter interaction. For solid targets irradiated at these intensities the peak-to-background intensity contrast of the laser pulse should exceed ~10^9:1 to avoid energy deposition in a plasma created by a much longer prepulse. Second-harmonic generation (SHG) in nonlinear crystals is thus important because, aside from extending the available wavelength range, it significantly improves the contrast ratio. Indeed, high-contrast, second-harmonic laser pulses have been used to produce high-density, high-temperature plasmas that emit short x-ray pulses in the keV region.[8]

The experiments reported here were carried out on a terawatt Nd:glass laser system.[5] In these experiments the laser delivered energies up to 1.5 J with a wavelength of 1.053 μm and a temporal full-width at half-maximum (FWHM) of 500 fs. The spatial profile was somewhat flatter than Gaussian with a diameter of 2.6 cm (FWHM). The intensity contrast ratio was 10^6:1, as measured with a third-order correlator. The pulse energies of the fundamental and its second harmonic were monitored by calorimeters. Three crystal configurations were examined: (a) a type-I crystal, optimum for the SHG of ultrashort 1-μm pulses because the fundamental and second-harmonic group velocities are, for this wavelength, almost equal; (b) a type-II crystal, limited by temporal walkoff between the fundamental *o* and *e* pulses; and (c) a predelay scheme using two type-II crystals,[9] in which compensation of this walkoff leads to improved efficiency, as was demonstrated in the collaborative experiments on T^3 with the ANU,[3] and second-harmonic pulse shortening.[10] Results from the current experiments have included high conversion from the type-I crystal (70%–80% throughout the range of 100 to 400 GW/cm^2) and evidence of pulse shortening (to ~100-fs FWHM) from the predelay scheme.

These experiments have been simulated with the LLE code *MIXER*,[11] enhanced to model group-velocity dispersion and $\chi^{(3)}$ effects. The code integrates equations of the form

$$\frac{\partial E_3}{\partial z}+\frac{1}{V_{g3}}\frac{\partial E_3}{\partial t} = -\frac{1}{2}\gamma_3 E_3 - iK_3E_1E_2\exp(i\Delta k\cdot z)$$

$$+i\left\{\alpha_{31}\left|E_1^2\right|+\alpha_{32}\left|E_2^2\right|+\alpha_{33}\left|E_3^2\right|\right\}E_3\,, \quad (1)$$

where, for wave i (waves 1 and 2 combining to generate wave 3), E_i is the electric field, V_{gi} is the group velocity, γ_i is the linear absorption coefficient, K_i is a nonlinear coefficient, and α_{ij} gives the change of refractive index due to the intensity of wave j [resulting from the third-order susceptibility tensor

$\chi^{(3)}$]. The quantity Δk is the wave-vector mismatch, z indicates propagation distance, and t denotes time. The coefficients α_{ij} are related to the more convenient coefficients γ_{ij} defined via the equation $n_i = n_{io} + \Sigma\gamma_{ij} I_j$, which gives the refractive index n_i of wave i in terms of its linear index n_{io} and a nonlinear correction summed over the intensities I_j of waves j. For an isotropic medium and in the absence of dispersion, $\gamma_{ij} = \gamma_0$ for $i = j$ (self-phase modulation); for $i \neq j$ (cross-phase modulation), $\gamma_{ij} = 2\gamma_0$ if the polarizations of waves i and j are parallel and $2\gamma_0/3$ if they are perpendicular.[12] The simulations have used $\gamma_0 = 0.27 \times 10^{-19}$ m^2/W at 1 μm.[13] Since no data is available for 0.5 μm, *MIXER* has used an *ad hoc* model where γ_{ij} is multiplied by a dispersion factor $F \equiv 1.5$ if both waves are second harmonic and $F^{1/2}$ if one is. The propagation and K_3 terms of Eq. (1) are solved in the frequency domain and the $\chi^{(3)}$ term in the time domain. (In the frequency domain, the group-velocity term is replaced by the simple translation of each Fourier mode with its phase velocity, thus including all orders of dispersion.) Predictions for the experimental energy-conversion efficiencies are obtained by averaging solutions to Eq. (1) over the measured two-dimensional spatial profile of the IR laser beam.

Results for the first experiment, doubling in a 4-mm, type-I crystal, are shown in Fig. 60.1(a). Conversion efficiencies of 70%–80% were found from 100 to 400 GW/cm^2, with consistency between the two data sets (from different crystals used five months apart). The nominal intensity plotted on the horizontal axis is close to the intensity in the center of the beam at the peak of the pulse. The beam was modeled as a bandwidth-limited Gaussian of FWHM 500 fs, consistent with experimental spectra and autocorrelations.

Agreement with the simulation for both $\chi^{(3)}$ and $\Delta\theta_1 = 0$ (dashed curve) is generally reasonable, except for a falloff at high intensities ($\gtrsim$100 GW/cm^2). One plausible explanation is nonlinear $\chi^{(3)}$-induced mismatch,[14] modeled here with the solid curves for various angular detunings $\Delta\theta_1$ from small-signal phase matching, measured outside the crystal, with positive $\Delta\theta_1$ indicating an increase in the angle between the propagation direction and the optic axis. The curve labeled $\Delta\theta_1 = 0$ would be followed if the small-signal tuning were sufficiently accurate to locate this direction. However, it was found necessary to fine tune the crystal at high intensity, and it is thus possible that one data set followed $\Delta\theta_1 \approx 0.5$–$0.7$ mrad and the other 0.3 mrad. Dispersion in the (unknown) γ_{ij} coefficients is critical to this explanation. Without dispersion ($F = 1$), the simulations do not depart significantly from the $\chi^{(3)} = 0$ curve even with γ_0 five times bigger; moreover, with

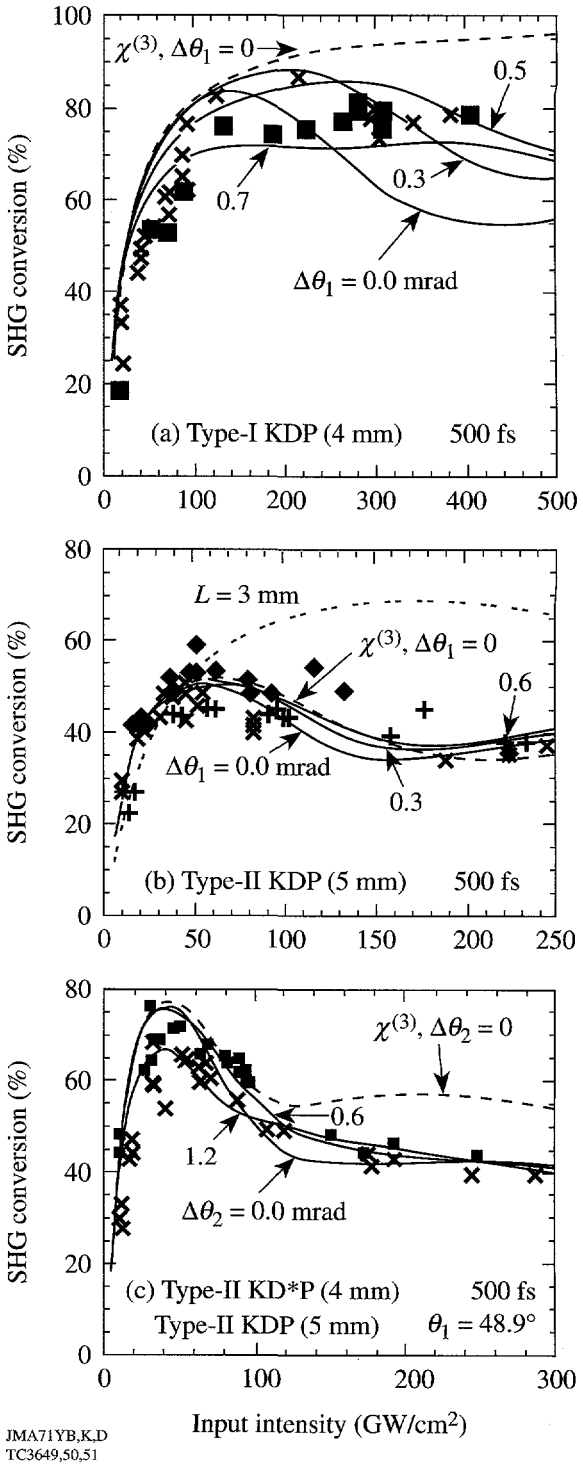

Figure 60.1
SHG efficiency as a function of input laser intensity for (a) a 4-mm, type-I KDP crystal; (b) a 5-mm, type-II KDP crystal; and (c) a 4-mm, detuned, type-II KD*P crystal followed by a 5-mm, type-II KDP crystal. Dashed curves: simulations for $\chi^{(3)} = 0$ and no detuning. Solid curves: simulations including $\chi^{(3)}$ with various angle detunings (in mrad away from the optic axis). The double-dotted curve in (b) is for a 3-mm crystal with $\chi^{(3)} = 0$.

more dispersion ($F = 2$), the simulations fall below the data at 400 GW/cm^2 for all $\Delta\theta_1$. It is worth noting that for any single intensity a $\Delta\theta_1$ can be chosen to fully compensate for the nonlinear phase error,[15] but it is impossible to simultaneously compensate for the full range of intensities in the beam in space and time.

Results for a single, 5-mm-thick, type-II crystal are shown in Fig. 60.1(b) for three data sets. Conversion efficiencies reach 50% at 50 GW/cm^2 and then fall off due to group-velocity walkoff between the fundamental *o* and *e* waves. [This causes incorrect photon ratios (deviating from 1:1) leading to reconversion.] This crystal is much less sensitive to mismatch than the type-I crystal, and the inclusion of $\chi^{(3)}$ terms thus makes little difference. The reconversion seen above 60 GW/cm^2 indicates that the crystal was too thick: the double-dotted curve shows that a 3-mm crystal would perform much better at the higher intensities. Thus, a type-I crystal has just a small advantage at 500 fs. For shorter pulses, however, it is strongly preferred: at 100 fs and comparable intensities the predicted loss is insignificant for type I but catastrophic for type II.

In the third experiment the 5-mm, type-II KDP crystal was preceded by a 4-mm, type-II KD*P crystal, detuned several degrees from phase matching, that provided a predelay between the fundamental *o* and *e* rays. Since the sign of the detuning was unknown, it was assumed that the propagation angle within the KD*P was $\theta_1 = 48.9°$, giving a predelay of 340 fs. [Predictions for the other possibility ($\theta_1 = 58.3°$, predelay = 430 fs) are similar.] Results are shown in Fig. 60.1(c) for experiments carried out on two separate days. Within the data scatter, all curves provide a reasonable fit to the data below ~100 GW/cm^2. At higher intensities, however, the data fall significantly below the prediction for $\chi^{(3)} = 0$ and lie much closer to the curves including $\chi^{(3)}$. As with the type-I case, there is an optimum positive detuning ($\Delta\theta_2$) of the KDP crystal, although here the sensitivity to $\Delta\theta_2$ is smaller. The role of the $\chi^{(3)}$ terms here is more complicated since phase retardations generated at one time in the pulse affect phase matching at other times due to the various group-velocity walkoffs.

The input polarization angle θ_p (the angle of the input electric field vector to the *o* direction of the first crystal[11]) was controlled with a half-wave plate. Two conversion scans carried out as a function of θ_p are shown in Fig. 60.2, one for the single type-II crystal and one for the predelay scheme. Agreement with simulations is generally close, confirming

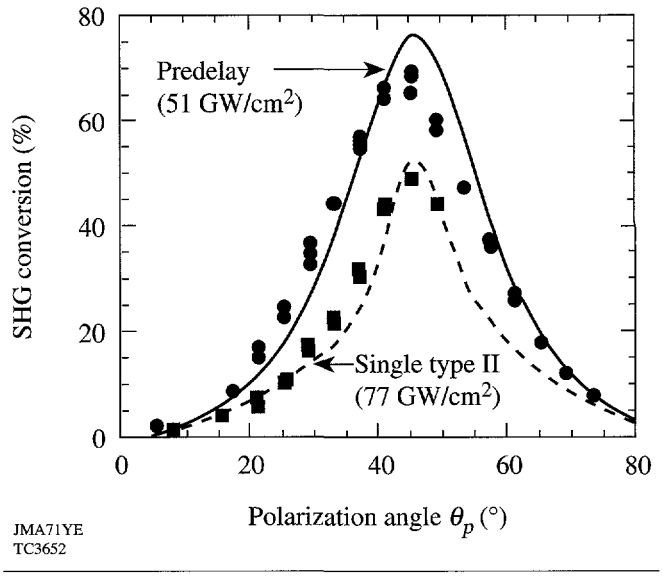

Figure 60.2
Dependence of the SHG efficiency on the polarization angle of the incident laser. Dashed curve: single, 5-mm, type-II KDP crystal at 77 GW/cm^2. Solid curve: predelay scheme at 51 GW/cm^2.

that the polarization state of the laser is substantially correct. The 10% discrepancy at the peak seen for the predelay scheme is consistent with the experimental scatter at the same intensity in Fig. 60.1(c).

The pulse shape of the second harmonic generated by the predelay scheme using a single-shot autocorrelator has been investigated.[16] A portion of the second harmonic was split into two beams that were downcollimated and passed through a 100-μm-thick BBO crystal, incident at angles ±10° to the crystal normal and timed such that the autocorrelation sampled the center of the beam. An experimental fourth-harmonic trace is shown in Fig. 60.3(a) for an estimated IR intensity of 119 GW/cm^2 in the sampled region together with a prediction, including the same $\chi^{(3)}$ model used in Fig. 60.1, for $\Delta\theta_2$ = 1.8 mrad (the optimum detuning at this intensity). The match is very close, except in the wings where the asymmetry is probably explained by spatial intensity variations in the beam. The predicted second-harmonic pulse shape generated by the KDP crystal [Fig. 60.3(b)] shows a narrow central spike with an intensity FWHM of 84 fs, superposed upon a broader wing at the ~15% intensity level. [With $\chi^{(3)} = 0$, a 49-fs FWHM is predicted.] The autocorrelation calculation included propagation through 1.5 cm of BK7 glass (which significantly broadened the pulse to 166-fs FWHM) and group-velocity dispersion within the BBO. It should be cautioned that the 1.8-mrad detuning was not measured but was chosen to illustrate a possible temporal pulse shape consistent with the measured

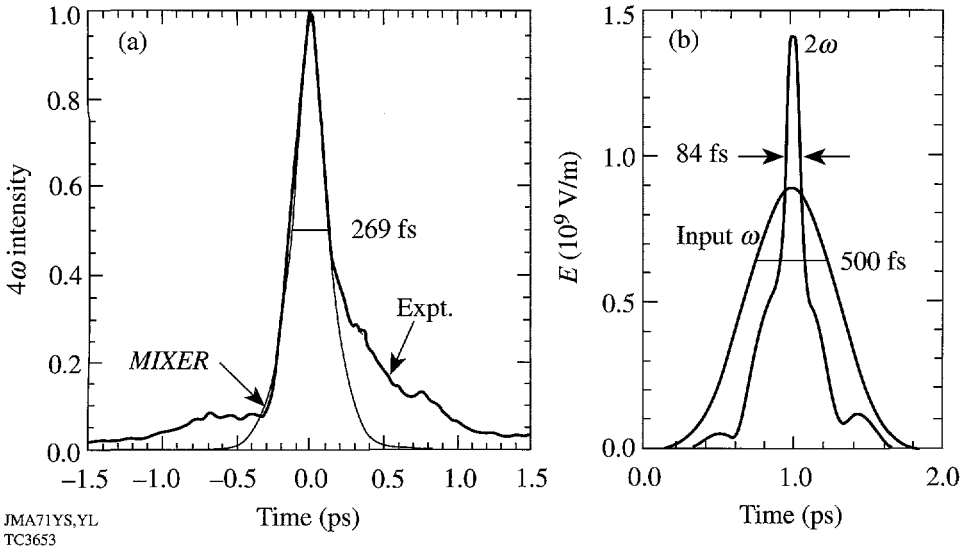

Figure 60.3
(a) Experimental and simulated second-harmonic autocorrelation intensity for the predelay scheme at 119 GW/cm^2. The simulation includes $\chi^{(3)}$ effects and assumes a detuning of 1.8 mrad. (b) Simulated second-harmonic pulse shape at the output of the KDP crystal (electric field versus time).

autocorrelation. Moreover, above ~100 GW/cm^2, structure was generated in the second-harmonic beam that limited its focusability, and the second-harmonic spectrum was broader than predicted with the $\chi^{(3)}$ model. The first demonstration of pulse shortening using the predelay scheme[10] (1.2 ps to 250 fs at 7 GW/cm^2) was unlikely to have been affected by $\chi^{(3)}$ terms.

In conclusion, an extensive series of SHG experiments have been conducted using intense, 500-fs laser pulses. Efficiencies of 70%–80% up to 400 GW/cm^2 were obtained from a type-I crystal without any obvious damage to the crystal or degradation of focusability. Lower efficiencies were obtained for a type-II crystal. The results for the predelay scheme were consistent with a pulse shortening to ≤100-fs FWHM, although with low contrast. All results are broadly in agreement with predictions of the code *MIXER*, with improved agreement obtained above ~100 GW/cm^2 by including a $\chi^{(3)}$ model that makes *ad hoc* assumptions about the dispersion of the self- and cross-phase-modulation coefficients. Further experiments are needed to measure these unknown coefficients. The most important practical consequence of the experiments reported here may be the extension of ultra-intense laser-matter experiments to shorter wavelengths.

ACKNOWLEDGMENT

These experiments were carried out at the University of Michigan by Drs. C. Y. Chien, G. Korn, J. S. Coe, J. Squier, and G. Mourou. This work was supported by the National Science Foundation through the Center for Ultrafast Optical Science under STC PHY 8920108 and by the U.S. Department of Energy Office of Inertial Confinement Fusion under Cooperative Agreement No. DE-FC03-92SF19460, the University of Rochester, and the New York State Energy Research and Development Authority. The support of DOE does not constitute an endorsement by DOE of the views expressed in this article.

REFERENCES

1. W. Seka, S. D. Jacobs, J. E. Rizzo, R. Boni, and R. S. Craxton, Opt. Commun. **34**, 469 (1980).
2. D. Strickland and G. Mourou, Opt. Commun. **56**, 219 (1985).
3. Y. Wang, B. Luther-Davies, Y.-H. Chuang, R. S. Craxton, and D. D. Meyerhofer, Opt. Lett. **16**, 1862 (1991).
4. F. G. Patterson, R. Gonzales, and M. D. Perry, Opt. Lett. **16**, 1107 (1991).
5. Y. Beaudoin *et al.*, Opt. Lett. **17**, 865 (1992).
6. G. Rouyer *et al.*, Opt. Lett. **18**, 214 (1993).
7. C. N. Danson *et al.*, Opt. Commun. **103**, 392 (1993).
8. C. Y. Chien *et al.*, Opt. Lett. **18**, 1535 (1993).
9. Y. Wang and R. Dragila, Phys. Rev. A **41**, 5645 (1990).
10. Y. Wang and B. Luther-Davies, Opt. Lett. **17**, 1459 (1992).
11. R. S. Craxton, IEEE J. Quantum Electron. **QE-17**, 1771 (1981).
12. G. P. Agrawal, *Nonlinear Fiber Optics* (Academic Press, San Diego, 1989).
13. D. Milam and M. Weber, Opt. Commun. **18**, 172 (1976).
14. L. S. Telegin and A. S. Chirkin, Sov. J. Quantum Electron. **12**, 1354 (1982).
15. C. J. McKinstrie and X. D. Cao, J. Opt. Soc. Am. B **10**, 898 (1993).
16. F. Salin, P. Georges, G. Roger, and A. Brun, Appl. Opt. **26**, 4528 (1987).

Multiple Cutoff Wave Numbers of the Ablative Rayleigh-Taylor Instability

The Rayleigh-Taylor instability occurs at the interface between heavy and light fluids when the heavy fluid is accelerated by the light fluid. The classical treatment of a sharp interface shows that a small perturbation at this boundary will grow as $e^{\gamma t}$, where γ is the linear growth.[1] The ablation front of an inertial confinement fusion (ICF) imploding target is subject to this instability because the compressed target is accelerated by the low-density ablating plasma. If small perturbations caused by either target imperfections or illumination nonuniformity grew classically, then these small perturbations would grow to sufficient amplitudes to destroy the shell of the target and degrade the performance of the implosion. It has recently been shown by several authors[2–9] that the ablation process will actually reduce the Rayleigh-Taylor growth rate at this interface and can, in fact, stabilize the interface at sufficiently short wavelengths. Calculations of the cutoff wave number for a diffuse density profile were carried out by Kull[7] and by Bud'ko and Liberman.[8] Using the assumption that the cutoff occurs at wavelengths shorter that the density-gradient scale length $L=\left[(1/\rho)(d\rho/dy)\right]^{-1}$, Bud'ko and Liberman[8] used the geometrical optics approximation of the Wentzel-Kramers-Brillouin (WKB) theory to derive the cutoff wave number in the limit of $V_a/\sqrt{gL}\rightarrow 0$, where V_a is the ablation velocity of the overdense portion of the target.

The role of the parameter $\Sigma = V_a/\sqrt{gL}$ can be easily deduced by using the following intuitive form of the instability growth rate, $\gamma \sim \sqrt{kg/(1+kL)} - kV_a$. By setting $\gamma = 0$, it is easy to show that for $\Sigma >> 1$ the cutoff wave number occurs at wavelengths longer than the density-gradient scale length $\left(k_c L \sim 1/\Sigma^2 << 1\right)$. On the contrary, for $\Sigma << 1$, the cutoff occurs a wavelength shorter than $L\left(k_c L \sim 1/\Sigma >> 1\right)$. The relative size of the cutoff wavelength to the density-gradient scale length suggests the type of mathematical technique that must be used. It is well known that short-wavelength modes with $k_c L >> 1$ can be investigated using the WKB approximation, and long-wavelength modes $\left(k_c L << 1\right)$ have a characteristic "boundary layer" structure in the sharp gradient region and can be studied with a sharp boundary model.

In this article, we derive the physical optics approximation of the WKB theory applied to the ablative Rayleigh-Taylor instability for $\Sigma << 1$, and we show the existence of multiple branches in the instability spectrum. Each branch has a different cutoff wave number and an eigenfunction characterized by a different number of zeros. Furthermore, since in typical ICF targets the density profiles are rather steep (direct drive) or the ablation velocity is rather large (indirect drive), the parameter $V_a/\sqrt{gL}$ is only approximately less than 1. The physical optics approximation also provides the next-order correction (in $V_a/\sqrt{gL} < 1$) to the largest cutoff wave number.

The WKB Approximation

We consider an equilibrium in the frame of reference of the ablation front with the heavy fluid of density ρ_h moving with velocity $U_h = -V_a \mathbf{e}_y$ (Fig. 60.4). The density smoothly varies from ρ_h to a lower value ρ_l, and the velocity increases according to the conservation of mass flow ($\rho U = constant$). The fluid is subject to a force field $\mathbf{g} = g\mathbf{e}_y$ opposite to the density gradient ($g < 0$), and the density profile has a finite density-gradient scale length in the ablation region ($y \approx 0$) with characteristic value L_0 $\left[L(0)/L_0 \sim 1\right]$. To treat the linear stability of ablation fronts, we consider a simplified incompressible model for the perturbation that is valid for subsonic ablation flow ($V_a << C_s$, where C_s is the sound speed)

$$\frac{d\rho}{dt} + \rho \nabla \cdot \mathbf{v} = 0$$

$$\rho \frac{d\mathbf{v}}{dt} = -\nabla p + \rho \mathbf{g} \qquad (1)$$

$$\nabla \cdot (\mathbf{v} - \mathbf{U}) = 0$$

where $\mathbf{U}$ is the equilibrium velocity and $d/dt = \partial/\partial t + \mathbf{v} \cdot \nabla$.

The set of linearized conservation equations can be written in the following form:

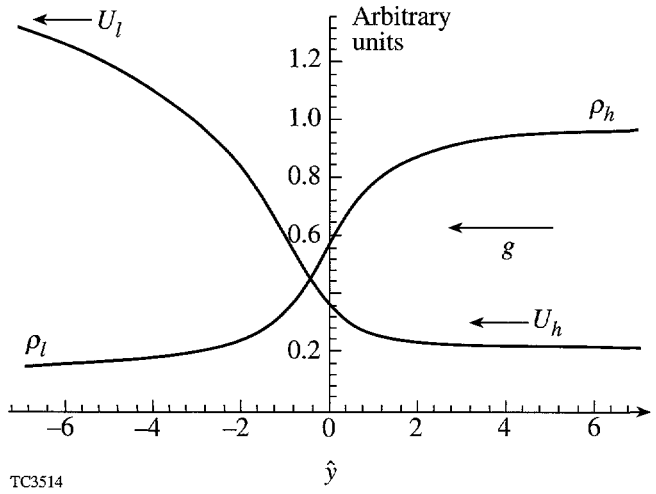

Figure 60.4
Density and velocity profiles. The subscripts l and h indicate the light and heavy fluid respectively.

$$\left(\frac{\Gamma}{\epsilon}+\partial_{\hat{y}}\right)\tilde{n}=-\tilde{v}_y/U\hat{L} \tag{2}$$

$$\left(\frac{\Gamma}{\epsilon}+\partial_{\hat{y}}\right)\tilde{v}_x=-i\tilde{p}/\epsilon\,\rho U \tag{3a}$$

$$\left(\frac{\Gamma}{\epsilon}+\partial_{\hat{y}}-1\Big/\hat{L}\right)\tilde{v}_y=-\partial_{\hat{y}}\left(\tilde{p}/\rho U\right)-\tilde{n}GL_0/U \tag{3b}$$

$$\partial_{\hat{y}}\tilde{v}_y=-i\tilde{v}_x/\epsilon\,, \tag{4}$$

where $\epsilon=1/(kL_0)$, $\hat{y}=y/L_0$, $\tilde{n}=\tilde{\rho}/\rho$, $G=-g-U^2/L$, $\hat{L}=L/L_0$, and $\Gamma=\gamma/kU$. Equations (2)–(4) can be combined into a single fourth-order ordinary differential equation

$$\left(\frac{\Gamma}{\epsilon}+\partial_{\hat{y}}-\alpha/\hat{L}\right)$$

$$\left[\epsilon^4\,\partial_{\hat{y}}\left(\frac{\Gamma}{\epsilon}+\partial_{\hat{y}}\right)\partial_{\hat{y}}\tilde{v}_y-\epsilon^2\left(\frac{\Gamma}{\epsilon}+\partial_{\hat{y}}-1/\hat{L}\right)\tilde{v}_y\right]$$

$$+\tilde{v}_y\sigma^2/\hat{L}=0, \tag{5}$$

where $\alpha=-\hat{L}\partial_{\hat{y}}\ln(U/G)$ and $\sigma^2=G/k^2U^2L_0$. Since Eq. (5) cannot be solved exactly, we look for an approximate solution when the parameter $\Sigma^2=V_a^2/gL_0$ is much less than unity, and we order $\epsilon\sim\Sigma\ll 1$, $\sigma\sim 1$, $G\simeq -g\left[1+O\left(\epsilon^2\right)\right]$, and $\alpha\simeq 1+O\left(\epsilon^2\right)$. The validity of the chosen ordering will be verified *a posteriori*. We apply the WKB theory to the fourth-order equation, and we adopt the following ansatz for the perturbation: $\tilde{v}_y=A(\hat{y})\exp\left[S(\hat{y})/\epsilon\right]$, where $A(\hat{y})$ and $S(\hat{y})$ are two slowly varying functions of $\hat{y}$, i.e., $\partial_{\hat{y}}\ln S\sim\partial_{\hat{y}}\ln A\sim 1$. The equation for $S(\hat{y})$ (geometrical optics) can be easily derived by retaining the lowest-order terms (~1) in Eq. (5):

$$\left(S'-\Gamma\right)^2\left(S'^2-1\right)+\sigma^2/\hat{L}=0. \tag{6}$$

This equation is identical to the one derived in Ref. 8. By focusing on the mode corresponding to the cutoff wave number k_c $\left[Lim_{k\to k_c}\gamma(k)\to 0^+\right]$, we solve Eq. (6) for $|\Gamma|\ll 1$ and find the four roots

$$\begin{aligned}
S_1&=\left(1/\sqrt{2}\right)\int_{\bar{y}}^{\hat{y}}\left[\left(q^+\right)^{1/2}-\tau^-\right]d\hat{y}\\
S_2&=-\left(1/\sqrt{2}\right)\int_{\bar{y}}^{\hat{y}}\left[\left(q^+\right)^{1/2}+\tau^-\right]d\hat{y}\\
S_3&=\left(1/\sqrt{2}\right)\int_{\bar{y}}^{\hat{y}}\left[\left(q^-\right)^{1/2}-\tau^+\right]d\hat{y}\\
S_4&=-\left(1/\sqrt{2}\right)\int_{\bar{y}}^{\hat{y}}\left[\left(q^-\right)^{1/2}+\tau^+\right]d\hat{y},
\end{aligned} \tag{7}$$

where

$$q^{\pm}=1\pm 2\sqrt{Q}\,,\qquad \tau^{\pm}=\frac{\Gamma}{\sqrt{2}}\left(1\pm\frac{1}{2\sqrt{Q}}\right), \tag{8}$$

$Q(\hat{y})\equiv 1/4-\sigma^2/\hat{L}$, and $\bar{y}$ is an arbitrary point. Observe that Eqs. (7)–(8) are valid for nonvanishing Q and the small t corrections are important only for $|\hat{y}|\to\pm\infty$, where $q^-\to 0$, and they can be neglected for any other value of $\hat{y}$. If Q vanishes at some point, Eq. (6) can be easily solved in the neighborhood of that point and $\Gamma\to 0^-$ yielding $S\cong\pm(\hat{y}-\bar{y})/\sqrt{2}$. This result can also be recovered from Eqs. (7)–(8) by neglecting τ even for $Q\approx 0$. We emphasize that the parameter τ is important for S_3 and S_4 only when $|\hat{y}|\to\infty$. While in Ref. 8 the analysis is limited to the geometrical optics [Eqs.(6)–(8)], here we extend the solution to include the physical optics approximation. By retaining the ϵ corrections

in Eq. (6), the following expressions for $A(\hat{y})$ are derived:

$$\begin{aligned} A_1 &= a_1 F^+(\hat{y}) \\ A_2 &= a_2 F^+(\hat{y}) \\ A_3 &= a_3 F^-(\hat{y}) \\ A_4 &= a_4 F^-(\hat{y}) \end{aligned} \tag{9}$$

$$F^{\pm}(\hat{y}) = \left(\frac{G}{|U|}\right)^{1/4} \frac{1}{Q^{1/4}\left(1 \pm 2\sqrt{Q}\right)^{1/4}} \exp\left[\mathrm{m}\frac{3}{8}\int_{\hat{y}}^{\hat{y}} \frac{d\hat{y}}{\hat{L}\sqrt{Q}}\right]. \tag{10}$$

It is important to recognize that none of the eigenfunctions represented by Eqs. (7)–(10) satisfies the boundary conditions of vanishing amplitude at both $+\infty$ and $-\infty$ simultaneously. This observation is supported by the form of the exponential terms in S_j and A_j and by the asymptotic behavior of $Q(\hat{y})$ [Fig. 60.5(a)]. It is readily derived from Eqs. (7)–(10) that in order to satisfy the boundary conditions at $y \to +\infty$, the coefficients a_1, a_3, a_4 must vanish ($a_1 = a_3 = a_4 = 0$ and $a_2 \neq 0$). On the contrary, to satisfy the boundary condition at $y \to -\infty$, the coefficient a_2 must vanish ($a_2 = 0$). Thus, the solution valid for positive y must be matched to a different solution valid for negative y. The necessary condition for the matching to occur is that $Q(\hat{y})$ vanishes at some point and the A_j's become singular. The solid line of Fig. 60.5(a) represents a possible behavior of $Q(\hat{y})$ that would allow the matching. In general there must be two points (turning points) where Q vanishes ($\hat{y} = \hat{y}_1$ and $\hat{y} = \hat{y}_2$ with $\hat{y}_1 > \hat{y}_2$) and at such points, the WKB approximation breaks down, i.e., the A_j's become singular. By defining $\hat{y}_0$ the point of minimum of

$$Q'(\hat{y}_0) = 0,\ Q(\hat{y}_0) < 0,\ Q''(\hat{y}_0) > 0,$$

we order $Q(\hat{y}_0) \sim \epsilon$ and $\hat{y}_1 - \hat{y}_2 \sim \sqrt{\epsilon}$. This ordering is verified later by the matching conditions of the solution between the turning points with the WKB approximations. As shown in Fig. 60.5(b), three regions can be identified: (1) the first outer region for $\hat{y} > \hat{y}_1$, where

$$\tilde{v}_y = A_2(\hat{y}) \exp\left[S_2(\hat{y})/\epsilon\right];$$

(2) the second outer region for $\hat{y} < \hat{y}_2$, where

$$\tilde{v}_y = A_1 \exp\left[S_1/\epsilon\right] + A_3 \exp\left[S_3/\epsilon\right] + A_4 \exp\left[S_4/\epsilon\right];$$

and (3) the inner region between the turning points $\hat{y}_2 < \hat{y} < \hat{y}_1$. To determine the solution in the inner region, we look at the behavior of the solution in the first outer region for $\sqrt{\epsilon} << \hat{y} - \hat{y}_0 << 1$ and approximate Q with its Taylor expansion $Q \approx Q_0 + Q_0''(\hat{y} - \hat{y}_0)^2/2$. By setting $\bar{y} = \hat{y}_0$, a straightforward manipulation yields

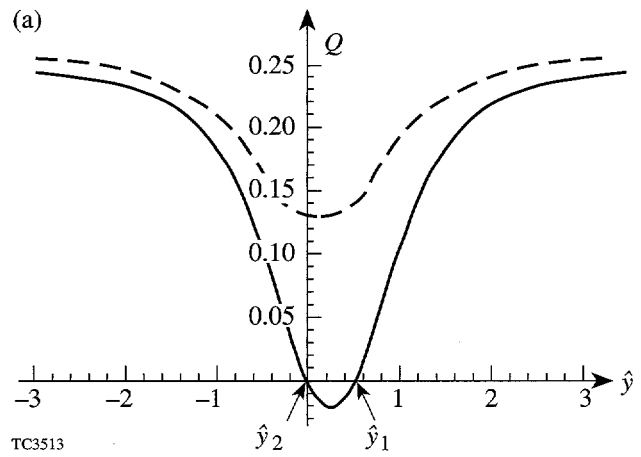

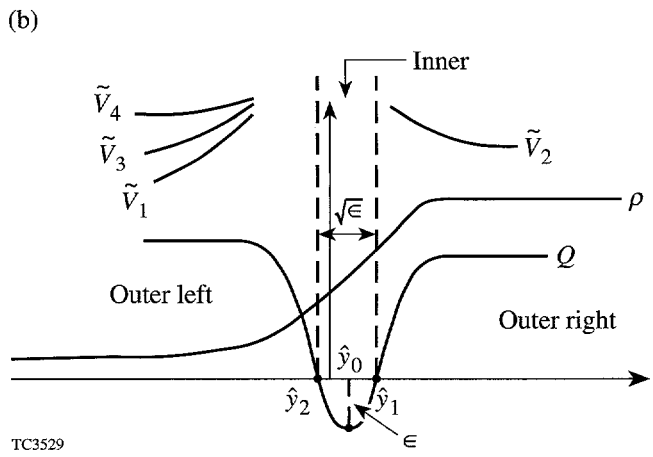

Figure 60.5
(a) Plot of Q versus $\hat{y}$. The dashed line represents a behavior without zeros $\left[(\sigma^2/\hat{L})_{\max} < 1/4\right]$. The solid line shows a $Q(\hat{y})$ with two zeros $\left[(\sigma^2/\hat{L})_{\max} > 1/4\right]$. For large $|\hat{y}|$, Q approaches 1/4. (b) Plot of the WKB solutions in the outer regions $\hat{y} >> \hat{y}_1$ and $\hat{y} << \hat{y}_2$.

$$\tilde{v}_y\left(\hat{y}\approx\hat{y}_0^-\right)=\hat{a}_2\hat{x}^\nu\exp\left[-\frac{1}{4}\sqrt{Q_0''}\hat{x}^2\right]\exp\left[-\frac{(\hat{y}-\hat{y}_0)}{\sqrt{2}\,\epsilon}\right], \quad (11)$$

where $\hat{x}=(\hat{y}-\hat{y}_0)/\sqrt{\epsilon}$, and

$$\nu=-\frac{1}{\sqrt{Q_0''}}\left(\frac{3}{2^{5/2}\hat{L}(\hat{y}_0)}\right)-\frac{1}{2}-\frac{Q_0}{\sqrt{Q_0''}}\frac{1}{2\epsilon} \quad (12)$$

$$\hat{a}_2=a_2\frac{\sqrt{2}}{Q_0^{1/4}}\left[\frac{G(\hat{y}_0)}{|U(\hat{y}_0)|}\right]^{1/4}\left(\frac{2\epsilon Q_0''}{Q_0}\right)^{\nu/2}. \quad (13)$$

The function given by Eq. (11) shows a two-scale structure (the two scales being ϵ and $\sqrt{\epsilon}$), different from what is found from the familiar second-order WKB solution near the turning points. Thus, in order to perform the matching, the solution between the turning points must retain the two-scale structure and behave as $\tilde{v}_y=\tilde{u}(\hat{x})\exp\left[-(\hat{y}-\hat{y}_0)/\sqrt{2}\,\epsilon\right]$. Substituting into the general Eq. (6) and retaining the lowest-order terms in ϵ leads to the following equation for $\tilde{u}$:

$$\left[\partial_\xi^2+\nu+\frac{1}{2}-\frac{1}{4}\xi^2\right]\tilde{u}=0, \quad (14)$$

where $\xi=\hat{x}(Q_0'')^{1/4}$. The equation for $\tilde{u}$ is just a second-order equation (instead of fourth order) and can be exactly solved. The solution of Eq. (13) is the combination of two parabolic cylinder functions $\tilde{u}=BD_\nu(\xi)+CD_\nu(-\xi)$. Matching the inner with the outer solution for $\hat{y}>\hat{y}_1$ leads to $C=0$ and $B=\hat{a}_2/(Q_0'')^{\nu/4}$. To match the rapidly varying exponential $\left\{\exp\left[-(\hat{y}-\hat{y}_0)/\sqrt{2}\,\epsilon\right]\right\}$ of the inner solution with the outer solution in the region $\hat{y}<\hat{y}_2$, the coefficients a_1 and a_3 of the outer solution must vanish. Therefore, as $\hat{y}$ approaches $\hat{y}_2$ $\left(\sqrt{\epsilon}<<\hat{y}_0-\hat{y}<<1\right)$, the outer solution assumes the following form:

$$\tilde{v}_y\left(\hat{y}\approx\hat{y}_0^+\right)=\hat{a}_4(-\hat{x})^\nu\exp\left[-\frac{1}{4}\sqrt{Q_0''}\hat{x}^2\right]\exp\left[-\frac{(\hat{y}-\hat{y}_0)}{\sqrt{2}\,\epsilon}\right], \quad (15)$$

where

$$\hat{a}_4=a_4\frac{\sqrt{2}}{Q_0^{1/4}}\left[\frac{G(\hat{y}_0)}{|U(\hat{y}_0)|}\right]^{1/4}\left(\frac{2\epsilon Q_0''}{Q_0}\right)^{\nu/2}. \quad (16)$$

Focusing on the inner solution, the asymptotic behavior of the parabolic cylinder function is easily derived:

$$D_\nu(\xi\to-\infty)\sim\xi^{-\nu-1}\exp\left[\xi^2/4\right] \qquad \nu\neq n \quad (17a)$$

$$D_n(\xi\to-\infty)\sim\xi^n\exp\left[-\xi^2/4\right] \qquad \nu=n, \quad (17b)$$

where n is an integer. By matching the inner solution with Eq. (15), we immediately deduce that ν must be an integer ($\nu=n$ with $n=0, 1, 2\ldots$), $a_4=(-1)^n a_2$, and

$$D_n(\xi)=2^{-n/2}\exp\left[-\xi^2/4\right]H_n\left[\xi/\sqrt{2}\right]$$

(H_n is the Hermite polynomial). The condition $\nu=n$ represents the equation for the cutoff wave number and can be rewritten in the extended form

$$\frac{Q_0}{\sqrt{Q_0''}}\frac{1}{2\epsilon}=-\left(n+\frac{1}{2}\right)-\frac{1}{4\sqrt{2Q_0''}}\frac{3}{\hat{L}(\hat{y}_0)}, \quad (18)$$

where $\epsilon=1/(k_cL_0)$. Observe that Eq. (18) yields $Q_0\sim\epsilon$ and $\sigma\sim 1$, in agreement with the initial assumptions. Equation (18) can be solved perturbatively by expanding k_c in powers of $\Sigma<1$ $(k_c=k_0-\Sigma k_1\ldots)$. A short calculation yields the following expression for the cutoff wave number

$$k_c=k_0\left\{1-\beta\Sigma\left[(2n+1)\sqrt{\frac{d^2Q}{d\hat{y}^2}(\hat{y}_0)}+\frac{3}{2^{3/2}}\frac{1}{\hat{L}(\hat{y}_0)}\right]\right\}, \quad (19)$$

where $k_0=2\left[|g|/L(\hat{y}_0)\right]^{1/2}/|U(\hat{y}_0)|$, $\beta=\sqrt{\hat{L}(\hat{y}_0)}\,\rho_h/\rho(\hat{y}_0)$, and $n=0, 1, 2\ldots$.

Discussion

The first important result of Eq. (19) is that multiple cutoff wave numbers exist for different values of n. In the γ, k plane, this leads to an unstable spectrum characterized by multiple branches lying one below the other. The branch with the largest cutoff and therefore the largest growth rate is for $n=0$. Although the lowest-order cutoff wave number k_0 was previously found in Ref. 8, we emphasize the importance of the first-order correction to determine the existence of the multiple branches and to provide a more accurate formula for the $n=0$ branch when $\Sigma\lesssim 1$. Table 60.I provides a comparison

between the cutoff wave number of the $n = 0$ branch predicted by Eq. (19) and the one of Ref. 8 for the following form of the density profile

$$\rho(y) = \frac{\rho_h}{1+A}\left[1 + \frac{2}{\pi} A \tan^{-1}\frac{y}{L_0}\right]. \tag{20}$$

Table 60.I Cutoff wave number for $n = 0$. Comparison of the cutoff wave number for the $n = 0$ branch predicted by Eq. (19) and Ref. 8 for $A = 0.9$, $g = 5 \times 10^{15}$ cm/s^2, $v_a = 7.5 \times 10^4$ cm/s, and varying L_0.

L_0 (μm)	Eq. (19) (μm^{-1})	Ref. 8 (μm^{-1})	Σ
50.0	1.05	1.10	0.015
10.0	2.22	2.66	0.034
5.0	2.99	3.48	0.047
3.0	3.68	4.49	0.061
2.0	4.28	5.50	0.075
1.0	5.33	7.78	0.11
0.5	6.10	11.01	0.15

Observe that the first-order correction in Σ becomes important when the density profile is rather steep (direct-drive ICF) or the ablation velocity is rather large (indirect-drive ICF). Since the eigenfunction in the inner region is proportional to $H_n(\xi)$, the integer n determines the number of zeros of the eigenfunction. Figure 60.6 shows the normalized eigenfunction for the $n = 0$, $n = 1$, and $n = 2$ modes for a smooth density profile. Observe the degradation of the matching between the outer WKB approximations and the inner solution as n increases. This effect is due to the increasing magnitude of the higher-order corrective terms that scale as $\Sigma k_1(n)/k_0$. Thus we expect that the matching cannot be performed for $\Sigma k_1(n)/k_0 > 1$ and the number of branches does not exceed N with $\Sigma k_1(N)/k_0 > 1$. Equation (19) has also been solved numerically, and the results have been compared with the analytical predictions. Figure 60.7 shows the unstable spectrum of an equilibrium configuration typical of direct-drive ICF with $g = 5 \times 10^{15}$ cm/s^2, $V_a = 7.5 \times 10^4$ cm/s, $A = 0.9$, and $L_0 = 2$ μm. Three branches have been found with $n = 0$, $n = 1$, and $n = 2$. For this set of parameters $\Sigma k_1(3)/k_0 = 1.01$, and the predicted number of branches is indeed $N = 3$. Equation (19) predicts the following values of the cutoff wave numbers: $k_c(n = 0) = 4.28$ μm^{-1}, $k_c(n = 1) = 2.83$ μm^{-1}, and $k_c(n = 2) = 1.37$ μm^{-1}. As expected the accuracy of Eq. (19) in predicting the cutoff wave number degrades as n increases. For the same equilibrium parameters, the geometrical optics approximation

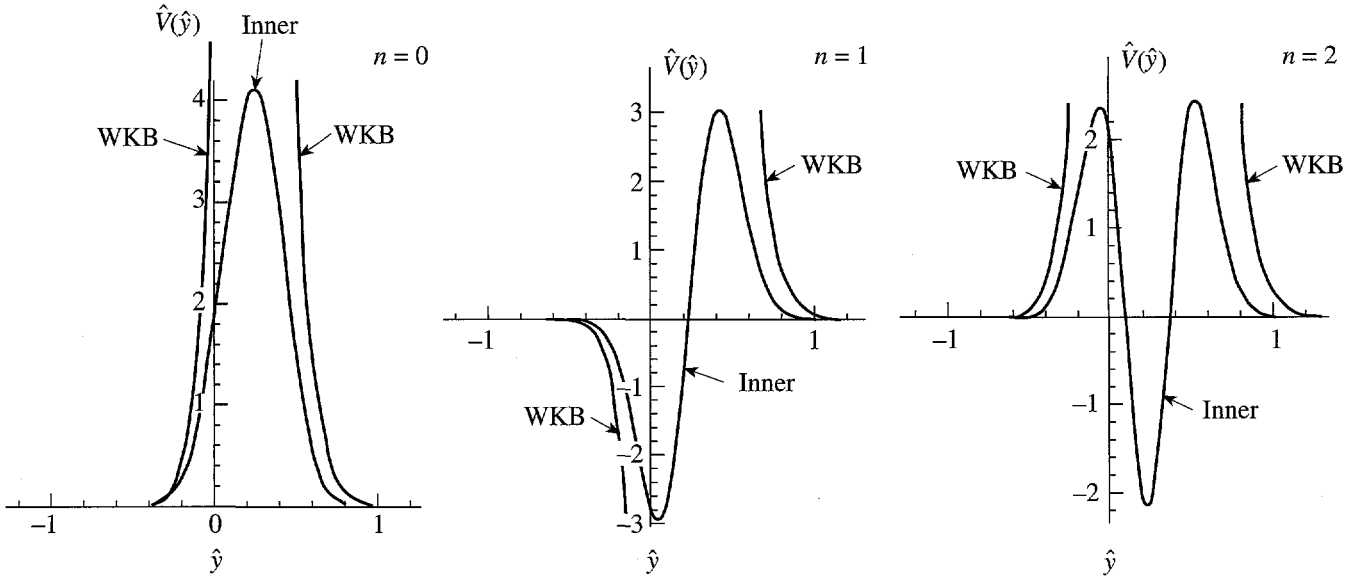

Figure 60.6
Plot of the normalized eigenfunction $\hat{V} = \tilde{v}_y(\hat{y})\exp\left[(\hat{y}-\hat{y}_0)/\sqrt{2}\epsilon\right]$, for the $n = 0$, 1, 2 modes and the following equilibrium parameters: $A = 0.8$, $g = 10^{15}$ cm/s^2, $v_a = 10^4$ cm/s, and $L_0 = 10$ μm.

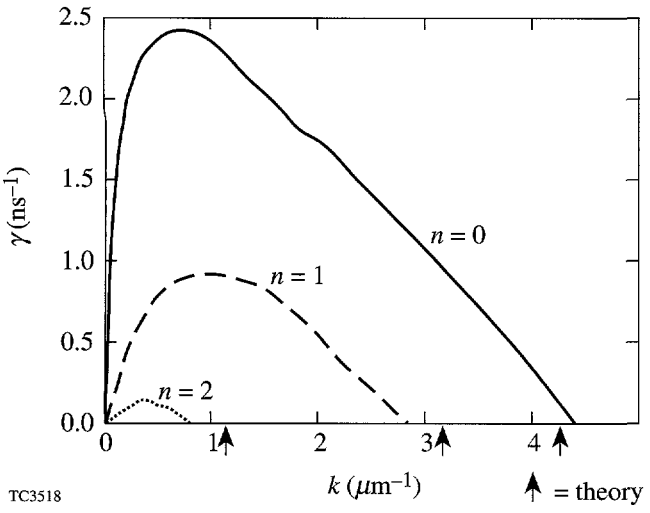

Figure 60.7
Plot of the growth rate versus the wave number for the $n = 0$, 1, 2 branches and the following equilibrium parameters: $A = 0.9$, $g = 5 \times 10^{15}$ cm/s^2, $v_a = 7.5 \times 10^4$ cm/s, and $L_0 = 2$ μm.

of Ref. 8 predicts a cutoff of the $n = 0$ mode at $k = 5.5$ μm^{-1} with a relative error of approximately 30%. To simplify Eq. (19), we focus on typical ICF equilibria with $A \approx 1$ and density profile given by Eq. (20) to determine an approximate value of $\hat{y}_0$, $\hat{y}_0 \approx 0.25\left(\sqrt{8+\pi^2}-\pi\right)$. Substituting $\hat{y}_0$ into the expressions for $Q(\hat{y}_0)$ and $\hat{L}(\hat{y}_0)$, we derived the following approximate form of the cutoff wave number:

$$k_c \simeq k_0\left[1-2\sqrt{\pi}\ \Sigma\left(n+\frac{7}{8}\right)\right] \qquad (n = 0, 1, 2 \ldots) \quad (21)$$

and $k_0 \simeq \left(\sqrt{2.17/\pi}\right)/\Sigma L_0$. In addition to the cutoff wave number, the WKB approximation also provides the position where the short-wavelength modes are localized. The peak of the eigenfunction is located at the point $\hat{y}^*$, where $S'(\hat{y}^*) = 0$. Using Eq. (6) at $\hat{y} = \hat{y}^*$ we derive an equation for $\hat{y}^*$:

$$\Gamma^2(\hat{y}^*) = \sigma(\hat{y}^*)^2 / \hat{L}(\hat{y}^*). \qquad (22)$$

For any given Γ, Eq. (22) can be solved for the unknown $\hat{y}^*$. It follows immediately that the mode corresponding to the cutoff wave number ($\Gamma = 0$) has the peak of the eigenfunction at $-\infty$, where $1/\hat{L} = 0$. More generally, it can be deduced from Eq. (22) that as the wave number of the mode increases and the growth rate decreases, the peak of the eigenfunction is shifted downstream in the light-fluid region. To verify the accuracy of the incompressible model in predicting the unstable spectrum for $\Sigma < 1$, we compare the growth rates derived from Eqs. (2)–(4) with the numerical results of Ref. 3, where the full set of fluid equations, including thermal transport, has been numerically solved. According to Ref. 3, the growth-rate dependence on the mode wave number is well fit by the following formula:

$$\gamma = 0.9\sqrt{kg} - \beta k V_a, \qquad (23)$$

where β is an adjustable parameter varying between 3 and 4. Figure 60.8 shows an unstable spectrum obtained from the numerical solution of the incompressible model for $\Sigma = 0.14$ and Takabe's formula for $\beta = 3$–4. Observe that the predictions of the incompressible model (for $\Sigma < 1$) are in good agreement with the more general results of Ref. 3. For the same value of Σ, Eq. (19) yields the normalized cutoff wave number $\sqrt{k_c V_a^2/g} = 0.26$. To check the validity of the incompressible mode for arbitrary equilibria, we also compare the incompressible spectrum for $\Sigma >> 1$ with the result of Ref. 3. We find that the incompressible model predicts a larger ablative stabilization than Eq. (23). For $\Sigma >> 1$, the incompressible growth rate can be written in the following form:

$$\gamma = \sqrt{AKg} - kV_a\frac{1+A}{1-A} \qquad (24)$$

in agreement with the results of Ref. 4. For $A \simeq 1$, Eq. (24) predicts a large stabilization that is not observed in the numerical simulations.[3,5,9] We conclude that the incompressibility assumption breaks down for $\Sigma >> 1$, and the effect of finite thermal conductivity must be retained.[7]

Conclusions

We have derived the physical optics approximation of the WKB theory applied to the incompressible ablative Rayleigh-Taylor instability, and we have found the existence of multiple branches in the unstable spectrum. The calculated cutoff wave number is also reasonably accurate for configurations with rather steep density gradients or large ablation velocity ($\Sigma \lesssim 1$). Although this is the first derivation of the multiple unstable branches in the presence of an equilibrium flow, this result is not surprising, as in the classical Rayleigh-Taylor instability, multiple modes also exist. However, no branch experiences a cutoff in the classical treatment, and the growth rate is monotically increasing with the mode wave number.

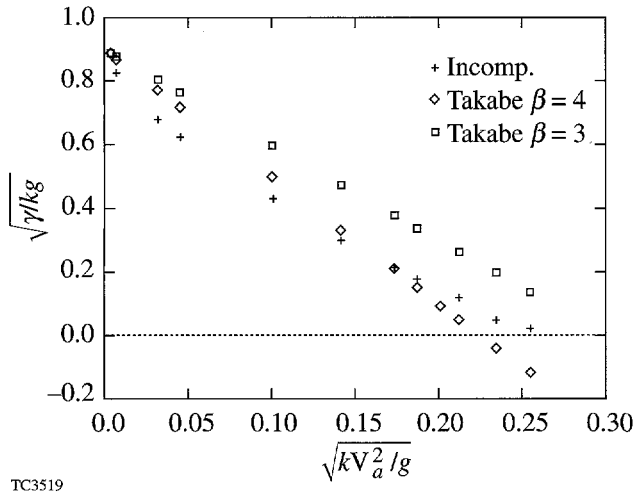

Figure 60.8
Plot of the normalized growth rate $\sqrt{\gamma/kg}$ versus the normalized wave number $\sqrt{kV_a^2/g}$, for the incompressible model (+), Eq. (23) with $\beta = 3$ (□), and Eq. (23) with $\beta = 4$ (◇). The equilibrium parameters are $L_0 = 0.5$ μm, $g = 10^{16}$ cm/s^2, $V_a = 10^5$ cm/s, and $A = 0.95$.

ACKNOWLEDGMENT

This work was supported by the U.S. Department of Energy Office of Inertial Confinement Fusion under Cooperative Agreement No. DE-FC03-92SF19460, the University of Rochester, and the New York State Energy Research and Development Authority. The support of DOE does not constitute an endorsement by DOE of the views expressed in this article.

REFERENCES

1. Lord Rayleigh, *Scientific Papers* (Cambridge University Press, Cambridge, England, 1900), Vol. II, p. 200.
2. S. Bodner, Phys. Rev. Lett. **33**, 761 (1974).
3. H. Takabe, K. Mima, L. Montierth, and R. L. Morse, Phys. Fluids **28**, 3676 (1985).
4. H. J. Kull and S. I. Anisimov, Phys. Fluids **29**, 2067 (1986).
5. J. H. Gardner, S. E. Bodner, and J. P. Dahlburg, Phys. Fluids B **3**, 1070 (1991).
6. K. O. Mikaelian, Phys. Rev. A **46**, 6621 (1992).
7. H. J. Kull, Phys. Fluids B **1**, 170 (1989).
8. A. B. Bud'ko and M. A. Liberman, Phys. Rev. Lett. **68**, 178 (1992).
9. C. P. Verdon, R. L. McCrory, R. L. Morse, G. R. Baker, D. I. Meiron, and S. A. Orszag, Phys. Fluids **25**, 1653 (1982).

Ultrafast, All-Silicon Light Modulator

The ability to send high-speed messages between integrated circuit devices requires both high-frequency receivers and transmitters. The vast majority of integrated circuits are made from silicon-based semiconductors. Suitable receivers of silicon integrated circuits can be constructed from either metal-semiconductor-metal photodiodes[1] or *P*-type, intrinsic, *N*-type (PIN) photodiodes. These receivers are capable of acting as interconnection devices for frequencies up to tens of gigahertz. The transmitter half of this interconnection for silicon has proved to be more problematic. A semiconductor laser has yet to be made from silicon and may prove to be an impossible task. It may be possible to use an optical modulator in place of a semiconductor laser as the transmitter for silicon-based integrated circuits. The refractive index of silicon can be modified by the free-carrier density (the carrier-refraction effect);[2] therefore, the refractive index can be changed by either the injection or depletion of free-carriers.

This effect has been utilized in all-silicon, light-intensity modulators.[3–6] These devices have typically two components: one is an optical phase modulator; the other converts the phase modulation to intensity modulation. In the phase-modulation device, carrier injection into a lightly doped layer provides an extended interaction region wherein the index of refraction may be externally controlled. However, using carrier injection poses two undesirable concerns: the injected current density must be high, and the devices are inherently slow because their speed is limited by the carrier lifetime (nanoseconds to microseconds).

For practical applications, a high-speed, low-power-dissipation, high-modulation-depth, small-sized modulator is desirable. In this article we propose an ultrafast light modulator made on silicon-on-insulator (SOI) substrates. It is a field-effect device, accompanied naturally with low-power dissipation. This modulator is based on carrier depletion instead of carrier injection; hence, its speed may be limited only by the device capacitance and is estimated to be as high as 70 GHz. Most importantly, this modulator is not based on phase modulation. It is a Bragg reflector induced by electric field, which efficiently converts the small index modulation to light-intensity modulation.

Figure 60.9 shows the schematic view of the modulator. The SOI structure acts as an optical waveguide. On top of the silicon layer are interdigitated metal fingers, which form Schottky contacts with silicon. A microstrip line guides the electrical signal to the metal fingers. When the metal fingers are alternately biased, they form forward- and reverse-biased Schottky junctions with silicon. There are larger depleted regions on the reverse-biased sides, as shown in the shaded part of Fig. 60.10. In a *P*-type silicon layer with a hole concentration of $3 \times 10^{18}/\text{cm}^3$, there is a refractive-index difference of $\Delta n = 0.005$ between the depleted and undepleted regions, assuming an optical wavelength of 1.55 μm.[2] The alternately depleted and undepleted areas form a Bragg reflector in the optical waveguide. Applying a time-dependent voltage to the metal fingers modulates the shape of the depleted regions and, in turn, the reflectivity of the Bragg reflector and the light intensity.

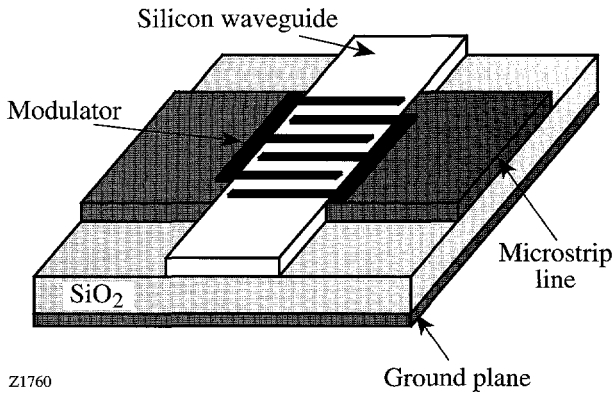

Figure 60.9
A schematic view of the waveguide modulator. The SOI structure acts as an optical waveguide. On top of the silicon layer are interdigitated metal fingers, which form Schottky contacts with silicon. A microstrip line guides the electrical signal to metal fingers.

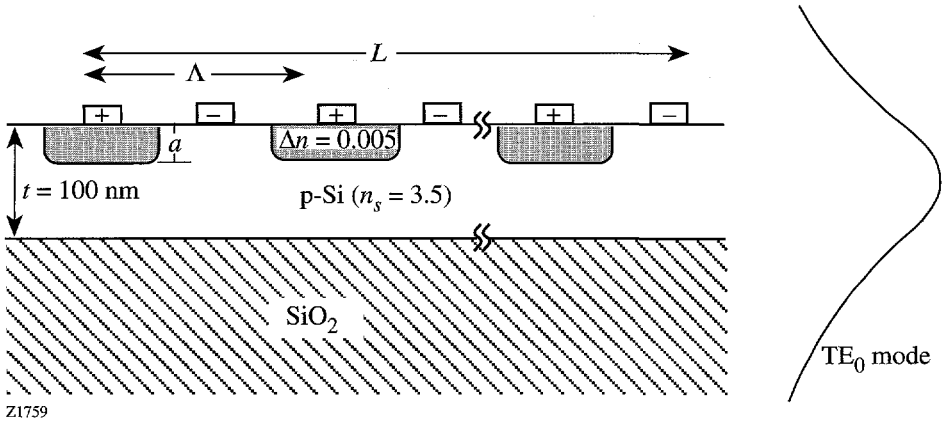

Figure 60.10
The reversed-biased Schottky contacts have larger depleted regions (shaded part), which have a larger refractive index. The alternating depleted and undepleted regions form a Bragg reflector in the waveguide. The electric-field-induced Bragg reflector converts the index modulation to light-intensity modulation. The TE_0 mode profile is shown to the right of the modulator.

The reflectivity, or the modulation depth of this device, can be calculated by using coupled-mode theory.[7] The modulation depth is maximized when the Bragg condition is satisfied, i.e., $\Lambda = \lambda/2$, where Λ is the period of finger electrodes as shown in Fig. 60.10 and λ is the light wavelength in the guiding layer. In this case, the reflectivity can be expressed as $R = \tanh^2(\kappa L)$, where L is the interaction length of the modulator and κ is the coupling constant. If the depleted region is assumed to have a rectangular shape and equal length with the undepleted region (as shown in Fig. 60.10), then κ is given by[7]

$$\kappa = \frac{\omega\varepsilon_0\left[\left(n_s + \Delta n\right)^2 - n_s^2\right]}{4\pi} \times \int_{-a}^{0} |E(x)|^2 \, dx, \qquad (1)$$

where ω is the frequency of the optical wave, $E(x)$ is the normalized wave solution of the optical waveguide, a is the depletion width, and n_s is the refractive index of the silicon layer. Here, n_s is taken to be 3.50. The indices of air and silicon dioxide are chosen to be 1 and 1.45. The thickness of the guiding layer is chosen to be 100 nm for single-mode operation and to sufficiently guide the TE_0 mode of light with wavelength of 1.55 μm. (For TM mode, the coupling constant is much smaller, characteristic of Bragg reflectors.) The guided wavelength in this SOI waveguide is 0.72 μm; thus, to satisfy the Bragg condition the period of the finger electrodes is 360 nm.

Since a is a function of the electrode voltage, the modulation depth is also voltage dependent. The modulation depth as a function of biasing voltage is shown in Fig. 60.11 for several interaction lengths. In this calculation, the hole concentration of the silicon layer is set to be $3 \times 10^{18}/\text{cm}^3$, and the built-in voltage of the Schottky contact is 0.5 V, which is typical for metal-semiconductor contacts. It shows that, with 5-V bias, a modulator with interaction length of 300 and

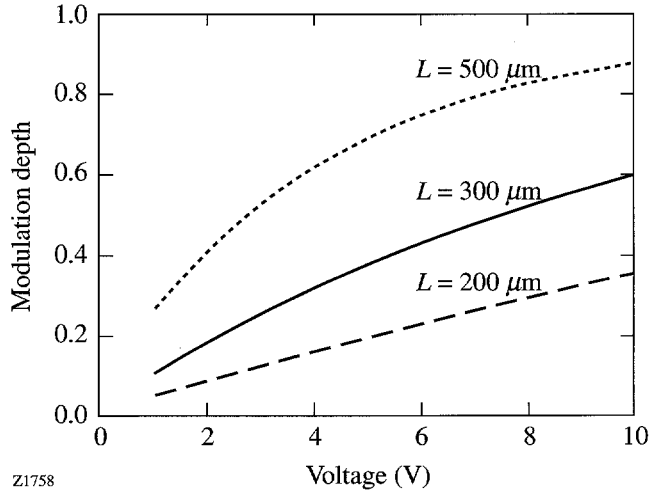

Figure 60.11
The modulation depth of modulators for TE_0 mode with different interaction lengths is shown as a function of biasing voltage. The thickness of the guiding layer is 100 nm, and the doping is $P = 3 \times 10^{18}/\text{cm}^3$.

500 μm has a modulation depth of about 40% and 70%, adequate for most applications.

In an actual device, the depletion region is, of course, not rectangular. Such a profile has been simulated using the MEDICI program[8] and is shown in Fig. 60.12. However, since the modulation depth depends only on the fundamental Fourier component of the shape of the depletion region, we expect the simulated results in Fig. 60.11 to closely approximate that of an actual device.

A similar structure has been used by Alferness and Buhl[9] on an electro-optic modulator, which provides the conversion between TE and TM modes. However, the co-directional coupling between TE and TM modes requires a much larger electrode period to satisfy the Bragg condition. As a result,

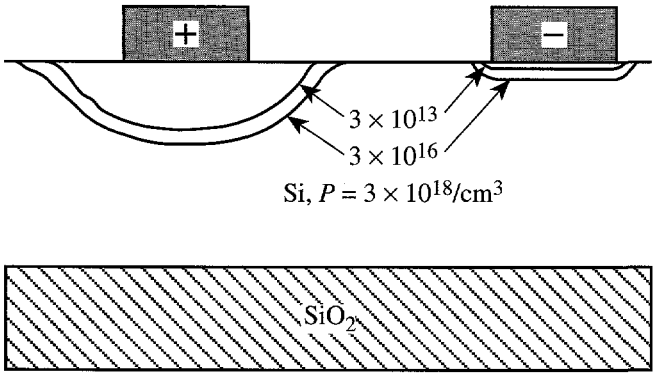

Figure 60.12
The shape of the depleted region is examined by using the MEDICI simulation program. There are alternately depleted and undepleted regions under the reverse- and forward-biased finger electrodes. The finger width and spacing are 60 and 120 nm, respectively. The doping of silicon is $P = 3 \times 10^{18}/\text{cm}^3$; the bias voltage is 5 V.

the size of this TE ↔ TM modulator is large (of the order of millimeters). Furthermore, Alferness's modulator is not integrable with silicon planar circuits because an external polarizer is required to convert polarization modulation to intensity modulation.

The fabrication of our proposed modulator is feasible with existing fabrication techniques. Bond-and-etchback SOI wafers have proven to be a good optical waveguide material with scattering loss of about 3.3 dB/cm for $\lambda = 1.55$ μm.[10] A grating coupler can be used to couple light into or out of the optical waveguide. The nanometer-sized finger electrodes can be fabricated by using modern electron-beam lithography.[11] A thin silicon-dioxide layer can be placed between the finger electrodes and the silicon layer to increase the breakdown voltage and avoid direct metal loading, which contributes to the attenuation of the guided wave.

The operational speed of this device is predominantly limited by the intrinsic device RC time constant, where R is the line impedance connecting to the modulator and C is the modulator capacitance. Parasitic capacitance for this structure is negligible, as shown from our previous measurements on a photodetector with similar structure.[11] For the inherent RC time constant, there is a trade-off between the modulation depth and the interaction length of the modulator, which affects its bandwidth. A modulator with 60-nm finger width, 120-nm finger spacing, 3-μm finger length, and 300-μm interaction length is calculated to have a capacitance of 0.22 pf.[12] (For the interdigitated structure, the capacitance is proportional to the interaction length and inversely proportional to the finger period.) If a microstrip line with 10-Ω impedance is used, the bandwidth of this modulator is $1/2\pi$ RC, or about 70 GHz. A thinner guiding layer may improve the bandwidth in two ways: by increasing the coupling constant, thus allowing a shorter interaction length, and by increasing the guided wavelength; as a result, the period of the metal fingers is increased and the capacitance is decreased.

For practical applications, the insertion loss to this modulator should be considered but is dependent on the configuration chosen. Free-carrier absorption would also contribute to the loss. For the proposed sample device, this effect is estimated to be about 0.6 dB[2]. Finally, for this Bragg reflector, an optical isolator such as a directional coupler at the insertion point is clearly necessary to prevent multiple reflections.

In conclusion, an ultrafast, all-silicon, light-intensity modulator has been proposed. An electric-field-induced Bragg reflector efficiently converts the small refractive-index modulation to light-intensity modulation. A modulator with 300-μm interaction length is shown to have a modulation depth about 40% with 5-V bias. Because it is a field-effect device, it has power dissipation dominated by leakage current and the resistance of the metal fingers. The speed of the modulator is limited only by the RC time constant, and a sample device has a bandwidth about 70 GHz. The same interdigitated structure has been demonstrated by us[13] to be usable as a picosecond photodetector. Both device structures are compatible with silicon circuits, lending themselves to potential use in integrated electronic-optoelectronic systems.

ACKNOWLEDGMENT

This work was supported by the University Research Initiative at the University of Rochester sponsored by the Army Research Office grant No. DAAL03-92-G-0112. We would like to acknowledge Dr. Xing Zhou for his computation of Fig. 60.12.

REFERENCES

1. S. Alexandrou, C.-C. Wang, T. Y. Hsiang, M. Y. Liu, and S. Y. Chou, Appl. Phys. Lett. **62**, 2507 (1993).

2. R. A. Soref and B. R. Bennett, IEEE J. Quantum Electron. **QE-23**, 123 (1987).

3. B. R. Hemenway, O. Solgaard, and D. M. Bloom, Appl. Phys. Lett. **55**, 349 (1989).

4. B. R. Hemenway, O. Solgaard, A. A. Godil, and D. M. Bloom, IEEE Photonics Technol. Lett. **2**, 262 (1990).

5. O. Solgaard, A. A. Godil, B. R. Hemenway, and D. M. Bloom, IEEE Photonics Technol. Lett. **2**, 640 (1990).

6. X. Xiao, J. C. Sturm, K. K. Goel, and P. V. Schwartz, IEEE Photonics Technol. Lett. **3**, 230 (1991).

7. A. Yariv and P. Yeh, *Optical Waves in Crystals: Propagation and Control of Laser Radiation* (Wiley, New York, 1984), Chap. 11.

8. Computer code MEDICI (Technology Modeling Associates, Inc., 3950 Fabian Way, Palo Alto, CA 94303-4605, USA, 1993).

9. R. C. Alferness and L. L. Buhl, Opt. Lett. **5**, 473 (1980).

10. A. F. Evans, D. G. Hall, and W. P. Maszara, Appl. Phys. Lett. **59**, 1667 (1991).

11. M. Y. Liu, S. Y. Chou, T. Y. Hsiang, S. Alexandrou, and R. Sobolewski, J. Vac. Sci. Technol. B **10**, 2932 (1992).

12. Y. C. Lim and R. A. Moore, IEEE Trans. Electron Devices **15**, 173 (1968).

13. C.-C. Wang, S. Alexandrou, D. Jacobs-Perkins, and T. Y. Hsiang, "Comparison of the Picosecond Characteristics of Silicon and Silicon-on-Sapphire Metal-Semiconductor-Metal Photodiodes," Appl. Phys. Lett. **64**, 3578 (1994).

Angular Dependence of Stimulated Brillouin Scattering in Homogeneous Plasma

Stimulated Brillouin scattering (SBS)[1] is the decay of an incident, or pump, light wave (0) into a frequency-downshifted, or Stokes, light wave (1) and an ion-acoustic wave (2). The conservation of energy and momentum in this process is reflected in the frequency and wave-vector matching conditions

$$\omega_0 = \omega_1 + \omega_2, \quad \mathbf{k}_0 = \mathbf{k}_1 + \mathbf{k}_2, \tag{1}$$

the second of which is illustrated in Fig. 60.13(a). For future reference, notice that the ion-acoustic wave number k_2 is maximal for directly backward scatterering and is equal to zero for directly forward scattering.

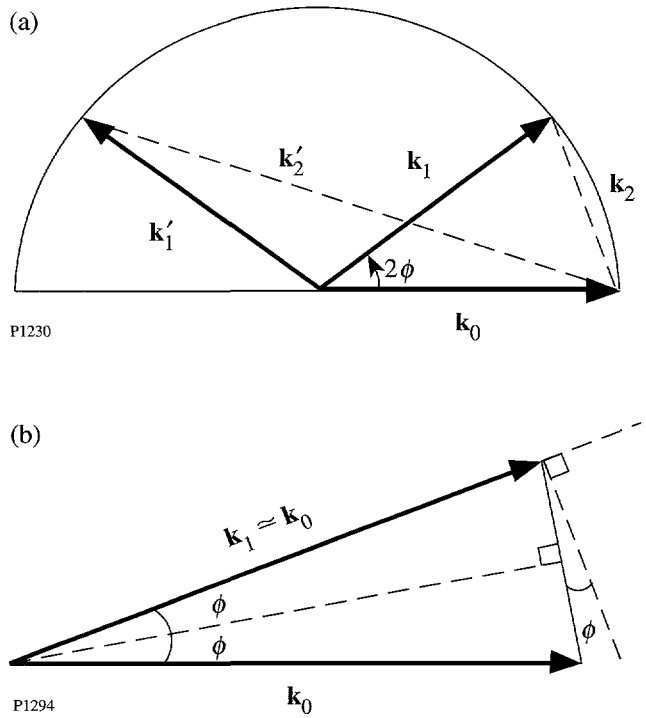

Figure 60.13
Interaction geometry for SBS. The angular dependence of γ_0, the temporal growth rate of SBS, stems from the fact that $k_2 \approx 2k_0 \sin\phi$.

SBS is important in the field of inertial confinement fusion (ICF)[2] because it can scatter the incident light away from the target, thereby reducing the amount of energy available to drive the compressive heating of the nuclear fuel. ICF experiments have involved plasmas with density and temperature scale lengths shorter than 100 μm for much of the last two decades, and analyses of parametric instabilities such as SBS have focused on the effects of these plasma inhomogeneities.[3] However, current experiments are designed to produce plasma conditions relevant to the proposed National Ignition Facility and involve plasmas with millimeter scale lengths. There has been a resurgence of interest in the predictions of the simpler homogeneous-plasma model because such long scale lengths diminish the importance of the effects of plasma inhomogeneities.

Traditionally, analyses of SBS begin with the determination of γ_0, the temporal growth rate of SBS in an infinite homogeneous plasma. It is well known that γ_0 is maximal for directly backward scattering and is equal to zero for directly forward scattering.[1] Physically, this behavior occurs because the ponderomotive force that drives the ion-acoustic wave is proportional to the square of the ion-acoustic wave number. Recognition of this behavior has led to the commonly held belief that backward SBS should dominate experiments involving long-scale-length plasmas.

The problem with this conclusion is that SBS cannot grow exponentially in time, with growth rate γ_0, for a time longer than that taken for light to cross the interaction region.[4] In current experiments, this transit time does not exceed a few picoseconds. In contrast, the temporal pulsewidth of a typical laser is a few nanoseconds, and the initial period of temporal growth is followed by a much longer period of spatiotemporal growth. If the incident laser intensity is less than the threshold intensity for the absolute instability, SBS will eventually saturate due to the convection of the Stokes and ion-acoustic waves out of the interaction region. If this convective saturation occurs on a nanosecond time scale, the angular dependence of the scattered light will be determined predominantly

by the physics of steady-state amplification. The goal of the work presented in this article is to determine how the convective amplification of the Stokes wave depends on the scattering angle and the conditions under which a steady-state analysis is applicable.

Governing Equations

The starting point for this investigation is Maxwell's wave equation

$$\left(\partial_{tt}^2 + \omega_e^2 - c^2\nabla^2\right)\mathbf{A}_h = -\omega_e^2 n_l \mathbf{A}_h \tag{2}$$

for the vector potential, together with the ion-acoustic wave equation

$$\left(\partial_{tt}^2 - c_s^2\nabla^2\right)n_l = \frac{1}{2}c_s^2\nabla^2\left\langle \mathbf{A}_h \cdot \mathbf{A}_h \right\rangle. \tag{3}$$

These equations were derived[5,6] under the assumption that the backgound plasma is uniform and at rest. The vector potential is normalized in such a way that $\mathbf{A}_h$ represents the velocity of electrons oscillating in the high-frequency electric field divided by a characteristic speed that is approximately equal to the electron thermal speed and n_l represents the low-frequency electron-density fluctuation associated with the ion-acoustic wave divided by the background elecron density. The symbol ω_e denotes the electron plasma frequency,[6] and the symbol c_s denotes the ion-acoustic speed.[7] Only the low-frequency plasma response to the ponderomotive force was retained, as is signified by the $\langle\ \rangle$ in Eq. (3).

SBS involves the interaction of two light waves and an ion-acoustic wave. These waves are coupled because of the electron current and the ponderomotive force, both of which are nonlinear. Because the effects of this coupling manifest themselves as slow spatial and temporal modulations of the wave amplitudes, the vector potential is written as

$$\mathbf{A}_h(\mathbf{r},t) = \mathbf{z}\Big\{A_0 \exp\left[i\left(\mathbf{k}_0\cdot\mathbf{r} - \omega_0 t\right)\right] + A_1(x,y,t)\exp\left[i\left(\mathbf{k}_1\cdot\mathbf{r} - \omega_1 t\right)\right]\Big\}, \tag{4}$$

where $\mathbf{k}_0$ and $\mathbf{k}_1$ are parallel to the xy plane, $(\omega_0,\mathbf{k}_0)$ and $(\omega_1,\mathbf{k}_1)$ satisfy the dispersion relation $\omega^2 = \omega_e^2 + c^2k^2$, and

$$\nabla A_1 \ll \mathbf{k}_1 A_1,\ \partial_t A_1 \ll \omega_1 A_1. \tag{5}$$

In this linearized analysis of the initial evolution of SBS, the amplitude of the incident wave is held fixed. The electron-density fluctuation is written as

$$n_l(\mathbf{r},t) = A_2(x,y,t)\exp\left[i\left(\mathbf{k}_2\cdot\mathbf{r} - \omega_2 t\right)\right], \tag{6}$$

where $\omega_2 = c_s k_2$ and A_2 satisfies an equation similar to Eq. (5). By substituting Ansaetze (4) and (6) into Eqs. (2) and (3), and collecting terms of like frequency and wave vector, one finds that

$$\begin{aligned}\left(\partial_t + \mathbf{v}_1\cdot\nabla + \nu_1\right)B_1 &= \gamma_0 B_2,\\ \left(\partial_t + \mathbf{v}_2\cdot\nabla + \nu_2\right)B_2 &= \gamma_0 B_1.\end{aligned} \tag{7}$$

In Eqs. (7) the dependent variables

$$B_1 = \omega_1^{1/2}A_1,\quad B_2 = -i\omega_e A_2^*/\omega_2^{1/2} \tag{8}$$

are proportional to the action amplitudes of the Stokes and ion-acoustic waves, respectively, and the group velocities

$$\mathbf{v}_1 = c^2\mathbf{k}_1/\omega_1,\quad \mathbf{v}_2 = c_s\mathbf{k}_2/k_2. \tag{9}$$

Phenomenological damping terms were added to each wave equation. The Stokes wave is damped by electron-ion collisions[6] and

$$\nu_1 = \omega_e^2\nu_{ei}/2\omega_1^2. \tag{10}$$

For plasmas in which $(T_i/m_i)^{1/2} \ll \omega_2/k_2 \ll (T_e/m_e)^{1/2}$, the Landau contribution to the ion-acoustic damping rate[7] is given by

$$\frac{\nu_2}{c_s k_2} \approx \left(\frac{\pi}{8}\right)^{1/2}\left[\left(\frac{ZT_e}{T_i}\right)^{3/2}\exp\left(-\frac{ZT_e}{2T_i} - \frac{3}{2}\right) + \left(\frac{Zm_e}{m_i}\right)^{1/2}\right]. \tag{11}$$

Relation (11) is based on the assumption that the ion-acoustic wavelength is much longer than the electron Debye length, an assumption that is also inherent in Eq. (3). The coupling parameter

$$\gamma_0 = \frac{\omega_e c_s k_2 A_0}{2(\omega_1 c_s k_2)^{1/2}}, \tag{12}$$

where the peak amplitude of the incident wave is given by the convenient formula

$$2A_0 \approx \frac{1.9\times10^{-8}\left[I(\mathrm{W/cm^2})\right]^{1/2}\lambda_0(\mu\mathrm{m})}{\left[T_e(\mathrm{keV})\right]^{1/2}\left[1+3(T_i/ZT_e)\right]^{1/2}}. \tag{13}$$

It is clear from Fig. 60.13(b) that $k_2 \approx 2k_0 \sin\phi$. Thus, one can exhibit the angular dependence of the coupling parameter and the ion-acoustic damping rate by writing

$$\gamma_0(\phi) = \gamma_b(\sin\phi)^{1/2}, \quad v_2(\phi) = v_b \sin\phi, \tag{14}$$

where the subscript b denotes values appropriate for backward SBS. In a similar vein,

$$v_{2x} = -c_s \sin\phi. \tag{15}$$

Steady-State Amplification of the Stokes Wave

In experiments typical of ICF the growth of the Stokes wave is initiated within the plasma by ion-acoustic fluctuations. This process is referred to in the nonlinear optics literature as Stokes generation and has been analyzed by Boyd, Rzazewski, and Narum.[8] By neglecting the convection of the acoustic wave, they showed that the time-asymptotic Stokes output can be written as the product of two terms: a source factor that depends on the amplitude of the acoustic fluctuations and an exponential gain factor that does not depend on the amplitude of the acoustic fluctuations. Furthermore, the exponent of the gain factor is identical to that for the Stokes amplification process, in which an externally generated Stokes wave is amplified convectively as it propagates through the medium. A preliminary analysis of Stokes generation in a plasma, which includes the convection of the ion-acoustic wave, has been made by McKinstrie *et al.*[9] The inclusion of ion-acoustic wave convection allows SBS to be absolutely unstable when the laser intensity is sufficiently high. However, in the convectively unstable regime, the Stokes output tends to a time-asymptotic steady state, and the gain exponents for Stokes generation and Stokes amplification are identical, as one should expect. Thus, one can avoid the mathematical difficulties associated with the analysis of Stokes generation and still obtain useful information regarding the angular dependence of SBS by analyzing Stokes amplification in the convectively unstable regime.

The interaction geometry for Stokes amplification is shown in Fig. 60.14(a). Initially,

$$B_1(x,y,0) = 0, \quad B_2(x,y,0) = 0. \tag{16}$$

At time $t = 0$ the leading edge of the externally generated Stokes wave enters the plasma with unit amplitude and initiates the instability. The ion-acoustic wave has zero amplitude at its entrance boundaries. For simplicity, we assume that the plasma is square and that its boundaries are aligned with the x and y axes. Thus, for $t > 0$,

$$B_1(0,y,t) = 1, \quad B_2(x,0,t) = 0, \quad B_2(l,y,t) = 0. \tag{17}$$

For a plasma with sides of length 100 μm, the transit time of the Stokes wave is 0.3 ps. In contrast, the transit time of the ion-acoustic wave is of the order of $7(m_i/m_e)^{1/2}$ ps for an electron temperature of 1 keV. Since the duration of a typical laser pulse is of the order of 1 ns, the information that a side boundary is present at $y = 0$ will not reach the plasma interior until the later stages of a typical experiment. Since the amplitude of the Stokes wave at its entrance boundary is independent of y, the initial evolution of SBS in the plasma interior is approximately one-dimensional and is governed approximately

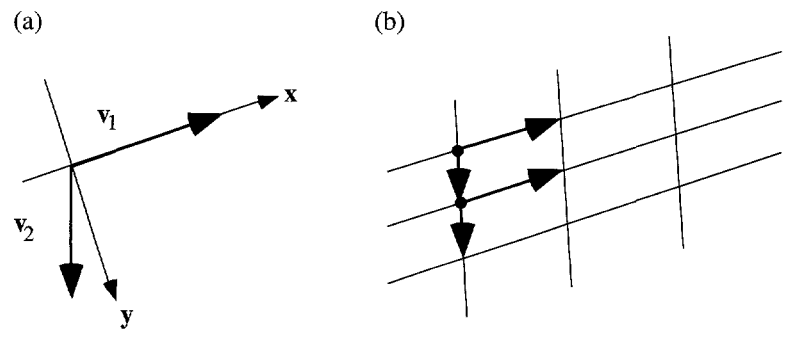

Figure 60.14
Group-velocity geometry for SBS. (a) The x component of $\mathbf{v}_2$ is always negative. (b) The initial evolution of SBS is approximately one-dimensional because the convection of portions of the ion-acoustic wave away from a particular Stokes ray is compensated by the convection of neighboring portions of the ion-acoustic wave toward that Stokes ray.

by the equations

$$\left(\partial_t + v_{1x}\partial_x + \nu_1\right)B_1 = \gamma_0 B_2\,,$$
$$\left(\partial_t - v_{2x}\partial_x + \nu_2\right)B_2 = \gamma_0 B_1\,, \tag{18}$$

where v_{2x} is defined to be positive.

Physically, this simplification occurs because the convection of portions of the ion-acoustic wave away from a particular Stokes ray is compensated by the convection of neighboring portions of the ion-acoustic wave toward that Stokes ray, as shown in Fig. 60.14(b). Notice that the preceding argument did not depend sensitively on the shape or alignment of the plasma.

The consequences of the one-dimensional model [Eqs. (18)] will now be studied, under the assumption that the instability grows and saturates convectively in a time that is short compared to the duration of the laser pulse. In steady state, the boundary conditions are

$$B_1(0) = 1, \quad B_2(l) = 0. \tag{19}$$

It is not difficult to show that

$$B_1(x) = \frac{\left\{\beta\cosh\left[\beta(l-x)\right] + \alpha_s \sinh\left[\beta(l-x)\right]\right\}\exp(\alpha_d x)}{\left[\beta\cosh(\beta l) + \alpha_s \sinh(\beta l)\right]},$$
$$B_2(x) = \frac{\gamma_0 \sinh\left[\beta(l-x)\right]\exp(\alpha_d x)}{v_{2x}\left[\beta\cosh(\beta l) + \alpha_s \sinh(\beta l)\right]}, \tag{20}$$

where the auxiliary parameters

$$\alpha_1 = \nu_1/v_{1x}\,,\ \alpha_2 = \nu_2/v_{2x}\,,$$
$$\alpha_s = (\alpha_2 + \alpha_1)/2,\ \alpha_d = (\alpha_2 - \alpha_1)/2, \tag{21}$$

and

$$\beta = \left(\alpha_s^2 - \gamma^2\right)^{1/2}\,,\quad \gamma = \gamma_0/\left(v_{1x}v_{2x}\right)^{1/2}. \tag{22}$$

The wave amplitudes $B_1(x)$ and $\left(v_{2x}/v_{1x}\right)^{1/2} B_2(x)$ are plotted in Fig. 60.15 for the case in which $\alpha_1 l = 0$, $\alpha_2 l = 52$, and $\gamma l = 17$. These parameters, which are used throughout most of this article, correspond to a singly ionized plasma with a background electron density of $10^{19}/\text{cm}^3$, an electron temperature of 1 keV, an ion temperature of 0.1 keV and a length of 100 μm, and a laser intensity of 5×10^{14} W/cm^2.

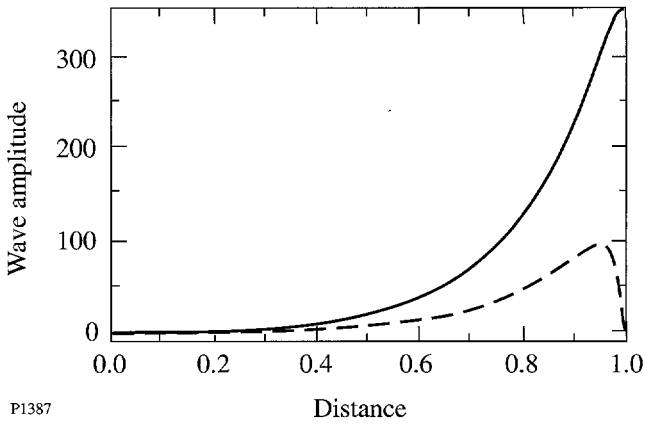

Figure 60.15
Steady-state amplitudes of the Stokes (solid line) and ion-acoustic (broken line) waves [Eqs. (20)] plotted as functions of distance for the case in which the damping parameters $\alpha_1 l = 0$ and $\alpha_2 l = 52$, and the pump-strength parameter $\gamma l = 17$. These parameters are all independent of the scattering angle 2ϕ. Distance is measured in units of the plasma length l.

It follows from the first of Eqs. (20) that the convective gain associated with the Stokes amplification process, which is defined as $B_1(l)/B_1(0)$, is given by[10]

$$G = \frac{\beta\exp(\alpha_d l)}{\beta\cosh(\beta l) + \alpha_s \sinh(\beta l)}. \tag{23}$$

It follows from Eqs. (14), (21), and (22) that the auxiliary parameters used in Eq. (23) are all independent of the scattering angle 2ϕ. This fact has two important consequences.

First, although γ_0, the temporal growth rate of SBS, is proportional to $(\sin\phi)^{1/2}$, the steady-state convective gain associated with this one-dimensional model of Stokes amplification is independent of the scattering angle.[11] Typically, $\alpha_1 \ll \alpha_2$. When $\beta l \ll 1$ one can write

$$G \propto \exp(gl), \tag{24}$$

where the spatial growth rate

$$g \approx \frac{\nu_b}{2v_2} - \left[\left(\frac{\nu_b}{2v_2}\right)^2 - \frac{\gamma_b^2}{v_1 v_2}\right]^{1/2}. \tag{25}$$

In typical nonlinear optics experiments the low acoustic speed results in strong spatial damping of the acoustic wave and

$$g \approx \gamma_b^2 / v_1 v_b . \tag{26}$$

Equation (26) is independent of the acoustic speed, as one should expect. The exact and approximate gain exponents [Eqs. (25) and (26)] are plotted as functions of the pump-intensity parameter $(\gamma l)^2$ in Fig. 60.16 for the case in which $\alpha_2 l = 52$. For a pump-intensity parameter of 600, which corresponds to a laser intensity of approximately 10^{15} W/cm^2, use of the approximate gain exponent leads to an estimate of the intensity of the Stokes output that is five orders of magnitude too low! This result shows the importance of retaining the effects of ion-acoustic wave convection in analyses of SBS in plasmas.[9]

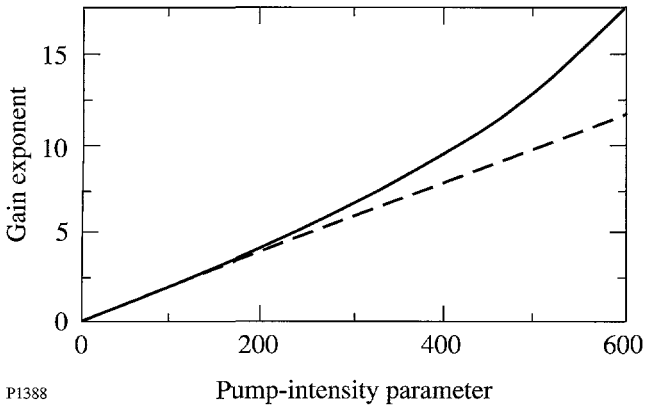

Figure 60.16
Exact (solid line) and approximate (broken line) gain exponents of SBS [Eqs. (25) and (26)] plotted as functions of the pump-intensity parameter $(\gamma l)^2$ for the case in which $\alpha_1 l = 0$ and $\alpha_2 l = 52$. The large discrepancy between the gain exponents demonstrates the importance of ion-acoustic wave convection. This result distinguishes plasmas from most other nonlinear optical media.

It is well known that the steady-state convective gain becomes infinite when the denominator of Eq. (23) vanishes. This singularity can occur when $\gamma > \alpha_2/2$ and signifies the onset of absolute instability. The second important consequence of the fact described after Eq. (23) is that, in the context of this one-dimensional model, the absolute instability condition for SBS is independent of the scattering angle.[11] Physically, the existence of absolute instability stems from the fact that the component of the ion-acoustic velocity in the direction of the Stokes velocity is always negative [Eq. (15)].

The results described in the preceding two paragraphs are in apparent contradiction to the well known fact that $\gamma_0 \to 0$ as $\phi \to 0$ and, hence, that directly forward SBS does not exist. One can resolve this apparent contradition by realizing that the response of the acoustic wave to the ponderomotive force of the pump and Stokes waves is like that of a driven harmonic oscillator, in which the oscillator takes several damping times to attain its steady-state response. Since v_2 is proportional to $\sin\phi$, the saturation time associated with this one-dimensional model of SBS tends to infinity as the scattering angle tends to zero, and use of the steady-state gain formula is inappropriate in this limit.

Transient Evolution of SBS

The exact solutions of Eqs. (18) have been obtained for a finite plasma by Bobroff and Haus[12] and by Williams and McGowan.[13] However, these solutions are written in terms of infinite sums of modified Bessel functions, and, because of their complexity, a different approach is taken here. Since the duration of a typical laser pulse is comparable to the transit time of the acoustic wave, one might suspect that the initial evolution of SBS does not depend sensitively on the finite-plasma boundary conditions. In this vein, consider the evolution of SBS in an infinite plasma. The arrival of an externally generated Stokes wave at $x = 0$ is modeled by adding a source term

$$S_1(x,t) = v_{1x}\delta(x)H(t) \tag{27}$$

to the first of Eqs. (18). The corresponding temporal growth and saturation of the Stokes output $B_1(l,t)$ will be studied analytically. The results obtained from this approximate analysis will then be verified by solving Eqs. (18) numerically for a finite plasma.

It is shown in the Appendix that, consistent with Eq. (27), the Stokes wave evolves according to

$$B_1(x,t) = v_{1x}\int_0^t G_{11}(x,t')dt', \tag{28}$$

where

$$
\begin{aligned}
G_{11}(x,t) &= \frac{\gamma_0}{v_{1x}+v_{2x}}\left(\frac{x+v_{2x}t}{v_{1x}t-x}\right)^{1/2} \\
&\times I_1\left(\frac{2\gamma_0\left[(x+v_{2x}t)(v_{1x}t-x)\right]^{1/2}}{v_{1x}+v_{2x}}\right) \\
&\times \exp\left[-\frac{\nu_1(x+v_{2x}t)}{v_{1x}+v_{2x}}-\frac{\nu_2(v_{1x}t-x)}{v_{1x}+v_{2x}}\right] \\
&\times H(x+v_{2x}t)H(v_{1x}t-x) \\
&+ H(x+v_{2x}t)\delta(v_{1x}t-x)\exp(-\nu_1 t) \qquad (29)
\end{aligned}
$$

is the Green function that describes the effect on the Stokes wave at the point (x,t) of an impulse applied to it at the point (0,0). The impulse response $G_{11}(l,t)$ is displayed in Fig. 60.17 for the case in which $\alpha_1 l = 0$, $\alpha_2 l = 52$, and $\gamma l = 17$. The impulse response grows in time until it attains its maximal amplitude at $t = t_*$. Subsequently, it decays in a time comparable to the growth time. Since the time-asymptotic Stokes output is proportional to the area under the impulse response curve [Eq. (28)], it is reasonable to define the saturation time t_s as $2t_*$. Using the fact that

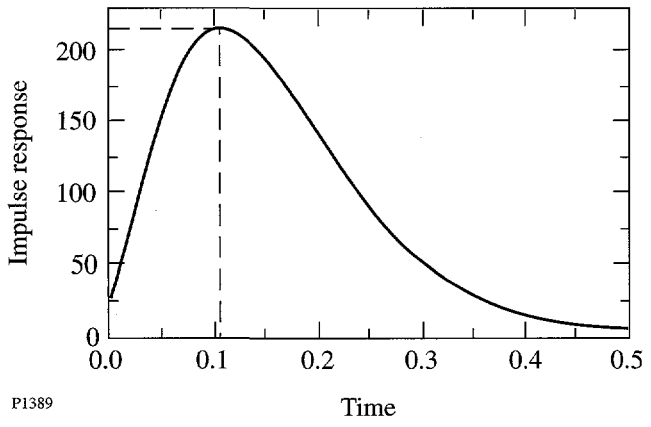

Figure 60.17
Impulse response of the Stokes wave at its exit boundary $x = l$ [Eqs. (28) and (29)] plotted as a function of time for the case in which $\alpha_1 l = 0$, $\alpha_2 l = 52$, and $\gamma l = 17$. Time is measured in units of the ion-acoustic transit time l/v_{2x}.

$$I_1(z) \sim \exp(z)/(2\pi z)^{1/2} \qquad (30)$$

as $z \to \infty$, one can see that

$$
\begin{aligned}
G_{11}(x,t) \propto \exp\Bigg(&\frac{2\gamma_0\left[(x+v_{2x}t)(v_{1x}t-x)\right]^{1/2}}{v_{1x}+v_{2x}} \\
&-\frac{\nu_1(x+v_{2x}t)}{v_{1x}+v_{2x}}-\frac{\nu_2(v_{1x}t-x)}{v_{1x}+v_{2x}}\Bigg) \qquad (31)
\end{aligned}
$$

for large values of t. Let $\psi(x,t)$ be the exponent in Eq. (31). Then t_*, the time of maximal growth, is found from the condition

$$\partial_t\left[\psi(l,t)\right]_{t_*} = 0. \qquad (32)$$

It is not difficult to show that

$$t_* = \frac{(\xi_2+\xi_1)\alpha_s-(\xi_2-\xi_1)\left(\alpha_s^2-\gamma^2\right)^{1/2}}{2\left(\alpha_s^2-\gamma^2\right)^{1/2}}, \qquad (33)$$

where

$$\xi_1 = l/v_{1x}, \quad \xi_2 = l/v_{2x}. \qquad (34)$$

It can also be shown that

$$B_1(l,t_*) \propto \exp\left[(\alpha_d-\beta)l\right], \qquad (35)$$

in keeping with Eqs. (23)–(25).

The preceding analysis is consistent with previous analyses in the plasma physics literature,[4] in which Fourier analysis was used to determine the impulse response function $\gamma(v_x)$, defined as the time-asymptotic temporal growth rate of the portion of the impulse response that convects with x velocity v_x. It follows from Eq. (31) that

$$\lim_{t\to\infty} G_{11}(v_x t,t) \propto \exp\left[\gamma(v_x)t\right], \qquad (36)$$

where

$$\gamma(v_x) = \frac{2\gamma_0\left[(v_x + v_{2x})(v_{1x} - v_x)\right]^{1/2}}{v_{1x} + v_{2x}} - \frac{\nu_1(v_x + v_{2x})}{v_{1x} + v_{2x}} - \frac{\nu_2(v_{1x} - v_x)}{v_{1x} + v_{2x}}. \quad (37)$$

The impulse response function $\gamma(v_x)$ is displayed in Fig. 60.18. Consider the portion of the impulse response that convects with velocity v_x. This portion of the impulse response travels a distance l in a time l/v_x, at which point it has grown by a factor proportional to $\exp\left[\gamma(v_x)l/v_x\right]$. Thus, $\gamma(v_x)/v_x$ is the spatial growth rate of this portion of the impulse response. In the figure this spatial growth rate is the slope of a straight line from the origin to the point $\left(v_x, \gamma(v_x)\right)$ on the impulse response curve. It follows from the figure that the amplitude of the impulse response at $x = l$ increases with time until $t_* = l/v_*$, where v_*, the velocity of maximal spatial gain, is found from the condition

$$\frac{d}{dv_x}\left[\frac{\gamma(v_x)}{v_x}\right]_{v_*} = 0. \quad (38)$$

Subsequently, the amplitude of the impulse response decreases with time. It is clear physically that definition (38) is identical to definition (32). To establish their equivalence mathematically, one need only observe that, with x fixed,

$$\frac{d}{dv_x}\left[\frac{\gamma(v_x)}{v_x}\right] = \frac{d}{d(x/t)}\left[\frac{\gamma(x/t)t}{x}\right] = -\frac{t^2}{x^2}\frac{\partial\psi}{\partial t}. \quad (39)$$

Since $v_2 \ll v_1$, $\xi_1 \ll \xi_2$ for all scattering angles, and it follows from Eqs. (15) and (33) that t_s is proportional to $l/\sin\phi$.[11] This result verifies the statement that the saturation time tends to infinity as the scattering angle tends to zero. The angular dependence of the saturation time is displayed in Fig. 60.19(a). For a scattering angle of 30°, the saturation time is longer than that for directly backward scattering by a factor of approximately 4. For a scattering angle of 10°, this factor is approximately equal to 11. Typically, $\alpha_1 \ll \alpha_2$, and it follows from Eq. (33) that

$$\frac{v_{2x}t_s}{l} \approx \frac{\alpha_2 - \left(\alpha_2^2 - 4\gamma^2\right)^{1/2}}{\left(\alpha_2^2 - 4\gamma^2\right)^{1/2}}. \quad (40)$$

The coefficient of the saturation time appearing on the right side of Eq. (40) is independent of the plasma length and the scattering angle. It is plotted as a function of γl in Fig. 60.19(b) for the case in which $\alpha_2 l = 52$. Provided that the value of γ is not too close to its absolute threshold value of $\alpha_2/2$, the saturation time is much less than the transit time of the ion-acoustic wave, and our use of the infinite-medium Green function seems reasonable. As a further check of the validity of this approximation, Eqs. (18) were solved numerically for a finite plasma by a computer code based on the method of characteristics. The numerically determined Stokes output is plotted as a function of time in Fig. 60.20 for the case in which $\alpha_2 l = 52$ and $\gamma l = 17$. The saturation time of 0.30 l/v_{2x} predicted by Eq. (40) is consistent with the numerically determined Stokes output displayed in Fig. 60.20. The coefficient of the saturation time is also plotted as a function of the electron density and temperature in Figs. 60.21(a) and 60.21(b), respectively. The assumption that backward SBS grows and saturates convectively in a time that is short compared to the duration of the laser pulse is valid for the parameters chosen to illustrate the results of this article. [See the description of Fig. 60.15 that follows Eq. (22).] However, if the plasma length, the background electron density, or the laser intensity is significantly longer, or higher, than the value chosen for this article, or the electron temperature is significantly lower, backward SBS does not saturate and the steady-state results of the section on steady-state amplification do not apply. In this

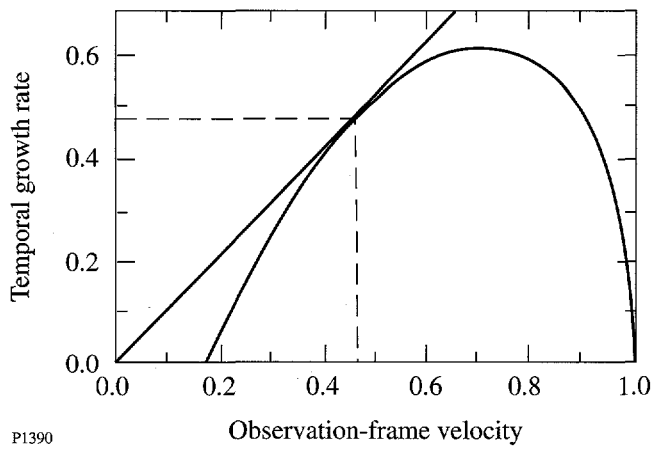

Figure 60.18
Sketch of the apparent temporal growth rate of the impulse response of the Stokes wave [Eq. (37)]. The temporal growth rate is measured in units of γ_0, and the observation-frame velocity is measured in units of v_{1x}.

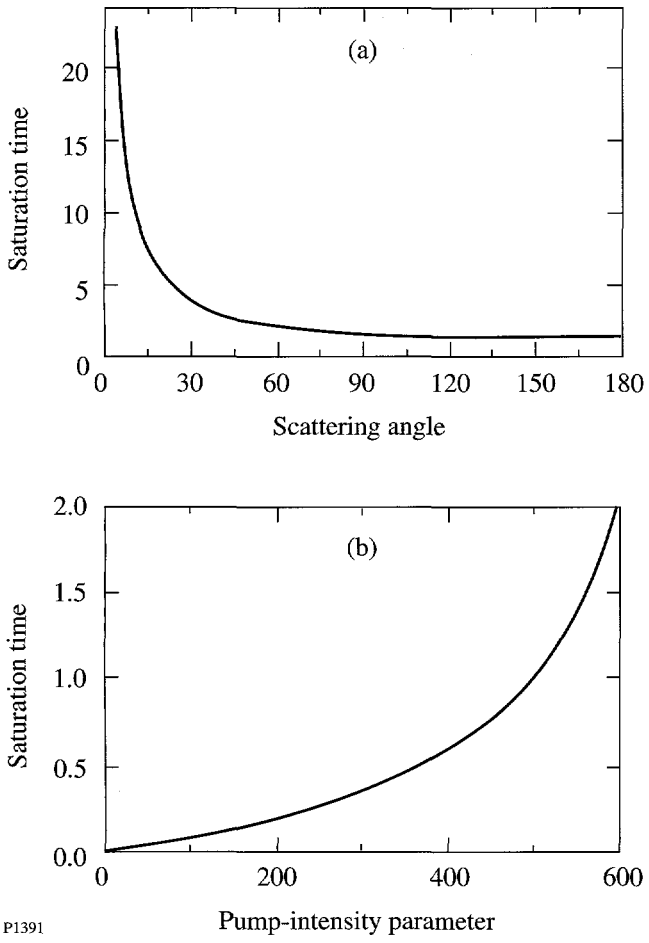

Figure 60.19
Characteristics of the convective saturation time of SBS [Eq. (40)]. (a) The saturation time, normalized to the saturation time of backward SBS, is plotted as a function of the scattering angle 2ϕ. (b) The saturation time of backward SBS, normalized to the transit time of the ion-acoustic wave, is plotted as a function of the pump-intensity parameter $(\gamma l)^2$.

case, a detailed spatiotemporal analysis of SBS[12,13] is required. In the strong damping regime typical of nonlinear optics experiments, Eq. (40) reduces to

$$v_2 t_s \approx 2\gamma_b^2 l / v_1 v_b . \qquad (41)$$

The saturation time is still proportional to $l/\sin\phi$, as it must be, but is independent of the acoustic speed.

As discussed in the preceding paragraph, the saturation time associated with the one-dimensional model described herein tends to infinity as the scattering angle tends to zero. It is reasonable to conclude that, at any instant of time, the Stokes output decreases as the scattering angle decreases. However, a detailed spatiotemporal analysis of SBS in a finite plasma[12,13] is required to quantify the angular dependence of the Stokes output. Furthermore, as the scattering angle decreases and the one-dimensional saturation time increases, other saturation mechanisms for SBS become more important. In the context of linear theory, the only other saturation mechanism is the convection of the ion-acoustic wave in the y direction. McKinstrie *et al.*[14] have shown that this lateral convection of the ion-acoustic wave can saturate forward SBS on a time scale short compared to the one-dimensional saturation time and that the importance of lateral convection increases as the scattering angle decreases. However, as early saturation reduces the Stokes output, the general conclusion of this article—that the Stokes output decreases as the scattering angle decreases—is still correct.

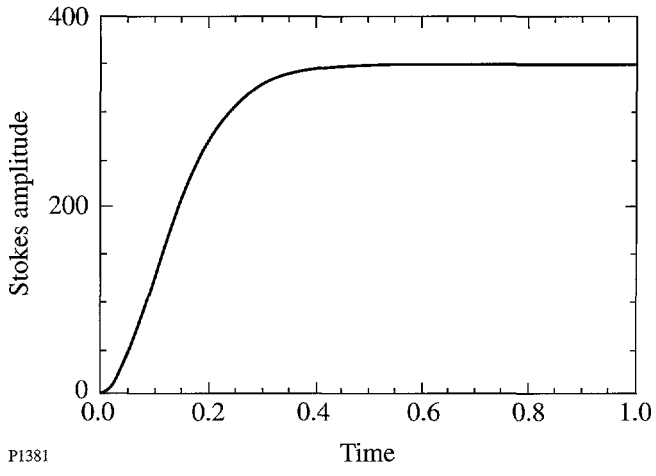

Figure 60.20
Stokes amplitude at $x = l$ plotted as a function of time for the case in which $\alpha_1 l = 0$, $\alpha_2 l = 52$, and $\gamma l = 17$. Time is measured in units of the ion-acoustic transit time. The evolution of the Stokes wave was determined by solving Eqs. (18) numerically for a finite plasma. The convective saturation time observed in this simulation is consistent with the prediction of Eq. (40).

Finally, it should be mentioned that numerical simulations of SBS in homogeneous plasma have been made by Amin *et al.*[15,16] for the complimentary case in which the ion-acoustic wave is subject to viscous damping. In principle, the preceding analysis applies also to this case; however, the second of Eqs. (14) should read $v_2 = v_b \sin^2\phi$. The consequences of this modified angular dependence for the one-dimensional model described herein are profound: First, forward SBS is absolutely unstable for arbitrary laser intensity. Second, even if the laser intensity is low enough that sideward and backward SBS are not absolutely unstable, the convective saturation time for

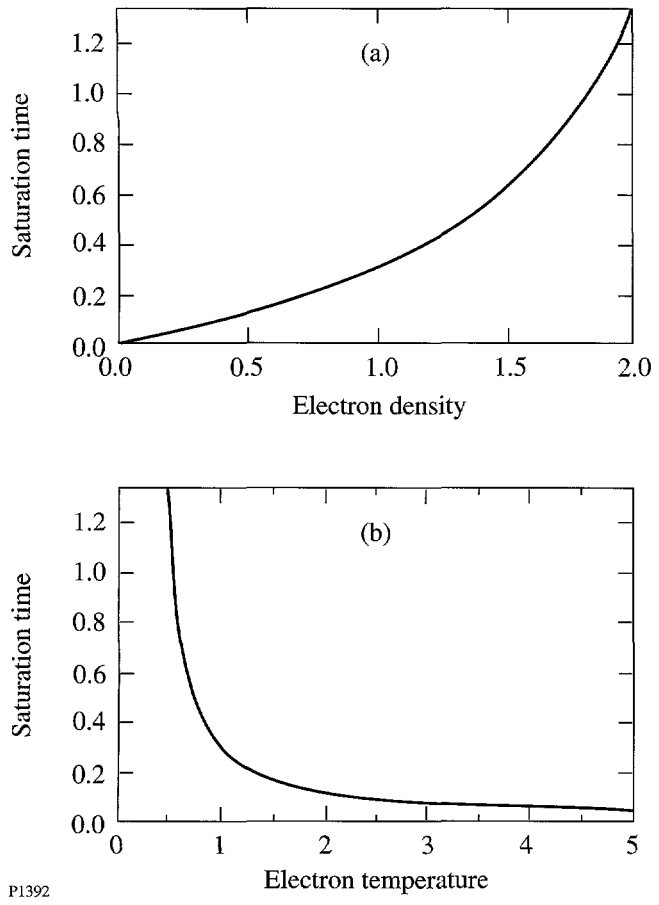

Figure 60.21
Characteristics of the convective saturation time of SBS [Eq. (40)]. (a) The saturation time, normalized to the transit time of the ion-acoustic wave, is plotted as a function of the background electron density, in units of $10^{19}/\text{cm}^3$, for an electron temperature of 1 keV. (b) The saturation time, normalized to the transit time of the ion-acoustic wave, is plotted as a function of the electron temperature, in keV, for a background electron density of $10^{19}/\text{cm}^3$. In both cases the ratio of the ion and electron temperatures is 0.1, and the laser intensity is 5×10^{14} W/cm^2.

sideward SBS is likely to be comparable to the temporal pulsewidth of the laser. In both cases a transient two-dimensional analysis of SBS[14] is required.

Summary

The angular dependence of stimulated Brillouin scattering (SBS) in a finite homogeneous plasma was studied. For parameters typical of current ICF experiments, the initial evolution of SBS is well approximated by a one-dimensional model. In the context of this model, the threshold intensity of the absolute instability and the steady-state spatial growth rate of the convective instability are both independent of the scattering angle. However, the saturation time of the convective instability exhibits a strong inverse dependence on the scattering angle: Forward SBS always occurs in the transient regime, and the intensity of the scattered light is less than that predicted by a steady-state analysis. In particular, no light is emitted in the direction parallel to the wave vector of the incident wave. Thus, the commonly held belief that backward SBS should dominate experiments involving long-scale-length plasmas is correct, but for reasons other than that on which it was originally based.

Finally, although the analysis of this article was directed at SBS, Eqs. (7) apply to other parametric instabilities such as stimulated Raman scattering (SRS). Thus, subject to the constraints described in the previous section, the main analytical results of this article should be valid for SRS.

ACKNOWLEDGMENT

This work was supported by the National Science Foundation under Contract No. PHY-9057093, the U. S. Department of Energy (DOE) Office of Inertial Confinement Fusion under Cooperative Agreement No. DE-FC03-92SF19460, the University of Rochester, and the New York State Energy Research and Development Authority. The support of DOE does not constitute an endorsement by DOE of the views expressed in this article.

Appendix: Green-Function Analysis of SBS in an Infinite Plasma

The wave amplitudes B_1 and B_2 defined in the section on governing equations evolve according to the equations

$$\begin{aligned}(\partial_t + v_1\partial_x + \nu_1)B_1 &= \gamma_0 B_2 + S_1(x,t),\\ (\partial_t - v_2\partial_x + \nu_2)B_2 &= \gamma_0 B_1 + S_2(x,t),\end{aligned} \tag{A1}$$

where S_1 and S_2 are phenomenological source terms that model the way in which SBS is initiated. Equations (A1) can be rewritten in the matrix form

$$LB = S, \tag{A2}$$

where

$$L = \begin{bmatrix}(\partial_t + v_1\partial_x + \nu_1) & -\gamma_0\\ -\gamma_0 & (\partial_t - v_2\partial_x + \nu_2)\end{bmatrix} \tag{A3}$$

and

$$B = \begin{bmatrix}B_1(x,t)\\ B_2(x,t)\end{bmatrix}, \quad S = \begin{bmatrix}S_1(x,t)\\ S_2(x,t)\end{bmatrix}. \tag{A4}$$

The Green matrix

$$G=\begin{bmatrix} G_{11}(x,t) & G_{12}(x,t) \\ G_{21}(x,t) & G_{22}(x,t) \end{bmatrix} \tag{A5}$$

satisfies the related equation

$$LG = D, \tag{A6}$$

where

$$D=\begin{bmatrix} \delta(x)\delta(t) & 0 \\ 0 & \delta(x)\delta(t) \end{bmatrix}. \tag{A7}$$

It is not difficult to verify that the solution of Eq. (A2) is

$$B(x,t)=\int_{-\infty}^{\infty}\int_{-\infty}^{\infty} G(x-x',t-t')S(x',t')dx'dt'. \tag{A8}$$

It follows from Eq. (A8) that the Green function $G_{ij}(x-x',t-t')$ describes the effect on wave i at the position (x,t) of an impulse applied to wave j at the position (x',t').

It is well known that the Green functions defined by Eqs. (A5)–(A7) can be written in terms of modified Bessel functions. However, as we are unaware of any derivation of this result published in the plasma physics literature, a simple derivation is included in this appendix for the benefit of the reader.

The determination of the Green matrix is facilitated by rewriting Eq. (A6) in terms of the characteristic variables

$$\xi = x+v_2t,\ \ \eta = v_1t-x. \tag{A9}$$

By using these variables and the fact that

$$\delta(x)\delta(t)=\delta(\xi)\delta(\eta)J(\xi,\eta;x,t), \tag{A10}$$

where

$$J(\xi,\eta;x,t)=v_1+v_2 \tag{A11}$$

is the Jacobian determinant associated with the transformation from (ξ,η) to (x,t), one can rewrite Eq. (A6) as

$$\begin{bmatrix} \left(\partial_\xi+\alpha_1\right) & -\gamma \\ -\gamma & \left(\partial_\eta+\alpha_2\right) \end{bmatrix}\begin{bmatrix} G_{11} & G_{12} \\ G_{21} & G_{22} \end{bmatrix}$$

$$=\begin{bmatrix} \delta(\xi)\delta(\eta) & 0 \\ 0 & \delta(\xi)\delta(\eta) \end{bmatrix}, \tag{A12}$$

where

$$\begin{aligned} \alpha_1 &= v_1/(v_1+v_2), \\ \alpha_2 &= v_2/(v_1+v_2), \\ \gamma &= \gamma_0/(v_1+v_2). \end{aligned} \tag{A13}$$

One can eliminate the damping terms α_1 and α_2 by defining

$$G(\xi,\eta)=\overline{G}(\xi,\eta)\exp(-\alpha_1\xi-\alpha_2\eta). \tag{A14}$$

The Green matrix $\overline{G}(\xi,\eta)$ satisfies the conservative equation

$$\begin{bmatrix} \partial_\xi & -\gamma \\ -\gamma & \partial_\eta \end{bmatrix}\begin{bmatrix} \overline{G}_{11} & \overline{G}_{12} \\ \overline{G}_{21} & \overline{G}_{22} \end{bmatrix}=\begin{bmatrix} \delta(\xi)\delta(\eta) & 0 \\ 0 & \delta(\xi)\delta(\eta) \end{bmatrix}, \tag{A15}$$

which is the simplest form of Eq. (A6).

The Green functions $\overline{G}_{11}(\xi,\eta)$ and $\overline{G}_{21}(\xi,\eta)$ satisfy the equations

$$\partial_\xi\overline{G}_{11}=\gamma\overline{G}_{21}+\delta(\xi)\delta(\eta),\ \ \partial_\eta\overline{G}_{21}=\gamma\overline{G}_{11}. \tag{A16}$$

It follows from Eqs. (A16) and the theory of characteristics that $\overline{G}_{11}(\xi,\eta)$ and $\overline{G}_{21}(\xi,\eta)$ can only be nonzero for $\xi\geq 0$ and $\eta\geq 0$. In other words, one has to solve an initial value problem in the retarded time variable η on the half-space $\xi\geq 0$. A natural way to solve such a problem is by Laplace transforming in the variable η. It is not difficult to show that

$$\overline{G}_{21}(\xi,\eta)=\mathcal{L}^{-1}\left\{\frac{\gamma\exp\left(\gamma^2\xi/s\right)}{s}\right\}$$

$$=\gamma I_0\left[2\gamma(\xi\eta)^{1/2}\right]H(\xi)H(\eta). \tag{A17}$$

The Laplace transform tables of Abramowitz and Stegun[17] were used to invert the Laplace transform, and the Heaviside step functions $H(\xi)$ and $H(\eta)$ were added to ensure that the Green function equals zero for points outside the domain of influence of the source point. Similarly,

$$\overline{G}_{11}(\xi,\eta) = \mathcal{L}^{-1}\left\{ s\frac{\exp\left(\gamma^2\xi/s\right)}{s} - 1 + 1 \right\}$$

$$= \partial_\eta I_0\left[2\gamma(\xi\eta)^{1/2}\right] + \delta(\eta)$$

$$= \gamma(\xi/\eta)^{1/2} I_1\left[2\gamma(\xi\eta)^{1/2}\right] H(\xi)H(\eta) + H(\xi)\delta(\eta). \quad \text{(A18)}$$

Notice that $\overline{G}_{11}(\xi,\eta)$ is related to $\overline{G}_{21}(\xi,\eta)$ by the second of Eqs. (A16), as it must be. It follows from Eq. (A15) that $\overline{G}_{12}(\xi,\eta) = \overline{G}_{21}(\eta,\xi)$ and $\overline{G}_{22}(\xi,\eta) = \overline{G}_{11}(\eta,\xi)$.

In terms of the original variables x and t, the conservative Green functions are

$$\overline{G}_{11}(x,t) = \frac{\gamma_0}{v_1+v_2}\left(\frac{x+v_2t}{v_1t-x}\right)^{1/2} I_1\left(\frac{2\gamma_0\left[(x+v_2t)(v_1t-x)\right]^{1/2}}{v_1+v_2}\right)$$

$$\times H(x+v_2t)H(v_1t-x) + H(x+v_2t)\delta(v_1t-x),$$

$$\overline{G}_{12}(x,t) = \overline{G}_{21}(x,t) = \frac{\gamma_0}{v_1+v_2} I_0\left(\frac{2\gamma_0\left[(x+v_2t)(v_1t-x)\right]^{1/2}}{v_1+v_2}\right)$$

$$\times H(x+v_2t)H(v_1t-x), \quad \text{(A19)}$$

$$\overline{G}_{22}(x,t) = \frac{\gamma_0}{v_1+v_2}\left(\frac{v_1t-x}{x+v_2t}\right)^{1/2} I_1\left(\frac{2\gamma_0\left[(x+v_2t)(v_1t-x)\right]^{1/2}}{v_1+v_2}\right)$$

$$\times H(x+v_2t)H(v_1t-x) + \delta(x+v_2t)H(v_1t-x).$$

According to Eq. (A14), the dissipative Green functions are related to the conservative Green functions by

$$G_{ij}(x,t) = \overline{G}_{ij}(x,t)\exp\left[-\frac{v_1(x+v_2t)}{v_1+v_2} - \frac{v_2(v_1t-x)}{v_1+v_2}\right]. \quad \text{(A20)}$$

REFERENCES

1. J. F. Drake *et al.*, Phys. Fluids **17**, 778 (1974).
2. R. S. Craxton, R. L. McCrory, and J. M. Soures, Sci. Am. **255**, 68 (1986).
3. C. S. Liu, in *Advances in Plasma Physics*, edited by A. Simon and W. B. Thompson (Wiley, New York, 1976), Vol. 6, p. 121.
4. A. Bers, in *Basic Plasma Physics*, edited by A. A. Galeev and R. N. Sudan, Handbook of Plasma Physics (North Holland, Amsterdam, 1983), Vol. 1, p. 45 and references therein.
5. C. J. McKinstrie and M. V. Goldman, J. Opt. Soc. Am. B **9**, 1778 (1992).
6. W. L. Kruer, *The Physics of Laser Plasma Interactions*, Frontiers in Physics (Addison-Wesley, CA, 1988), Vol. 73, Chap. 8.
7. S. Ichimaru, *Basic Principles of Plasma Physics: A Statistical Approach*, Frontiers in Physics (Benjamin, Reading, MA, 1973), p. 71.
8. R. W. Boyd, K. Rzazewski, and P. Narum, Phys. Rev. A **42**, 5514 (1990).
9. C. J. McKinstrie, J. S. Li, R. Betti, and E. A. Williams, Paper 1O3, presented at the 23rd Annual Anomalous Conference, Wintergreen, VA, 21–25 June 1993. This work is being prepared for submittal to Physics of Plasmas.
10. C. J. McKinstrie and A. Simon, Phys. Fluids **29**, 1959 (1986) and references therein.
11. C. J. McKinstrie and R. E. Giacone, Bull. Am. Phys. Soc. **37**, 1440 (1992); R. E. Giacone, C. J. McKinstrie, R. Betti, and H. Chen, Bull. Am. Phys. Soc. **38**, 1914 (1993).
12. D. L. Bobroff and H. A. Haus, J. Appl. Phys. **38**, 390 (1967).
13. E. A. Williams and R. R. McGowan, in *Research Trends in Physics: Inertial Confinement Fusion*, edited by K. A. Brueckner (American Institute of Physics, New York, 1992), p. 325.
14. C. J. McKinstrie, R. Betti, R. E. Giacone, T. Kolber, and J. S. Li, Phys. Rev. E **50**, 2182 (1994).
15. M. R. Amin *et al.*, Phys. Rev. Lett. **71**, 81 (1993).
16. M. R. Amin *et al.*, Phys. Fluids B **5**, 3748 (1993).
17. M. Abramowitz and I. A. Stegun, eds., Handbook of Mathematical Functions (National Bureau of Standards, Washington, D.C., 1964), Chap. 29.

Femtosecond Excited-State Dynamics of a Conjugated Ladder Polymer

Among the known classes of nonlinear optical materials, π-conjugated polymers are very attractive because of their large, third-order optical susceptibilities and ultrafast response times.[1–5] The large optical nonlinearity of conjugated polymers has long been recognized as arising from the π-electron delocalization along the polymer chains.[2] Recently, aromatic heterocyclic ladder-type polymers, such as poly(benzimidazobenzophenanthroline) ladder (BBL) and semi-ladder (BBB), have received growing attention as a new class of nonlinear optical (NLO) polymers[3–5] because of their desirable physical properties and their ready processibility into good optical-quality thin films.[6] For example, BBL has an excellent thermal stability up to 700°C in a nitrogen atmosphere (~650°C in air) and has good mechanical properties in the form of films or fibers;[6] both of these features suggest that the optical damage threshold may be very high. The rigid, planar, "double stranded," and quasi-two-dimensional structure of BBL (inset of Fig. 60.22) suggests maximum π-electron delocalization, leading to a large, third-order optical susceptibility $\chi^{(3)}$ as found in picosecond degenerate four-wave mixing (DFWM)[4] and picosecond third-harmonic-generation (THG) experiments.[5] However, the temporal resolution of the nonlinear optical response of BBL was limited to 30 ps by the experimental equipment in both of these prior studies.[4,5]

The excited-state dynamics of conjugated polymers has been extensively studied following the theoretical prediction that new intragap states can be generated by photoexcitation within an optical phonon cycle (<100 fs).[7] Because of the normally strong electron-phonon coupling in conjugated polymers, self-localized excited states are formed upon photoexcitation. Examples of these structurally relaxed states include solitons, polarons, bipolarons, and excitons.[8–10] These photoexcitations play a critical role in the nonlinear optical behavior of the conjugated polymers, which are often considered to be quasi-one-dimensional systems. Ultrafast transient spectroscopy studies of photoexcitations in conjugated polymers have been widely reported on single-stranded, non-ladder-type polymers such as trans-polyacetylene (PA), polydiacetylenes (PDA's), polythiophenes (PT's), poly(p-phenylene vinylenes) (PPV's), and poly(thiophene vinylenes) (PTV's).[11–19] The unique topological features of BBL among the known conjugated polymers give rise to novel charge transport properties.[20] This and the recent interest in its nonlinear optical and optoelectronic properties make this ladder polymer an excellent candidate for a detailed investigation of its ultrafast excited-state dynamics.

In this article we report studies of the time-resolved femtosecond (fs) dynamics following photoexcitation in a BBL thin film. The experimental results reveal a sub-picosecond response of the optical nonlinearity. We show that the nonlinear excitations in the ladder polymer are similar to those observed in single-stranded conjugated polymers.

The measurements were performed at room temperature on a BBL thin-film sample. The sample was spin coated on a sapphire substrate and was approximately 500 Å thick. The details of the synthesis of BBL and fabrication of thin films have been described elsewhere.[6] An amplified colliding-pulse mode-locked (CPM) laser system was employed for the pump and probe measurements. Light pulses of approximately 100 fs centered at 620 nm were generated from the CPM laser and further amplified by a copper vapor laser–pumped dye amplifier to the energy level of about 1 μJ per pulse at a repetition rate of 8.7 kHz. Ninety percent of the amplified pulses were focused onto an ethylene glycol jet to generate a white-light continuum that provided probe pulses tunable from 500 nm to 900 nm. The remaining 10% were used as pump pulses. The intensity of the pump pulses on the sample was ~1 GW/cm^2. A cross-polarization arrangement of the pump and probe beams was used to eliminate the coherent artifact. The BBL sample exhibited excellent stability throughout the experiments, and no signal degradation was found.

Figure 60.22 shows the room-temperature linear absorption spectrum and the chemical structure of BBL. The onset of major optical absorption occurs at 690 nm (1.8 eV). The pump pulses (2 eV) used in the experiments were well above the optical gap. The results of the pump- and continuum-probe

experiment on BBL are shown in Fig. 60.23. The transient photoinduced probe transmission change ($\Delta T/T$) was measured as a function of the probe time delay. For probe wavelengths above the optical gap ($\lambda = 620$ nm and 650 nm), increased transmission (bleaching) was observed. For probe below the gap ($\lambda > 690$ nm), photoinduced absorption was observed. Both bleaching and absorption signals appear promptly (within our time resolution) following the excitation. Figure 60.24 shows the fit of the bleaching and absorption signals for three different probe wavelengths. Neither bleaching nor absorption decay can be fitted by a single exponential function. The decay of the bleaching signal is best fitted to a biexponential function and a constant term of the form $\Delta T/T = A\exp(-t/\tau_1) + B\exp(-t/\tau_2) + C$. For the 620-nm probe, the initial fast decay has a time constant $\tau_1 = 0.39$ ps, whereas the slow component is $\tau_2 = 2.11$ ps. The best fit to all the transient absorption traces is a biexponential function with a fast component and a slow component of the form $\Delta T/T = A\exp(-t/\tau_1) + B\exp(-t/\tau_2)$. The decay of the photo-induced absorption is much slower than that of the photo-induced bleaching and is also wavelength dependent. The slowest decay occurs at 770 nm when $\tau_1 = 1.03$ ps and $\tau_2 = 29.5$ ps. The results of fitting the photoinduced bleaching and absorption data are summarized in Table 60.II.

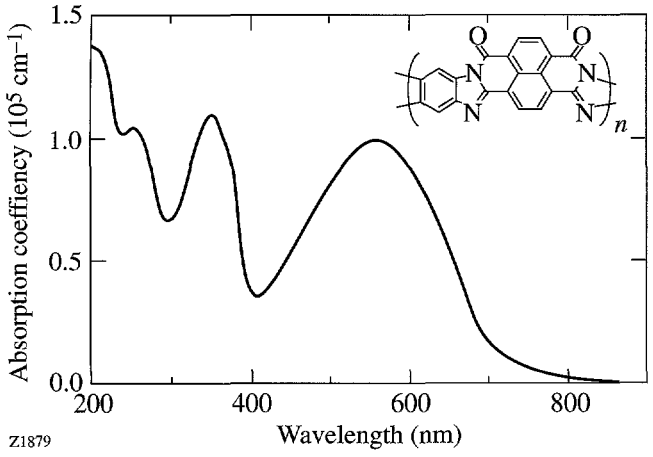

Figure 60.22
The room-temperature absorption spectrum and the chemical structure (inset) of BBL.

The ultrafast dynamics can be explained by the photogeneration and decay of self-trapped excitons (STE's) or polaron-excitons.[16,17] In nondegenerated ground-state polymers, photogenerated electron-hole pairs are confined through the preferred sense of bond alternation on the polymer chain and cannot be totally separated. The main product of intra-

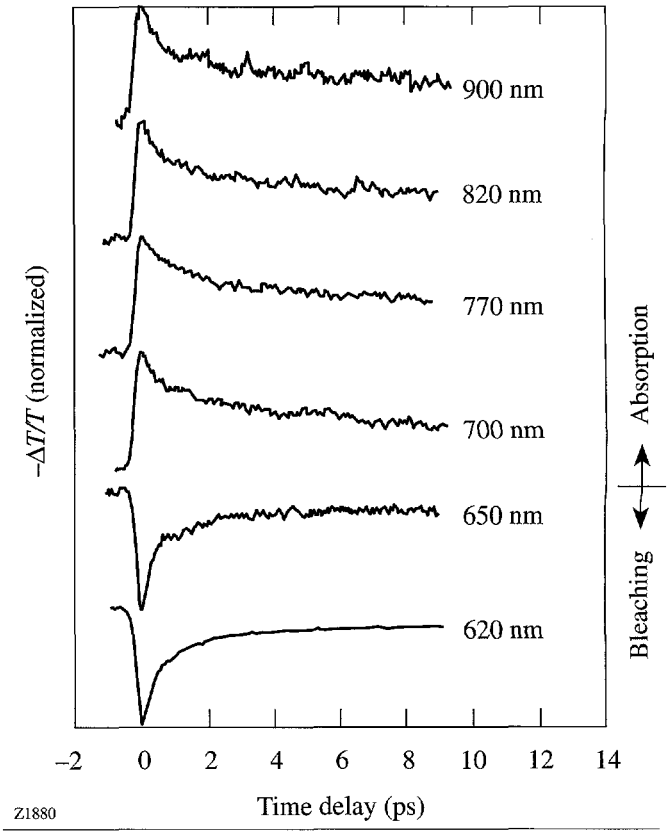

Figure 60.23
Transient photoinduced transmission change ($\Delta T/T$) measured as a function of the probe delay time at different probe wavelengths following excitation at 620 nm. The traces have been displaced vertically for clarity. Bleaching is observed above E_g and induced absorption below E_g.

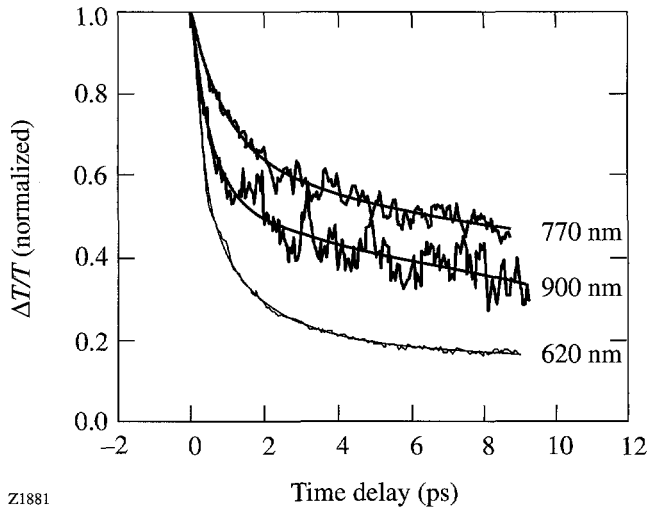

Figure 60.24
Fitting of the decay curves of the bleaching signal (probe at 620 nm) and absorption signals (probe at 770 nm and 900 nm). The smooth curves are fits as described in the text.

Table 60.II The lifetimes resulting from fitting of the decay curves at different probing wavelengths λ.

λ (nm)	τ_1 (ps)	τ_2 (ps)
620	0.39±0.01	2.11±0.1
650	0.25±0.02	1.46±0.1
700	0.60±0.05	15.3±0.5
770	1.03±0.06	29.5±2.2
820	0.59±0.05	18.9±1.0
900	0.59±0.05	20.5±1.6

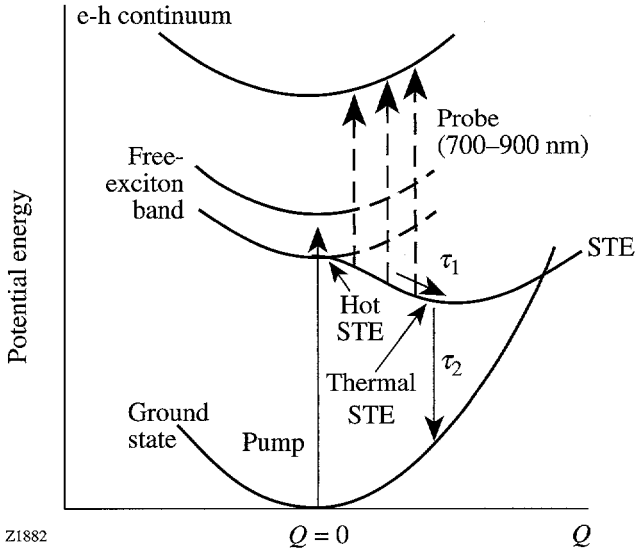

Figure 60.25
The adiabatic potential energy curves of the excited and ground states plotted against the lattice deformation Q.

chain photoexcitation is neutral, self-trapped excitons.[10] Kobayashi *et al.* studied photoexcitations in polydiacetylene and explained their results by the self-trapped exciton model.[16,17] Greene *et al.* have studied the excitonic absorption saturation effect in polydiacetylene and explained their results by exciton phase-space filling.[21] Recently, Samuel *et al.* have studied the picosecond photoinduced absorption in PTV and PPV and have assigned the observed signals to polaron-excitons.[22] Since BBL has a nondegenerated ground state and the observed photoinduced absorption and bleaching signals in BBL resemble those in PDA and PPV, we attribute them to STE's. Other excitations such as bipolarons or triplet excitons have very little contribution to the signals within the time window (10 ps) of our experiments.

Figure 60.25 shows the adiabatic potential energy curves of the ground and excited states of the system as functions of the lattice deformation Q. The ground and excited states are represented by parabolic curves. The equilibrium lattice deformation $Q=0$ corresponds to a perfect dimerized lattice resulting from the Peierls instability. Free excitons are created by π–π^* photoexcitation. Due to the strong electron-phonon coupling, free excitons are unstable and undergo self-trapping quickly after creation. Since in a quasi-one-dimensional system there is no barrier between the potential curves of the free excitons and the STE's, self-trapping takes place within the coupled phonon period (<100 fs) and produces hot STE's.[23,24] The hot STE's then thermalize toward the bottom of the STE potential surface by emission of phonons. Simultaneously, the hot STE's can relax directly to the ground state. This occurs via an oscillation passing over the point where the STE potential crosses the ground state potential.[16,17] The initial decay of the bleaching is due to the combination of these two processes. The thermalized excitons then decay to the ground state either radiatively or nonradiatively. We find that the characteristic decay time of STE's is of the order of 10 ps, which is much shorter than the expected radiative lifetime of STE's (~1 ns), indicating that the nonradiative pathways play a significant role. This is consistent with our observation of the low photoluminescence quantum yield in BBL. The nonradiative decay of STE's is considered to be either tunneling between the potential energy curves from the exciton state to the ground state or the evolution of excitons to form new intermediate species between the exciton and the ground state, such as excimers.[25] There is a constant component in bleaching signals that accounts for about 20% of the maximum signal. This constant component may be associated with the formation of new species, which results in a very slow recovery of the ground-state populations.

The induced absorption is assigned to the transitions from the self-trapped excitons to higher excited continuum states. Although both the bleaching signal and the absorption signal contain a fast decay component and a slow decay component, the decay of the absorption is much slower than that of the bleaching. The decay of the photoinduced absorption is also wavelength dependent, with the slowest decay at 770 nm. One possible reason for this can be seen by examining the thermalization and cooling of the hot STE's. The hot excitons reach the bottom of the potential curve in two steps. They thermalize first to form quasi-thermalized STE's by phonon emission. These quasi-thermalized excitons have still not reached the bottom of the potential curve; they cool to the bottom by

coupling with phonon modes of lower frequencies.[16] Thus by probing at different wavelengths, we follow the evolution of the STE's as shown in Fig. 60.25. The bleaching signal that monitors the disappearance of free excitons is due to both hot STE's and quasi-thermalized STE's. The absorption signal, however, comes mainly from thermalized or cold STE's, depending on the probing wavelength. Since the thermalized excitons are closer to the bottom of the potential curve than the hot excitons, their decay to the ground state is by tunneling through a higher and thicker potential barrier and is expected to be slower than that of hot excitons. When probing at longer wavelengths (820 nm, 900 nm), the signal comes from excitons that are hotter than those seen by probing at 770 nm; therefore, the decay should be faster, in agreement with the experimental data.

In conclusion, the dynamics of the photoexcitations in the conjugated ladder polymer BBL has been studied for the first time by femtosecond time-resolved absorption measurements. Photoinduced bleaching of the π–π^* absorption band and intragap photoinduced absorption were observed. The observed excited-state decay dynamics is consistent with the self-trapped exciton model and is tentatively explained by the generation and decay of the STE's. The observed signals arise within our time resolution and feature both a fast and a slow component. The fast component is attributed to the self-trapping and thermalization of free excitons, while the slow component was assigned to the relaxation of the quasi-thermalized and/or cold STE's to other excited state species or the ground state. The difference between the decay dynamics of bleaching and absorption has been explained by the thermalization and cooling of hot STE's.

ACKNOWLEDGMENT

This work was supported in part by the National Science Foundation (CTS 9311741) and the Center for Photoinduced Charge Transfer. Y. Kostoulas acknowledges support of the Link Foundation.

REFERENCES

1. *Materials for Nonlinear Optics: Chemical Perspectives,* edited by S. R. Marder, J. E. Sohn, and G. D. Stucky (American Chemical Society, Washington, DC, 1991).
2. G. P. Agrawal, C. Cojan, and C. Flytzanis, Phys. Rev. B **17**, 776 (1978).
3. A. K. Agrawal *et al.*, J. Phys. Chem. **96**, 2837 (1992).
4. J. R. Lindle *et al.*, Appl. Phys. Lett. **56**, 712 (1990).
5. S. A. Jenekhe *et al.*, Mater. Res. Soc. Symp. Proc. **214**, 55 (1991).
6. S. A. Jenekhe and P. O. Johnson, Macromolecules **23**, 4419 (1990).
7. W. P. Su and J. R. Schrieffer, Proc. Natl. Acad. Sci. USA. **77**, 5626 (1980).
8. K. Fesser, A. R. Bishop, and D. K. Campbell, Phys. Rev. B **27**, 4804 (1983).
9. A. J. Heeger *et al.*, Rev. Mod. Phys. **60**, 781 (1988).
10. R. H. Friend, D. D. C. Bradley, and P. D. Townsend, J. Phys. D: Appl. Phys. **20**, 1367 (1987).
11. C. V. Shank *et al.*, Phys. Rev. Lett. **49**, 1660 (1982).
12. J. Orenstein, in *Handbook of Conducting Polymers*, edited by T. A. Skothein (Marcel Dekker, New York, 1986), Vol. 2, p. 1297.
13. G. M. Carter *et al.*, Appl. Phys. Lett. **49**, 998 (1986).
14. B. I. Green *et al.*, Chem. Phys. Lett. **139**, 381 (1987).
15. G. J. Blanchard *et al.*, Chem. Phys. Lett. **158**, 329 (1989).
16. T. Kobayashi *et al.*, J. Opt. Soc. Am. B **7**, 1558 (1990).
17. M. Yoshizawa, A. Yasuda, and T. Kobayashi, Appl. Phys. B **53**, 296 (1991).
18. J. M. Huxley *et al.*, Appl. Phys. Lett. **56**, 1600 (1990).
19. B. C. Hess *et al.*, Phys. Rev. Lett. **66**, 2364 (1991).
20. H. Mizes and E. Conwell, Phys. Rev. B **44**, 3963 (1991).
21. B. I. Greene *et al.*, Phys. Rev. Lett. **61**, 325 (1988).
22. I. D. Samuel *et al.*, Synth. Met. **55–57**, 15-21 (1993).
23. E. I. Rashba and M. D. Sturge, in *Excitons*, edited by E. I. Rashba and M. D. Sturge (North-Holland, Amsterdam, 1982), p. 578.
24. K. Nasu, J. Lumin. **38**, 90 (1987).
25. S. A. Jenekhe and J. A. Osaheni, Science **265**, 765 (1994).

OMEGA Upgrade Status Report 10/1/93–9/30/94

The design effort for the OMEGA Upgrade project was finished and the project transitioned to the manufacturing phase during the first two quarters of FY94. The manufacturing of the OMEGA Upgrade consists of fabrication, assembly and testing of all components installed into the laser system, and then integration of all subsystems into a complete facility. The status of the project is indicated by the DOE milestones completed and started during FY94.

DOE project milestones completed this fiscal year are

- KD3′ design
- Operations readiness review, facility
- Laser drivers design
- Pulse-generation room activation
- Target chamber installation
- KD3a transition to operations (pending DOE approval)
- Delivery of
  - laser bay structures
  - target bay structures
  - disk amplifier power conditioning

DOE project milestones started this fiscal year are

- Assembly of rod and disk amplifiers
- Laser bay integration
- Power conditioning installation
- Target bay integration
- Installation of laser and target structures
- Target bay optomechanical assemblies (in-house mfg.)
- Laser optics installation
- Delivery of KDP crystals

A total of 104 mechanical structures are required to mount the optical assemblies on the OMEGA Upgrade laser facility. All of these laser and target bay structures and optical tables have been received, aligned, and grouted into their final positions. The 243 spatial filter tube sections were received, cleaned, and installed into their support frames.

The contractor delivered, assembled, and resistive load tested all 120 SSA (disk amplifier) power conditioning units (PCU's). These units are now ready for live-load testing and amplifier activation. The project received and assembled 11 of the 17 rod amplifier PCU's needed for the first three stages of amplification (stages A, B, and C), and completed mechanical assembly of all rod PCU's needed for the fourth amplification stage (stage D—the final rod amplifiers).

The hardware to transport the main driver pulse from the pulse-generation room (PGR) to the driver line (preamplifier section) was installed, tested, and activated. The main-pulse driver line construction and testing was completed and has delivered a 10-J laser pulse at the output of the driver line ready for injection into the power amplifier section of the laser. Transport from the PGR and driver line for the foot pulse is in work and is scheduled for completion by the end of FY94. These tasks include the construction and testing of large-aperture ring amplifiers (LARA's) used in both the main- and foot-pulse driver lines.

The design for the rod and disk amplifiers resulted in approximately 500,000 parts. The fabrication procurements for these parts were placed and nearly over-subscribed the local machine shops. There are 97 rod amplifiers, 60 15-cm SSA amplifiers, and 60 20-cm SSA amplifiers needed for the OMEGA Upgrade laser system. We have installed 38 rod, 15 15-cm SSA, and one 20-cm SSA amplifier assemblies into their structures on the laser bay floor.

The Thin Film Coating Group has processed through their facility 1047 of the 2430 optics required for the laser system. The remaining 1383 optics are due for delivery to the installation teams by mid-December. The optics are being supplied on an as-needed schedule to minimize the need for clean room storage space.

For FY94 the laser bay integration alignment progress follows closely behind the installation of optical components delivered to the facility. This effort began in early March with the installation and activation of a continuous IR laser source and the optics required for a full-aperture alignment beam. Laser beamline alignment requires the installation of several alignment diagnostics, including a collimation sensor capable of measuring the system collimation at any point in the IR laser between the 243 Upgrade spatial filters. All optics are installed and aligned through the stage-C alignment sensor packages (ASP's) at the conclusion of FY94. The stage-C ASP is mid-chain alignment diagnostic installed just prior to the final beam splitters (C-D splitter). The C-D splitter is currently under alignment as are beamlines starting at the stage-D rod amp and propagating to the stage-F alignment sensor packages (F-ASP's). Most optics have been installed in the ten-beam cluster-3 assemblies, and alignment is progressing smoothly in this cluster.

The target bay integration alignment has concentrated on the ultraviolet alignment table (UVAT), periscope mirror assembly (PMA), and the F-ASP. These three subsystems are required to establish the baseline alignment for all optics in the laser and target bays. The UVAT is fully operational, as are the PMA's. The F-ASP's have all 60 primary and secondary grouting frames installed and aligned. The cluster-3 F-ASP has all ten alignment relay subsystems installed and is fully supported by a control system and alignment image processing.

The activation process of a system stage closely follows the integration alignment of that stage. The driver line is fully activated and calibrated and is operational to support the daily activation requirements. Cluster-3 beamline 9 (39) was selected as the first line to be activated. Amplifiers A3, B34, and C34 have been test fired, fully activated, and calibrated to support the activation of this beam line. All the splitters in beam line 34 have been optically balanced with ratiometers. Full activation for beam line 39 is to be completed by mid-October. Lessons learned from beamline 39 will increase the efficiency of activation for the remaining 59 beamlines.

The project schedule called for the delivery of an Acceptance Test Plan by the end of the third quarter of FY94 and a Final Safety Analysis Document by the end of the second quarter of FY95. These are related to a final operations readiness review and the Key Decision #4 "Project Complete Start Operations" milestone. These are embodied in two project documents that were completed and submitted to DOE in advance of the Acceptance Test Plan milestone.

The Operational Readiness Review Plan (S-AA-M-11) sets up an LLE "Operations and Safety Review Committee" that will conduct an extensive, independent review of the safety aspects of the design and operation of the OMEGA facility. The committee will prepare a report summarizing its activities and findings that will be provided to DOE in advance of the DOE Final Project review.

The Acceptance Test Plan (S-AA-M-08) sets up a system performance review process that is similar to the operations review: An LLE "System Performance Review Committee" will monitor the activation of the system and review test data to verify that the project performance baselines have been met. The committee's report will be provided to DOE in advance of the DOE Final Project review.

NLUF News

Six NLUF proposals for FY94 were submitted to DOE for the consideration of the Steering Committee (see Table 60.III). All of the principal investigators, representing four universities and two government laboratories, have had previous proposals approved for experiments at LLE. Three of the experiments involve x-ray or XUV spectroscopy, one is a plasma interaction experiment, one a diagnostics development, and one a target fabrication effort.

On 1 October 1993 these proposals were reviewed via conference call by the Steering Committee and **Dr. James Knauer** (NLUF Manager). Voting members included **Dr. Michael Boyle**, **Dr. Phillip Goldstone**, **Prof. Chandrasakar Joshi**, and **Dr. Robert Turner**. The Steering Committee evaluated the proposals for their technical merit and submitted their recommendation to the Oakland office of DOE.

DOE decided to fund all of the submitted proposals. The monies were allocated according to the technical ranking provided by the Steering Committee. These proposals were primarily directed to the development of diagnostics for the OMEGA Upgrade laser system. Two projects that were to use the GDL laser system were either conducted at other laser systems or are awaiting the availability of the GDL system.

A brief summary of each proposal funded for FY94 follows:

Proposal 180
"Measurements of Quantum Electrodynamic Sensitive Transitions in Na-like and CU-like Ions"
Principal Investigator:
J. Reader, National Institute of Standards and Technology (NIST)

The Principal Investigator proposes to use GDL to measure QED effects in high-Z ions. There are 11 proposed targets ranging in Z from 47 to 92. The GDL laser system will be used to study Na-like and Cu-like ions of these elements. The primary diagnostic is a 2.2-m Rowland Spectrograph owned by NIST with its own attached target chamber. The optics used for Dr. Reader's previous experiments are not usable on the current GDL system because of the increased beam diameter and energy. We do have optics available but the focusing lens assembly must be adapted to his target chamber.

Table 60.III: The numerical listing of NLUF proposals.

Proposal Number	Investigator	Institution	Proposal Title
180	J. Reader	National Institute of Standards and Technology	Measurements of Quantum Electrodynamic Sensitive Transitions in Na-like and Cu-like Ions
181	J. F. Seely	Naval Research Laboratory	Normal-Incidence Multilayer Mirror X-Ray Microscope
182	A. Honig	Syracuse University	Temperature-Dependent Tensile Strength, Surface Roughness Diagnostics, and Magnetic Support and Positioning of Polymer ICF Shells at Temperatures between 4K and 300K
183	K. Mizuno	Plasma Physics Research Institute University of California, Davis	The Ion Acoustic Decay Instability in a Large-Scale, Hot Plasma Relevant to Direct-Drive Laser Fusion—Applications to a Critical Surface Diagnostic and Thermal Smoothing
184	C. F. Hooper Jr.	University of Florida	Plasma Spectroscopy: Theoretical and Experimental Diagnostic Development / Tests
185	H. R. Griem	University of Maryland	Development of Density and Temperature Profile Diagnostics for ICF Targets

Proposal 181
"Normal-Incidence Multilayer Mirror X-Ray Microscope"
Principal Investigator:
J. F. Seely, Naval Research Laboratory (NRL)

Dr. Seeley's group at NRL is building a Cassegrain-type microscope for use at a wavelength of 33.7 Å. The work builds upon the successful fielding of a similar instrument on the OMEGA laser system in 1992 and development work supported by NASA. The microscope will have a 1.8-μm resolution at the target and a magnification of 10, and will use a 1024 × 1024 CCD as the detector. Most of the work is being done at NRL. The microscope fits into a LLNL SIM cart, allowing it to be tested on either GDL or NOVA.

Proposal 182
"Temperature-Dependent Tensile Strength, Surface Roughness Diagnostics, and Magnetic Support and Positioning of Polymer ICF Shells at Temperatures between 4 K and 300 K"
Principal Investigator:
A. Honig, Syracuse University

There are three independent tasks to this proposal for work to be done at Syracuse University. The first task will study the material properties of CH shells at cryogenic temperatures; the second task will use the measured shell properties with precharacterized shells to determine if there is a correlation between accommodation coefficients and surface roughness; and the third task will develop the use of ferrite-doped plastic shells for magnetic levitation and positioning. Ferrite-doped plastics have been delivered to LLE for shell fabrication.

Proposal 183
"The Ion Acoustic Decay Instability in a Large-Scale, Hot Plasma Relevant to Direct-Drive Laser Fusion—Applications to a Critical Surface Diagnostic and Thermal Smoothing"
Principal Investigator:
K. Mizuno, Plasma Physics Research Institute (UCD)

This group is studying the critical surface using the ion-acoustic decay instability. The development of this diagnostic for the OMEGA Upgrade is being done at PPRI; subsequent testing of thermal-smoothing techniques is to be done on GDL. There is a second task that will use the GDL facility to test the second-harmonic diagnostic and x rays emitted from flat targets to study thermal smoothing and lateral heat transport. This second task requires that GDL have full pulse shaping and smoothing by spectral dispersion capability. The GDL tasks have been delayed until the laser system is available for experiments.

Proposal 184
"Plasma Spectroscopy: Theoretical and Experimental Diagnostic Development/Tests"
Principal Investigator:
C. F. Hooper Jr., University of Florida

The Principal Investigator continues to develop atomic physics computer codes to calculate the effects of high temperature and density on x-ray line emission and transport. There are three tasks associated with this work. The analysis of *L*-shell spectra is considered (by the Principal Investigator) the next step in the extension of the atomic models with ion dynamics formalism. It is also proposed to extend the "multielectron line broadening theory" to conditions expected for OMEGA Upgrade target implosions. The third task is to develop micro-dot spectroscopy to study laser-plasma interactions.

Proposal 185
"Development of Density and Temperature Profile Diagnostics for ICF Targets"
Principal Investigator:
H. R. Griem, University of Maryland

The work done primarily at the University of Maryland is to extend the development of previous work in x-ray and XUV spectroscopy to OMEGA Upgrade target conditions. The diagnostics are being constructed and tested before the experiments can be done on the OMEGA Upgrade. The Trident laser system at the Los Alamos National Laboratory is being used to test the instrumentation.

Publications and Conference Presentations

Publications

S. Alexandrou, C.-C. Wang, M. Currie, R. Sobolewski, and T. Y. Hsiang, "Loss and Dispersion at Subterahertz Frequencies in Coplanar Waveguides with Varying Ground-Plane Widths," in *Technologies for Optical Fiber Communications*, edited by G. J. Brown *et al.* (SPIE, Bellingham, WA, 1994), Vol. 2149, pp. 108–118.

S. Alexandrou, C.-C. Wang, T. Y. Hsiang, M. Y. Liu, and S. Y. Chou, "A 75-GHz Silicon Metal-Semiconductor-Metal Schottky Photodiode," Appl. Phys. Lett. **62**, 2507 (1993).

S. Alexandrou, C.-C. Wang, R. Sobolewski, and T. Y. Hsiang, "Generation of Subpicosecond Electrical Pulses by Nonuniform Illumination of GaAs Transmission Line Gaps," IEEE J. Quantum Electron. **30**, 1332 (1994).

J. J. Armstrong and T. J. Kessler, "Large-Aperture High-Efficiency Holographic Gratings for High-Power Laser Systems," in *Laser Coherence Control: Technology and Applications*, edited by H. T. Powell and T. J. Kessler (SPIE, Bellingham, WA, 1993), Vol. 1870, pp. 47–52.

R. Betti, R. L. McCrory, and C. P. Verdon, "Stability Analysis of Unsteady Ablation Fronts," Phys. Rev. Lett. **71**, 3131 (1993).

X. D. Cao, G. P. Agrawal, and C. J. McKinstrie, "Self-Focusing of Chirped Optical Pulses in Nonlinear Dispersive Media," Phys. Rev. A **49**, 4085 (1994).

X. D. Cao and D. D. Meyerhofer, "Nonlinear Birefringence of Optical Fibers," Opt. Commun. **109**, 151 (1994).

X. D. Cao and D. D. Meyerhofer, "Soliton Collisions in Optical Birefringent Fibers," J. Opt. Soc. Am. B **11**, 380 (1994.)

Y.-H. Chuang, T. J. Kessler, and S. Skupsky, "Laser-Beam Pulse Shaping Using Dispersive Spectral Filtering," in *Laser Coherence Control: Technology and Applications*, edited by H. T. Powell and T. J. Kessler (SPIE, Bellingham, WA, 1993), Vol. 1870, pp. 34–46.

R. S. Craxton, F. S. Turner, R. Hoefen, C. Darrow, E. F. Gabl, and Gar. E. Busch, "Characterization of Laser-Produced Plasma Density Profiles Using Grid Image Refractometry," Phys. Fluids B **5**, 4419 (1993).

M. J. Cumbo and S. D. Jacobs, "Determination of Near-Surface Forces in Optical Polishing Using Atomic Force Microscopy," Nanotechnology **5**, 70 (1994).

J. A. Delettrez, D. K. Bradley, and C. P. Verdon, "The Role of the Rayleigh-Taylor Instability in Laser-Driven Burnthrough Experiments," Phys. Plasmas **1**, 2342 (1994).

A. Denysenko, S. Alexandrou, C.-C. Wang, D. K. Bradley, W. R. Donaldson, T. Y. Hsiang, R. Sobolewski, and P. M. Bell, "Picosecond Electrical Characterization of X-Ray Microchannel-Plate Detectors Used in Diagnosing Inertial-Confinement-Fusion Experiments," Rev. Sci. Instrum. **64**, 3285 (1993).

H. E. Elsayed-Ali, J. W. Herman, and E. A. Murphy, "Ultrafast Laser Superheating of Metal Surfaces," in *Beam Solid Interactions: Fundamentals and Applications*, edited by M. Natasi *et al.* (Materials Research Society, Pittsburgh, PA, 1993), Vol. 279, pp. 685–690.

H. E. Elsayed-Ali and T. Juhasz, "Femtosecond Time-Resolved Thermomodulation of Thin Gold Films with Different Crystal Structures," Phys. Rev. B **47**, 13599 (1993).

E. M. Epperlein, "Effect of Electron Collisions on Ion-Acoustic Waves and Heat Flow," Phys. Plasmas **1**, 109 (1994).

E. M. Epperlein, "Fokker-Planck Modeling of Electron Transport in Laser-Produced Plasmas," Laser Part. Beams **12**, 257 (1994).

E. M. Epperlein, "Implicit and Conservative Difference Scheme for the Fokker-Planck Equation," J. Comput. Phys. **112**, 291 (1994).

E. M. Epperlein and R. W. Short, "Comments on 'Theory and Three-Dimensional Simulation of Light Filamentation in Laser-Produced Plasmas' [Phys. Fluids B 5, 2243 (1993)]," Phys. Plasmas **1**, 1364 (1994).

E. M. Epperlein and R. W. Short, "Generalized Electron Fluid Equations in the Presence of Laser Irradiation," Phys. Plasmas **1**, 3003 (1994).

E. M. Epperlein and R. W. Short, "Nonlocal Electron Transport in the Presence of High-Intensity Laser Irradiation," Phys. Rev. E **50**, 1697 (1994).

E. M. Epperlein, R. W. Short, and A. Simon, "Transport and Sound Waves in Plasmas with Light and Heavy Ions," Phys. Rev. E **49**, 2480 (1994).

P. Gierlowski, G. Jung, W. Kula, S. J. Lewandowski, B. Savo, R. Sobolewski, A. Tebano, and A. Vecchione, "Low Frequency Voltage Noise in Current Biased HTSC Thin Films," Physica B **194–196**, 2043 (1994).

T. Gong and P. M. Fauchet, "Carrier-Carrier Interactions in GaAs Investigated by Femtosecond Spectroscopy," in *Ultrafast Pulse Generation and Spectroscopy* (SPIE, Bellingham, WA, 1993), Vol. 1861, pp. 227–236 (invited).

T. Gong, Y. Kostoulas, L. X. Zheng, W. Xiong, W. Kula, R. Sobolewski, and P. M. Fauchet, "Femtosecond Optical Nonlinearities in $YBa_2Cu_3O_{7-x}$," in *Ultrafast Pulse Generation and Spectroscopy*, edited by T. R. Gosnell *et al.* (SPIE, Bellingham, WA, 1993), Vol. 1861, pp. 355–362.

T. Gong, J. F. Young, G. W. Wicks, P. J. Kelly, and P. M. Fauchet, "Hot-Carrier Dynamics Near the Fermi Edge of N-Doped GaAs," Semicond. Sci. Technol. **9**, 459 (1994).

D. Gupta, "A New Optically Triggered Superconducting Opening Switch for High-Power Applications," in *Research Reports of the Link Energy Fellows*, edited by B. J. Thompson (The University of Rochester Press, Rochester, NY, 1994), Vol. 9, pp. 25–41.

D. Gupta, W. R. Donaldson, and A. M. Kadin, "Fast Inductively Coupled Superconducting Opening Switch Triggered by Short Laser Pulses," in the *Proceedings of the Ninth IEEE International Pulsed Power Conference* (IEEE, New York, 1993), pp. 131–133.

D. Gupta, W. R. Donaldson, and A. M. Kadin, "Fast Optically Triggered Superconducting Opening Switches," in *Optically Activated Switching III*, edited by H. T. Powell and T. J. Kessler (SPIE, Bellingham, WA, 1993), Vol. 1873, pp. 139–143.

D. Gupta, W. R. Donaldson, and A. M. Kadin, "High-Temperature Superconducting Opening Switches," in the *Proceedings of the Fifth SDIO/ONR Pulse Power Meeting 1992* (Office of Naval Research, Arlington, VA, 1993), pp. 75–82.

D. Gupta, W. R. Donaldson, and A. M. Kadin, "A Laser-Triggered, Inductive Opening Switch Using High-Temperature Superconducting Thin Films," in *Advances in Cryogenic Engineering*, edited by P. Kittel (Plenum Press, New York, 1994), Vol. 39B, pp. 2015–2020.

J. W. Herman and H. E. Elsayed-Ali, "Time-Resolved Structural Studies of the Low-Index Faces of Lead," Phys. Rev. B **49**, 4886 (1994).

S. D. Jacobs, "Progress at the Center for Optics Manufacturing," in *Optical Fabrication, Testing, and Surface Evaluation*, edited by J. Tsujiuchi (SPIE, Bellingham, WA, 1992), Vol. 1720, pp. 169–174.

M. Kauranen, A. L. Gaeta, and C. J. McKinstrie, "Transverse Instabilities of Two Intersecting Laser Beams in a Nonlinear Kerr Medium," J. Opt. Soc. Am. B **10**, 2298 (1993).

J. H. Kelly, M. J. Shoup III, M. M. Tedrow, and K. Thorp, "Energy Transort in a Modern Disk Amplifier," in *Solid State Lasers III* (SPIE, Bellingham, WA, 1992), Vol. 1627, pp. 286–297.

T. J. Kessler, Y. Lin, J. J. Armstrong, and B. Velazquez, "Phase Conversion of Lasers with Low-Loss Distributed Phase Plates," in *Laser Coherence Control: Technology and Applications*, edited by H. T. Powell and T. J. Kessler (SPIE, Bellingham, WA, 1993), Vol. 1870, pp. 95–104.

H. Kim and M. D. Wittman, "Interferometric Microscopy—An Overview of the Optical Characterization of Inertial-Fusion Targets," in *Multidimensional Microscopy*, edited by

P. C. Cheng, T. H. Lin, W. L. Wu, and J. L. Wu (Springer-Verlag, New York, 1994), pp. 103–121.

L. E. Kingsley and W. R. Donaldson, "Numerical Analysis of Electric Field Profiles in High-Voltage GaAs Photoconductive Switches and Comparison to Experiment," IEEE Trans. Electron Devices **40,** 2344 (1993).

E. M. Korenic, S. D. Jacobs, J. K. Houghton, F. Kreuzer, and A. Schmid, "Nematic Polymer Liquid-Crystal Waveplate for High-Power Lasers at 1054 nm," Appl. Opt. **33**, 1889 (1994).

Y. Kostoulas, P. M. Fauchet, T. Gong, B. C. Tousley, G. W. Wicks, and P. Cooke, "Femtosecond Carrier Dynamics in Low-Temperature-Grown III–V Seminconductors," in *Ultrafast Phenomena in Semiconductors*, edited by D. K. Ferry and H. M. Van Driel (SPIE, Bellingham, WA, 1994), Vol. 2142, pp. 100–109.

Y. Kostoulas, T. Gong, and P. M. Fauchet, "Investigation of Carrier-Carrier Scattering by Three-Pulse Pump-Probe Spectroscopy," Semicond. Sci. Technol. **9**, 462 (1994).

W. Kula and R. Sobolewski, "Charging Effect in Partially Oxygen-Depleted, Superconducting Y-Ba-Cu-O Thin Films," Phys. Rev. B **49,** 6428 (1994).

W. Kula and R. Sobolewski, "Electric-Field Effect in Partially Deoxygenated YBCO Thin Films," Physica B **194–196**, 2083 (1994).

W. Kula and R. Sobolewski, "Electric-Field-Effect Devices Based on Partially Oxygen-Depleted, Superconducting Y-Ba-Cu-O Thin Films," in *Advances in Cryogenic Engineering*, edited by R. P. Reed *et al.* (Plenum Press, New York, 1994), Vol. 40, pp. 377–383.

B. S. W. Kuo and A. W. Schmid, "Effects of Thin-Film Thermal Conductivity on the Optical Damage Threshold of a-Si Film on c-Si Substrate at 1064 nm," J. Appl. Phys. **74,** 5159 (1993).

W. Lang, W. Kula, and R. Sobolewski, "Superconducting Fluctuations: Paraconductivity, Excess Hall Effect, and Magnetoconductivity in 2223-BiSrCaCuO Thin Films," Physica B **194–196**, 1643 (1994).

Y. Lin, T. J. Kessler, J. J. Armstrong, and G. N. Lawrence, "Laser System Power Balance Effects from Stimulated Rotational Raman Scattering in Air," in *Laser Coherence Control: Technology and Applications*, edited by H. T. Powell and T. J. Kessler (SPIE, Bellingham, WA, 1993), Vol. 1870, pp. 14–25.

A. I. Lobad, P. J. Rodney, S. M. Mehta, B. C. Tousley, and P. M. Fauchet, "The Starting Mechanism in Coupled-Cavity Mode-Locked Laser Systems," IEEE J. Quantum Electron. **30**, 812 (1994).

A. I. Lobad, P. J. Rodney, B. C. Tousley, S. M. Mehta, and P. M. Fauchet, "The Starting Mechanism in Coupled-Cavity, Mode-Locked Laser Systems," in *Generation, Amplification, and Measurement of Ultrashort Laser Pulses*, edited by R. P. Trebino and I. A. Walmsley (SPIE, Bellingham, WA, 1994), Vol. 2116, pp. 109–117.

F. J. Marshall, J. A. Delettrez, R. Epstein, and B. Yaakobi, "Diagnosis of Laser-Target Implosions by Space-Resolved Continuum Absorption X-Ray Spectroscopy," Phys. Rev. E **49**, 4381 (1994).

J. C. Mastrangelo and S.-H. Chen, "New Thermotropic Chiral Nematic Polymers. 3. Copolymers Containing Cyanobiphenyl Group and (S)-(-)-1-Phenylethanol or (S)-(–)-1-Phenylethylamine," Macromolecules **26**, 6132 (1993).

W. N. Maung, D. P. Butler, W. Xiong, W. Kula, and R. Sobolewski, "Microwave Properties of Monolithic Y-Ba-Cu-O Transmission Line Devices Fabricated by the Laser-Writing Patterning Technique," in *High-T_c Microwave Superconductors and Applications* (SPIE, Bellingham, WA, 1994), Vol. 2156, pp. 174–180.

W. N. Maung, D. P. Butler, W. Xiong, W. Kula, and R. Sobolewski, "Propagation Characteristics of Monolithic Y-Ba-Cu-O Coplanar Strip Transmission Lines Fabricated by Laser Writing Patterning Technique," IEEE Microw. Guid. Wave Lett. **MGWL-4**, 132 (1994).

R. L. McCrory, "Direct-Drive Implosion Experiments for Laser Fusion on OMEGA and the OMEGA Upgrade," in *Proceedings of the 21st ECLIM*, edited by H. Fiedorowicz, J. Wolowski, M. Mroczkowski, M. Szczurek, and A. Ulinowicz (ECLIM, Warsaw, Poland, 1992), pp. 197–200.

R. L. McCrory, J. M. Soures, C. P. Verdon, T. R. Boehly, D. K. Bradley, R. S. Craxton, J. A. Delettrez, R. Epstein, R. J. Hutchison, P. A. Jaanimagi, S. D. Jacobs, J. H. Kelly, R. L.

Keck, T. J. Kessler, H. Kim, J. P. Knauer, R. L. Kremens, S. A. Kumpan, S. A. Letzring, F. J. Marshall, P. W. McKenty, S. F. B. Morse, W. Seka, R. W. Short, M. D. Skeldon, S. Skupsky, and B. Yaakobi, "Direct-Drive Laser Fusion Target Physics Experiments," in *Plasma Physics and Controlled Nuclear Fusion Research*, 1992 (IAEA, Vienna, 1993), Vol. 3, pp. 31–38.

P. W. McKenty, S. Skupsky, J. H. Kelly, and C. T. Cotton, "Numerical Investigation of the Self-Focusing of Broad-Bandwidth Laser Light with Applied Angular Dispersion," J. Appl. Phys. **76**, 2027 (1994).

C. J. McKinstrie, R. Betti, R. E. Giacone, T. Kolber, and J. S. Li, "Two-Dimensional Stimulated Brillouin Scattering," Phys. Rev. E **50**, 2182 (1994).

C. J. McKinstrie, X. D. Cao, and J. S. Li, "Nonlinear Detuning of Four-Wave Interactions," J. Opt. Soc. Am. B **10**, 1856 (1993).

D. D. Meyerhofer and J. Peatross, "Angular Distributions of High-Order Harmonics," in *Super-Intense Laser-Atom Physics*, edited by B. Piraux, A. L'Huillier, and K. Rzazewski, NATO ASI Series B, Physics, Vol. 316 (Plenum Press, New York, 1993), pp. 19–29.

L. Mu and W. R. Donaldson, "Simulating Photoconductive Switches in a Microwave Transmission Line," in the *Proceedings of the Ninth IEEE International Pulsed Power Conference* (IEEE, New York, 1993), pp. 629–632.

E. A. Murphy, H. E. Elsayed-Ali, K. T. Park, and Y. Gao, "Temperature-Dependent X-Ray Photoelectron Diffraction of Pb(100): Experimental Results and the Single-Scattering Cluster Model," J. Vac. Sci. Technol. A **11**, 3106 (1993).

S. Papernov and A. W. Schmid, "Atomic Force Microscopy Studies of Laser-Triggered Morphology Changes in Y_2O_3 Monolayer Coatings," in *Laser-Induced Damage in Optical Materials: 1993* (SPIE, Bellingham, WA, 1994), Vol. 2114, pp. 381–386.

J. Peatross, J. L. Chaloupka, and D. D. Meyerhofer, "High-Order Harmonic Generation with an Annular Laser Beam," Opt. Lett. **19**, 942 (1994).

J. Peatross and D. D. Meyerhofer, "Measurement of the Angular Distribution of High-Order Harmonics Emitted from Rare Gases," in *OSA Proceedings on Shortwavelength V: Physics with Intense Laser Pulses*, edited by P. B. Corkum and M. D. Perry (Optical Society of America, Washington, DC, 1993), Vol. 17, pp. 122–126.

J. Peatross and D. D. Meyerhofer, "Novel Gas Target for Use in Laser Harmonic Generation," Rev. Sci. Instrum. **64**, 3066 (1993).

J. K. Samarabandu, R. Acharya, C. D. Edirisinghe, P. C. Cheng, H. Kim, T. H. Lin, R. G. Summers, and C. E. Musial, "Analysis of Multi-Dimensional Confocal Images," in *Biomedical Image Processing II*, edited by A. C. Bovik and V. Howard (SPIE, Bellingham, WA, 1991), Vol. 1450, pp. 296–322.

L. Shi and S.-H. Chen, "New Thermotropic Liquid Crystal Polymers Containing High Birefringence Cyanotolan Moiety," Macromolecules **26**, 5840 (1993).

L. Shi, T. Gong, X. Xiong, X. Weng, Y. Kostoulas, R. Sobolewski, and P. M. Fauchet, "Femtosecond Reflectivity of 60-K Y-Ba-Cu-O Thin Films," Appl. Phys. Lett. **64**, 1150 (1994).

M. D. Skeldon and S. T. Bui, "Temporal Pulse-Width Control of a Regenerative Amplifier with Intracavity Etalons," in *Intracavity and Extracavity Control of Laser Beam Properties*, edited by R. L. Facklam, K. H. Guenther, and S. P. Velsko (SPIE, Bellingham, WA, 1993), Vol. 1869, pp. 120–127.

S. Skupsky and T. J. Kessler, "Speckle-Free Phase Plate (Diffuser) for Far-Field Applications," J. Appl. Phys. **74**, 4310 (1993).

S. Skupsky and T. J. Kessler, "Strategies for Ultra-High Laser Uniformity Using Zero-Correlation Phase Masks," in *Laser Coherence Control: Technology and Applications*, edited by H. T. Powell and T. J. Kessler (SPIE, Bellingham, WA, 1993), Vol. 1870, pp. 112–119.

R. Sobolewski, L. Shi, T. Gong, W. Xiong, X. Weng, Y. Kostoulas, and P. M. Fauchet, "Femtosecond Optical Response of Y-Ba-Cu-O Thin Films and Their Applications in Optoelectronics," in *High-Temperature Superconducting Detectors: Bolometric and Nonbolometric*, edited by M. Nahum and J.-C. Villegier (SPIE, Bellingham, WA, 1994), Vol. 2159, pp. 110–120.

R. Sobolewski, W. Xiong, W. Kula, and J. R. Gavaler, "Laser Patterning of Y-Ba-Cu-O Thin-Film Devices and Circuits," Appl. Phys. Lett. **64**, 643 (1994).

R. Sobolewski, W. Xiong, W. Kula, W. N. Maung, and D. P. Butler, "Monolithic Y-Ba-Cu-O Structures Fabricated Using the Laser-Writing Patterning Technique," Supercond. Sci. Technol. **7**, 300 (1994).

R. Sobolewski, W. Xiong, W. Kula, and B. McIntyre, "Electrical and Structural Properties of the YBCO Superconducting-Semiconducting Interface," Physica B **194–196**, 2143 (1994).

B. Soom, H. Chen, Y. Fisher, and D. D. Meyerhofer, "Strong K_α Emission in Picosecond Laser-Plasma Interactions," in *OSA's Proceedings on Shortwavelength V: Physics with Intense Laser Pulses*, edited by P. B. Corkum and M. D. Perry (Optical Society of America, Washington, DC, 1993), Vol. 17, pp. 192–195.

B. Soom, H. Chen, Y. Fisher, and D. D. Meyerhofer, "Strong K_α Emission in Picosecond Laser-Plasma Interactions," J. Appl. Phys. **74**, 5372 (1993).

J. M. Soures, "High-Technology Advances from LLE Research," Rochester Business Profiles Journal, August 1991, 40–41.

J. M. Soures, "Solid State Lasers for ICF," in *Nuclear Fusion by Inertial Confinement*, edited by G. Velarde, Y. Ronen, and J. M. Martinez-Val (CRC Press, 1993), Chap. 14, pp. 351–370.

J. M. Soures, "The OMEGA Upgrade Laser Facility for Direct-Drive Experiments," J. Fusion Energy **10**, 295 (1991).

J. Sweetser, T. J. Dunn, I. A. Walmsley, C. Radzewicz, S. Palese, and R. J. D. Miller, "Characterization of an FM Mode-Locked Nd:YLF Laser Synchronized with a Passively Mode-Locked Dye Laser," Opt. Commun. **97**, 379 (1993).

C. J. Twomey, S.-H. Chen, T. N. Blanton, A. Schmid, and K. L. Marshall, "Poly[(Methylene Oxide)Oligo(Ethylene Oxide)] Vs. Poly(Ethylene Oxide) as Hosts for Neodymium Compounds," J. Polym. Sci. B, Polym. Phys. **32**, 1687 (1994).

C. J. Twomey, S.-H. Chen, T. Blanton, A. W. Schmid, and K. L. Marshall, "Solid Polymers Doped with Rare Earth Metal Salts. II. Thermal Behavior and Morphology of the Neodymium Acetate-Poly(Ethylene Oxide) System," J. Polym. Sci. B, Polym. Phys. Ed. **31**, 647 (1993).

C. J. Twomey, S.-H. Chen, T. Blanton, A. W. Schmid, and K. L. Marshall, "Solid Polymers Doped with Rare Earth Metal Compounds. III. Formation and Stability of Macromolecular Complexes Comprising Neodymium Nitrate and Dipivaloylmethane in Poly(Ethylene Oxide)," J. Polym. Sci. B, Polym. Phys. **32**, 551 (1994).

C. J. Twomey, S.-H. Chen, T. N. Blanton, A. W. Schmid, and K. L. Marshall, "Stoichiometry and Morphology in Terbium Nitrate-Poly(Ethylene Oxide) Macromolecular Complex," J. Polym. Sci. B, Polym. Phys. **32**, 1573 (1994).

C.-C. Wang, S. Alexandrou, D. Jacobs-Perkins, and T. Y. Hsiang, "Comparison of the Picosecond Characteristics of Silicon and Silicon-on-Sapphire Metal-Semiconductor-Metal Photodiodes," Appl. Phys. Lett. **64**, 3578 (1994).

C.-C. Wang, S. Alexandrou, D. Jacobs-Perkins, and T. Y. Hsiang, "Picosecond Characteristics of Silicon-on-Insulator Metal-Semiconductor-Metal Photodiodes," in *Technologies for Optical Fiber Communications*, edited by G. J. Brown *et al.* (SPIE, Bellingham, WA, 1994), Vol. 2149, pp. 271–275.

C.-C Wang, M. Currie, S. Alexandrou, and T. Y. Hsiang, "Ultrafast, All-Silicon Light Modulator," Opt. Lett. **19**, 1453 (1994).

W. Xiong, W. Kula, R. Sobolewski, and J. R. Gavaler, "Laser Writing: A New Technique for Fabrication of Electronic and Optoelectronic Y-Ba-Cu-O Devices and Circuits," in *Superconductive Devices and Circuits*, edited by R. A. Buhrman, J. Clarke, K. Daly, R. H. Koch, J. A. Luine, and R. W. Simon (SPIE, Bellingham, WA, 1994), Vol. 2160, pp. 16–24.

W. Xiong, W. Kula, and R. Sobolewski, "Fabrication of High-T_c Superconducting Electronic Devices Using the Laser-Writing Patterning Technique," in *Advances in Cryogenic Engineering* (Plenum Press, New York, 1994), Vol. 40A, pp. 385–391.

J. F. Young, T. Gong, P. J. Kelly, and P. M. Fauchet, "Carrier-Carrier Scatterings within Athermol Distributions," Semicond. Sci. Technol. **9**, 465 (1994).

M. Yu, C. J. McKinstrie, and G. P. Agrawal, "Instability Due to Cross-Phase Modulation in the Normal Dispersion Regime," Phys. Rev. E **48**, 2178 (1993).

Conference Presentations

The following presentations were made at the 1993 OSA Annual Meeting, Toronto, Canada, 3–8 October 1993:

J. J. Armstrong and T. J. Kessler, "Holographic Diffractive Optics for Use in High-Peak-Power Laser Systems."

D. L. Brown, I. Will, R. G. Roides, C. K. Merle, M. D. Skeldon, and W. Seka, "Regenerative Amplifier with Negative Feedback for Enhanced Amplitude Stability and External Synchronizability."

D. Fried, J. D. B. Featherstone, W. Seka, R. Glena, and B. Bordyn, "Light Scattering in Dental Hard Tissues."

C. Kellogg, K. Kubath, A. Maltsev, and T. J. Kessler, "The Fabrication and Testing of a High-Damage-Threshold, UV Transmissive, Lens Array Telescope."

J. H. Kelly, K. A. Thorp, R. L. Keck, M. D. Tracy, C. Cotton, R. G. Roides, C. K. Merle, M. M. Tedrow, B. Staat, and I. Will, "Design and Performance of a Flexible, kJ-Class, Frequency-Converted, Single-Beam Nd:Glass Laser."

Y. Lin, T. J. Kessler, and G. Lawrence, "Optical-Phase-Plate Design and Modeling for Laser Fusion."

J. Peatross and D. D. Meyerhofer, "Observation of Intensity-Dependent Phase of Atomic High-Harmonic Emission in the Far-Field Angular Distribution."

W. Seka, I. Will, J. Chow, D. L. Brown, M. D. Skeldon, C. K. Merle, R. G. Roides, and W. Ragg, "Highly Reliable, Stable, and Synchronizable Long-Pulse Mono-Mode Oscillator for Laser-Fusion Drivers."

M. D. Skeldon, "Transverse Modulational Instabilities in the Presence of Stimulated Rotational Raman Scattering with a High-Power Laser."

R. Stewart, S. Bui, and T. J. Kessler, "Spectral Masks for Optical Pulse Shaping of Lasers in Fusion."

M. D. Tracy, I. Will, C. K. Merle, R. G. Roides, K. Thorp, M. D. Skeldon, J. H. Kelly, and W. Seka, "Versatile Front-End Laser System for Laser-Fusion Drivers."

J. D. Zuegel and W. Seka, "Direct Measurements of Gain-Saturation Phenomena in Nd:YLF," ILS IX (1993), Toronto, Canada, 3–8 October 1993.

S. A. Letzring, "Design of a 60-kJ, 60-Beam Upgrade to the OMEGA Laser at the Laboratory for Laser Energetics, University of Rochester," 15th Symposium on Fusion Engineering, Hyannis, MA, 11–15 October 1993

T. E. Fortner and M. J. Shoup III, "Cooling Flow Management System for the OMEGA Laser System," Sensors Expo, Philadelphia, PA, 26–28 October 1993.

The following presentations were made at the XXV Boulder Damage Symposium on Optical Materials for High Power Lasers, Boulder, CO, 27–29 October 1993:

S. Papernov and A. W. Schmid, "Atomic Force Microscopy Observations of Water-Induced Morphological Changes in Y_2O_3 Monolayer Coatings."

S. Papernov and A. W. Schmid, "Atomic Force Microscopy Studies of Laser-Triggered Morphology Changes in Y_2O_3 Monolayer Coatings."

The following presentations were made at the 35th Annual Meeting of the American Physical Society, Division of Plasma Physics, St. Louis, MO, 1–5 November 1993:

R. Betti and J. P. Freidberg, "Stability of the m = 1 Internal Kink in Ignited Plasmas."

R. Betti, R. L. McCrory, and C. P. Verdon, "Linear Growth Rates of the Ablative Rayleigh-Taylor Instability."

T. R. Boehly, R. S. Craxton, R. J. Hutchison, J. H. Kelly, T. J. Kessler, S. A. Kumpan, S. A. Letzring, R. L. McCrory, S. F. B. Morse, W. Seka, S. Skupsky, J. M. Soures, and C. P. Verdon, "Progress on the Upgrade to the OMEGA Laser System."

D. K. Bradley, J. A. Delettrez, P. A. Jaanimagi, S. Skupsky, and C. P. Verdon, "Measurements of the Effects of Pulse Shaping on Rayleigh-Taylor Growth in Burnthrough Targets."

A. V. Chirokikh, W. Seka, R. S. Craxton, R. E. Bahr, A. Simon, R. W. Short, E. M. Epperlein, H. Baldis, and R. P. Drake, "Stimulated Brillouin Scattering at 1.053 μm in OMEGA Long-Scale-Length Interaction Experiments."

R. S. Craxton, T. Afshar-Rad, M. Dunne, and O. Willi, "Numerical Modeling of a Thermal Smoothing Experiment."

G. Cripps, M. A. Russotto, C. P. Verdon, S. Skupsky, and R. L. Kremens, "Simulation of Laser-Fusion Activation Diagnostics."

J. A. Delettrez, G. Bonnaud, P. Audebert, J. P. Geindre, and J. C. Gauthier, "PIC Code Simulations of the Interaction of 100-fs Gaussian Laser Pulses with Targets of Varying Scale Lengths."

E. M. Epperlein, "Implicit-Conservative Fokker-Planck Simulations of Heat Flowing Laser Fusion."

R. Epstein, S. Skupsky, and C. P. Verdon, "Smoothing of Laser Irradiation of Spherical ICF Targets Using a Pre-Formed Refracting Atmosphere Containing Small Inhomogeneities."

Y. Fisher, B. Soom, and D. D. Meyerhofer, "Ion Emission from High-Contrast, Picosecond, Laser-Plasma Interactions."

R. E. Giacone, C. J. McKinstrie, and R. Betti, "Angular Dependence of SBS in Homogeneous Plasma."

J. P. Knauer, C. P. Verdon, T. J. Kessler, S. Skupsky, R. L. McCrory, J. M. Soures, S. G. Glendinning, S. V. Weber, R. J. Wallace, S. N. Dixit, M. A. Henesian, J. D. Kilkenny, and H. T. Powell, "Stabilization of the Rayleigh-Taylor Unstable Ablation Interface with Trace Amounts of Chlorine."

J. S. Li, C. J. McKinstrie, and C. Joshi, "Thermal Filamentation of Counterpropagating Light Waves."

C. J. McKinstrie, J. S. Li, and C. Joshi, "Sideward SBS of Counterpropagating Light Waves."

D. D. Meyerhofer, H. Chen, J. A. Delettrez, E. M. Epperlein, Y. Fisher, and B. Soom, "Thermal Heat Front Penetration in Picosecond Laser-Plasma Interactions."

W. Seka, R. E. Bahr, R. S. Craxton, A. Chirokikh, R. W. Short, A. Simon, H. Baldis, and R. P. Drake, "OMEGA Long-Scale-Length Laser-Plasma Experiments."

R. W. Short, "Stimulated Brillouin Scattering Driven by Smoothed Laser Beams."

A. Simon, "The Effect of Jets of Accelerated Ions on Scattered Laser Light Near ω_0."

M. D. Tracy and E. M. Epperlein, "Eigenvalue Solution of the Fokker-Planck Equation for Ion-Acoustic and Entropy Waves in Multi-Species Plasmas."

C. P. Verdon, "High-Performance Direct-Drive Capsule Designs for the National Ignition Facility."

C. P. Verdon, R. Betti, and R. L. McCrory, "Dynamic Stability of Imploding Shells."

M. Yu, C. J. McKinstrie, and W. L. Kruer, "Relativistic Saturation of Forward SRS."

L. D. Lund, A. Rigatti, P. Glenn, and J. Glenn, "Characterization of Surface Particulate Contamination on Liquid-Crystal Optics for Laser Fusion," ASPE 8th Annual Meeting, Seattle, WA, 7–12 November 1993.

The following presentations were made at the 40th National AVS Symposium & Topical Conference, Orlando, FL, 15–19 November 1993:

R. Q. Gram, D. S. Brennan, S. G. Noyes, R. A. Mangano, and R. L. Fagaly, "A Low-Mass Mounting Method for Cryogenic Inertial-Fusion Targets."

H. Kim, P. W. McKenty, and P. Cheng, "Confocal Microscopy of Inertial-Fusion Fuel Capsules."

C. P. Verdon, "Target Requirements for the OMEGA Upgrade."

M. D. Wittman, "Compensation of the Lens Effects of Thick Cryogenic Layers Using an Interferometric Imaging System."

The following presentations were made at the Materials Research Society 1993 Fall Meeting, Boston, MA, 29 November–3 December 1993:

P. Gierlowski, W. Kula, S. J. Lewandowski, and R. Sobolewski, "Microwave Response of Mixed-Phase $Bi_2Sr_2Ca_2Cu_3O_x$/ $Bi_2Sr_2Ca_1Cu_2O_y$ Thin Films."

W. Kula and R. Sobolewski, "Hydrogen Doping of Y-Ba-Cu-O Thin Films with Various Oxygen Content."

L. Shi, T. Gong, W. Xiong, X. Weng, Y. Kostoulas, R. Sobolewski, and P. M. Fauchet, "Dependence of Femtosecond Reflectivity on the Oxygen Content in Y-Ba-Cu-O Thin Films."

W. Kula and R. Sobolewski "Electric-Field Effect in Partially Oxygen-Depleted, Superconducting Y-Ba-Cu-O Thin Films," 1994 Gordon Research Conference on Superconductivity, Oxnard, CA, 2–7 January 1994.

The following presentations were made at SPIE's OE/LASE '94, Los Angeles, CA, 22–28 January 1994:

S. Alexandrou, C.-C. Wang, M. Currie, R. Sobolewski, and T. Y. Hsiang, "Loss and Dispersion at Subterahertz Frequencies in Coplanar Waveguides and Varying Ground-Plane Widths."

D. P. Butler, W. N. Maung, W. Xiong, W. Kula, and R. Sobolewski, "Microwave Properties of Monolithic Y-Ba-Cu-O Transmission Line Devices Fabricated by the Laser-Writing Patterning Technique."

D. Fried, S. F. Borzillary, S. M. McCormack, R. E. Glena, J. D. B. Featherstone, and W. Seka, "The Thermal Effects on CO_2 Laser-Irradiated Dental Enamel at 9.3, 9.6, 10.3, and 10.6 mm."

Y. Kostoulas, P. M. Fauchet, T. Gong, B. C. Tousley, G. W. Wicks, and P. Cooke, "Femtosecond Carrier Dynamics in Low-Temperature-Grown III–V Semiconductors."

A. I. Lobad, P. J. Rodney, B. C. Tousley, S. M. Mehta, and P. M. Fauchet, "The Starting Mechanism in Coupled-Cavity, Mode-Locked Laser Systems."

R. Sobolewski, L. Shi, W. Xiong, X. Weng, Y. Kostoulas, and P. M. Fauchet, "Femtosecond Optical Response of Y-Ba-Cu-O Films and Their Applications in Optoelectronics."

C.-C. Wang, S. Alexandrou, D. Jacobs-Perkins, and T. Y. Hsiang, "Picosecond Characteristics of Silicon-on-Insulator Metal-Semiconductor-Metal Photodiodes."

W. Xiong, W. Kula, R. Sobolewski, and J. R. Gavaler, "Laser Writing: A New Technique for Fabrication of Electronic and Optoelectronic Y-Ba-Cu-O Devices and Circuits."

W. R. Donaldson, D. Gupta, and A. M. Kadin "High-Temperature, Superconducting Switches for SMES Applications," The Advisory Group on Electron Devices 1994 High-Voltage Workshop, Smyrna, GA, 1–3 March 1994.

The following presentations were made at the Materials Research Society Spring '94 Meeting, San Francisco, CA, 4–8 April 1994:

S. D. Jacobs, A. L. Rigatti, D. J. Smith, L. D. Lund, H. M. D'Alessandro, K. L. Marshall, and A. W. Schmid, "Design and Manufacture of Laser Quality Liquid Crystal Optics." (invited)

E. M. Korenic and S. D. Jacobs, "Selective Reflection Properties of Embedded Pre-Aligned Cholesteric Domains as Functions of Incident Angle."

J. C. Mastrangelo and S. H. Chen, "Thermotropic Side-Chain Polymers Carrying High Optical Birefringence Nematogenic Group."

H. Shi and S. H. Chen, "Novel Glassy Nematic and Chiral Nematic Oligomers Derived from 1,3,5-Cyclohexanetricarboxylic and (1R,3S)-(+)-Camphoric Acids."

L. Shi, T. Gong, W. Xiong, X. Weng, R. Sobolewski, and P. M. Fauchet, "Femtosecond Optical Spectroscopy in Partially Deoxygenated Y-Ba-Cu-O Thin Films," Ultrafast Phenomena Ninth International Meeting, Dana Point, CA, 1–5 May 1994.

The following presentations were made at the APS 10th Annual High-Temperature Plasma Diagnostics, Rochester, NY, 8–12 May 1994:

T. R. Boehly, R. S. Craxton, R. J. Hutchison, J. H. Kelly, T. J. Kessler, S. A. Kumpan, S. A. Letzring, R. L. McCrory, S. F. B. Morse, W. Seka, S. Skupsky, J. M. Soures, and C. P. Verdon, "The Upgrade to the OMEGA Laser System."

D. K. Bradley, P. M. Bell, O. L. Landen, J. D. Kilkenny, and J. Oertel, "Development and Characterization of a Pair of 30-40 ps X-Ray Framing Cameras."

P. A. Jaanimagi, R. C. Elton, B. L. Welch, Y. Leng, and H. R. Griem, "Extending X-Ray Streak Camera Operation to VUV Wavelengths."

J. P. Knauer, R. L. Kremens, M. A. Russotto, and S. Tudman, "Using Cosmic Rays to Monitor Large Scintillator Arrays."

R. L. Kremens, M. A. Russotto, and S. Tudman, "Performance Simulations of the MEDUSA Neutron Detector."

S. A. Letzring, "Laser and Plasma Diagnostics for the OMEGA Laser System." (invited)

F. J. Marshall and B. Yaakobi, "Quantitative Measurements with X-Ray Microscopes in Laser-Fusion Experiments."

B. Yaakobi, R. Epstein, Q. Su, F. J. Marshall, and D. Shvarts, "Target Imaging and Backlighting Diagnostic on the OMEGA Upgrade."

B. Yaakobi, F. J. Marshall, R. Epstein, D. K. Bradley, P. A. Jaanimagi, and Q. Su, "New Diagnostic Features in the Laser Implosions of Argon-Filled Targets."

The following presentations were made at CLEO '94, Anaheim, CA, 8–13 May 1994:

S. Alexandrou, C.-C. Wang, M. Currie, R. Sobolewski, and T. Y. Hsiang, "Terahertz Spectral Analysis of Straight and Bent Coplanar Transmission Lines."

X. D. Cao, G. P. Agrawal, and D. D. Meyerhofer, "Optimization of Optical Beam Steering in Nonlinear Kerr Media Via Spatial Phase Modulation."

C. Y. Chien, G. Korn, J. S. Coe, X. Liu, J. Squier, G. Mourou, R. S. Craxton, and J.-C. Kieffer, "High-Efficiency Frequency Doubling of Ultra-High Intensity Nd: Glass Laser Pulses."

J. H. Kelly, T. R. Boehly, D. L. Brown, and M. D. Tracy, "The Upgrade to the OMEGA Laser System: A Status Report." (invited)

A. Okishev, M. D. Skeldon, and W. Seka, "Optical Pulse Compression by Stimulated Scattering for Pulse-Shaping Applications in the OMEGA Upgrade Laser."

L. Zheng and D. D. Meyerhofer, "A Linear Cross-Correlation Technique for Single-Shot Measurements of Weak Light Pulses."

The following presentations were made at IQEC '94, Anaheim, CA, 8–13 May 1994:

D. D. Meyerhofer, J. Chaloupka, and J. Peatross, "High-Harmonic Generation with an Annular Laser Beam."

C. I. Moore, J. P. Knauer, and D. D. Meyerhofer, "Observations of Ponderomotively Accelerated Electrons from the Focus of a Very-High-Intensity Laser."

R. A. London, R. P. Ratowsky, A. L. Osterheld, and R. S. Craxton, "Complete X-Ray Laser Modeling: Hydrodynamics, Kinetics, and Optics," 4th International Colloquium on X-Ray Lasers, Williamsburg, VA, 16 May 1994.

The following presentations were made at the 24th Annual Anomalous Absorption Conference, Pacific Grove, CA, 5–10 June 1994:

U. Alon, J. Hecht, D. Ofer, D. Mukamel, and D. Shvarts, "Bubble-Competition Model for Hydrodynamically Unstable Interfaces."

R. Betti, V. Goncharov, R. L. McCrory, E. Turano, and C. P. Verdon, "Cutoff Wave Numbers of the Incompressible Ablative Rayleigh-Taylor Instability."

A. Chirokikh, W. Seka, R. E. Bahr, R. S. Craxton, R. W. Short, A. Simon, and M. D. Skeldon, "Stimulated Brillouin Scattering at 1 μm in Long-Scale-Length Laser Plasmas."

R. S. Craxton, M. Dunne, O. Willi, and T. Afshar-Rad, "Simulations of Soft X-Ray Generated Plasmas Created to Enhance Thermal Smoothing."

J. A. Delettrez, "An Interactive Mix Model in *LILAC* for Linear and Near-Linear Regimes of the Rayleigh-Taylor Instability."

E. M. Epperlein, R. W. Short, and A. Simon, "Ion Thermal Conductivity and Viscosity for Plasmas with Light and Heavy Ions."

E. M. Epperlein and R. W. Short, "Nonlocal Electron Transport in the Presence of High-Intensity Laser Irradiation."

R. Epstein, S. Skupsky, and C. P. Verdon, "Smoothing of Laser Irradiation of ICF Targets Using Pre-Formed Refracting Atmospheres with Small-Scale Inhomogeneity and Time Dependence."

J. Hecht, D. Ofer, U. Alon, T. Tlusty, D. Shvarts, C. P. Verdon, R. L. McCrory, and S. A. Orszag, "Three-Dimensional Simulation of the Late Nonlinear Stage of the Rayleigh-Taylor Instability."

T. Kolber, C. J. McKinstrie, R. Betti, and R. E. Giacone, "Numerical Simulations of Two-Dimensional Stimulated Brillouin Scattering."

J. S. Li, C. J. McKinstrie, C. Joshi, and K. Marsh, "Thermal Filamentation of Counterpropagating Laser Beams."

C. J. McKinstrie, R. Betti, R. E. Giacone, T. Kolber, and J. S. Li, "Two-Dimensional Stimulated Brillouin Scattering."

D. D. Meyerhofer, H. Chen, J. A. Delettrez, E. M. Epperlein, Y. Fisher, and B. Soom, "Flux Limiter in Picosecond Laser-Plasma Interactions."

D. Ofer, U. Alon, D. Shvarts, C. P. Verdon, and R. L. McCrory, "A Modal Model for the Nonlinear Evolution of Multimode Rayleigh-Taylor Mixing Zone."

R. W. Short and E. M. Epperlein, "Generalized Fluid Models for Laser-Irradiated Plasmas."

A. Simon and R. W. Short, "Stimulated Scattering from Low-Frequency Modes in Laser-Produced Magneto-Plasmas."

C. T. Cotton, "The Design of an All-Spherical, Three-Mirror, Off-Axis Telescope Objective," International Optical Design Conference, Rochester, NY, 6–9 June 1994.

M. J. Cumbo, D. Fairhurst, S. D. Jacobs, and B. E. Puchebner, "The Effect of Chemically Modulated Surface Charge in the Polishing of Optical Glass," OSA Science of Finishing (1994), Rochester, NY, 6–8 June 1994.

The following presentations were made at the OSA Optical Fabrication and Testing Workshop, Rochester, NY, 7–9 June 1994:

P. D. Funkenbusch, Y. Y. Zhou, C. Lohnes, D. J. Quesnel, S. D. Jacobs, B. E Puchebner, D. Golini, and A. Lindquist, "Deterministic Microgrinding of Glass with Polycrystalline Diamond Tools."

W. I. Kordonsky, I. V. Prokhorov, S. D. Jacobs, B. E. Puchebner, Y. Hsu, D. Pietrowski, and D. Stafford, "Glass Polishing Experiments Using Magnetorheological Fluids."

W. I. Kordonsky, I. V. Prokhorov, B. E Kashevsky, S. D. Jacobs, B. E. Puchebner, Y. Hsu, D. Pietrowski, and D. Stafford, "Basic Properties of Magnetorheological Fluids for Optical Finishing."

W. Ng, B. E. Puchebner, and S. D. Jacobs, "Evaluation of Bound Abrasive Media for Fabrication of Ring Tool Polishers."

B. E. Puchebner, "Chlorofluorocarbons in the Workplace: A Summary of Guidelines and Alternatives."

B. E. Puchebner, A. Feltz, W. Ng, and S. D. Jacobs, "Coolant Performance in Bound Diamond Ring Tool Grinding of K7 Optical Glass."

B. E. Puchebner, A. Feltz, and S. Patterson, "The Effect of Additives in a Commercial Coolant on the Glass Grinding Process."

E. M. Korenic, "Fractured Cholesteric Liquid Crystal Polymers," UNY-VAC American Vacuum Society Annual Meeting, Rochester, New York, 9 June 1994.

The following presentations were made at M_2S-HTSC IV, Grenoble, France, 5–9 July 1994:

W. Kula and R. Sobolewski, "Effect of Hydrogen Doping on Electrical Properties of Y-Ba-Cu-O Thin Films."

D. Wu, W. Kula, and R. Sobolewski, "Hopping Transport in Y-Ba-Cu-O Films with Different Oxygen Content."

E. M. Korenic and S. D. Jacobs, "Selective Reflection Properties of Cholesteric Liquid Crystal Polymers," 3rd Annual Symposium on Materials Research, Rochester, NY, 16 August 1994.

The following presentations were made at the High Field Interactions and Short Wavelength Generation Topical Meeting, St. Malo, France, 21–25 August 1994:

D. D. Meyerhofer, J. Chaloupka, and J. Peatross, "High-Order Harmonics Emitted from Low-Density Gas Targets."

D. D. Meyerhofer, C. I. Moore, and J. P. Knauer, "Forward Ponderomotive Acceleration of Electrons from the Focus of a High-Intensity Laser."

J. L. Peatross, J. Chaloupka, and D. D. Meyerhofer, "High-Order Harmonic Generation with an Annular Laser Beam."

C. P. Verdon and R. L. McCrory, "Direct-Drive Capsule Physics," ECLIM '94, Oxford, England, 19–23 September 1994.

R. L. McCrory, J. M. Soures, C. P. Verdon, T. R. Boehly, D. K. Bradley, R. S. Craxton, J. A. Delettrez, R. Epstein, P. A. Jaanimagi, S. D. Jacobs, R. L. Keck, J. H. Kelly, T. J. Kessler, H. Kim, J. P. Knauer, R. L. Kremens, S. A. Kumpan, S. A. Letzring, F. J. Marshall, P. J. McKenty, S. F. B. Morse, A. Okishev, W. Seka, R. W. Short, M. D. Skeldon, S. Skupsky, M. Tracy, and B. Yaakobi, "Direct-Drive Laser Fusion Experimental Program at the University of Rochester Laboratory for Laser Energetics," 15th International Conference on Plasma Physics and Controlled Nuclear Fusion Research, Madrid, Spain, 26 September–1 October 1994.